Synthesis, Nanoparticle Encapsulation, and Magnetic Resonance Studies of Metal-Based Anticancer Complexes

by

Gregory MacNeil

B.Sc., Mount Allison University, 2016

Thesis Submitted in Partial Fulfillment of the
Requirements for the Degree of
Doctor of Philosophy

in the
Department of Chemistry
Faculty of Science

SIMON FRASER UNIVERSITY
Summer 2023

Declaration of Committee

Name:	**Gregory MacNeil**
Degree:	**Doctor of Philosophy (Chemistry)**
Thesis title:	**Synthesis, Nanoparticle Encapsulation, and Magnetic Resonance Studies of Metal-Based Anticancer Complexes**
Committee:	**Chair:** **Paul Li** Professor, Chemistry
	Charles Walsby Supervisor Associate Professor, Chemistry
	Tim Storr Committee Member Professor, Chemistry
	Andrew Bennet Committee Member Professor, Chemistry
	Jeffrey Warren Examiner Associate Professor, Chemistry
	Annie Castonguay External Examiner Professeure Agrégée, Organometallic Chemistry Laboratory Institut National de la Recherche Scientifique

Abstract

Since the discovery of cisplatin, metal complexes continue to gain interest as anticancer agents. Though a breadth of research has been conducted in this field, many pitfalls and questions remain, such as off-target activity and how exactly metal complexes exhibit their activity. In the search for novel complexes that address these issues, ruthenium and copper have become leading choices. Though a vast array of complexes employing these metals have been reported, their clinical development has often been hindered by low activity and a lack in understanding of their mechanism of action. The work in this thesis looks to address these issues in two ways: (i) by developing novel complexes and methods to breath new life into well-studied metal compounds and (ii) employ magnetic resonance spectroscopies to examine their behaviour in relevant biological environments. Chapter 2 discusses the synthesis of a novel Ru(II)-arene complex appended with a selective estrogen receptor modifier to target breast cancer. These novel complexes were subjected to several different cell assays, including the National Cancer Institute NCI-60 screen, which showed increased activity over the inactive parent ruthenium scaffolds. Chapter 3 presents ^{19}F magnetic resonance imaging methods to develop the theranostic applications of a CF_3-appended Keppler-type Ru(III) complex. It is shown that these methods can be used to spatially resolve redox and speciation events in tumour tissues, which is important to understanding their mechanism of action. Chapter 4 presents a robust method to encapsulate these CF_3 appended Ru(III) anticancer complexes in polymer nanoparticles to increase their aqueous stability. Cell studies revealed an over 10-fold increase in anticancer activity over the free complexes. Chapter 5 presents and in-depth magnetic resonance study of the aqueous solution behaviour of the copper anticancer complex CasIII-ia. EPR and NMR studies were used to characterize Cu species following dissolution in complex solutions containing HSA, and in the presence of whole cells. Finally, Chapter 6 presents a novel Ru(II)-Ru(III) complex combing the unique biological activities of an organometallic Ru(II) RAPTA-type scaffold and a Ru(III) Keppler-type coordination complex. Cytotoxicity studies of the new dinuclear complex show increased activity relative to mononuclear parent compounds.

Keywords: Medicinal inorganic chemistry; magnetic resonance; polymer nanoparticles; cancer

This thesis is dedicated to Mom and Dad.

Acknowledgements

I must first extend my thanks to my supervisor Dr. Charles Walsby. Thank you for accepting me into your group, supporting my sporadic work-life balance, and pushing me to be a better scientist. I would have been lost down the magnetic resonance rabbit hole without your guidance and your trust in my use of your EPR spectrometer. I would also like to thank my committee member Dr. Tim Storr for your enthusiastic suggestions and always being available to chat over the course of my degree. You've helped me to stay excited about my work over the years and it has been a great opportunity to collaborate with your group. Thank you to Dr. Andrew Bennet for agreeing to be on my committee and for your helpful synthetic insights. To Dr. Eric Ye, thank you for all the time you put into teaching about and training me on NMR and MRI. Our chats in the imaging lab helped me realise how much I enjoyed these techniques, and I would not have been able to publish my MRI manuscript without your help. I must also thank NSERC (CGS-D) and SFU for the generous funding they provided me over the course of my degree. I would like to extend a sincere thank you to Devon Heroux in Marcel Bally's lab at the BCCancer Agency for all the work he has done for me over the course of my degree, from cytotoxicity assays to excised tumours. I must also thank Tristen Bridle who ran ICP-AES experiments in Jurgen Gailer's lab for some of my nanoparticle data which required a lot of difficult problem solving. To Wen Zhou, thank you not only for your endless help with x-ray crystallography and with keeping the department instruments in working order, but also for your friendship. I must also thank Bryton Varju for all your crystallographic assistance and for being a great friend and climbing partner.

I will not do justice all the help my lab-mates have given me during my time in the Walsby Lab. To Kate Prosser, thank you for being there from picking me up the very first day I landed in Vancouver, to putting up with my endless questions, to planning wine tours in Penticton, to lending me your car so I could escape to the mountains. I feel I cannot thank you enough for how much you've taught me about chemistry and spectroscopy but also for making the Walsby lab such a fun and welcoming environment. To Shaner, thanks for always being willing to listen to my incessant complaining, for teaching me everything I needed to know about synthetic chemistry, and for always being down to have a beer. Thanks for showing me the best places to eat in Vancouver – looking forward to more life contemplation over cheap beers at the Hyde.

I must also thank Aryan and Saeid for putting up with my perpetual morning coffee complaining. I would not have made it through the pandemic with my sanity without your friendship and company in the lab. Thanks to Saeid for making the ups and downs of diving into the world of nanoparticle formulation world tolerable. I had the pleasure of working with several undergraduates throughout my degree and they all made my experience more fulfilled, especially seeing some of them continuing their careers in chemistry. I must specifically thank Kaitlin Branch and Ian Chagunda as they each had to put up with me for an entire summer. Thank you for all your hard work and for making the time worked together some of the most enjoyable of my graduate career. I must also extend a huge thank you to Myles Peeters for all his hard work on the CasIII-ia spectroscopy project in Chapter 5.

Words will not suffice in thanking my family for the support they've provided me throughout my time at SFU. To Mom and Dad, thank you for always being there for me from bouncing between different graduate programs to moving across the country for my PhD. You are both my biggest role models and I wouldn't be where I am today without your support. To Nan, I wouldn't be here without your endless smoothies and hugs – sorry it took so long to graduate. To Lauren, thanks for always being there for me to chat about life and keeping my head on straight about what's truly important. I've always looked up to you and you've always been a big inspiration for me when life is feeling hard. I can't wait to show Mavi the "cool" pictures in here, the rest may put her to sleep. I have to extend a sincere thank you to Mel for being the best adventure, ski, and crossword pal. I would not have made it through the writing of this thesis without your support. To the boys, thanks for keeping your sense of humour and for keeping my ego in check. You all have been a second family to me. To Curtis, thanks for being a great roommate and a better friend throughout our journeys at SFU. I would not have survived the lockdowns without you, and I would not have made it through this writing process without your company at Bomber and Slappy. I must especially thank C.J. and Zach for putting up with me since elementary school and still agreeing to be my friend – this is no easy feat. Thank you, Zach, for putting the effort in to visit me, CLR, and for changing the khakis. Thanks to Marge for being team mom and planning all the get togethers and for the friendship during those Sackville Summers.

Table of Contents

List of Tables

List of Figures

List of Abbreviations

acac	acetylacetone, pentane-2,4-dione
AES	atomic emission spectroscopy
BOLD-100	Na[trans-Ru(III)Cl_4(indazole)$_2$], sodium *trans*-[tetrachlorobis(1*H*-indazole)ruthenate(III)]
bpy	bipyridine
Cas	Casiopeinas
CasIII-ia	Casiopeinas III-ia
cat B	Cathepsin B
CF3Im	4-(trifluoromethyl)imidazole
CHESS	chemical shift selective imaging
CPMG	Carr-Purcell-Meiboom-Gill
CSI	chemical shift imaging
Ctr1	high affinity copper transport protein 1
CV	cyclic voltammetry
DCM	dichlormethane
dha	dihydroanthracene
dip	diphenylphenanthroline
DIPEA	di(isopropyl)ethylamine
DLS	dynamic light scattering
dmbpy	4,4'-dimethylbipyridine
DMEM	Dulbecco's Modified Eagle Medium
DMSO	dimethyl sulfoxide
DNA	deoxyribonucleic acid
DOSY	diffusion ordered spectroscopy
dppz	dipyridophenazine
en	ethylenediamine
ENDOR	Electron-nuclear double resonance
EPR	electron paramagnetic resonance
EPRe	enhanced permeability and retention effect
ER	estrogen receptor
ESI	electrospray ionization
ESR	electron spin resonance
Et_2O	diethylether
EtOH	ethanol
Fc	ferrocene
FDA	The United States Food and Drug Administration

FID	free induction decay
FLASH	fast low-angle shot
FOV	field of view
FWHH	full width at half height
GI	growth inhibition
GSH	glutathione
GST P1-1	glutathione S-transferase P
HATU	1-[Bis(dimethylamino)methylene]-1*H*-1,2,3-triazolo[4,5-*b*]pyridinium 3-oxid hexafluorophosphate, hexafluorophosphate azabenzotriazole tetramethyl uronium
HEWL	hen egg white lysozyme
HSA	human serum albumin
ICP	inductively coupled plasma
IndCF3	5-(Trifluoromethyl)-1H-indazole
KP1019	indazolium [trans-Ru(III)Cl_4(indazole)$_2$], idazolium *trans*-[tetracholorbis(1*H*-indazole)ruthenate(III)]
MeOH	methanol
MES	2-(N-morpholino)ethanesulfonic acid
MR	magnetic resonance
MRI	magnetic resonance imaging
NaDT	sodium dithionite
NHE	normal hydrogen electrode
NMR	nuclear magnetic resonance
NP	nanopaticle
PB	phosphate buffer
PBS	phosphate buffered saline
PDI	polydispersity index
PEG	polyethyelene glycol
PF127	Pluronic F127
PLA	poly(lactic acid)
PLGA	poly(lactic-co-glycolide)
PRE	paramagnetic relaxation enhancement
PSMA	prostate-specific membrane antigen
PTA	1,3,5-triaza-7-phosphaadamantane
PTFE	polytetrafluoroethylene
RARE	rapid acquisition with refocused echoes
RF	radio frequency
RMSE	root mean standard error
ROI	region of interest
ROS	reactive oxygen species

SERM	selective estrogen receptor modulator
SI	signal intensity
SNR	signal-to-noise ratio
TA	acquisition time
TCA	trichloroacetic acid
TE	echo time
THF	tetrahydrofuran
TLC	thin layer chromatography
TR	repetition time
TSC	thiosemicarbazone
XAS	x-ray absorption spectroscopy

1 Introduction

1.1. Metal-based anticancer agents

Interest in the use of metal complexes as anticancer agents increased significantly following the serendipitous discovery of the anticancer activity of *cis*-diamminedichloroplatnium(II) (**Figure 1**), commonly known as cisplatin, in 1965 by Rosenberg *et al*.[1] While investigating the effects of an applied electric field on bacterial growth they noticed abnormal elongation of the bacterial cells – a typical indication of bacterial cell death. This was eventually attributed to the exposure of the bacteria to platinum leaching from the electrodes, forming the later-identified cisplatin through coordinate interactions with ammonium chloride in the growth media. Today, cisplatin is still one of the most widely administered chemotherapeutics for several types of malignancies including ovarian, testicular, lung, and head and neck cancers.[2] Eventually, it was determined that cisplatin exhibited its anticancer activity by forming coordinate interactions with DNA, mainly with the N_7 of the guanine nucleotide, following hydrolysis of one or more of the chloride ligands.[3,4] These interactions, typically referred to as DNA lesions, form inter- and intra-strand cross-links that can trigger apoptosis leading to cell death. Since the early success of cisplatin numerous Pt(II) analogues have been reported with a small number being approved for clinical use (**Figure 1.1).**[5]

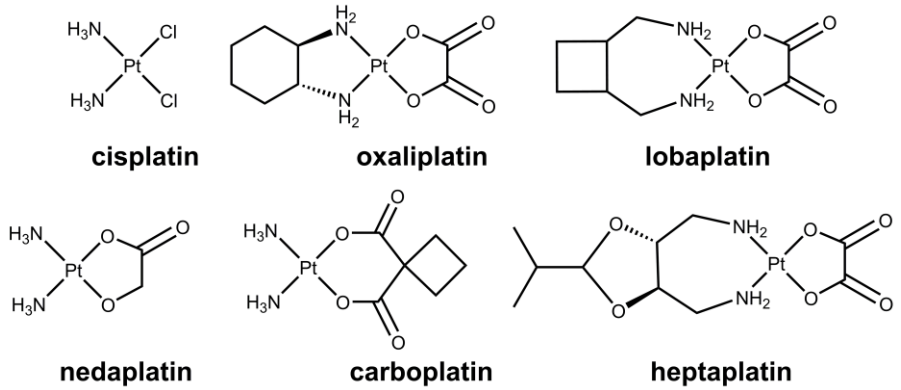

Figure 1.1 Clinically approved platinum anticancer agents.

Unfortunately, cisplatin lacks selectivity and forms DNA lesions in both cancerous and healthy cells. Such off-target interactions cause harmful side-effects such as nausea, vomiting, hair loss, and kidney and neuro toxicity.[6] This is problematic as patients may not be inclined to follow their optimal treatment regime and there dosage

may be restricted. Furthermore, many cancers display intrinsic or acquired resistance to cisplatin further complicating chemotherapy.[7–11] Though some of the above-mentioned derivatives of cisplatin have improved toxicity profiles,[12–19] generally attributed to increased aqueous stability in the bloodstream, they still display off-target activity and suffer from similar resistance pathways to cisplatin.[20] These issues have sparked extensive research into other-metal containing complexes as anticancer agents. Several entities containing non-platinum metal have even reached various stages of clinical,[21] and preclinical development such as gold,[22,23] gallium,[24] copper,[25–27] arsenic,[28–31] titanium,[32–34] rhenium,[35–39] osmium,[40–43] iridium,[44–48] and ruthenium.[49–52]

1.2. Ruthenium Anticancer Complexes

Ruthenium has become one of the leading metal candidates in the search for metal-based anticancer agents beyond cisplatin. It is an attractive transition metal for use in biological environments for several reasons including: (i) a thoroughly established coordination chemistry, (ii) ligand exchange rates that are slow enough to be within the window of cell division (10^{-3} to 10^{-2} s^{-1} for water exchange rates with the Ru ion), (iii) a variety of accessible oxidation states with 2+ and 3+ being the most common under physiological conditions, and (iv) octahedral coordination geometry which allows for a diverse range of ligands and biological activity that differ from classical Pt(II)-type anticancer compounds.[53–55] This last point is particularly important as the chemistry and biological activity of a ruthenium anticancer agent can be controlled through modification of its ligand set. Compounds can, therefore, be designed in which the ligands tune the properties of the ruthenium, provide complementary anticancer activity, act as targeting agents, or provide a spectroscopic handle for mechanistic investigations.[56–59]

Investigations into the biological activity of ruthenium complexes date back to the 1950s.[60] Even the dye ruthenium red $[Ru_3O_2(NH_3)_{14}]Cl_6$ (**Figure 1.2**), originally developed as a cell membrane stain, has been thoroughly investigated for its antitumour activity.[61,62] The first ruthenium anticancer complexes of note were reported by Clarke and coworkers in the 1980s.[63] These compounds, *cis*-$[RuCl_2(NH_3)_4]Cl$ (**Figure 1.2a**) and *fac*-$[RuCl_3(NH_3)_3]$ (**Figure 1.2b**), both displayed activity against primary tumours, with the tetra-amine complex showing activity against a wide variety of cell lines.[64] Unfortunately, these pioneering complex ions of ruthenium showed low aqueous solubility which limited their use as anticancer drugs. In an effort to address this issue, Alessio *et al*. developed

several water soluble ruthenium(III) complexes containing a varying number of dimethyl sulfoxide ligands, such as *cis*-[$RuCl_2$(DMSO-S)$_3$(DMSO-O)] (**c**) (**Figure 1.2c**) and *trans*-[$RuCl_2$(DMSO-S)$_4$] (**d**) (**Figure 1.2d**).[65] Compound **c** did not display cytotoxicity *in vitro* but did display primary antitumour activity and antimetastatic activity in mouse studies. Interestingly, **d** was shown to be more selective toward metastases than cisplatin though it was less active against primary tumours.[66]

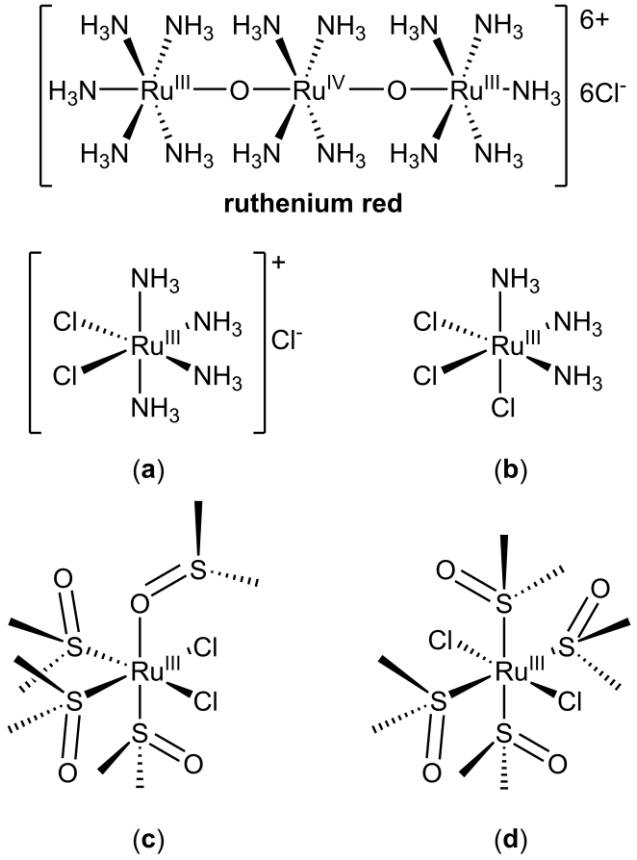

Figure 1.2 Examples of some of the first ruthenium complexes that were investigated for their anticancer activity.

1.2.1. Ruthenium(III) anticancer complexes bearing heterocyclic N-donor ligands

As the hunt continued for the next ruthenium anticancer agent, reports of a new class of compounds that contained one or more nitrogen-containing heterocycles began to emerge. Keppler and coworkers were the first to report this type of ruthenium complex in which two imidazole (**Figure 1.3, KP418**)[67,68] or two indazole (**Figure 1.3, KP1019**)[69] ligands are coordinated in a *trans* configuration along with four axial chloride ligands. A

protonated imidazolium (**KP418**) or indazolium (**KP1019**) act as counterions, respectively. Promisingly, both compounds showed good activity against colorectal cancer and even showed activity in cisplatin resistant tumours.[70,71] Unfortunately, **KP418** displayed a poor toxicity profile in mouse models and focus was shifted toward the further development **KP1019**.[72] The differences in toxicities is thought to arise from the influence that the axial ligand set has on interactions with serum proteins, such as human serum albumin (HSA).[73] Eventually **KP1019** entered phase-I clinical trials, but limits on aqueous solubility inhibited maximum tolerable dose studies.[74] To address this issue, a sodium compensated analogue was developed that displayed much higher aqueous solubility (**Figure 1.3, KP1339**). This compound has since been studied in several rounds of clinical trials, and is currently branded as BOLD-100 in a phase-IIb clinical trial spearheaded by Bold Pharmceuticals.[75–78]

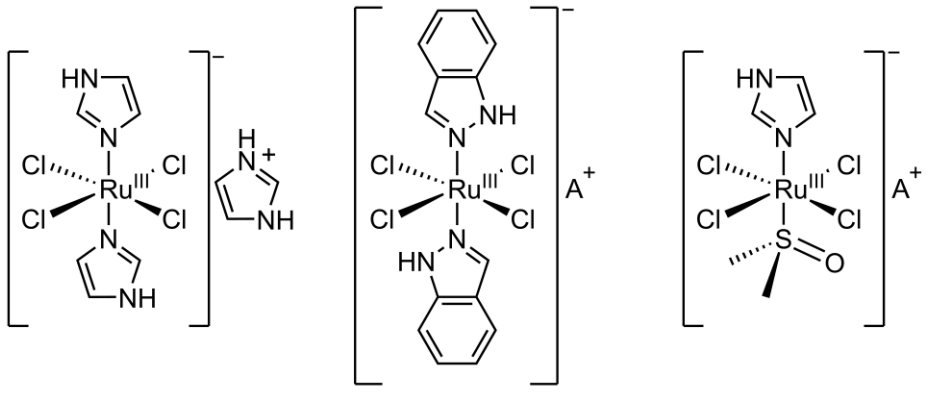

Figure 1.3 Ruthenium(III) anticancer agents that have entered varying stages of clinical trials.

Alongside the pioneering work of Keppler *et al.*, Alessio and coworkers reported a ruthenium(III) complex that was structurally similar to **KP418** except one of the axial imidazole ligands was replaced with dimethyl sulfoxide (DMSO). This sodium-compensated complex, called **NAMI** (**Figure 1.3**), showed low cytotoxicity but was able to selectively inhibit the formation of metastases in mice.[79] The Alessio group also synthesized the imidazolium-compensated analogue of **NAMI**, **NAMI-A** (**Figure 1.3**), which displayed similar antimetastatic activity and was found to be more suitable for clinical formulations than **NAMI**. In 1999, **NAMI-A** became the first ruthenium complex to enter phase-I clinical trials. **NAMI-A** eventually made it through an initial phase-II study

but did not proceed to an expanded phase-II trial as it was found to be no more efficacious than the standard of care at the time of study, gemcitabine.[80]

Though the ruthenium(III) anticancer complexes described above have undergone extensive preclinical and clinical studies, their mechanisms of action have yet to be fully elucidated. Many groups have presented interesting hypotheses on the main function or biological targets of these complexes including: (i) activation-by-reduction leading to more labile ruthenium(II) species that can then interact with biomolecules; (ii) DNA lesion formation similar to cisplatin; and (iii) mitochondrial damage via ROS generation. Following the successful clinical trials by Bold Pharmaceuticals, new work has suggested that BOLD-100 acts by damaging DNA repair mechanisms likely through ROS generation.[81] It has also been suggested that the complexes are delivered to cells by iron mimicking interactions with transferrin[64] and via adduct formation with serum proteins such as HSA.[64] Underlying most of these theories is the initial exchange of one or more of the parent ligands with water. A plethora of research has, therefore, gone into understanding how these exchange events occur and, in more complex systems, the subsequent biomolecule adducts that form following aquation.

It has been shown that Keppler- and NAMI-type complexes exchange ligands in aqueous media in a somewhat similar fashion to their platinum predecessors. Under physiological conditions, **KP1019** undergoes relatively slow chloride ligand exchange on the order of tens of minutes.[82,83] **NAMI-A** initially hydrolyzes at a faster rate than the Keppler-series, on the order of minutes, and first exchanges a DMSO or chloride ligand to give mono-aquo complexes.[84] Eventually, through further chloride ligand exchange events, oligomeric ruthenium complexes become the majority species in solution. These aqueous exchange events are pH and temperature dependant for both series of complexes.[85,86] Originally, the aqueous ligand exchange for **NAMI-A** and **KP1019** was thought to be a required event for DNA lesion formation, as with cisplatin. It was found that both complexes do, in fact, bind irreversibly to DNA, with **NAMI** displaying faster binding than cisplatin and **NAMI-A,** and **KP1019** showing slower binding. This difference in binding rates was attributed to differences in rates of hydrolysis and to the larger steric bulk of the axial ligand set for **KP1019**. It was also determined that the mode by which these complexes bound to DNA was different from cisplatin which may help to further explain the differences in cytotoxicity from their platinum predecessor.[87,88]

An important component of the mechanism of action of these ruthenium(III) complexes likely involves binding with serum proteins, such as HSA and transferrin, which leads to increased cellular uptake. These interactions for **NAMI-A** and **KP1019** have been extensively studied. Since the ruthenium(III) centres are paramagnetic (d^5, S = ½), electron paramagnetic resonance (EPR) spectroscopy has been valuable in elucidating the various adducts that form with serum proteins. Using EPR, the Walsby group has shown that both complexes rapidly bind in a non-covalent fashion to hydrophobic binding pockets of HSA, which preceeds aqueous ligand exchange and coordination to side-chain residues such as histidine.[89,90] X-ray absorption spectroscopy (XAS) and electron nuclear double resonance (ENDOR) spectroscopy have also been employed to further corroborate these interactions.[91–93] Using these techniques, adducts of **NAMI-A** and **KP1019** with various proteins such as HSA,[94] hen egg-white lysozyme (HEWL),[95,96] and carbonic anhydrase[97] have now been structurally elucidated, some at high resolution. These studies, in tandem with electrospray ionization-mass spectrometry (ESI-MS), suggest that the ruthenium complexes shed their original ligand set to form aquo-complexes coordinated to protein side-chain residues such as histidine. Even the more kinetically inert **KP1019** appears to shed both imidazole ligands to form adducts with HSA, suggesting both the KP- and NAMI-series of complexes are prodrugs. Fortunately, it has been shown that these Ru-protein adducts can still contribute to biological activity. For example, **NAMI-A**-HSA adducts display antimetastatic activity and promote increased cell adhesion.[98,99]

Interestingly, though the two complexes are structurally similar, **NAMI-A** displays negligible cytotoxicity compared to **KP1019** but higher antimetastatic activity. It has been shown to primarily accumulate in the extracellular matrix and on cell membranes whereas **KP1019** displays significantly higher cell uptake.[100] This difference in localization may explain the variance in their activities and highlights the need for more work to be conducted to gain a complete understanding of the mechanism of action of these iconic ruthenium complexes.

1.2.2. Ruthenium(II)-arene anticancer complexes

Following the successes of the pioneering ruthenium(III) anticancer agents, a new class of ruthenium(II) organometallic anticancer complexes began to emerge. These compounds also shared similar properties to cisplatin in that they contained labile

chloride ligands for aquation and eventual coordination with biomolecules. As discussed in section **1.2.1**, there was also a, now debated, idea that ruthenium(III) complexes were first activated by reduction within cells to form a more labile, 'activated' ruthenium(II) species.[101] This idea stimulated the initial development of this class of organometallic anticancer complexes.[102] These compounds usually consist of an η^6-arene ligand and a subset of non-organometallic ligands, either mono- or bidentate, that together make up a pseudo-octahedral coordination geometry about the ruthenium(II) centre. These 18-electron (d^6, S = 0) complexes are air stable and diamagnetic allowing for convenient synthesis and characterization. The arene ligand serves to stabilizes the ruthenium in the 2+ oxidation state and also presents as a hydrophobic surface for favourable lipophilicity, an important property for increased cell-uptake.[103] The non-arene ligand subset can then be chosen to modulate properties such as aquation rates, reduction potential, or selectivity. Early reports of promising biological activity, along with convenient and modular synthesis, have led Ru(II) organometallic complexes of this type to be some of the most derivatized ruthenium anticancer scaffolds reported.[104]

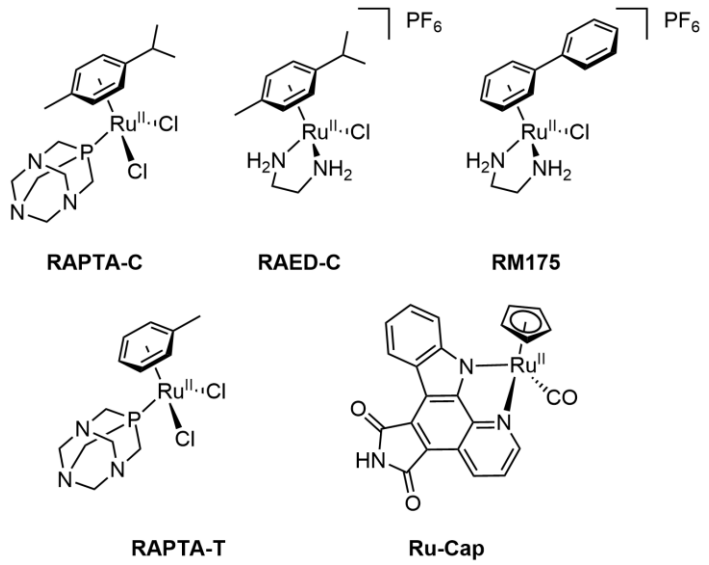

Figure 1.4 Leading ruthenium(II)-arene with promising anticancer activity.

Dyson and coworkers first presented the monodentate, or **RAPTA,** class of these complexes with the general formula (η^6-arene)Ru(PTA)X_2 (PTA = 1,3,5,-triaza-7-phosphatricyclo[3.3.1.1]decane; X_2 = halide) (**Figure 1.4, RAPTA**).[105–107] These complexes contain two exchangeable chlorides and a monodentate PTA ligand that greatly improves aqueous solubility. Interestingly, leading candidates, such as **RAPTA-C**

(**Figure 1.4**) in which the arene ligand is *p*-cymene, showed negligible cytotoxicity *in vitro* but displayed antimetastatic activity similar to **NAMI-A**.[108,109] In efforts to introduce cytotoxicity, many derivatives have been reported in which the PTA ligand was modified or the chloride ligands were replaced with other halogens or exchangeable ligands, such as oxalate, to adjust lipophilicity and aquation rates.[110–113] Unfortunately, it was found that such modifications had little affect on anticancer activity or biomolecule binding.[114] Increasing the hydrophobicity of the complex by replacing one of the chloride ligands with a neutral sigma-donor ligand, such as triphenylphosphine, was even found to decrease selectivity.[112] These results indicate that aquation and subsequent DNA-interactions may not be the primary mechanism in which RAPTA-type complexes display their activity. It was suggested that one of the main targets through which RAPTA-type complexes display their antimetastatic activity is by disrupting the function of proteins in the extracellular matrix, such as fibronectin. This has been suggested for RAPTA derivatives such as the toluene derivative, **RAPTA-T**, where the *p*-cymene is substituted for toluene (**Figure 1.4**).[108,115] Further evidence for protein and enzyme interactions being important in the biological activity of RAPTA-type complexes was presented by Messori and coworkers who reported that **RAPTA-C** displayed good inhibition of other enzymes important to cellular function such as thioredoxin reductase and cathepsin B (cat B).[116] They investigated a suite of RAPTA complexes with modified ligand sets, including direct arene modification, and found several derivatives to be excellent inhibitors of both enzymes. These findings led to the further development of half-sandwich complexes which vary from RAPTA-type ligand sets but still take advantage of the intrinsic three-dimensional structure that is advantageous for protein and enzyme interactions. For example, the complex **Ru-cap** (**Figure 1.4**), containing a cyclopentadienyl ligand, has been shown to mimic the carbohydrate fragment of the protein kinase inhibitor staurosporine (**Figure 1.4**).[117–119]

Another important class of ruthenium-arene anticancer complexes was originally reported by Sadler *et al.* with the general formula $[(\eta^6\text{-arene})Ru(L)X]^+$ where L is a bidentate ligand such as 1,2-diaminoethane (ethylenediamine, en) and X is a labile halide ligand such as chloride or iodide. Two of such complexes, **RAED-C** and **RM175** (where L = en =, X = Cl^-, and the arene ligands are *p*-cymene and biphenyl, respectively) showed promising activity against primary tumours with favourable toxicity profiles in mouse studies (**Figure 1.4**).[120] **RM175** has been shown to form DNA adducts analogous

to cisplatin following loss of chloride in aqueous media. It is thought that the extended biphenyl ligand works synergistically to increase these coordinate interactions through intercalation between DNA base pairs.[121] This intercalation can also induce damage to DNA. This strategy has been investigated further by appending extended aromatic systems to the ruthenium centre. For example, substitution of biphenyl for dihydroanthracene (dha) resulted in an increase in DNA distortions resulting from the greater ability of dha to intercalate between DNA base pairs.[121] While **RAED-C** does not contain an arene prone to intercalation, it has also been found to form coordinate interactions with DNA following loss of chloride. In certain cancer cell lines, such as cisplatin resistant ovarian carcinoma, A2780cisR, **RAED-C** has displayed anticancer activity in the low μM range.[121]

Recently, Davey and coworkers sought to shed led on the mechanistic differences between **RAPTA-C**, which primarily displays antimetastatic activity but shows negligible cytotoxicity, and **RAED-C** which displays high cytotoxicity.[122] Their study looked at the chromatin of cells treated with both **RAPTA-C** and **RAED-C** via size-exclusion chromatography-ICP-MS. They found that **RAPTA-C** was primarily associated with the protein component of the chromatin whereas **RAED-C** was associated with the DNA component. This was confirmed by X-ray structures of chromatin adducts of each complex which suggested the same variances in the primary location of the two complexes, possibly explaining their different biological activity. Unfortunately, neither **RAPTA-C** nor **RAED-C** have entered clinical trials.

Since the initial discoveries by Sadler and Dyson, much work has gone into the development of new ruthenium(II) arene anticancer candidates through modification of their ligand set. One such strategy involves coordination of a biologically active molecule as one of the non-arene ligands and several examples with promising biological activity are presented in **Figure 1.5**.[123] For example, Dyson *et al*. employed this strategy and replaced the two chloride ligands in **RAPTA-C** with curcumin or bisdemethoxycurcumin (**Figure 1.5a**).[124] Curcumin is shown to possess promising anticancer activity but is unstable and poorly soluble in aqueous media.[125] It was found that coordination to the ruthenium(II) complex not only mitigated these issues but also induced cytotoxicity in the low μM range against several cell lines including the cisplatin resistant ovarian carcinoma A2780cisR. This general method of derivatization has also been reported to

be successful in other studies, indicating it is a promising way to induce cytotoxicity in RAPTA-type complexes that typically display only antimetastatic activity.

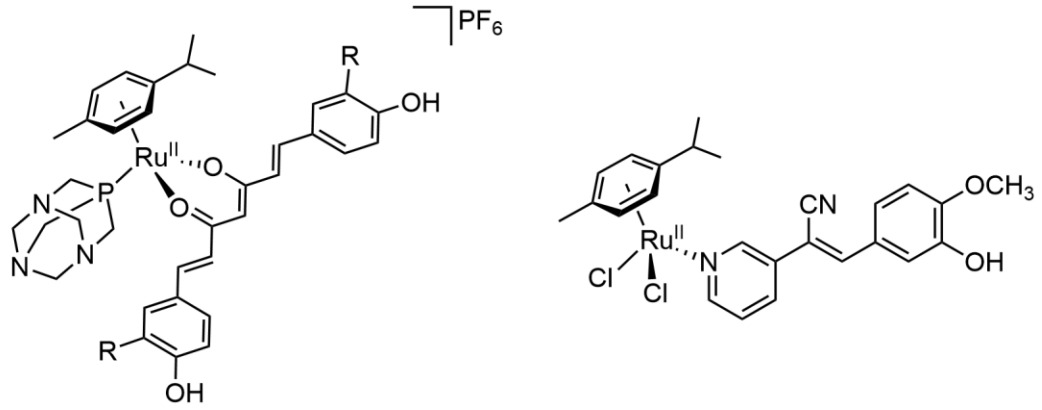

a) curcumin: R = OCH_3
bisdemethyoxycurcumin: R = H

b) Ru-EGFR

Figure 1.5 Examples of ruthenium(II)-arene anticancer complexes containing biologically active ligands as the non-arene ligand set.

Though it has been shown that ruthenium-arene anticancer complexes display improved toxicity profiles compared to cisplatin, some still suffer from a lack of selectivity. Parallel to the strategy of using cytotoxic molecules for the non-arene ligand set, several groups have explored appending molecules that are known to interact with specific biological targets to address issues of selectivity.[123] An interesting example of this strategy was reported by Schobert and co workers in which they coordinated epidermal growth factor receptor (EGFR) inhibitors to ruthenium-arene complexes (**Figure 1.5b**).[126] These complexes showed selectivity toward EGFR(+) cancer cell lines, such as MCF7 breast carcinoma cells, with IC_{50} values in the low nanomolar range.

A less common strategy to control the activity and selectivity of organometallic ruthenium anticancer complexes involves direct modification of the arene ligand. Dyson and coworkers demonstrated this approach by tethering the glutathione transferase (GST P1-1) inhibitor, ethacrynic acid, to the arene of a RAPTA-type complex in effort to mitigate resistance pathways exhibited by some cancers (**Figure 1.6a**).[127] As GST P1-1 is often overexpressed in solid tumours it presents as a good target for the selective release of ruthenium from dual functioning complexes of this type.[128] They found that the ethacrynic acid moiety binds to GST P1-1 and the RAPTA fragment is eventually cleaved, with the ruthenium moiety free to disrupt other cellular functions. The ethacrynic

acid fragment remains bound to GST and functions as an inhibitor, helping to mitigate ruthenium efflux through this known drug resistance pathway.[129–135] In similar work, the Dyson group has also appended the RAPTA-type complex to HSA through the arene ligand and saw increased internalization in cancer cells (**Figure 1.6b**). Interestingly, the HSA-Ru conjugate displayed an IC_{50} of 11 μM against A2780 ovarian carcinoma cells while RAPTA alone was inactive, suggesting the differences in activity may be associated with cellular uptake.[136] Some groups have also explored appending a secondary cytotoxic molecule to the RAPTA scaffold through the arene. For example, Dyson *et al.* attached the anticancer drug chlorambucil to the arene ligand using amide coupling chemistry, and found that the resulting dual functioning complex was more cytotoxic than the parent ruthenium and chlorambucil fragments alone (**Figure 1.6c**).[137] These examples point to the need for further exploration of targeted, multifunctional RAPTA- and RAED-type complexes via direct arene modification.

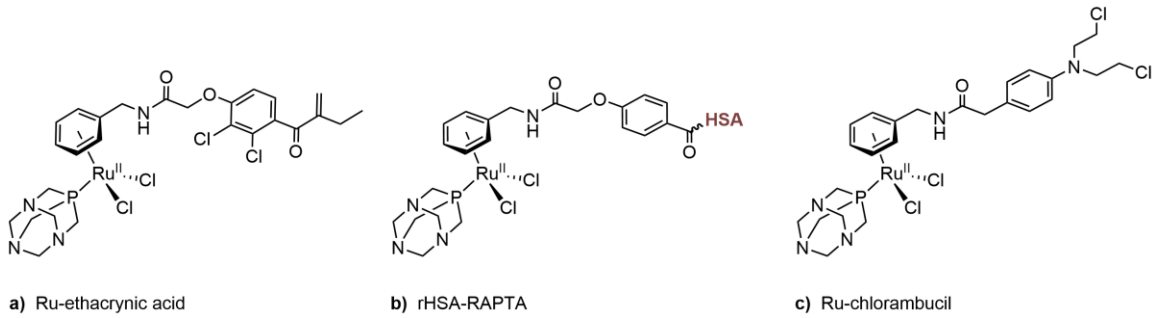

a) Ru-ethacrynic acid **b)** rHSA-RAPTA **c)** Ru-chlorambucil

Figure 1.6 Examples of ruthenium(II)-anticancer complexes modified with biologically relevant molecules through the arene ligand.

1.2.3. Other ruthenium anticancer complexes

Another major class of ruthenium anticancer agents are the so-called ruthenium polypyridyl complexes. These complexes were originally investigated for their biological toxicity in 1952 by Dwyer and Gyarfas.[60] Today, there are a plethora of this type of complex reported not just for their anticancer activity but also for their use as imaging probes and in photodynamic therapy.[104] Most often these complexes contain two or more *N,N*-chelating pyridyl ligands coordinated in an octahedral geometry about the Ru centre. These stable ruthenium(II) complexes are positively charged, which helps to encourage their interactions with biomolecules, like DNA, and leads to preferential lipophilicity and cell uptake.[138,139] Since the polypyridyl ligand sets are intrinsically planar, intercalation between base pairs is another common mode of anticancer activity

exhibited by these complexes.[140,141] Furthermore, they have been shown to generate ROS either through in-cell redox reactions or from photo-induced singlet oxygen generation.[142,143] Barton and coworkers have extensively studied many derivatives of ruthenium polypyridyl complexes with the general formula $[Ru(dip)_2(dppz)]^{2+}$ (dip = 4,7-diphenylphenanthroline; dppz = dipyridophenazine) in an effort to increase cell-uptake (**Figure 1.7a**). They found that in all cases the complexes entered the cells via passive diffusion and the most lipophilic derivatives displayed the highest cellular accumulation.[144,145] Further investigations by Gill *et al*. found that increasing the lipophilicity affected the cytotoxicity of these types of complexes and also where they localized in cells. For example, in their series of dinuclear-polypyridyl compounds, the most lipophilic complex was found to mostly interact with the endoplasmic reticulum membrane and had an IC_{50} of 7 μM against MCF7 breast cancer cells. The least lipophilic derivative was found to localize in the nucleus and had an IC_{50} of 138 μM (**Figure 1.7b**).[146] Findings like these have led to new strategies to target other parts of the cell, such as the mitochondria.[147] More recently, McFarland and coworkers have developed a polypyridyl complex (**TLD1433**) that has entered phase-II clinical trials for the photodynamic treatment of bladder cancer (**Figure 1.7c**).[148]

A new family of Ru polypyridyl compounds has emerged where one of the pyridyl groups is substituted for a phenyl ring, which forms an organometallic bond with the ruthenium centre (**Figure 1.7d**). These Ru-C bonds are more stable than their Ru-N counterparts and have been shown to increase lipophilicity by decreasing the valence charge on the ruthenium.[149] Cyclometalated complexes of this type have also been extensively derivatized and studied for their anticancer activity with several compounds showing activity comparable to cisplatin.[150–152] Similarly to the *N,N*-chelating polypyridyls, it was found that properties controlled by the ligand set, such as lipophilicity and reduction potential, are key to tuning the anticancer activity.

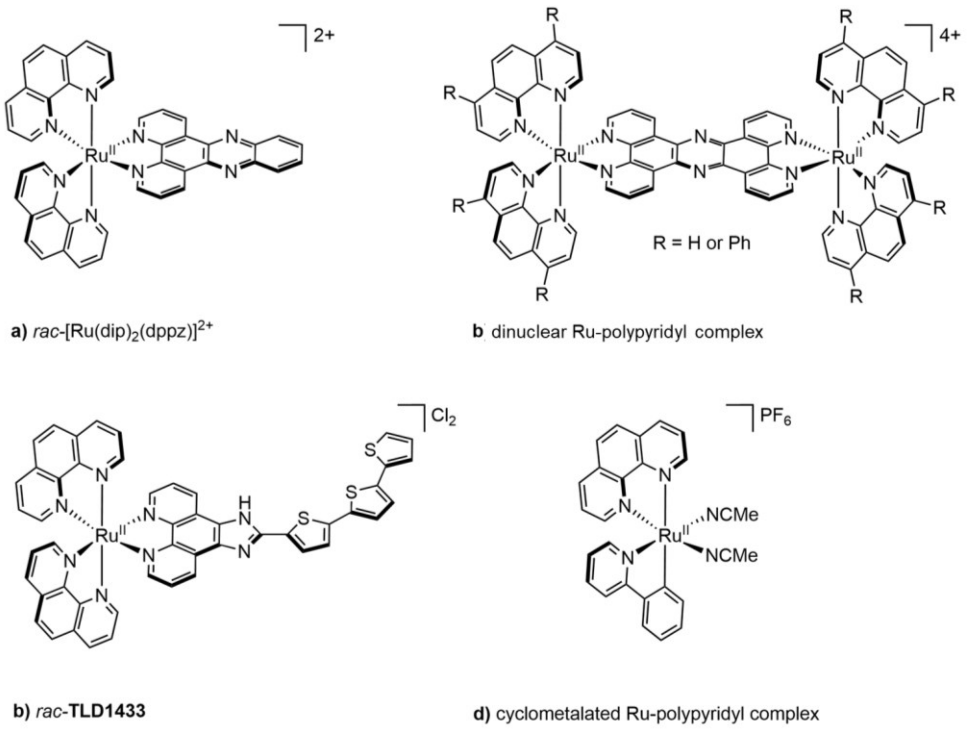

a) *rac*-$[Ru(dip)_2(dppz)]^{2+}$ **b** dinuclear Ru-polypyridyl complex

b) *rac*-**TLD1433** **d)** cyclometalated Ru-polypyridyl complex

Figure 1.7 Examples of ruthenium(II) polypyridyl complexes.

An interesting approach in the development of ruthenium anticancer complexes is to couple two or more complexes together that have shown promising biological activity. This has sometimes led to an induction of cytotoxicity greater than their mononuclear analogues. Furthermore, combining complexes that display different mechanisms of action can help to overcome resistance pathways encountered for the individual metal-centre components. A second metal centre also provides another degree of freedom to tune properties such as lipophilicity, reduction potential, and ligand-exchange kinetics, all of which affect biological activity.

Alessio and coworkers began to explore symmetric dinuclear ruthenium anticancer complexes in 1999, using compounds modeled on the antimetastatic NAMI-type complexes (**Figure 1.8a**).[153] Promisingly, they found that the dimers displayed similar antimetastatic activity in human carcinoma cell lines to **NAMI-A**.[154] These results encouraged *in vivo* studies in mice where the dimers, again, displayed comparable antimetastatic activity to **NAMI-A**.[155] Though the anticancer activity of the dimers was similar to their monomeric components, mechanistic investigations revealed that the complexes undergo novel biomolecule interactions. It was found that the dimers,

especially those with longer linkers, have the potential to form inter-strand crosslinks with DNA and other biological targets that are not possible with **NAMI-A**.

A similar strategy was applied in linking ruthenium(II)-arene complexes to form symmetric dinuclear complexes. An example of this is **di-RM175** developed by Sadler and coworkers (**Figure 1.8b**).[156] They found that this complex showed improved DNA interactions over its mononuclear analogue and that it was able to inhibit RNA synthesis *in vitro*. In this study they coined the term 'induced-fit-recognition' in which they suggested the complex could adjust its conformation thanks to a flexible bridging ligand set. This flexibility is thought to further enhance DNA binding and demonstrates the promise of linking two metal complexes with non-rigid bridging ligands. Keppler and coworkers presented a set of similar dinuclear ruthenium(II)-arene complexes that showed good cytotoxicity over their inactive mononuclear analogue (**Figure 1.8c**).[157] Interestingly, as the linker length increased they found an increase in activity toward both A2780 and SW480 cell lines, with the longest linker displaying an IC_{50} in the nanomolar range. This increase in cytotoxicity suggested more than just an additive effect of the mononuclear Ru centres. Likely a synergistic effect was occurring, which further emphasizes the utility of linking two ruthenium anticancer complexes. Though a clear mechanism of action was not established it was proposed that the longer linker length led to more favourable lipophilicity and enhanced interactions with biomolecules such as DNA.

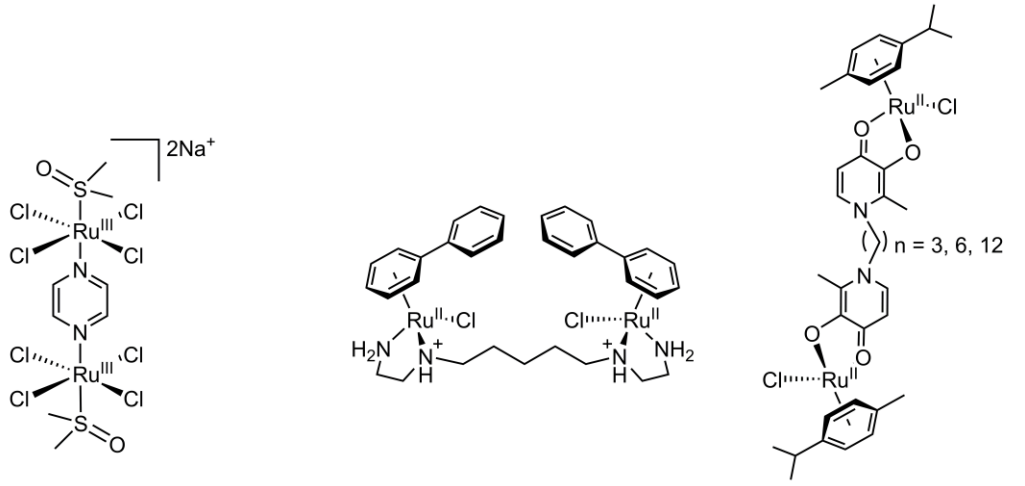

a) $Na_2[\{trans\text{-}RuCl_4(Me_2\text{-}SO\text{-}S)\}_2(\mu\text{-}pyz)]$ **b) di-RM175** **c)** dinuclear Ru-arene series

Figure 1.8 Examples of biologically active dinuclear ruthenium arene anticancer complexes.

1.3. Copper Anticancer Complexes

1.3.1. Copper Metabolism

Copper is an essential metal for all living organisms. It functions as a cofactor for enzymes responsible for energy production such as cytochrome *c* oxidase and plastocyanin and even plays an important role in oxygen-carrying structures such as hemocyanin.[158] Though essential, copper is present in low concentrations (1-2 ppm in humans) and its metabolism is tightly regulated. Dietary copper that is absorbed through the GI tract enters the blood stream and is immediately sequestered by proteins such as albumin and transcuprein.[159,160] These proteins transport the copper to the liver where it is either secreted in the bile, used within the liver, or incorporated into ceruloplasmin. The ceruloplasmin protein is used to store and recirculate the copper into the bloodstream for delivery to various tissues throughout the body. Transport of copper across cell membranes is facilitated by transmembrane proteins such as Ctr1.[161] Copper is also known to be an important factor in the function of other biological systems such as superoxide dismutase and even in the production of stress-response neurotransmitters such as norepinephrine.[162,163] Whether it be radical scavenging, molecular transformation, or oxygen transportation, the ability for copper to cycle between the Cu(I) and Cu(II) oxidation state is at the core of these important biological functions. This redox activity is also the reason copper is tightly regulated at endogenous concentrations.[158] When left unchecked, copper can generate reactive oxygen species (ROS) through Fenton-type chemistry. Catalytically generated ROS damages important biological structures such as DNA which can lead to apoptosis (**Figure 1.9**).

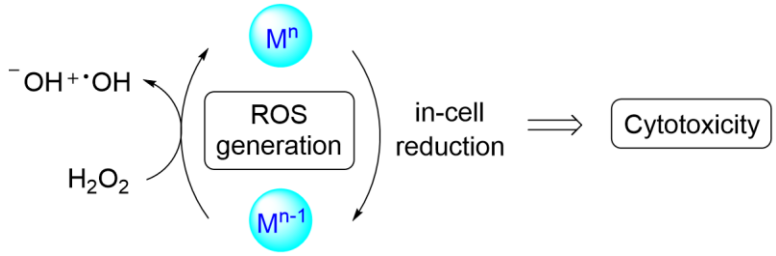

Figure 1.9 **Schematic diagram of a metal ion catalytically generating reactive oxygen species.**

Interestingly, some cancers have been found to have higher intracellular concentrations of copper than healthy cells. It has been suggested that the higher levels

of copper could be a result of the increased need for blood vessel formation, known as angiogenesis, in which copper plays a key role.[164] Diving further into the literature can result in a contradictory view on the role of copper in the cell and its use in cancer treatment. On the one hand, as discussed above, it is suggested that high levels of copper can damage cells through oxidative stress, which can even lead to cancer. On the other, cancers cells have been found with high levels of copper and are able to continue to proliferate.[164–166] The copper anticancer literature describes both compounds that are designed to chelate excess copper and complexes that deliver copper to cancers.[27,167] Furthering the enigma of copper's role in cancer is that even for complexes designed with copper at their core, their anticancer mechanisms and cellular targets remain a topic of debate.[168] No matter the consensus, copper continues to play an interesting role in the development of anticancer treatments.

1.3.2. Copper Coordination Chemistry

Copper is an attractive metal for the design of anticancer complexes thanks to a wide variety of accessible geometries and biologically-relevant redox potentials. Copper anticancer complexes are most commonly found in the Cu(II) oxidation state but Cu(III) and Cu(I) complexes have also been reported.[169] Complexes of Cu(II) (d^9, S = ½) take on a range of coordination numbers including: four coordinate, square planar; five coordinate, trigonal bipyramidal; and six coordinate, octahedral. Complexes of Cu(I) (d^{10}, S = 0) are less geometrically flexible, preferring four-coordinate tetrahedral conformations. The Cu(II)/Cu(I) redox couple has been found to range from -1.7 to 1.3 V versus NHE.[170] This is an important component of the design of Cu anticancer complexes, since ligand sets can be chosen to ensure the reduction potential lies within a physiologically relevant range (-1 to 1 V).[171] Furthermore, Cu(II) complexes can be designed to release a ligand as a payload or probe upon reduction to Cu(I) due to the geometric rearrangement that occurs with oxidation state change. Lastly, the effect of the paramagnetism of the Cu(II) centre on its ligands can be exploited in the development of probe molecules that 'turn on' once the copper is reduced to its diamagnetic Cu(I) state.[172] The paramagnetic Cu(II) also allows for the investigation of structural and chemical changes in solution via methods such as electron paramagnetic resonance spectroscopy.[173] Aqueous ligand exchange studies are particularly important as Cu(II) water exchange rates are on the order of 10^8 s^{-1}, making them much less

kinetically inert than their Pt- and Ru-anticancer predecessors. Consequently, in biological systems Cu complexes are prone to rapid ligand loss. This versatility of copper chemistry, as well as its relatively low cost, has led it to become one of the most studied metals for cancer treatment.[174]

1.3.3. Copper Anticancer Complexes

One of the first classes of copper anticancer complexes was reported in the 1960s and contained a thio(semicarbazone) (TSC) ligand. Following the initial success of cisplatin, extensive research was focused on this class of copper anticancer compounds and a plethora of derivatives with promising *in vitro* anticancer activity have been presented in the literature.[175–181] TSC ligands present a versatile scaffold consisting of a C,N,S backbone that coordinates through at least one nitrogen and a sulfur donor. These ligands can exist in the thione, thiol, or anionic form (**Figure 1.10a**). Denticity ranges from bidentate to tetradentate in which the third and fourth donor atoms are commonly N, O, or another S atom. The TSC scaffold also allows for convenient synthetic modification of the backbone atoms not directly involved in copper coordination. The facile access to such modifications allows for the tuning of properties such as lipophilicity, water solubility, and the overall stability of the TSC ligand. One of the major mechanisms of action postulated for Cu-TSC complexes is their ability to cycle between Cu(II) and Cu(I) oxidation states leading to the generation of ROS.

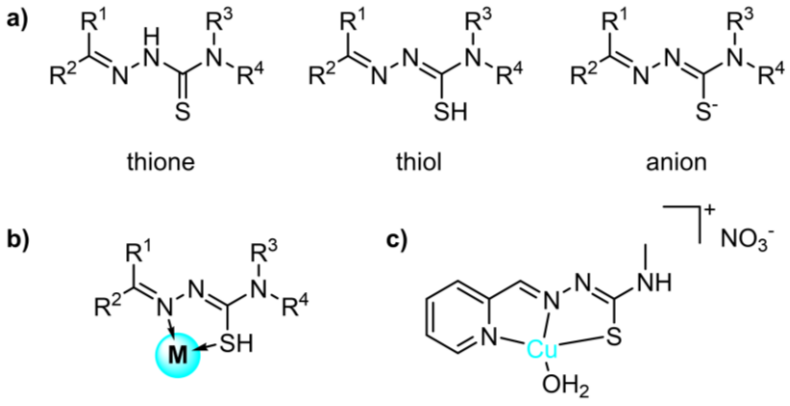

Figure 1.10 **a) Examples of the general TSC ligand scaffolds and b) their general metal binding motif. c) Example of a tridentate (N,N,S) copper TSC complex in which R^1, R^4 = H, R^2 = pyridine, and R^3 = methyl.[182]**

Another similar family of widely studied copper anticancer complexes contain a bis(thiosemicarbazone) ligand. These molecules contain two thiosemicarbazone groups and typically coordinate to copper in a tetradentate manner through N_2S_2 donors. This results in a square planar geometry about the Cu(II) centre which, along with the tetradenticity, results in more stable complexes compared to analogous mono-TSC ligands.[183] Copper complexes of diacetyl-bis(4-methylthiosemicarbazone) (ATSM) are often stable enough for chelation of radioisotopes of Cu for both diagnostic and therapeutic applications; ^{64}Cu-ATSM complexes have entered clinical trials.[184] Other similar ligand scaffolds derived from 2-keto-3-ethoxybutyrlaldehyde-bis(4,4-dimethylthiosemicarbazone), such as KTSM, have also shown promising anticancer activity when complexed with Cu(II) (**Figure 1.11**).

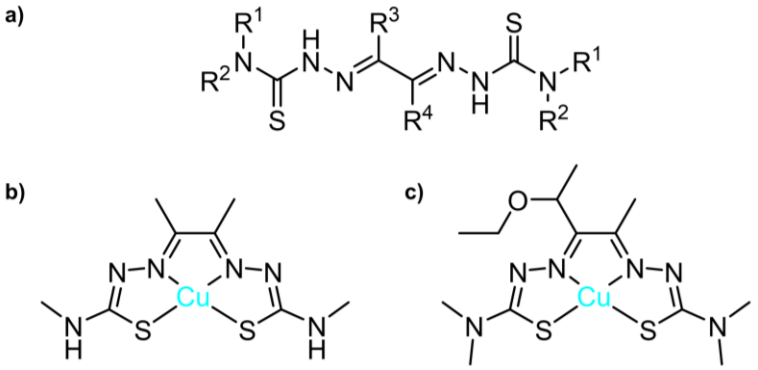

Figure 1.11 a) General bis(thiosemicarbazone) scaffold. b) Cu-ATSM. c) Cu-KTSM.

There is a truly impressive library of copper anticancer complexes in the literature today. A wide array of ligand systems have been studied including phosphines,[185] carbenes,[186] diimines,[187,188] amino acids,[189] benzimidazoles,[190] salens,[191,192] Schiff bases,[193] curcuminoids,[194] and flavonoids,[195] to name a few. This breadth of copper anticancer work has led to an array of proposed mechanisms of action such as DNA intercalation, topoisomerase inhibition, proteasome inhibition, and ROS generation. Surprisingly, given the breadth of research into copper anticancer complexes, the source of their anticancer activity likely remains a complex combination of the many possible mechanisms stated above.

1.3.4. Casiopeinas-type Copper Anticancer Complexes

A promising class of copper anticancer compounds are the Casiopeinas-type (Cas) complexes, first synthesize and named by Ruiz-Azuara *et al* in 1987.[196] These nitrate compensated Cu(II) salts generally consist of a planar 4,4'-disubstituted phenanthroline or bipyridine backbone with a variety of bidentate ligands used in the remaining coordination sites of the copper (**Figure 1.12a**).

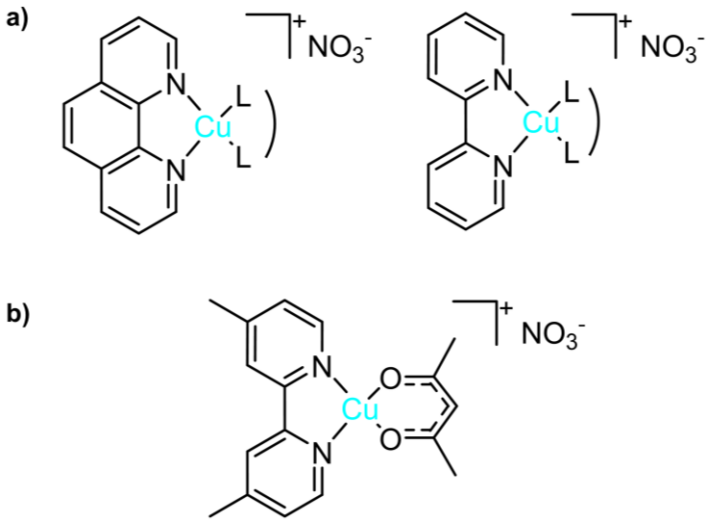

Figure 1.12 **a) General structure of the Casiopeinas-type copper anticancer complexes in which the 1,10-phenanthroline and 2,2'-bipyridine can be modified in various positions and the ancillary L,L-bidentate ligands are typically O,O acetylacetonate or N,O amino acid donors. b) The structure of Cas III-ia.**

One of the most widely studied complexes of this family, Cas III-ia, is comprised of a Cu(II) centre coordinated to a 4,4'-dimethylbipyridine and an acetylacetonate (acac) ancillary ligand (**Figure 1.12b**).[197] This compound displayed promising antitumour activity against HCT-15 transplanted nude mice and has since entered phase-I human clinical trials in Mexico for the treatment of cancer.[198] The main mechanisms of action for Cas complexes have been extensively studied *in vitro* and are suggested to be: DNA intercalation, an interaction that is enhanced by the planar aromatic backbone ligands;[199,200] DNA damage through ROS generation and coordinate interactions;[201,202] exhaustion of cellular antioxidants such as GSH (through both coordination and redox events);[203–205] and mitochondrial damage.[206–208] These copper compounds also have been found to induce apoptosis via caspase activation in murine leukaemia and human ovarian carcinoma cells.[209] Since the initial discovery that Cas complexes displayed

promising activity, much effort has been put into determining structure-activity relationships. For example, several N,O and O,O-donor ancillary ligands have been explored using the Cas III-ia scaffold including an array of amino acids. It was found that the secondary ligand had little to no affect on the anticancer activity of the complexes.[210] Several other approaches taking advantage of the Cas-type backbone have been reported including the use of biologically active molecules, such as norfloxacin, as the ancillary ligand or appending larger planar systems to introduce other mechanisms of action or enhance DNA interactions.[211,212] Dinuclear copper complexes containing a Cas-type moiety have also been reported and displayed *in vitro* anticancer activity in the low micromolar range.[213] Though Cas-type complexes have been widely studied and work continues into the development of different derivatives, many questions still remain regarding their mechanism of action. Even for complexes like Cas III-ia, which has entered human clinical trials, its exact coordination environment in various aqueous media has been poorly characterized.

1.4. Polymer nanoparticles for the encapsulation and delivery of anticancer agents

Polymer nanoparticles (NPs) have gained increasing interest for the delivery of anticancer drugs over the past several years.[214,215] Nanoparticle encapsulation, particularly for metal complexes susceptible to hydrolysis, is advantageous as they provide a level of 'protection' to the complexes once within the bloodstream. This is particularly important for complexes that undergo aquation like the platinum-, ruthenium-, and copper-based anticancer agents discussed in the preceding sections. Particles that are 100-300 nm in diameter have also been shown to selectively accumulate in tumours by permeating through defects in blood vessels arising from abnormal development during tumour growth.[216,217] This phenomenon, known as the enhanced permeability and retention effect (EPRe), provides an intrinsic mode of selectivity toward tumours for nanoparticles of a certain size distribution. Furthermore, thanks to wide selection of terminal-groups, the nanoparticles can be decorated with targeting molecules or macromolecules, such as aptamers, to provide another degree of selectivity towards target cancer cells.[218] This chemistry is robust, especially when using polymers such as poly(D,L-lactide-co-glycolide) (PLGA) that are terminated with carboxylic acid groups (**Figure 1.13**). Appending targeting moieties then involves simple amide couplings under

mild, usually aqueous, conditions.[219,220] PLGA polymers have become commonplace in the development of nanoparticle delivery systems and have been approved by the FDA for medical use since the late 1970s.[221,222] They contain ester bonds that are hydrolytically cleavable allowing the particles to be easily broken down post drug delivery. Drug release from PLGA NPs is thought to occur through a combination of surface 'erosion' (hydrolysis) of the polymer matrix, diffusion, and cleavage of the polymer within the bulk polymer matrix (non-surface hydrolysis).[223] Of the aforementioned processes, drug release is dominated by diffusion. Conveniently, these processes occur relatively slowly and allow for the sustained delivery of a drug, from days to weeks, increasing the effective dose.[224] Conveniently, the ratio of lactide to glycolide in PLGA can be modified to vary the hydrophilicity of the resulting polymer. This affects the rate of degradation and amount of drug encapsulation.[225,226]

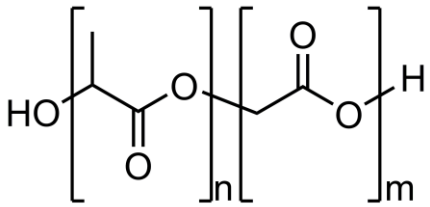

Figure 1.13 The individual units lactide (left) and glycolide (right) of the PLGA copolymer.

1.4.1. Polymer nanoparticle encapsulation of metal-based anticancer complexes

As discussed above, many metal-based anticancer complexes are thought to exhibit their anticancer activity through coordinate interactions with biomolecules. The caveat being if they become active (i.e. undergo aqueous ligand exchange) prior to entering the target environment they can damage healthy tissues. This can be mitigated by encapsulation in polymer nanoparticles. Complexes in the core of the particles are protected from undergoing exchange events and can be slowly released once within the target environment. Lippard and coworkers have explored the use of PLGA NPs for the encapsulation and delivery of platinum anticancer complexes.[227] They found that encapsulating a variety of cisplatin derivatives in PLGA and PLGA-*b*-poly(ethylene glycol) (PLGA-PEG) NPs resulted in increased cytotoxicity and lower systemic toxicity over cisplatin *in vivo*. For example, they encapsulated the Pt(IV) complex *c,t,c*-[$Pt(NH_3)_2$-$(O_2C(CH_2)_4CH_3Cl_2]$ in PLGA-PEG NPs decorated with an aptamer designed to target the

prostate specific membrane antigen (PSMA) which is upregulated in prostate cancer.[228] Not only did they see an increase in anticancer activity over cisplatin alone but they also found the targeted NPs to be an order of magnitude more effective than the non-targeted NPs against PSMA positive LNCaP cells. They postulated the increase in activity was thanks to the increased stability and uptake of the complexes by the polymer NPs. Similarly, Keppler *et al* studied the encapsulation of the ruthenium anticancer complex, **KP1019,** in poly(lactic acid) NPs to decrease unwanted hydrolysis events that often occurs relatively quickly in aqueous media for the free complex.[229] Promisingly, they found a 2-fold increase in anticancer activity against SW480 and Hep3B cancer cell lines over non-encapsulated **KP1019**. Interestingly, they also found that the NP-KP1019 formulation turned green after 24 h at 25 °C and that this solution showed approximately a 10-fold increase in cytotoxicity over the original formulation. The current hypothesis for this increase in activity is that the surfactant used during the formulation is reducing the **KP1019** to an 'activated' ruthenium(II) analogue. The NPs and surfactant were then suggested to stabilize the more labile Ru(II) species prior to its release in target cells. These results promote the utility of encapsulating metal-based anticancer complexes in degradable polymer nanoparticles to breath new life into well studied anticancer agents.

1.5. Magnetic resonance spectroscopy

Magnetic resonance (MR) spectroscopy is the study of the interaction of magnetic moments (μ) of particles such as nuclei, electrons, and muons with their local environment in an applied magnetic field (B_0). The magnetic moments for these particles arise from intrinsic spin angular momentum. When the spin angular momentum, denoted *I* for nuclei and *S* for electrons, is ≥ ½ the resulting magnetic moment can interact with other magnetic moments in their local environment. When these interactions are subjected to an applied magnetic field, a wide array of information can be discerned such as molecular structure, solution behaviour, chemical reaction progression, and the spatial distribution of chemical species. Some common MR techniques include nuclear magnetic resonance (NMR) spectroscopy, magnetic resonance imaging (MRI), and electron paramagnetic resonance (EPR) or electron spin resonance (ESR) spectroscopy. In this work, NMR and EPR are used to study the structure and solution speciation of ruthenium and copper anticancer agents. MRI is also employed to spatially resolve the speciation of a select Ru(III) anticancer agent in excised tumours.

1.5.1. Nuclear magnetic resonance spectroscopy

Nuclear magnetic resonance spectroscopy is a technique that takes advantage of the intrinsic nuclear spin of nuclei.[230] All nuclei have a nuclear spin quantum number, *I*, that is greater than or equal to zero and is found in multiples of ½. Nuclei that have *I* = 0, corresponding to an even atomic mass and atomic number, do not have nuclear spin and are NMR silent. Fortunately, most nuclei have at least one isotope with *I* > 0 allowing for their observation via NMR spectroscopy. Nuclei typically observed in NMR spectroscopy include: ^{1}H, ^{13}C, ^{19}F, and ^{31}P. These nuclei have *I* = ½ with an isotopic abundance of 100 %, except for ^{13}C which has an isotopic abundance of only 1.11 %. Since these nuclei have an uneven number of protons and neutrons, combined with the nuclear spin angular momentum, *I*, arising from the intrinsic spin (*I* = ½m for the above nuclei), this results in a magnetic moment, μ. For any nuclei with *I* > 0, the magnitude of the magnetic moment can be described as:

$$\mu = \boldsymbol{\gamma I}$$ **Equation 1.1**

where γ is the gyromagnetic ratio, or how 'strongly magnetic' the nucleus is, and is constant for each element. When these magnetic moments are placed in an external magnetic field, B_0, they align with the magnetic field in discrete orientations or states defined by the magnetic quanted number, m_I, where $m_I = I, I = 1, \ldots -1$. For example, the ^{1}H nucleus with *I* = ½, can align parallel (m_I = +½) or antiparallel (m_I = -½) to B_0, with the parallel state being of lower energy. The interaction of the magnetic moments with the applied magnetic field can be described by the semi-classical model, where B_0 exerts a torque on the magnetic moments, which causes them to precess about the B_0 direction. The frequency of this precession is known as the Larmor frequency (ν_L) in NMR and is unique for each nuclide in a given B_0. The value of the Larmor frequency is given by:

$$\boldsymbol{\nu_L} = \frac{-\boldsymbol{\gamma B_0}}{\boldsymbol{2\pi}}$$ **Equation 1.2**

in Hz. Considering a collection of ^{1}H nuclei in an applied magnetic field, there will be an excess of nuclei in the lower energy, parallel ($N_\uparrow$), state versus the antiparallel state ($N_\downarrow$) as defined by the Boltzmann distribution:

$$\frac{N_\uparrow}{N_\downarrow} = \boldsymbol{e^{\Delta E/k_B T}}$$ **Equation 1.3**

where k_B is the Boltzmann constant and T is temperature in Kelvin. ΔE is known as the Zeeman energy splitting between the states and can be described as:

$\boldsymbol{\Delta E = \frac{h\gamma B_0}{2\pi}}$ **Equation 1.4**

where h is Planck's constant. The greater population of nuclei in the lower energy state results in a bulk magnetization *M* from the sum of individual magnetic moments. NMR uses radiation at a frequency (ν, usually radiofrequency, rf) that satisfies the resonance condition, $\Delta E = h\nu$, which for ^{1}H leads to excitation from the lower energy state (m_I = +½) to the higher energy (m_I = -½) state. In other words, a transition can occur when the frequency of the applied radiation equals the Larmor frequency.

It is convenient to describe NMR using a simplified vector model of the bulk magnetization of nuclei in an applied magnetic field. This is known as the Bloch vector model and describes the resulting bulk magnetization as a vector, *M*. This is a representation of the collection of spins at equilibrium randomly precessing about B_0, which also serves to define the *z*-axis. As the spins are randomly distributed about this z-axis, there is no net magnetization in the transverse (x-y) plane. Therefore, $M = M_0 = M_z$, where M_0 is the initial bulk magnetization and the contribution from M_x and M_y is zero (**Figure 1.14a**).

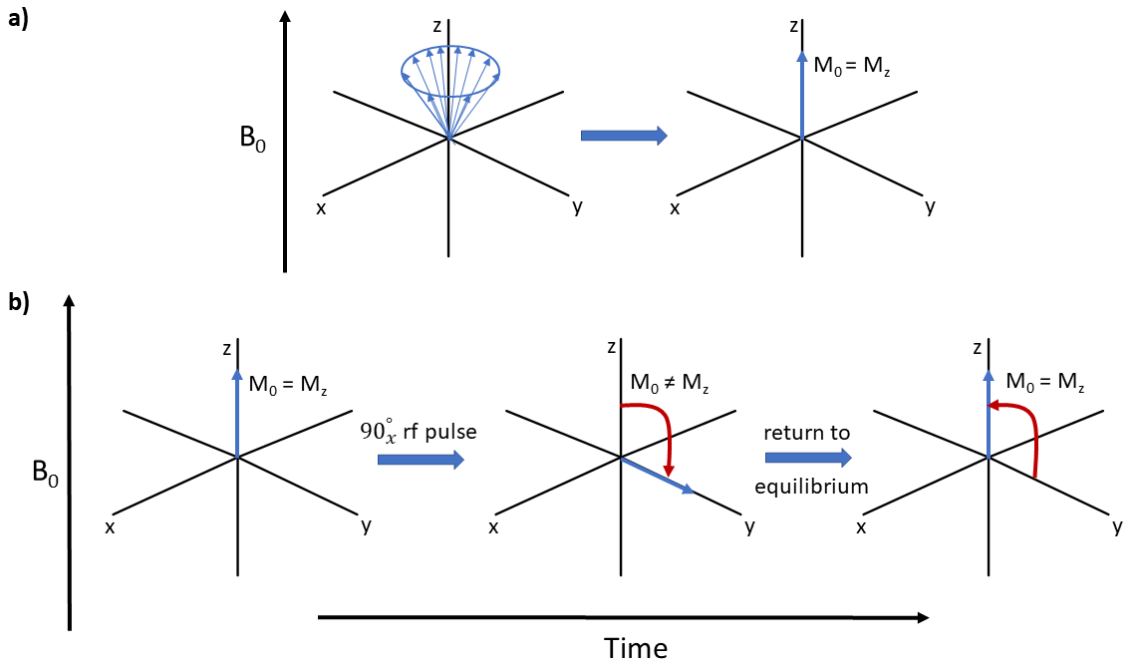

Figure 1.14 **a) Vector representation of the net magnetization of spins randomly oriented about an external applied magnetic field B_0. b) A net magnetization vector M_0 in an external applied magnetic field is tipped into the transverse plane by a 90˚rf pulse along the +x axis and then relaxes back to equilibrium.**

NMR experiments are usually conducted using rf pulses, with the electromagnetic radiation is applied from a coil surrounding the sample. The magnetic component of this radio frequency, B_1, oscillates at the Larmor frequency of the nuclei and is applied in the transverse plane, perpendicular to B_0. To further simplify the visualization of these processes, it is convenient to consider the x,y, and z axis in a rotating frame in which they are precessing about B_0 at the Larmor frequency. This allows one of the magnetic vectors of the oscillating rf to be considered as static about one of the transverse axes, such as the +x axis, and the other to be ignored as it is no longer oscillating at the Larmor frequency. The applied rf exerts a torque on M_0 that is perpendicular to the magnetic component of the light, B_1, and causes the bulk magnetization vector to rotate towards the transverse plane. The angle of M_0 rotation (θ), known as the flip angle, is dependent on the duration (t) and amplitude of the rf pulse, given by B_1:

$$\boldsymbol{\theta = 360\frac{\gamma}{2\pi}B_1 t}$$ **Equation 1.5**

If the pulse is applied along the x direction for a duration that results in M_0 aligning with the y-axis it is considered a 90˚$_x$ pulse and, similarly a longer pulse that results in alignment along -z is defined as a 180˚ pulse. Following a 90˚$_x$ excitation pulse, the bulk magnetization is no longer at equilibrium such that M_z now equals zero and $M_{(x,y)} > 0$. Immediately following this 90˚ pulse, the bulk magnetization in the transverse plane begins to rotate about the z-axis at the Larmor frequency as it returns to equilibrium (**Figure 1.14b**). This rotating magnetic vector induces an oscillating voltage in the detector coil surrounding the sample. The return of the bulk magnetization to the z-axis is known as relaxation and the resulting NMR signal is detected as a free induction decay (FID) (**Figure 1.15**). This signal, which is in the time domain, is then Fourier transformed to the frequency domain:

$$\boldsymbol{f(\omega) = \int_{-\infty}^{\infty} f(t) e^{i\omega t} dt} \quad \textbf{Equation 1.6}$$

where $f(\omega)$ represents the frequency domain and $f(t)$ represents the time domain. The Fourier transform results in a spectrum of lines that correspond to the Larmor frequency of each nucleus in a unique chemical environment (**Figure 1.15**). These signals can then be used to determine structural information about the observed molecule.

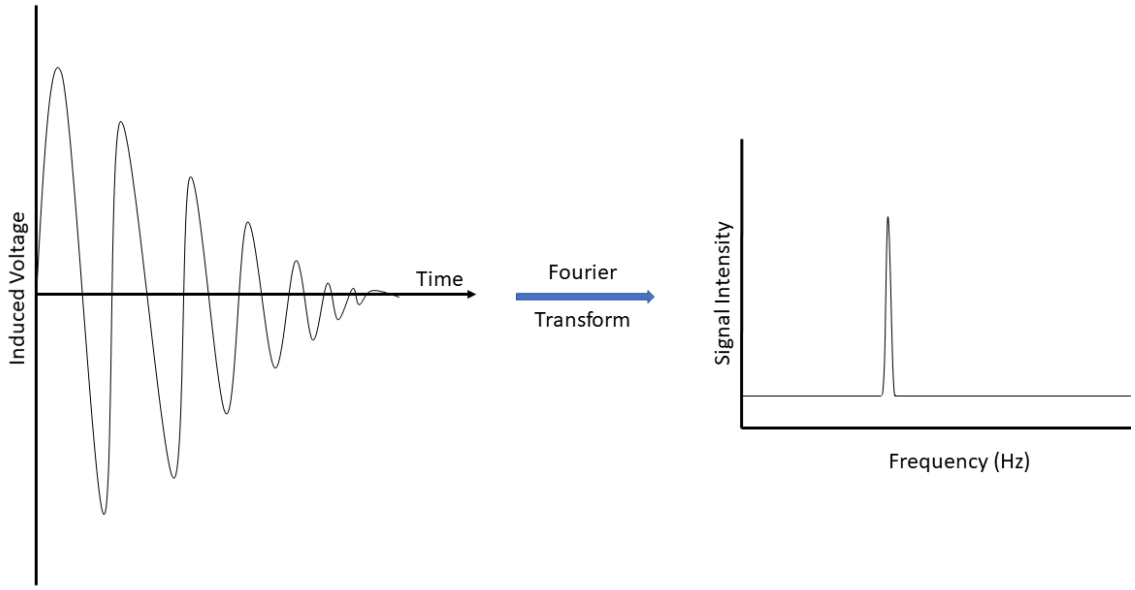

Figure 1.15 Free induction decay signal of a spin in an applied magnetic field as it returns to equilibrium along B_0 following a 90˚ rf pulse and its corresponding Fourier transform to the time domain.

The rate at which the *M* returns to the equilibrium state, or the rate of signal decay, is defined as the longitudinal, or spin-lattice, relaxation time, T_1 (**Figure 1.16a**). This type of relaxation occurs as the spins transfer energy into the surrounding environment, or lattice, initially via interactions with nearby oscillating magnetic dipoles, then as heat, with the rate of relaxation given by:

$$\boldsymbol{M_z = M_0(1 - e^{-t/T_1})}$$ **Equation 1.7**

where M_0 is the initial bulk magnetization immediately following the excitation pulse and M_z is the bulk magnetization at time *t*. This is not the only type of magnetic relaxation following an excitation pulse. As discussed above, immediately following a 90˚ pulse along the x-axis the bulk magnetization becomes aligned along the y-axis. As the individual nuclei begin to relax toward equilibrium along the z-axis, their magnetic vectors also begin dispersing in the x-y plane (**Figure 1.16b**). This loss of coherence also contributes to the rate of signal decay and is defined as the transverse, or spin-spin, relaxation time, T_2:

$$\boldsymbol{M_{(x,y)} = M_{0(y,x)} e^{-t/T_2}}$$ **Equation 1.8**

where $M_{0(y,x)}$ is the magnetization vector in the x-y plane immediately following the 90°_{x} excitation pulse and $M_{(x,y)}$ is the bulk magnetization in the x,y plane at time *t*. The transverse relaxation time is influenced by the slight differences in local magnetic field that each nuclei experience.

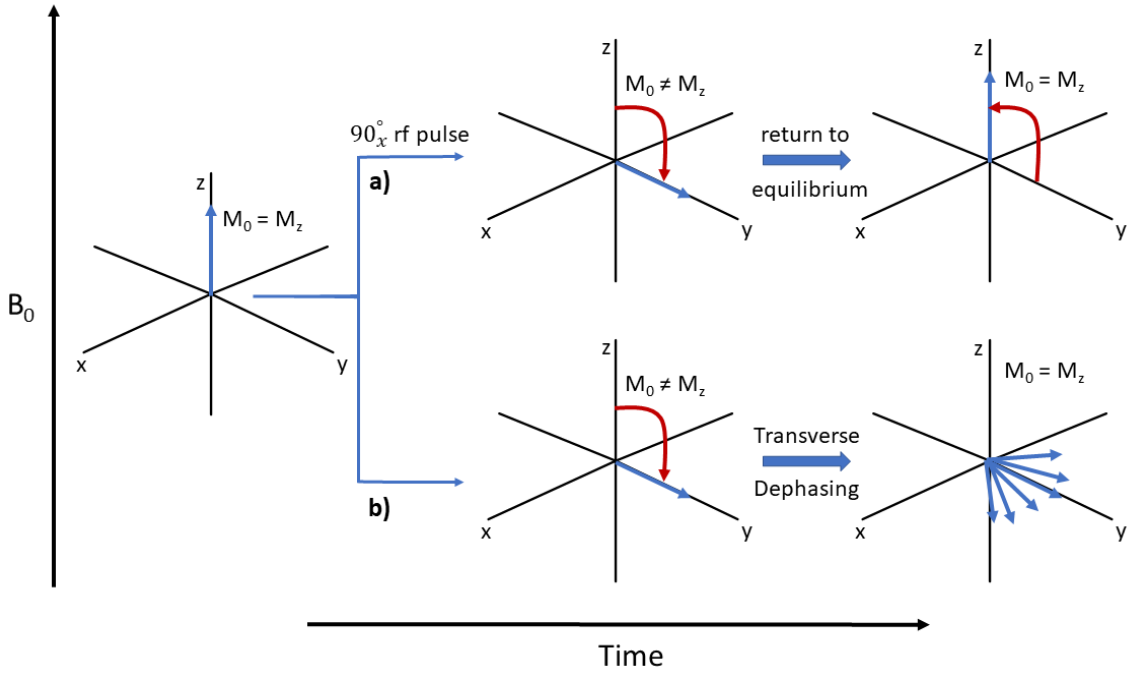

Figure 1.16 **a) Following a 90°_{x} rf pulse the net magnetization returns to equilibrium along B_0 at a rate dictated by the longitudinal relaxation time, T_1. b) Following a 90°_{x} rf pulse the magnetic moments of the spins begin to diphase in the (x-y) plane according to the transverse relaxation time, T_2.**

These differences can arise both from intra- and intermolecular, or spin-spin, dipolar interactions and from magnetic field inhomogeneities in B_0. A relaxation time constant can be designated that considers both sources of magnetic field differences, T_2^*:

$$\frac{1}{T_2^*} = \frac{1}{T_2} + \frac{1}{T_{2(\Delta B_0)}}$$ **Equation 1.9**

where T_2 represents the contribution from dipolar interactions and $T_{2(\Delta B_0)}$ is the contribution from inhomogeneities in the local applied magnetic field. The linewidths of NMR signals are inversely proportional to T_2^* and for exponential relaxation the resulting line shape is Lorentzian and allows for T_2^* to be calculated using:

$$\Delta\nu_{1/2} = \frac{1}{\pi T_2^*}$$ **Equation 1.10**

where $\Delta\nu_{1/2}$ is the half-height line width of the observed resonance.

In practice, it is important to have a good estimate of T_1 and T_2 values to optimize the signal-to-noise ratio (SNR) and acquisition time of an NMR experiment. T_1 relaxation dictates the minimum time between excitation pulses when collecting multiple NMR experiments to be averaged. This is known as the repetition time (TR) and must not be so short that the net magnetization does not have sufficient time to relax to equilibrium. This can cause spin saturation in which the spins remain in an excited state and FID cannot occur. In typical NMR experiments, an optimized excitation pulse angle is used to maximize the SNR in the least amount of time while avoiding this spin saturation and is known as the Ernst angle.[231] The T_2 dictates the delay between the excitation pulse and when the detector 'listens' for the FID signal. This is known as the echo-time and must be sufficiently short such that the net transverse magnetization has not reached zero prior to signal detection.

Generally, $T_2 < T_1$ and the same relaxation parameters are used across most NMR experiments measuring ^{1}H nuclei in diamagnetic molecules. However, depending on the nuclei and their environment, it can be important for experimental measurement of both relaxation values. A technique called inversion-recovery is typically used for measuring T_1 relaxation times. In this experiment, a 180˚ excitation pulse is applied aligning the net magnetization along the -z-axis. Since net magnetization cannot be measured along the z-axis, a second 90˚ pulse is applied following a given period of time, τ, which tips the net magnetization back to the x-y plane. As τ is varied, so does the resulting signal intensity, M_τ, which can be related to T_1 by the following equation:

$$\boldsymbol{M_\tau = M_0(1 - 2e^{-\tau/T_1})}$$ **Equation 1.11**

A common experiment used to measure T_2 is the Carr-Purcell-Meiboom-Gill (CPMG) sequence. This spin-echo sequence involves an initial 90˚ pulse followed by a period of time, τ, after which a 180˚ pulse along the y-axis is applied to refocus the spins along the +y-axis after which the echo is observed. This refocusing pulse is repeated several times following τ, and as τ is varied, so is the signal intensity, M_τ, which allows for the calculation of T_2 using the equation:

$$\boldsymbol{M_\tau = M_0 e^{-\tau/T_2}}$$ **Equation 1.12**

The value of T_2 can also be determined with reasonable accuracy by measuring the full-width-at-half-height of NMR lines and using **Equation 1.10**.

1.5.2. Magnetic resonance imaging

Magnetic resonance imaging is a technique that involves the spatial resolution of the magnetic moments of nuclei within a sample. It was first developed in the mid 1970s, with the first experiments using selective excitation pulse sequences to create two- and three-dimensional images of cylinders containing water.[232] Following the suggestion that this method could be used to collect images of tissues in humans, the race to develop commercial MRI began and the first systems became available in 1983.[233] Today, MRI is widely used in the clinic for diagnostic imaging.

As with NMR, MRI spectrometers involve placing a sample inside a probe coil that is positioned in an applied magnetic field, B_0. In MRI spectrometers the probe coil is surrounded by gradient coils that can generate magnetic fields, additional to B_0, along the x,y, and z axes. These additional coils generate linear magnetic field gradients across the sample along the desired axis. Since the frequency at which nuclei resonate is dependent of B_0, applying a field gradient across the sample causes the nuclei to precess at slightly different frequencies depending on their position in the sample. These signals are then considered to be frequency encoded, which allows for the position of the signals to be resolved along a single axis (**Figure 1.17a**). To generate a two-dimensional (2D) image, a magnetic field gradient must be applied along a second axis. In this case, the second gradient causes the magnetic moments to be systematically out of phase relative to their position within the sample. This is known as phase-encoding and, when combined with frequency-encoding along a perpendicular axis, allows for discrete planes of spins in a sample to be resolved in 2D (**Figure 1.17b**). A third magnetic gradient can be applied along the remaining axis to cause the plane of encoded spins to resonate at unique frequencies across a volume of the sample.[234] This 'slice' of unique frequencies allows for a selective rf pulse ($\Delta\omega$) to be generated that only excites a selected volume, or voxel, of spins (**Figure 1.17c**). The rf pulse does not match the Larmor frequency of the spins outside the selected slice and, therefore, those nuclei do not contribute to the observed signal. The order and magnitude of the applied field gradients can be varied to manipulate image contrast and spatial, or temporal, resolution. Furthermore, as with NMR, parameters of the excitation pulse sequence, such as the TE and TR, can be varied to further enhance image detail and minimize spectral acquisitions times (TA).

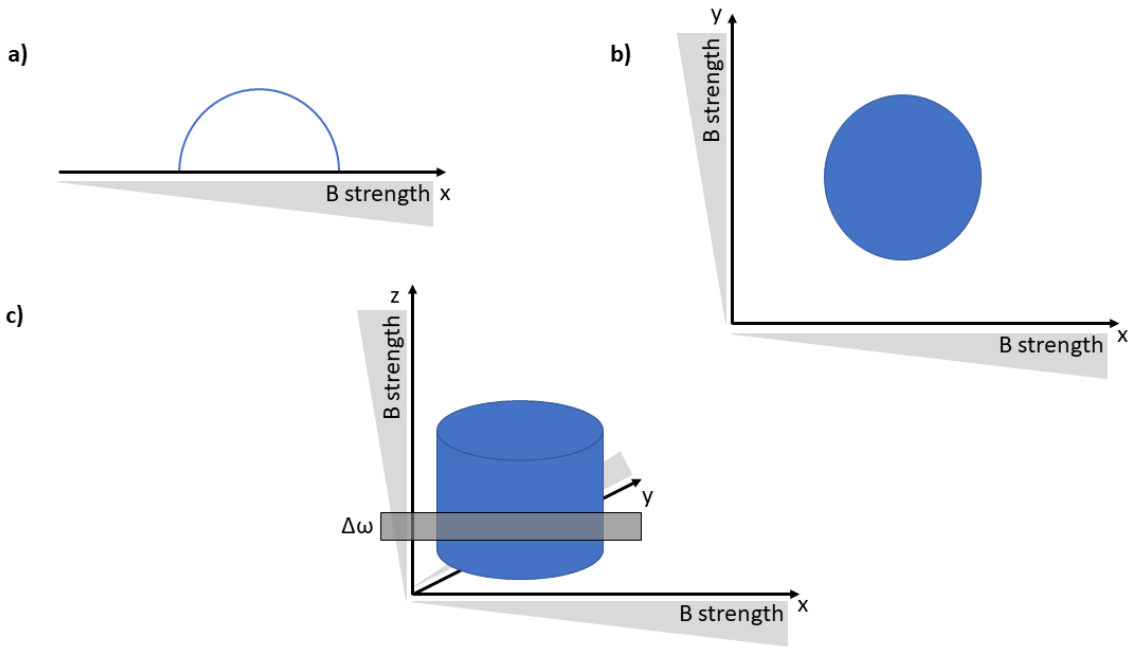

Figure 1.17 Graphical depiction of a vial of water in an MR experiment and the resulting images. a) A single field gradient along the x-axis results in a projection along the x-axis. b) A 2D image resulting from gradients applied along two axis. c) How a 3D image can be generated by applying field gradients along the x,y, and z-axis and selectively exiting a slice of the vial.

Clinical MRI experiments typically rely on the differences in water-proton concentrations and relaxation times in different tissues to generate an image of suitable contrast. The variance in contrast is really a difference in signal intensity in different regions of the tissue and allows for the resolution of biological features. This arises from the difference in T_1 and T_2 relaxation times, which vary in different environments depending on the type of tissue.[235] This variability in water-proton relaxation times can be used in imaging experiments by altering TE and TR to enhance specific regions while decreasing signal intensity in others. This can also contribute to a minimization of TA by optimizing the pulse sequence for the tissue of interest. Using a standard clinical spin-echo pulse sequence the signal intensity (SI) in a given tissue can be described by:

$$\boldsymbol{SI = \rho(1 - e^{-TR/T_1})(e^{TE/T_2})} \quad \textbf{Equation 1.13}$$

where ρ is the proton density. As shown in **Equation 1.13**, SI is dependent on relaxation times and can be manipulated by adjusting the parameters of the pulse sequence.

Conveniently, this is also true for other nuclei of interest, such as ^{19}F, and sequences can be optimized to ensure optimal SI for specific compounds.

In this thesis, the pulse sequences FLASH and RARE, as well as simple spin-echo pulse sequences were employed for both ^{1}H and ^{19}F MRI experiments. The RARE, or rapid acquisition with refocused echoes, pulse sequence was developed to decrease acquisition times in clinical MRI experiments by Hennig in 1986.[236,237] This pulse sequence involves an initial 90˚ excitation pulse followed by a series of 180˚ rf pulses that refocus the spins along the transverse plane. Conveniently, a different phase-encoding gradient can be applied between each refocusing pulse so multiple regions of the desired image slice, known as *k*-space lines, can be collected following a single excitation pulse (**Figure 1.18a**).

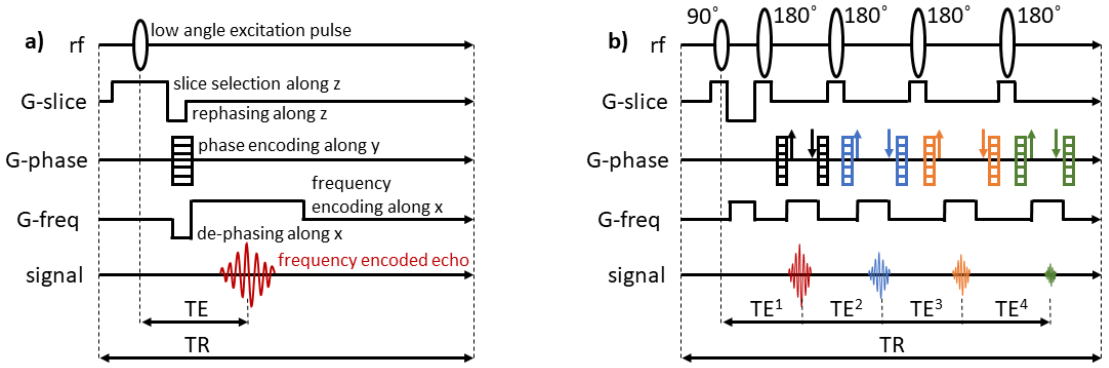

Figure 1.18 Pulse sequence diagrams for: a) fast low-angle shot (FLASH) and b) rapid acquisition with refocused echoes (RARE).[238]

This can greatly decrease TA for signals with sufficiently long T_2 over simple spin-echo pulse sequences. For example, if the sequence has 10 refocusing pulses, or a RARE factor of 10, the TA would be reduced by a factor of 10 over a typical spin-echo sequence. FLASH, or fast low angle shot, also decreases TA over typical spin-echo sequences by using a low flip angle during the excitation pulse (**Figure 1.18b**).[239] When combined with a short TR, many signal acquisitions can be collected rapidly, resulting in images of suitable contrast over a short period of time. As discussed above the optimal flip angle, known as the Ernst angle (α), is dependant on the T_1 of the observed spins and on TR as described by:

$$\alpha = cos^{-1}e^{TR/T_1}$$ **Equation 1.14**

1.5.3. Diffusion ordered spectroscopy

Characterization of molecular diffusion provides insight into properties such as molecular size, shape, and aggregation. Diffusion-ordered spectroscopy (DOSY) is an NMR method that is used for diffusion measurements and can estimate the diffusion coefficient (D) of molecules, and separate signals from mixtures. This technique uses pulsed field gradients to determine diffusion constants of molecules in an applied magnetic field.[240,241] Like MRI, an external gradient coil is used to apply a pulsed linear gradient across the sample. In the simplest experiment, known as a pulsed field-gradient spin echo, nuclear spins in the sample are initially excited and then frequency-encoded with an applied gradient pulse. Then, after a specified delay, known as the diffusion time (Δ), the signals are refocused with a 180˚ pulse. Then, nuclear spins that have diffused away from their original position during frequency encoding will be out of phase and no longer contribute to signal intensity (**Figure 1.19**). This signal attenuation is larger for larger field gradients and for species with large (diffusing quickly) diffusion coefficients. Several experiments are usually conducted, and signal height is the plotted against gradient pulse strength or diffusion times. A Gaussian decay function is used to fit the signal decay to the following equation:

$$\boldsymbol{Signal\ intensity} \propto \boldsymbol{e^{-(\gamma g \delta)^2 D(\Delta - \frac{\delta}{3})}}$$ **Equation 1.15**

where γ is the gyromagnetic ratio of the observed nucleus, g is the applied gradient strength, δ is the gradient pulse duration, Δ is the diffusion time, and D is the diffusion coefficient.

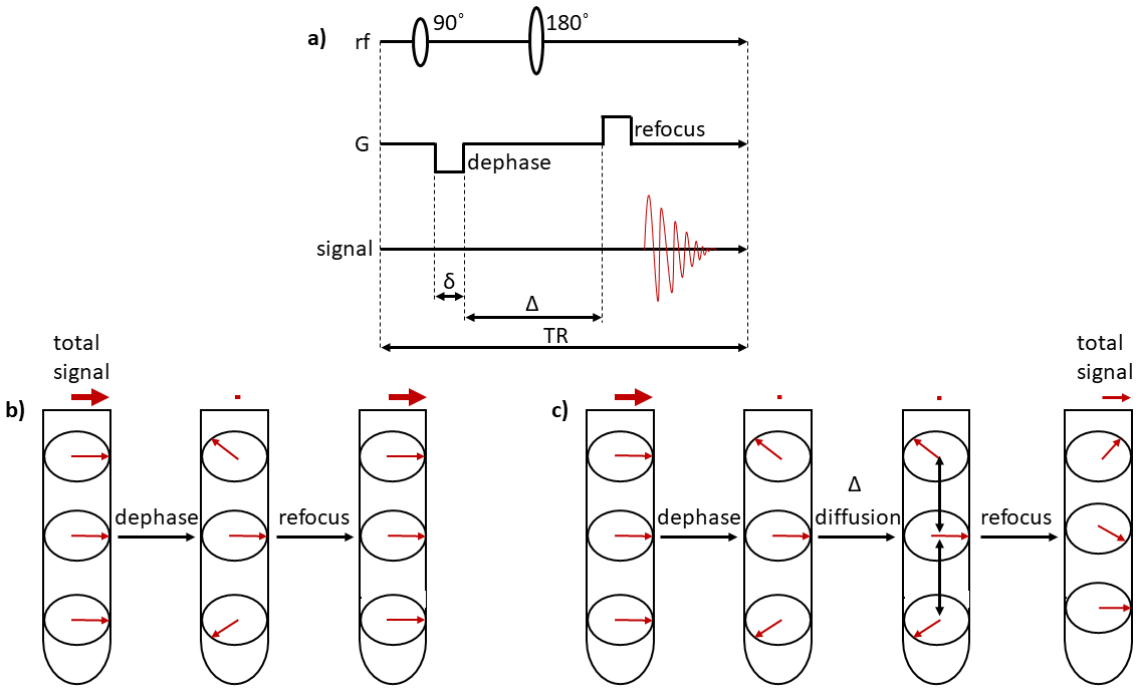

Figure 1.19 **a) Pulse sequence diagram for a standard DOSY experiments. b) Graphical depiction of spins during a DOSY pulse sequence assuming no diffusion time where the total signal is the same before and after the gradients are applied. c) Graphical depiction of how the total signal is reduced after the spins are allowed to diffuse for a given diffusion time, Δ.**

The fit can then be used to calculate a value of D, from which the size of species can also be estimated using the Stokes-Einstein equation:

$$r = \frac{kT}{6\pi\eta D}$$ **Equation 1.16**

where r is the van der Waals radius of the molecule, k is the Boltzmann constant, T is temperature, and η is solution viscosity. Although this approach assumes that the particles measured are perfectly spherical, it can be a useful method to further characterize the observed species. In this thesis, fluorine DOSY is used as a tool to determine whether ruthenium anticancer agents have been encapsulated within polymer nanoparticles, with the assumption that their diffusion rate will decrease once within the larger particles.

1.5.4. Electron paramagnetic resonance spectroscopy

EPR has become an important tool for characterizing paramagnetic, metal-based anticancer agents.[173,242,243] The oxidation state, ligand geometry, and identity, among many other properties of a metal complex can be elucidated via EPR. This has allowed for the study of the solution behaviour of many paramagnetic anticancer complexes, such as NAMI-A and KP1019. EPR has also been used to observe the interactions of paramagnetic complexes with biomolecules, such as HSA, and speciation within cell-containing media, leading to a better understanding of their mechanisms of action.[244]

EPR, much like NMR, involves the interaction of a magnetic moment with an external applied magnetic field. In EPR, the magnetic moment being observed arises from the intrinsic spin angular moment (S = ½) of one or more unpaired electrons. In an external magnetic field (B_0), the magnetic moments (μ_e) of the unpaired electrons align against (M_S = -½) or with (M_S = +½) the magnetic field, with populations given by the Boltzmann distribution. The difference in energy between the ground and excited spin states, known as the Zeeman splitting, is given by:

$$\Delta E_{Zeeman} = g_e \mu_B B_0$$ **Equation 1.17**

where g_e is the free electron g-value, and μ_B is the Bohr magneton. In EPR experiments, microwave radiation is applied at a fixed frequency and a magnetic field, generated by an electromagnet, is swept over a desired range. A transition between the two electron spin states occurs when the resonance condition is satisfied, $g_e \mu_B B_0 = h\nu$, and this absorption is detected as the signal that is observed in EPR spectroscopy (**Figure 1.20a**). The most common microwave frequency used in EPR is 9 - 10 GHz, in the X-band range, although many other frequencies are used for specific experiments.

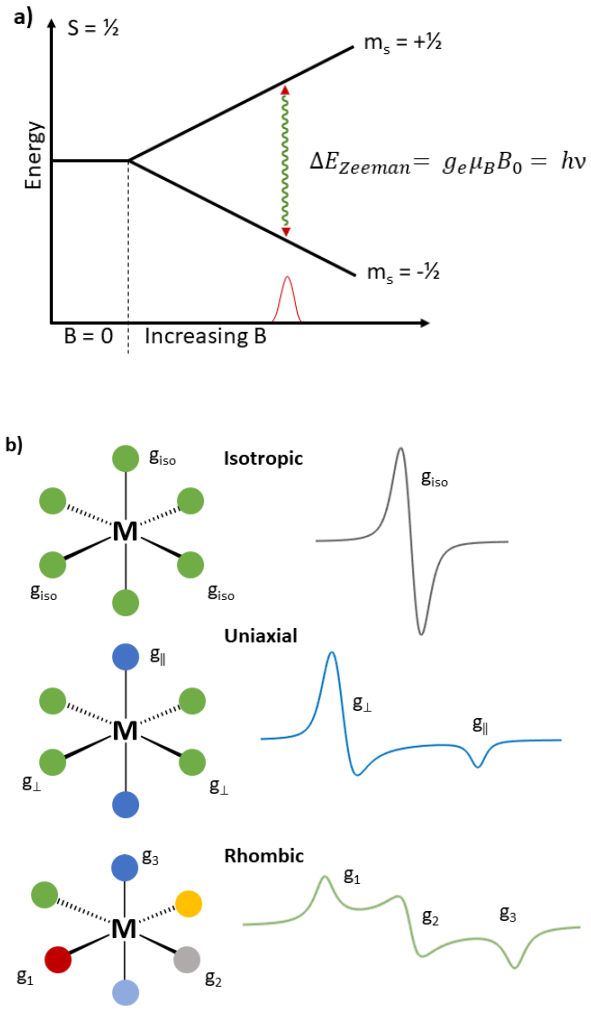

Figure 1.20 **Energy diagram for the Zeeman interaction of an unpaired electron in an applied magnetic field. b) Relation of the structure of a paramagnetic metal complex to its resulting powder pattern/frozen solution EPR spectral line shape.**

The local magnetic field (B_{local}) of an unpaired electron differs from the applied magnetic field (B_0), by and amount (ΔB) that is due to contributions from the chemical environment. Thus, the resonant frequency is shifted according to:

$$\Delta E_{Zeeman} = g_e \mu_B (B_0 + \Delta B) = g_e \mu_B (B_{local}) = h\nu \quad \textbf{Equation 1.18}$$

This effect of the local environment is quantified in terms of change in the electron g value, which is usually written as:

$$g = \frac{h\nu}{\mu_B B_{local}} \quad \textbf{Equation 1.19}$$

where $B = B_0$ is the field at which the transition occurs and g is the g-value of the electron in the local effective field.

The observed g-values of a paramagnetic metal complex are determined by spin-orbit coupling and the ligand field. The geometry of the ligand field is reflected in the observed g values, which are defined relative to the x, y, and z molecular axes. In liquid solution, rapid molecular tumbling averages g_x, g_y, and g_z to give a single g value, g_{av}, and an isotropic spectrum. In frozen solutions, these molecular motions are prevented, and the resulting "powder pattern" spectrum is the statistically averaged sum of the individual metal complexes randomly oriented with respect to the applied magnetic field. Under these conditions, the local symmetry of the ligand field results in distinct spectral profiles (**Figure 1.20**): (i) isotropic, $g_x = g_y = g_z$, corresponding to spherical or octahedral symmetry; (ii) uniaxial $g_x = g_y \neq g_z$ or $g_x \neq g_y = g_z$ (equivalent g values described as $g_\perp$ and the unique g value is written as $g_\parallel$); and rhombic, $g_1 \neq g_2 \neq g_3$, due to lower symmetry. Analysis of the spectral type and individual g values enables identification of specific paramagnetic species and have been used, for example to characterize the ligand exchange processes of Ru(III) anticancer compounds.[73,92,245]

Further information can be obtained from the interactions of unpaired electrons with nuclei having $I > 0$, known as hyperfine (HF) interactions. These are derived from through space (anisotropic, dipole-dipole) and through bond (isotropic) contributions. The energy levels for an isotropic paramagnetic system with $S = ½$ and $I = ½$ are given by:

$$E = g\mu_B B_{local} M_S + a M_S M_I \quad \textbf{Equation 1.20}$$

where a is the hyperfine coupling constant and M_I is the nuclear magnetic quantum number. The hyperfine interactions result in characteristic splitting patterns in an EPR spectrum spectrum with the number of hyperfine lines caused by a nucleus given by:

$$Number\ of\ HF\ lines = 2NI + 1 \quad \textbf{Equation 1.21}$$

where N is the number of equivalent nuclei. This information can be used to further understand the environment about an unpaired electron. In paramagnetic transition metal complexes, hyperfine interactions can be used to characterize both the spin density and orbital occupancy of the metal ion itself (if I > 0), and coordinated ligands.

The latter is particularly valuable since it enables characterization of: (i) identity of ligand sets, (ii) geometry, (iii) bonding, and (iv) ligand-based redox processes.

In this work, X-band EPR spectra were collected from both liquid and frozen solutions of metal complexes. Specifically, EPR was used to study fluorinated ruthenium(III) anticancer agents encapsulated in PLGA nanoparticles. Furthermore, the solution behaviour and biomolecule interactions of the copper anticancer complex Cas III-ia was characterized by EPR. Experimental spectra were analyzed by spectral simulations using the MATLAB based program EasySpin.[246]

1.6. Research goals

The discovery of cisplatin continues to inspire the search for new metal-based chemotherapeutics. However, despite the vast catalogue of anticancer metallodrug candidates that have been reported, their mechanisms of action often remain ambiguous. Furthermore, research into particular therapeutic metal complexes often ebbs and flows with their academic and clinical popularity, leaving some promising families of complexes underexplored. The goal of the work in this thesis is two-fold: (i) to develop novel anticancer complexes with high activity and selectivity (Chapters 2, 4, and 6) and, (ii) to improve understanding of the mechanisms of known families of metal-based chemotherapeutics (Chapters 3 and 5). These studies seek to inform the design future generations of metal-based anticancer agents and also demonstrate the utility of magnetic resonance methods to these developments.

2 RAPToxifen: Tethering a selective estrogen receptor modulator to the RAPTA-scaffold

2.1. Introduction

Organometallic ruthenium(II) anticancer complexes of the RAPTA- and RAED-type have been widely studied for their application as anticancer agents. Their stable, 18-electron configuration makes them attractive drug candidates, because the arene and non-halogen ligands typically remain coordinated following introduction into complex biological systems. Exchangeable chloride ligands allow for coordinate interactions with proteins and DNA, while auxiliary ligands such as PTA help to increase aqueous solubility. The arene-ligand is a convenient, but underexplored, site for modification. Functionalization of the arene does not typically affect the overall stability of the complex and such modifications can be designed to promote biomolecule interactions, such as DNA intercalation or receptor binding. A number of Ru-arene complexes, such as RAED-C and RAPTA-C, have been evaluated both *in vitro* and *in vivo,* with promising anticancer and antimetastatic activity demonstrated. The mechanisms by which these complexes exhibit their activity are still under investigation but have been suggested to originate from both coordinate and non-coordinate interactions with biomolecules, such as DNA and proteins in the extracellular matrix, as well as the generation of ROS, each of which can lead to the interruption of normal cell function.

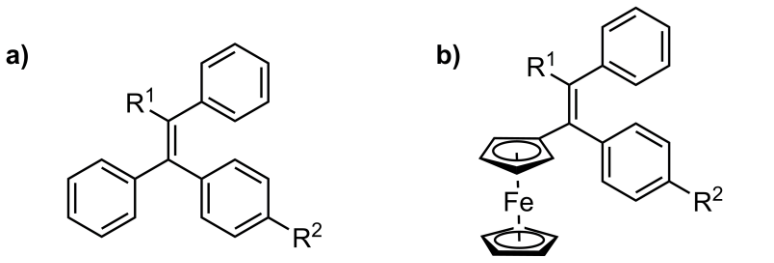

Tamoxifen
$R^1 = CH_2CH_3$
$R^2 = OCH_2CH_2N(CH_3)_2$

Ferrocifen
$R^1 = CH_2CH_3$
$R^2 = OCH_2CH_2N(CH_3)_2$

Figure 2.1 The triphenylethylene ER SERM core and the anti-breast cancer drug tamoxifen. b) the structure of ferrocifen.

In this chapter, a selective estrogen receptor (ER) modulator (SERM) was coupled to the RAPTA scaffold through the arene-ligand. A prominent family of SERMs

are designed around a triphenylethylene core that can bind the estrogen receptor and affect estrogen uptake.[247] A prominent example of a compound containing the SERM backbone is tamoxifen (**Figure 2.1a**) which is currently used in the clinic for the treatment of breast cancer. Unfortunately, it has been found that its activity becomes hindered due to acquired resistance.[248] A promising strategy to overcome this replaces one of the phenyl rings of the triphenylethylene scaffold with ferrocene (Fc). This compound, known as ferrocifen, and other related molecules have been found to display equivalent or better activity than tamoxifen, with IC_{50} values in the single-digit micromolar range (**Figure 2.1b**).[249,250] Furthermore, ferrocifens are suggested to overcome resistance pathways through multiple modes of activity such as estrogen receptor antagonism coupled with ROS generation by the Fc. This strategy has since been explored with other metallocenes such as Ru,[251] Re,[252] and Ti[253] with good *in vitro* anticancer activity. Since SERMs bind specifically to the estrogen receptor, they can also selectively target breast cancer cells. Attaching a SERM to a non-selective metal anticancer complex then becomes an attractive idea to overcome off-target activity of the metal compound. More recently, this has been proven to be a viable strategy by attaching well known metal-based anticancer complexes, such as cisplatin and its platinum(IV) derivatives, to tamoxifen-type SERMs.[254–257] In most cases, increased uptake and cytotoxicity in ER+ breast cancer cells was observed relative to the unmodified platinum complexes. Using a similar approach, the compounds developed in this chapter couple RAPTA- and RAED-type complexes to a SERM via the arene ligand of the Ru(II) centre. The SERM ligand can potentially act as a targeting agent for ER+ breast cancer cells and can also display activity through receptor antagonism. This activity can be augmented by the ruthenium arene component, generating multifunctional anticancer species. More generally, the complexes presented in this chapter demonstrate the viability of introducing pharmacophore functionalities to Ru(II) anticancer complexes through direct modification of the arene ligand. In this chapter, this approach resulted in enhanced cytotoxicity and selectivity as compared to the unmodified Ru(II) complexes.

2.2. Experimental

2.2.1. Synthesis

The materials phenylacetic acid, benzylamine, 4-methoxybenzophenone, 3-chloropropiophenone, 3-benzoylpropionic acid, α-phellandrene, titanium tetrachloride, zinc dust, tetrakis(hydroxymethyl) phosphonium chloride, hexamethylene tetraamine, sodium azide, 1-[bis(dimethylamino)methylene]-1*H*-1,2,3-triazolo[4,5-*b*]pyridinium-3-oxid hexafluorophosphate (HATU), and *N,N*-diisopropyl ethylamine (DIPEA) were purchased from Combi-Blocks and used without further purification. Hydrated ruthenium trichloride was purchased from Sigma Aldrich and any ruthenium-oxide species were converted to Ru(III) by boiling in concentrated hydrochloric acid to dryness three times. Syntheses of triphenylethylene molecules resulted in 1:4, *E*:*Z* isomeric mixtures; ^{1}H NMR chemical shifts are reported for the *Z* isomer. If overlapping resonances made the assignments ambiguous, NMR signals are reported as a multiplet of approximately average chemical shift of both isomers.

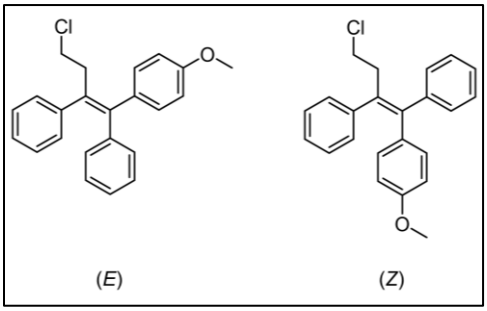

(E/Z)-(4-chloro-1-(4-methoxyphenyl)but-1-ene-1,2-diyl)dibenzene, **2-1**. **2-1** was synthesized following a literature preparation.[258] Zinc dust (430 mg, 6.5 mmol) was dissolved in dry THF (10 mL), cooled to -10 °C, and purged with N_2. Titanium tetrachloride (390 µL, 3.5 mmol) was then added dropwise over 20 minutes. The bright yellow solution was refluxed until the solution turned purple (approximately 2 hours). The purple solution was then cooled to 0 °C and 4-methoxybenzophenone (212 mg, 1.0 mmol) and 3-chloropropiophenone (168 mg, 1.0 mmol) dissolved in dry THF (5 mL) was added dropwise. The solution was refluxed for another 2 hours and then allowed to cool to room temperature. The mixture was then neutralized with 10 % (w/v) sodium bicarbonate (50 mL) and then passed through a celite plug. The resulting clear-yellow solution was then placed on the rotary evaporator to remove the THF solvent. The remaining aqueous solution was extracted with ethyl acetate (3 x 50 mL), the ethyl acetate layers were combined, washed with water (50 mL) and brine (50 mL) and then dried with magnesium sulphate. The solution was filtered and dried on a rotary evaporator giving the crude product as a yellow oil. This crude product was dissolved in

a minimum amount of DCM and then dry loaded onto a silica gel column for purification. The pure product was obtained as a white solid by eluting with a 50:50 mixture of toluene:hexanes and removal of the solvent under vacuum. Yield: 343 mg, 76 %; MS (ESI^+): *m/z* 313.152 $[M\text{-}Cl]^+$ (calc'd), 313.150 $[M\text{-}Cl]^+$ (found); ^1H NMR (500 MHz, $CDCl_3$): δ 2.94 (t, J = 7.5 Hz, 2H), 3.43 (t, J = 7.5 Hz, 2H), 6.57 (d, J = 8.8 Hz, 2H), 6.81 (d, 8.9 Hz, 2H), 7.14 – 7.17 (m, 3H), 7.20 – 7.23 (m, 2H), 7.29 – 7.31 (m, 3H), 7.37 – 7.40 (m, 2H); $^{13}C\{^1H\}$ NMR (100 MHz, $CDCl_3$): δ 38.6, 42.9, 55.0, 112.9, 113.8, 126.6, 126.9, 128.1, 128.2, 128.4, 129.4, 130.6, 131.7, 134.8, 135.2.

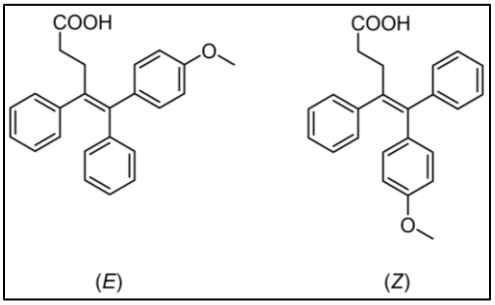

(*Z*)-5-(4-methoxyphenyl)-4,5-diphenylpent-4-enoic acid, **2-2**. **2-2** Was synthesized following the procedure above for **2-1**, but with 3-benzoylpropionic acid (178 mg, 1.0 mmol) used instead of 3-chloropropionic acid. Instead of quenching the reaction with base, upon completion the reaction was quenched with 6M HCl to ensure the carboxylic acid remained protonated and the product was extracted with DCM. A crude yellow, oily solid was collected and purified by silica gel column chromatography with an eluent mixture of 50:50 ethyl acetate:hexanes. The pure product, which was a mixture of *E*- and *Z*-isomers (1:4), was obtained as a white solid. Yield: 2.21 mg, 45 %; MS (ESI^+): *m/z* 358.168 $[M]^+$ (calc'd), 359.171 $[M + H]^+$ (found); ^1H NMR (500 MHz, $CDCl_3$): δ 2.34 (m, 2H), 2.75 (m, 2H), 3.68 (s, 3H), 6.55 (d, J = 8.86 Hz, 2H), 6.78 (d, J = 8.86 Hz), 7.08 – 7.21 (m, 8H), 7.34 (m, 2H).

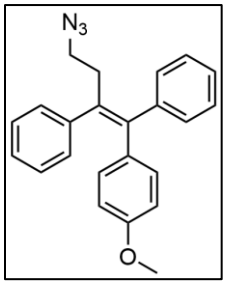

(*E/Z*)-(4-azido-1-(4-methoxyphenyl)but-1-ene-1,2-diyl)dibenzene, **2-3**. **2-1** (348 mg, 1.0 mmol) was dissolved in dry DMF (5 mL). Sodium azide (325 mg, 5 mmol) was added slowly as a solid. The resulting suspension was stirred at 80 °C for 18 h, cooled to room temperature, and then poured over ice. The aqueous solution was extracted with ethyl acetate (3x25 mL) and the combined ethyl acetate layers were washed with water (5x25 mL) and brine (5x25 mL). The ethyl acetate solution was dried with magnesium sulphate and filtered, followed by removal of the solvent by rotary evaporation. The resulting pale-yellow oil was used without further purification. Yield: 313.0 mg, 94.4 %; MS (ESI^+): *m/z* 355.618 $[M^+]$ (calc'd), 356.600

$[M+H]^+$ (found), 342.700 $[M-N+H]^+$ (found), 328.700 $[M-2N+H]^+$ (found), 314.700 $[M-3N+H]^+$ (found).

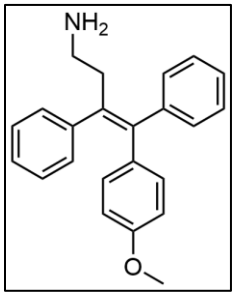

(**E/*Z*)-4-(4-methoxyphenyl)-3,4-diphenylbut-3-en-1-amine**, **2-4**. **2-3** (355 mg, 1.0 mmol) was dissolved in ethanol:water (4:1, 10 mL). Zinc dust (393 mg, 6.0 mmol) and ammonium chloride (375 mg, 7.0 mmol) were added as solids and the suspension was refluxed for 18 h. The resulting solution was then filtered to removed unreacted zinc dust and ammonium hydroxide (28 % in water) was added until the pH > 10. Solvents were removed by rotary evaporation and the residue was redissolved in ethyl acetate (20 mL). The solution was then washed with water (20 mL) and brine (20 mL), dried with magnesium sulphate, and filtered. The ethyl acetate solution was removed by rotary evaporation and the product was recovered as white solid and was used without further purification. Yield: 308 mg, 93.8 %. MS (ESI^+): *m/z* 329.178 $[M]^+$ (calc'd), 330.190 $[M+H]^+$ (found).

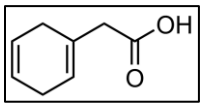

2-(cyclohexa-1,4-dien-1-yl)acetic acid, **2-5**. This compound was synthesized from phenylacetic using acid the Birch reduction, as follows. Phenylacetic acid (226 mg, 1.65 mmol) was dissolved in anhydrous ethanol (10 mL) and added to anhydrous liquid ammonia (100 mL, -78 °C) under N_2 in a 500 mL three-neck round-bottom flask equipped with a dry ice condenser. Lithium metal was added in small pieces until the vivid blue colour persisted, after which the solution was stirred at -78 °C for an additional 3 hours. The solution was then diluted with anhydrous ethanol (10 mL) and ammonium chloride (420 mg, 7.6 mmol) was added as a solid. The mixture was allowed to slowly warm to room temperature and the round-bottom flask was left at the back of the fume hood overnight to allow for complete evaporation of the ammonia. Water (20 mL) was added to the residue and the pH was adjusted to 2 with concentrated hydrochloric acid. This solution was extracted with ether (3x20 mL), the ether layers were combined, washed with brine (20 mL), and dried with magnesium sulphate. The ether was filtered then removed via rotary evaporation leaving behind a pure white solid. Yield: 198 mg, 88 %; ^1H NMR (500 MHz, $CDCl_3$): δ 2.72 (m, 4H), 3.02 (s, 2H), 5.63 (s, 1H), 5.70 (m, 2H), 9.84 (br s, 1H); $^{13}C\{^1H\}$ (100 MHz, $CDCl_3$): δ 26.8, 29.0, 42.8, 123.7, 123.8, 123.9, 178.0.

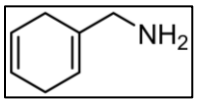

Cyclohexa-2,5-dien-1-ylmethanamine, **2-6**. **2-6** was synthesized following the same Birch reduction conditions stated above for the synthesis of **2-5,** except benzylamine (400 µL, 4.50 mmol) was used instead of phenylacetic acid as the starting material with solid sodium used instead of lithium. A modified extraction was used in which the solution was not acidified prior to extraction with ether. Yield: 401 mg, 83 %; ^{1}H NMR (500 MHz, $CDCl_3$): δ 1.45 (br s, -NH_2, 2H), 2.61 (m, 2H), 2.68 (m, 2H), 3.15 (s, 2H), 4.55 (br s, 1H), 5.70 (m, 2H).

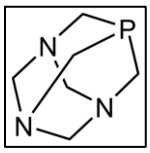

1,3,5-triaza-7-phosphaadamantane, (**PTA**). **PTA** was synthesized according to a literature procedure.[259] Tetrakis(hydroxymethyl) phosphonium chloride (80 % in water) (2.9 g, 12.5 mmol) was dissolved in water (15 mL) and cooled to 0 °C. Sodium hydroxide (50 % w/v in water) (0.64 g) is added slowly and the solution was allowed to warm to room temperature. Formaldehyde (37% w/v in water) (4.64 g) and hexamethylenetetraamine (1.4 g, 10.0 mmol) were added and the solution was allowed to stand for 18 hours at room temperature. The solution was concentrated to approximately 10 % of the initial volume under a stream of air and the resulting white precipitate was suction filtered and washed with cold ethanol (5x5 mL). The solid is then redissolved in minimal DCM and excess sodium chloride removed by filtration. The DCM was removed by rotary evaporation and the resulting white solid was recrystallized from hot ethanol (approximately 20 mL per gram of product). Yield: 1.38 g, 88 %; ^{1}H NMR (400 MHz, $CDCl_3$): δ 4.05 (d, J_{H-P} = 9.87 Hz, 6H), 4.60 (s, 6H); ^{31}P NMR (162 MHz, $CDCl_3$): δ -102.4.

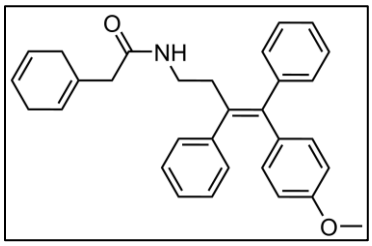

(*E/Z*)-2- (cyclohexa-1,4-dien-1-yl) -N-(4-(4-methoxyphenyl) -3,4-diphenylbut -3-en-1-yl)acetamide, **2-7**. **2-5** (130 mg, 0.94 mmol), HATU (360 mg, 0.94 mmol), and DIPEA (330 µL, 1.88 mmol) were dissolved in dry DCM (10 mL) and stirred for 20 minutes at room temperature. The solution changed from pale yellow to dark yellow and was then cooled to 0 °C. **2-4** (340 mg, 1.04 mmol) dissolved in dry DCM (5 mL) was then added dropwise to the cooled solution. The mixture was then allowed to warm to room temperature and stirred for an additional 4 hours. The reaction was then diluted with DCM (30 mL) and washed with 20 mL each of 1 M hydrochloric acid, water, and brine. The DCM was dried with magnesium sulphate, filtered, and removed by rotary evaporation leaving an orange oil. The orange oil was purified by silica gel column chromatography with an eluent of

50:50 ethyl acetate:hexanes to give a white solid. Yield: 388 mg, 91 %; MS (ESI^+): *m/z* 449.235 $[M]^+$ (calc'd), 450.232 $[M + H]^+$ (found); ^1H NMR (400 MHz, $CDCl_3$): δ 2.61 (m, 2H), 2.69 (t, J = 7.0 Hz, 2H), 2.76 (t, J = 7.1 Hz, 2H), 2.81 (s, 2H), 3.26 (m, 2H), 3.71 (s, 3H), 5.57 (br s, 1H), 5.62 (m, 1H), 5.72 (m, 2H), 6.58 (d, J = 9.0 Hz, 2H), 6.79 (d, J = 8.8 Hz, 2H), 7.12 – 7.25 (m, 8H), 7.38 (t, J = 7.67, 2H); $^{13}C\{^1H\}$ NMR (100 MHz, $CDCl_3$): δ 26.9, 29.1, 35.0, 38.5, 43.9, 55.0, 112.9, 123.7, 124.0, 124.1, 127.4, 128.3, 129.4, 129.5, 131.7, 134.9, 136.2, 141.4, 141.7, 157.8, 170.3.

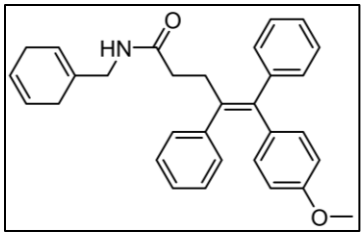

(*E/Z*)-N-benzyl-5-(4-methoxyphenyl) -4,5-diphenylpent-4-enamide, **2-8**. **2-8** was synthesized under similar HATU-coupling conditions as for **2-7**, with **2-2** (560 mg, 1.56 mmol) and **2-6** (188 mg, 1.72 mmol) used instead of **2-5** and **2-4**, respectively. As for **2-7**, the final crude product **2-8** was purified by silica gel column chromatography with an eluent mixture of 50:50 ethyl acetate:hexanes to give the pure product **2-8** as a white solid. Yield: 488 mg, 70 %; MS (ESI^+): *m/z* 449.24 $[M]^+$ (calc'd), 450.23 $[M + H]^+$ (found); ^1H NMR (400 MHz, $CDCl_3$): δ 2.22 (m, 2H), 2.57 (m, 2H), 2.69 (m, 2H), 2.86 (m, 2H), 3.70 (s, 3H), 3.86 (s, 2H), 5.24 (m, amide, 1H), 5.53 (m, 1H), 5.70 (m, 2H), 6.58 (m, 2H), 6.80 (m, 2H), 7.09 – 7.40 (m ,10H); $^{13}C\{^1H\}$ NMR (100 MHz, $CDCl_3$): δ 26.7, 27.1, 31.8, 35.7, 44.9, 55.1, 112.9, 113.7, 120.8, 125.9, 126.5, 126.8, 127.4, 128.0, 128.2, 128.4, 129.3, 129.7, 130.8, 131.9, 141.4, 143.2 157.8, 158.9, 172.5.

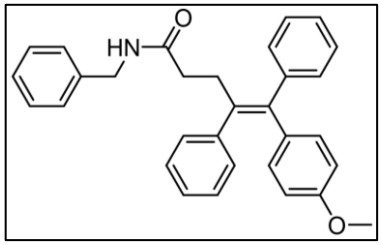

(E/Z)-N-benzyl-5-(4-methoxyphenyl)-4,5-diphenylpent-4-enamide, **2-8-ctrl**. **2-8-ctrl** was synthesized by the same method as **2-8** but with benzylamine (153 µL, 1.72 mmol) instead of **2-6** as the starting material. The crude product was purified via silica-gel column chromatography with an eluent of 50:50 ethyl acetate:hexanes. The pure product **2-8-ctrl** was then obtained as a white solid. Yield: 85 %; MS (ESI^+): *m/z* 447.22 (calc'd), 448.20 $[M + H]^+$ (found); ^1H NMR (400 MHz, $CDCl_3$): δ 2.20 (m, 2H), 2.83 (m, 2H), 3.68 (s, 3H), 5.41 (m, amide, 1H), 6.54 (m, 2H), 6.77 (m, 2H), 7.06 – 7.23 (m, 10H), 7.27 – 7.36 (m, 5H); $^{13}C\{^1H\}$ NMR (100 MHz, $CDCl_3$): δ 31.7, 35.7, 35.7, 55.0, 112.8, 126.4, 126.9, 127.5, 128.7, 129.3, 129.7, 131.8, 135.0, 137.7, 138.2, 143.2, 157.7, 172.0.

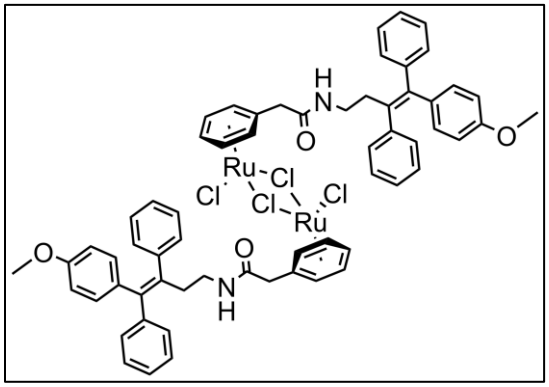

[(*E/Z*)-(2-7)RuCl$_2$]$_2$, **2-9**. Ruthenium trichloride (80.0 mg, 0.38 mmol) was dissolved in degassed ethanol (20 mL). **2-7** (700 mg, 1.6 mmol) was added as a solid and the suspension was refluxed for 18 hours. During this time, the suspension changed colour from brown-red to yellow-orange and a yellow-orange precipitate formed. The solution was concentrated to half the original volume to induce further precipitation, and the precipitate was collected by suction filtration and washed with ethanol (3x5 mL), DCM (3x5 mL) and ether (5 mL). The orange precipitate was dry loaded onto a silica-gel column and then eluted with a solvent mixture of DCM:methanol (80:20) to give pure **2-9** as an orange solid. Yield: 125 mg, (54 %); ^{1}H NMR (500 MHz, DMSO-d$_6$): δ 2.53 (m, 4H), 2.99 (m, 4H), 3.23 (s, 4H), 3.62 (s, 6H), 5.74 (m, 4H), 5.80 (m, 2H), 6.00 (t, J = 5.96 Hz, 4H), 6.61 (d, J = 8.86 Hz, 4H), 6.76 (d, J = 8.76 Hz, 4H), 7.12-7.23 (m, 16H), 7.38 (t, J = 7.54 Hz), 4H).

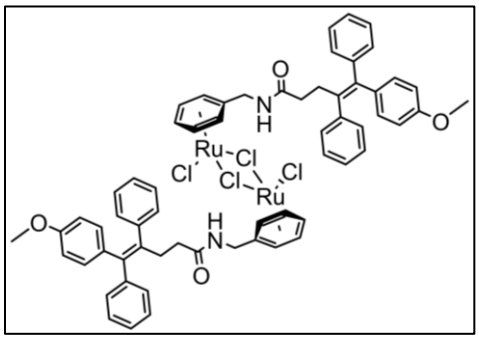

[(*E/Z*)-(2-8)RuCl$_2$]$_2$, **2-10**. **2-10** was synthesized using the same method as **2-9** but using **2-8** (935 mg, 2.08 mmol) instead of **2-7**. The product was purified using the same method as **2-9** to give **2-10** as an orange solid. Yield: 156 mg, 12 %; ^{1}H NMR (500 MHz, $CDCl_3$): δ 2.51 (m, 4H), 2.88 (m, 4H), 3.71 (s, 6H), 4.35 (m, 4H), 5.32 (m, 4H), 5.60 (m, 4H), 5.66 (m, 2H), 6.57 (d, J = 8.82 Hz, 4H), 6.81 (d, J = 8.88 Hz, 4H), 7.12 – 7.37 (m, 16H), 7.39 – 7.47 (m, 4H).

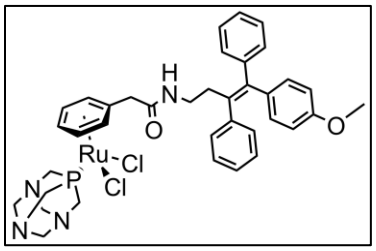

[(*E/Z*)-(2-7)(PTA)RuCl$_2$], 2-11. **2-9** (25 mg, 0.02 mmol) and **PTA** (7.0 mg, 0.05 mmol) added as solids to dry DCM (5 mL) to give an orange suspension. The suspension was stirred for 18 hours at room temperature upon which the solution turned clear orange. The DCM was then removed by rotary evaporation yielding a brown-orange residue. The residue was purified via silica gel chromatography with an eluent mixture of DCM:MeOH, 80:20. Solvent was removed under vacuum to give **2-11** as a crystalline brown solid. Yield 17.5

mg, 56 %; MS (ESI$^+$): 776.70 $[M]^+$ (calc'd), 777.74 $[M + H]^+$, 741.21 $[M – Cl]^+$ (found); ^{1}H NMR (400 MHz, $CDCl_3$): δ 2.72 (t, J =7.61 Hz, 2H), 3.31 (m, 4H), 3.68 (s, 3H), 4.32 (br s, 6H), 4.54 (br s, 6H), 5.17 (br s, 1H), 5.26 (m, 1H), 5.52 (m, 2H), 5.58 (m 2H), 6.57 (d, J = 8.82 Hz, 2H), 6.81 (d, J = 8.75, 2H), 7.12 – 7.29 (m, 8H), 7.36 – 7.40 (m, 2H); ^{31}P{^{1}H} NMR (162 MHz, $CDCl_3$): δ -32.7.

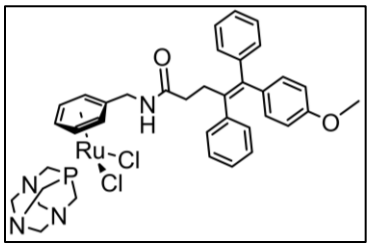

[(*E/Z*)-(2-8)(PTA)RuCl$_2$], 2-12. **2-12** was synthesized following the procedure for **2-11** where **2-10** (80 mg, 0.065 mmol) was used instead of **2-9**. Yield: 36 mg, 35 %; MS (ESI$^+$): 776.14 (calc'd), 741.18 $[M – Cl]^+$ (found), 777.16 $[M + H]^+$ (found). ^{1}H NMR (400 MHz, $CDCl_3$): δ 2.33 (m, 2H), 2.88 (m, 2H), 3.70 (s, 3H), 3.86 (s, 2H), 4.33 (br s, 6H), 4.56 (br s, 6H), 5.14 (m, 1H), 5.48 (m, 2H), 5.59 (m, 2H), 6.57 (m, 2H), 6.80 (m, 2H), 7.13 – 7.24 (m, 8H), 7.42 (t, J = 7.49 Hz, 2H); ^{31}P{^{1}H} NMR (162 MHz, $CDCl_3$): δ -33.4; Elemental analysis %: .

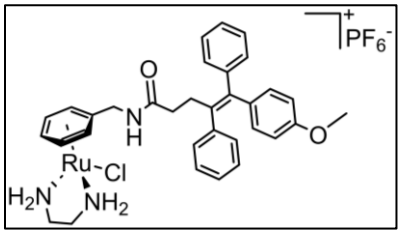

[(*E/Z*)-(2-8)(en)RuCl$_2$][PF$_6$], 2-13. **2-10** (50 mg, 0.04 mmol) was dissolved in dry DCM (5 mL) and ethylenediamine (**en**) (5.6 µL, 0.085 mmol) was added and the solution was allowed to stir at room temperature overnight. The solution turned from red to brown-orange and NH_4PF_6 (13.8 mg, 0.085 mmol) was then added as a solid. The solution was allowed to stir at room temperature for 4 hours leading to the precipitation of NH_4Cl as a white solid. The NH_4Cl was removed by filtration and washed with DCM to collect any residual product. DCM was removed via rotary evaporation to give crude **2-13** as a brown solid. The crude product was purified by silica gel column chromatography with an eluent mixture of 80:20 DCM:MeOH. Pure **2-13** eluted as a yellow band and, following removal of solvent under vacuum, gave a crystalline yellow solid. Yield: 18.6 mg, 28 %; MS (ESI$^+$): 644.16 $[M]^+$ (calc'd), 644.15 $[M]^+$ (found); ^{1}H NMR (400 MHz, MeOD): δ 2.31 (m, 2H), 2.38 (m, 2H), 2.50 (m, 2H), 2.81 (m, 2H), 3.66 (s, 3H), 4.18 (s, 2H), 5.52 (t, J = 5.99 Hz, 2H), 5.59 (t, J = 5.92 Hz, 1H), 5.70 (td, J = 5.88, 1.60 Hz, 2H), 6.56 (m, 2H), 6.76 (m, 2H), 7.12 – 7.19 (m, 8H), 7.37 (t, J = 7.42 Hz, 2H); ^{31}P{^{1}H} NMR (162 MHz, MeOD): δ -144.2 (sep, J_{P-F} = 714 Hz, PF_6); Elemental analysis %: calc'd ($C_{33}H_{37}ClN_3O_2PRu•CH_3OH$): C 49.73, H 5.03, N 5.12; found: C 48.82, H 4.72, N 5.00.

2.2.2. NMR Stability Studies in Aqueous Media

^{31}P NMR experiments were performed on a Bruker AVANCE III 400 MHZ spectrometer equipped with a 5 mm BBOF ATM probe. Solutions were prepared in 1X 2-(*N*-morpholino)ethanesulfonic acid (MES) buffered saline with a chloride concentration of 154 mM. A 20 mM stock solution of the complex in DMSO was used to aid with aqueous solubility and diluted to a final concentration of 1 mM with MES buffer for a sample volume of 600 µL. This sample was then placed in an NMR tube and sealed to prevent evaporation during incubation. ^{31}P NMR spectra were collected immediately following dissolution in the MES buffer and after 24 hours at 37 °C.

2.2.3. UV-Vis Measurements

Experiments were conducted on a PerkinElmer Lambda 850 spectrophotometer. Solutions were prepared from 20 mM stocks in DMSO to aid with aqueous solubility and diluted to a final volume of 1 mL (200 µM complex) with 1X MES (PBS) with a chloride concentration of 154 mM. All spectra were collected at 25 °C.

2.2.4. Cell Studies

Cytotoxicity Assays*

MCF7 and MDA-MB-231 cells (ATCC) were maintained at 37 °C with 5 % CO_2 in DMEM (Gibco) supplemented with 10 % fetal bovine serum (Gibco) and L-glutamine (2 mM, Gibco). Cells were then seeded at 2000 cells per well in quadruplicate in 384-well plates (Greiner Bio-One). After 24 hours, the wells were dosed with compound (from a 20 mM DMSO stock solution) at concentrations from 1 to 400 µM. The final DMSO concentration in each well was 1 %. After 72 hours of compound exposure, cells were incubated with 4.8 µM Hoescht33342 (Life Technologies) and 1 µM of ethidium homodimer (Biotium) for 20 minutes. The dyes allowed for total nuclei and dead cell counts, respectively. Plates were imaged with an IN-Cell Analyzer 2500 (GE Healthcare). Cells were counted using the IN-Cell Developer Toolbox which classified

* Cytotoxicity studies were performed by Devon Heroux under the supervision of Dr. Marcel Bally at the BC Cancer Agency, 686 West Broadway, Suite 500, Vancouver, BC, Canada, V5Z 1G1.

cells as dead if > 30 % of both stains overlapped. Plots of the resulting data were generated using Prism 6.0 (GraphPad Software) which interpolated IC_{50} values from the resulting sigmoidal-curve fit. P-values of < 0.05 were considered statistically significant determined using one-way ANOVA.

NCI-60

Compounds were submitted to the NCI-60 Human Tumor Cell Lines Screen provided by the National Cancer Institute, Division of Cancer Treatment & Diagnosis. Compounds submitted to the NCI-60 screen were prepared in DMSO:glycerol 9:1 at a concentration of 4 mM. Preparation of 96 well plates involved the addition of 100 µL of 10 % glycerol in isopropanol to each well. Then 400 µL of the DMSO:glycerol stock solution (4 mM compound) is added to each well. The plates were then transferred to a SpeedVac system to remove all solvents leaving a glycerol-drug residue in each well. Dry plates are stored at -70 °C until testing day. On testing day, a strip of standards (Adriamycin, NSC 123127 prepared in the same way as the test compounds above) is added to the detachable well plate. Then, 90 µL of DMSO is added to each well, followed by sonication to ensure complete dissolution of the compound residue. Next, 75 µL of the solution is transferred to 12 channel reservoir plates (column plates) using a 12 channel hand pipettor. These plates were sealed and stored under nitrogen in a desiccator box for delivery to the testing lab. Human tumour cell lines are grown in RPMI 1640 media containing 5 % fetal bovine serum and 2 mM L-glutamine. For testing, 100 µL of cells (density ranged from 5000 to 40000 cells per well) are inoculated into 96 well plates. The plates are then incubated at 37 °C under 5 % CO_2, 95 % air, 100 % relative humidity for 24 hours prior to compound addition. Following the 24 hour incubation, two plates of each cell line are fixed *in situ* with trichloroacetic acid (TCA) and used as a measurement of cell population at the time of compound addition (time zero, Tz). Next, aliquots of the compounds in DMSO were diluted to twice the final desired concentration (20 µM) with complete cell medium containing 50 µg/mL gentamicin. Finally, 100 µL aliquots of the diluted compound solutions were added to the wells containing the cells and 100 µL of cell media for a final compound concentration of 10 µM in each well. After compound addition, the plates were incubated for 48 hours at 37 °C under 5 % CO_2, 95 % air, 100 % relative humidity. The addition of cold TCA was used to terminate the assays involving adherent cells. Cells were then fixed in situ by the addition of 50 µL of

cold 50 % (w/v) TCA for a final TCA concentration of 10 % per well and incubated for 60 minutes at 4 °C. The supernatant in each well was discarded and the plates were washed 5 times with tap water and air dried. Cells were stained with a sulforhodamine B (SRB) solution (100 µL, 0.4 % w/v) in 1 % acetic acid is added to each well and the plates were then incubated for 10 minutes at room temperature.[260] Unbound dye was then removed by 5 washes with 1 % acetic acid followed by air drying. Bound stain was then solubilized with 10 mM trizma base and the absorbance was read on an automated plate reader at a wavelength of 515 nm. For non-adherent cells, the procedure was the same except the assays were terminated by fixing settled cells by the addition of 50 µL of 80 % TCA for a final TCA concentration of 16 %. Percent growth was calculated by comparing the absorbance of cells fixed at time zero (Tz), the absorbance of control growth of untreated wells (C), and the absorbance from cell growth in the presence of compound (Ti) using the following equations:

$$\frac{Ti - Tz}{C - Tz} \times 100$$

for the case in which Ti absorbance ≥ Tz, or

$$\frac{Ti - Tz}{Tz} \times 100$$

for the case in which Ti < Tz.

2.3. Results and Discussion

2.3.1. Synthesis

A robust and widely used method to synthesize Ru(II)-arene complexes involves reacting substituted 1,4- or 1,3-cyclohexadienes with ruthenium(III) trichloride in refluxing ethanol. This strategy led to the choice to perform a Birch reduction on phenylacetic acid to synthesize its corresponding 1,4-diene, which could later be coordinated to ruthenium. The acetic acid functional group provided a modification site in which simple amide coupling chemistry could be used to attach the triphenylethylene SERM. The Birch reduction was carried out as described in the literature and the resulting diene was synthesized in good yield with 96 % conversion as determined by ^{1}H NMR.[261] The triphenylethylene SERM was synthesized following the method reported by Kaur and

coworkers.[262] The first step of the synthesis involved a McMurray coupling of 4-methoxybenzophenone and 3-chloropropiophenone and resulted in and isomeric mixture of **2-1** with an E/Z ratio of approximately 3:7 (**Figure 2.2a**). This was determined by integrating the downfield shifted ^{1}H NMR signals arising from one of the methylene groups *trans* to a phenyl group versus *trans* to the 4-methoxypehnyl group. The isomers were not separable during purification via silica gel column chromatography and were carried through the remaining steps of the synthesis. Both isomers of SERMs have been shown to have tissue-specific ER agonist or antagonist activity.[263] Therefore, having a mixture of *E* and *Z* isomers was not a concern once appended to ruthenium as they will both act as a vector for the complex to target estrogen receptors. The next step involved a nucleophilic substitution of the alkyl chloride with sodium azide. This reaction proceeded at scales of up to 500 mg and conversion was essentially quantitative as determined by thin layer chromatography (TLC) and mass spectrometry (MS). The azide, **2-3**, was used without further purification in the subsequent reductive amination using ammonium chloride and zinc dust. The amine, **2-4**, was formed in good yield and was pure enough to be used in subsequent reactions as determined by ^{1}H NMR and MS. A HATU-coupling reaction was then performed to form an amide bond between **2-4** and the previously synthesized diene of phenylacetic acid. The SERM **2-7** was purified by dry loading onto a silica-gel column with an eluent of ethyl acetate:hexanes (50:50) and isolated in good yield. The isomeric ratio of 3:7 (*E*/*Z*) was, again, confirmed by ^{1}H NMR.

Subsequently, a shorter route to the SERM ligand was determined in which the amide bond was reversed relative to that of **2-7**. This new route involved the Birch reduction of benzylamine to form its corresponding diene (**Scheme 2.1a**). To form a SERM with a carboxylic acid group to be coupled with the Birch-reduction product of benzylamine, a McMurray coupling of 2-benzoylpropionic acid and 4-methoxybenzophenone was performed to give **2-2** (**Scheme 2.1b**). Interestingly, this SERM was synthesized in an *E*/*Z* ratio of 1:1 confirmed by ^{1}H NMR (**Figure 2.2b**).

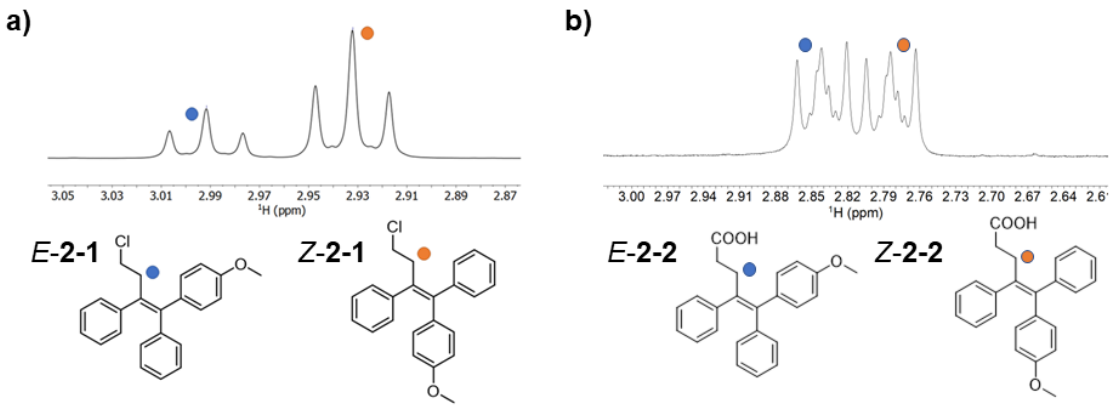

Figure 2.2 **^{1}H NMR signals arising from the indicated methylene protons (orange and blue circles) for the *E* and *Z* isomers of a) 2-1 and b) 2-2.**

The McMurray product and the diene of benzylamine could then be directly coupled using HATU chemistry to form the ligand **2-8**. This new route removed several steps compared to the original synthesis and no longer required the use of sodium azide, allowing it to be more safely scaled.

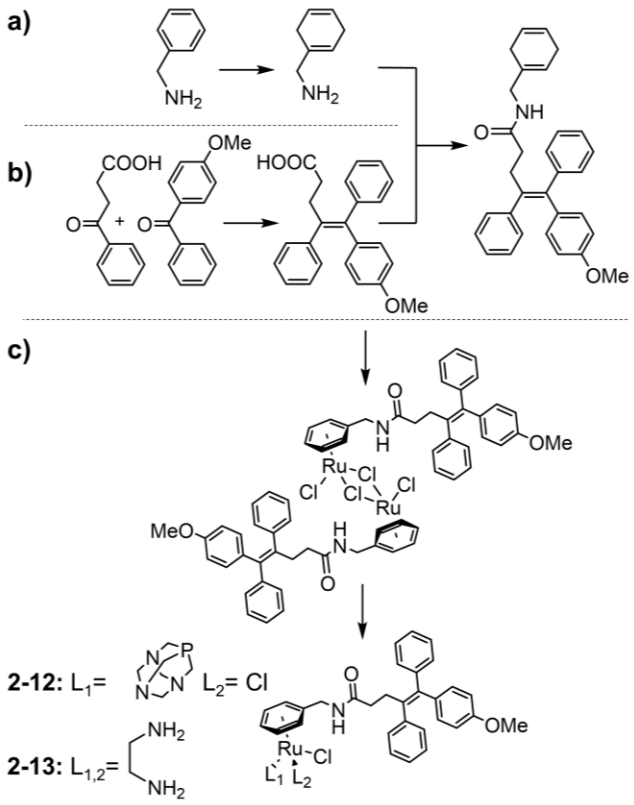

Scheme 2.1 General synthetic route to the ruthenium complexes 2-12 and 2-13 where a) depicts a Birch-reduction, b) depicts a McMurray coupling, and c) depicts the formation of the ruthenium-SERM dimer followed by coordination of PTA and en to form the 2-12 and 2-13.

To coordinate the SERM **2-8** to ruthenium, a procedure similar to synthesis reported by Bennett and coworkers of the ruthenium-(*p*-cymene) dimer[264] was followed in which a four-fold excess of **2-8** was refluxed in ethanol in the presence of ruthenium trichloride. This resulted in the ruthenium-SERM dimer, **2-10**, in reasonable yield following purification by silica-gel column chromatography (**Scheme 2c)**. Fortunately, unreacted **2-8** could also be recovered from the column and was used in subsequent syntheses of **2-10**. With the original ligand, **2-7**, in hand, its corresponding ruthenium dimer (**2-9**) was synthesized following the same procedure. Successful formation of the dimer can be conveniently confirmed by monitoring the change in the ^{1}H signals in the 5-6 ppm region corresponding to the 3 diene protons of the reduced aromatic ring. Upon coordination to ruthenium, the ring becomes re-aromatized and the signals in this region now account for 5 protons, characteristic of organometallic complexes of this type.[264] The resulting spectra for the diene of phenylacetic acid and the ruthenium dimer **2-9** are presented in **Figure 2.3**.

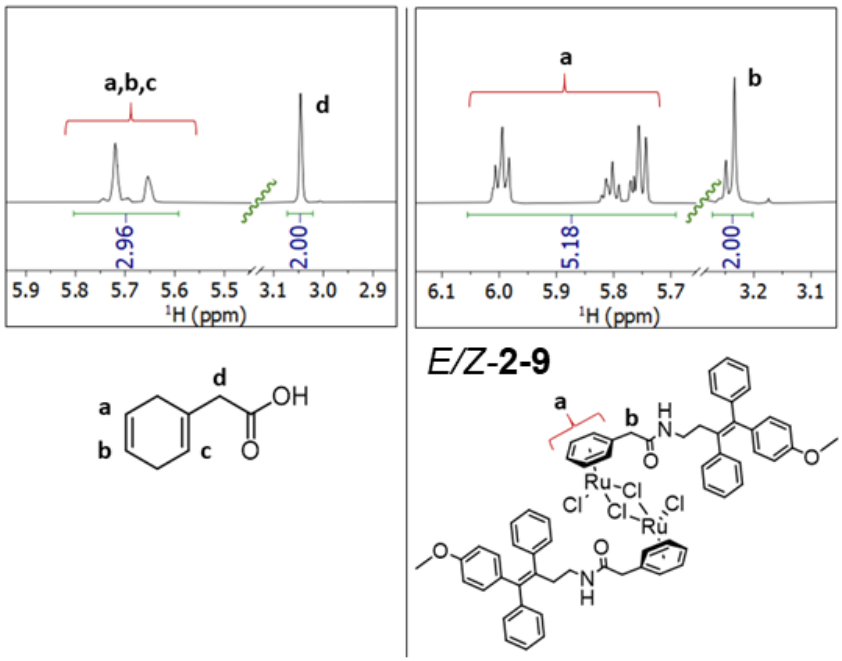

Figure 2.3 **^{1}H NMR of the diene region of reduced phenylacetic acid and how that region changes upon coordination to ruthenium to form the dimer 2-9. The integrations are referenced to the methylene protons of phenylacetic acid in both cases, with 2-9 showing a singlet for each *E* and *Z* isomer arising from proton b.**

Prior to the final step of the synthesis, the phosphorous-donor ligand, **PTA**, was then synthesized following a report on ligands for water-solubilizing organometallic compounds by Daigle.[259] Two equivalents of **PTA** was then reacted with either **2-9** or **2-10** in DCM and the resulting product was purified by column chromatography to yield the final compound **2-11** and **2-12** (**Scheme 2c**). The synthesis was confirmed by ^{1}H NMR and MS. The ^{31}P NMR presented with a single resonance at -32.7 ppm, which is indicative of coordination of PTA to Ru(II)-arene complexes of this type, and also demonstrated that only one phosphorous species was present following purification by silica-gel column chromatography.[105,265] To form the RAED-derivative **2-13**, 2 equivalents of ethylenediamine (en) were added to a solution of **2-10** in DCM. The resulting precipitate was purified by silica gel column chromatography and the successful synthesis was confirmed by ^{1}H NMR and MS.

2.3.2. Aqueous Solution Behaviour

Many metal-based anticancer complexes, such as cisplatin and KP1019, are thought to be prodrugs that become 'activated' following exchange of one or more of their ligands with water. These 'activated' complexes contain exchangeable aqua-ligands that allow for coordinate interactions with important biological targets such as proteins and DNA. These interactions, such as the lesions cisplatin forms with DNA, are key to the anticancer activity of such complexes.[2] Initial RAPTA-type ruthenium(II) complexes were designed with this type of aqueous ligand exchange in mind.[266] It is now suggested that coordination with DNA is not the only mechanism of action for such complexes, it is still thought that similar interactions with other biomolecules, such as proteins in the extracellular matrix, also contribute to the observed activity.[267] It is, therefore, important to understand aqueous ligand-exchange processes under physiological conditions when designing novel metal-based anticancer complexes. For the complexes synthesized in this chapter, ^{1}H and ^{31}P NMR were used to determine their ligand-exchange behaviour in buffered aqueous solutions.

The PTA ligand in RAPTA-type complexes provides a convenient spectroscopic handle to study the species that arise in aqueous media via ^{31}P NMR. Since PTA contains a single phosphorous atom, $^{31}P\{^{1}H\}$ measurements give a single resonance for each unique species in solution. This presents as a simple method for monitoring for aqueous ligand exchange processes.

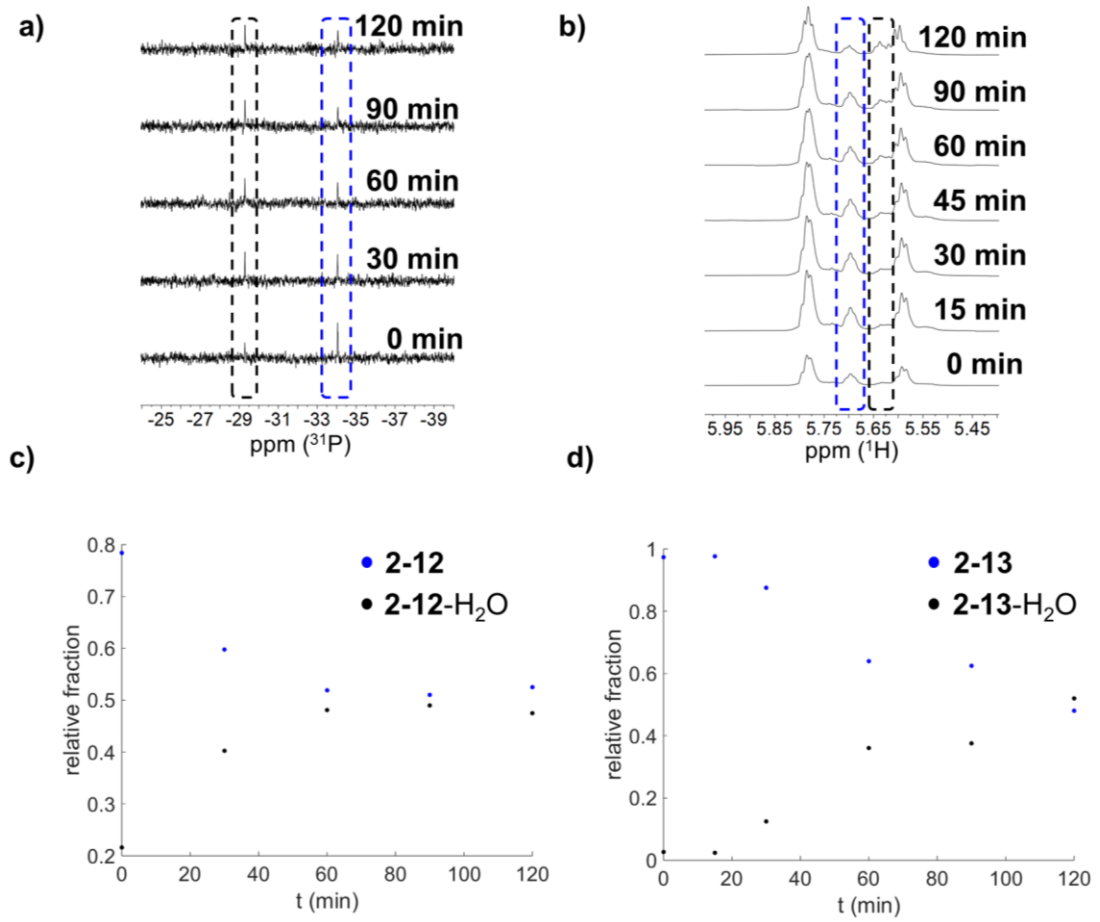

Figure 2.4 **a) ^{31}P NMR spectra of 2-12 in MES buffer (pH 6.4, 154 mM NaCl) from 0 – 120 minutes. The final solution contained 10 % DMSO to aid in solubility. b) ^{1}H NMR of 2-13 in PBS (pH 7.4, 154 mM NaCL) from 0 – 120 minutes. The solution contained 10 % DMSO to aid in solubility. Relative contribution from the parent complexes and the mono-aqua complexes as determined by the area under the fitted NMR peaks (MesReNova) for c) 2-12 and d) 2-13.**

NMR spectra of **2-12** in MES buffer (pH 6.5) displayed a resonance at -34.0 ppm immediately following dissolution. There was already a second resonance arising at -29.3 ppm attributed to hydrolysis of one chloride ligand. This exchange continued over approximately 1 hour until an equilibrium was reached between **2-12** and the aquated **2-12**-H_2O (**Figure 2.4a**). These data suggest that **2-11** and **2-12** will exchange one chloride ligand for water within the first hour of dissolution in aqueous media and are consistent with reports of other complexes of this type, such as RAPTA-C, in similar biologically-relevant solutions.[109,268–270] Since **2-13** did not contain a convenient ^{31}P NMR handle, its solution behaviours in PBS (pH 7.4, 154 mM NaCl) was followed by monitoring the ^{1}H NMR arene resonance at 5.69 ppm over time. Over 120 minutes, this

signal at 5.69 ppm decreased while a new multiplet at 5.63 ppm increased in intensity (**Figure 2.4b**). The new signal was attributed to the hydrolysis of the chloride ligand of **2-13** to form **2-13**-H_2O. At 120 minutes, an equilibrium appeared to be reached in which **2-13**-H_2O became the dominant species by a slight margin. The results of hydrolysis of **2-13** are typical for other RAED-type complexes reported in aqueous solutions of similar Cl^- concentration.[122,271] These data indicate that the complexes developed in this chapter will undergo, at least, partial hydrolysis over the duration of, for example, *in vitro* cytotoxicity studies. This is promising, as discussed above, because it is likely the key to 'activating' the ruthenium portion of the molecules toward biological activity.

2.3.3. Anticancer Activity

To examine the effects of the addition of a SERM to the RAPTA-scaffold the antiproliferative activity of **2-11** was tested against both MCF7 and MDA-MB-231 breast cancer cells. As well, tamoxifen and RAPTA-C were subjected to the same cell lines allowing for the comparison of **2-11** with, essentially, its separate components. The MCF7 cell line is positive for both oestrogen, progesterone, and human-growth factor receptors and is susceptible to SERMs such as tamoxifen.[272,273] The MDA-MB-231 cell line expresses none of these receptors and similar triple-negative tumor cells account for 10-20 % of diagnosed breast cancer.[274] These cancers are typically aggressive and less sensitive to receptor modulating anticancer agents like tamoxifen. Comparing the activity of **2-11** against both cell lines allowed evaluation of whether appending the tamoxifen-type SERM to the RAPTA scaffold induced increased activity over RAPTA-C alone and if it was more selective for the receptor-positive MCF7 cell line.

Compound **2-11** demonstrated reasonable cytotoxicity against MCF7 and MDA-MB-231 cells lines with IC_{50} values of 46.9 and 72.0 μM. Promisingly, **2-11** displayed 1.5 times higher activity against MCF7, which suggests some selectivity toward ER-positive breast cancer cells. The activity against the triple-negative cell line was higher than expected and may indicate that the complex exhibits activity via other mechanisms, in addition to estrogen receptor antagonism. The complex **2-11** displayed approximately 2-fold higher activity than RAPTA-C alone against MCF7. RAPTA-C displayed no activity against the triple negative cell line MDA-MB-231, which further highlights the utility of appending an anticancer moiety to the RAPTA scaffold to induce toxicity. The activity of **2-11** was lower than the activity of tamoxifen, which had a IC_{50} values of 14.8 and 19.0

μM against MCF7 and MDA-MB-231, respectively. A surprising result was that **2-11** displayed greater selectivity for the receptor positive MCF7 cell line than tamoxifen. This may be due to the generally lower cytotoxicity of **2-11** versus tamoxifen which may be exaggerating the difference in activity between the two cell lines.

a)

	IC_{50} (μM)	
Compound	MCF-7	MDA-MB-231
2-11	46.9	72.0
RAPTA-C	113.5	ND
tamoxifen	14.8	19.0

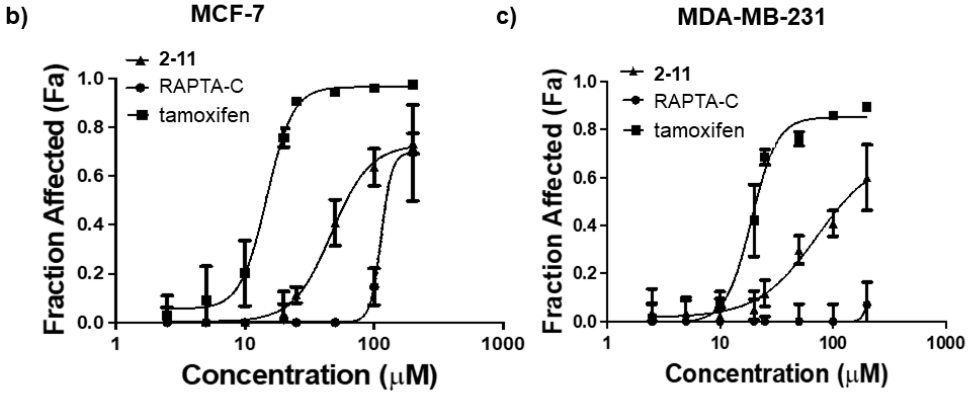

Figure 2.5 **a) Summary of IC_{50} values for 2-11, RAPTA-C, and tamoxifen versus MCF-7 and MDA-MB-231 cell lines. Dose-response data versus b) MCF-7 and c) MDA-MB-231 cell lines.**

Following the promising anticancer activity of **2-11**, it was then submitted to the National Cancer Institute NCI-60 Human Tumor Cell Lines Screen (NCI-60), along with the newly synthesized **2-12** and **2-13.** This screen initially tests a compound at a concentration of 10 μM against up to 60 different cancer cell lines and gives a growth inhibition percent compared to untreated controls. The resulting data can show trends in activity against certain cancer types and can be further compared against other compounds in the NCI-60 database to suggest possible mechanisms of action. Surprisingly, the well-studied **RAPTA-C** and **RAED-C** were not yet in the NCI-60 catalogue. Therefore, they were both synthesized and subjected to the NCI-60 screen, allowing for the direct comparison of anticancer activity to that of **2-11** and **2-12**.

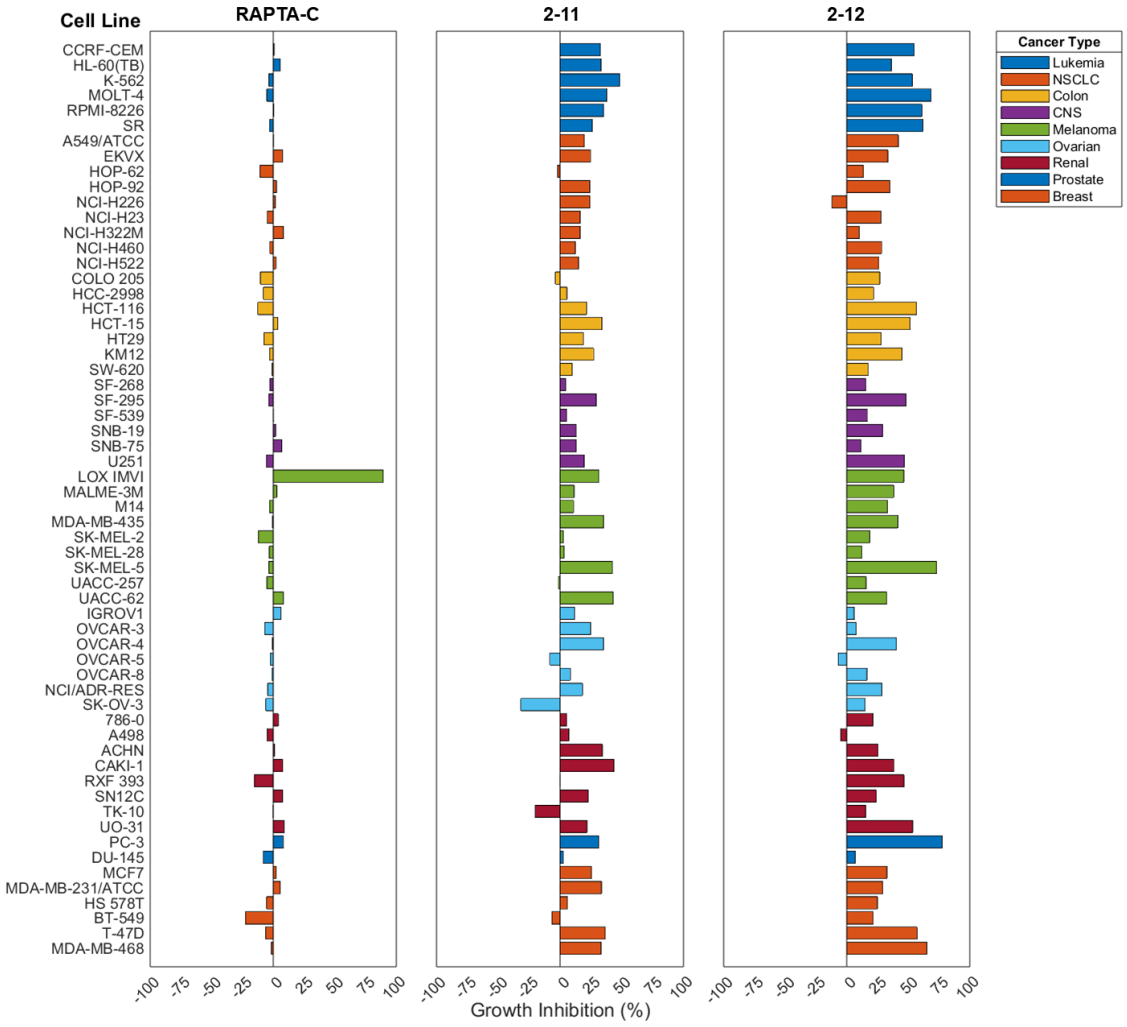

Figure 2.6 **Growth inhibition values for 10 μM treatments of RAPTA-C, 2-11, and 2-12 represented as a percent growth inhibition compared to untreated controls. A more positive value means a greater growth inhibition. Negative growth inhibition values suggest an increase in growth over the untreated control. The various colour groups represent different families of cancer (see legend).**

Figure 2.6 summarizes the growth inhibition for **RAPTA-C**, **2-11**, and **2-12** resulting from the NCI-60 screen. With the exception of the LOX IMVI melanoma cell line, **RAPTA-C** is essentially inactive at 10 μM doses, which is consistent with the reported lack in cytotoxicity for the complex. Promisingly, both **2-11** and **2-12** show good growth inhibition against the majority of cell lines and a marked increase in activity over **RAPTA-C**. Interestingly, though both complexes are structurally similar, **2-12** displayed generally higher growth inhibition (GI) with an average GI of 31.8 % versus 17.9 % for **2-11**.

To understand if the difference in activity can be contributed to differences in mechanism of action, the activity profiles of both complexes were subjected to the NCI-60 COMPARE algorithm.[275] The COMPARE algorithm evaluates Pearson correlation coefficients (PCC) using GI responses, or fingerprints, for compounds like the data displayed in **figure 2.6**. The PCC gives a quantitative assessment of the similarity between compounds and are presented as a score. The PCC measures the linear correlation between two data sets, or joint variability of two variables, and is calculated as the covariance (cov(*x,y*)):

$$\boldsymbol{cov}(\boldsymbol{x},\boldsymbol{y}) = \frac{\sum_{i=1}^{n}(x_i - \overline{x})(y_i - \overline{y})}{n} \qquad \textbf{Equation 2.1}$$

where $\bar{x}$ and $\bar{y}$ are the mean values of the populations and *n* is the population size divided by the product of their standard deviation:

$$\boldsymbol{\rho}(\boldsymbol{x},\boldsymbol{y}) = \frac{\boldsymbol{cov}(\boldsymbol{x},\boldsymbol{y})}{\sigma_x \sigma_y} \qquad \textbf{Equation 2.2}$$

where cov(*x,y*) is the covariance of the variable *x,y* and σ_x and σ_y are their standard deviations. PCC scores range from +1 to -1, with +1 corresponding to a perfectly linear positive correlation, 0 indicating no correlation, and -1 corresponding to a perfectly linear negative correlation. To understand the results obtained from the COMPARE algorithm, the PCC scores between compounds can be used to understand similarities in mechanisms of actions where a value between 1 – 0.7 indicates a strong linear relationship, 0-7 – 0.5 indications a moderate linear relationship, and 0.5 – 0.3 indicates a weak linear relationship.

To examine why the GI values were different for **2-11** and **2-12** their activity fingerprints of were compared using the COMPARE algorithm. The resulting PCC of 0.62 suggests the two compounds have moderately similar modes of action. The variance in activity, therefore, may arise from the conformational differences between the two complexes upon dissolution due to the reversed amide bond. The carbonyl oxygen in **2-11** is closer to the ruthenium and may form coordinate interactions which could hinder hydrogen-bonding with water, lowering aqueous solubility and cell uptake. Though **2-11** and **2-12** were designed to target breast cancer, their NCI-60 profile displayed the highest GI against leukemia cells. With that said, both complexes still had good GI against the breast cancer group but did not display selectivity toward ER-

positive breast cancer. For example, **2-11** actually showed lower GI against MCF7 ER positive cells than the triple-ER-negative MDA-MB-231 cell line. This counterintuitive result may be due to the low concentration in which the cells were dosed as 10 μM lies below the IC_{50} determined above for **2-11**. In general, the induction of GI over the inactive parent **RAPTA-C** highlights the utility of appending cytotoxic molecules to metal scaffolds previously thought to be inactive.

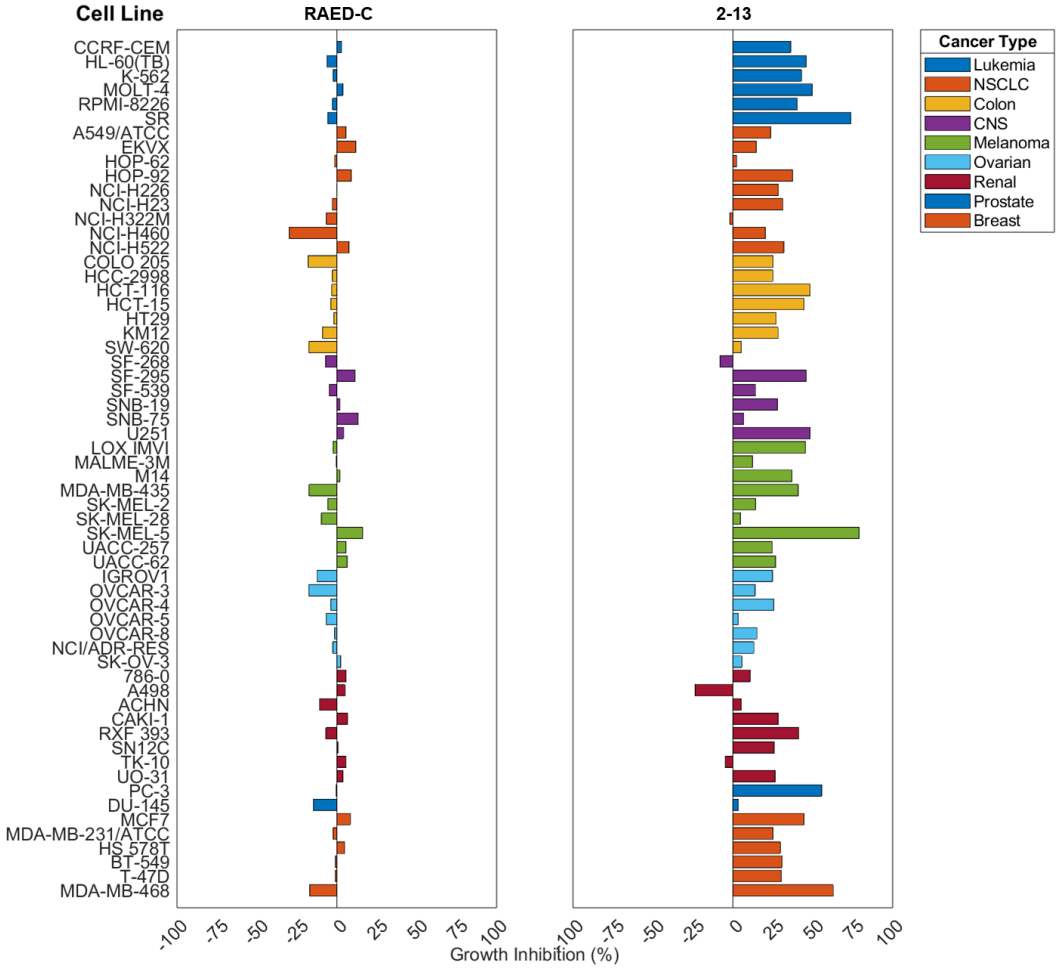

Figure 2.7 **Growth inhibition values for 10 μM treatments of RAED-C, and 2-13 represented as a percent growth inhibition compared to untreated controls. A more positive value means a greater growth inhibition. Negative growth inhibition values suggest an increase in growth over the untreated control. The various colour groups represent different families of cancer (see legend).**

Next, the results from the NCI-60 screen for **2-13** and **RAED-C** were compared. This data is presented in **Figure 2.7**. Again, a marked induction of GI for **2-13** over **RAED-C** was observed against virtually all cell lines. Though **RAED-C** has been shown

to be cytotoxic, it displayed only a small increase in GI over **RAPTA-C** at this concentration. Interestingly, though **2-13** was expected to be more cytotoxic than **2-11** and **2-12** because of the more cytotoxic ruthenium parent complex, it displayed a similar activity to **2-12** with a mean GI of 27.6 %. The increase in activity of **2-13** over **RAED-C** at a dose of 10 μM, again, underscores the utility of appending a biologically active moiety to cytotoxic metal complexes to induce further activity. Upon initial examination, the GI profiles of both **2-12** and **2-13** look quite similar. To further examine the similarities in activity, the NCI-60 GI data for both complexes as well as the SERM ligand **2-8-ctrl** and tamoxifen were subject to the COMPARE algorithm developed by the NCI-60 (**Figure 2.6**).

	Tamoxifen	**2-12**	**2-13**	**2-8-ctrl**
Tamoxifen	1	0	0.07	-0.06
2-12	0	1	0.8	0.75
2-13	0.07	0.8	1	0.73
2-8-ctrl	-0.06	0.75	0.73	1

Figure 2.8 COMPARE results showing correlations in GI between 2-8-ctrl, 2-12, 2-13, and tamoxifen. The COMPARE algorithm was seeded with GI values from the one dose at 10 μM assay. Darker green and values closer to 1 indicate a greater similarity in GI activity.

The COMPARE algorithm used the GI data of the compounds to determine similarities in patterns of activity and ranked them using a PCC (see above). This can be used to either compare a novel compound to the NCI-60 drug databases to identify similarities to compounds with known mechanisms of action, or to compare GI activity between novel compounds. **Figure 2.8** shows the COMPARE results between **2-8-ctrl**, **2-12**, **2-13**, and tamoxifen. A good correlation between **2-12** and **2-13** compared to **2-8-ctrl** of 0.75 and 0.73, respectively, suggests a similar mode of action between the ruthenium complexes and the organic SERM. This becomes more obvious when comparing the GI data between the three Ru-SERM molecules (**Figure 2.9**) where patterns in GI can be readily noted, with differences arising mostly in magnitude of the GI. Interestingly, a higher correlation score of 0.80 between **2-12** and **2-13** indicates a strong similarity in the mechanism of action between the two complexes, even though

they differ in their ancillary ruthenium ligand set (PTA vs. en, and number of chlorides), and overall charge. These data suggest that the SERM moiety acts more specifically, such as receptor antagonism, while the ruthenium centre induces a more general increase in activity (the mean GI for **2-8-ctrl** is 12.4 %).

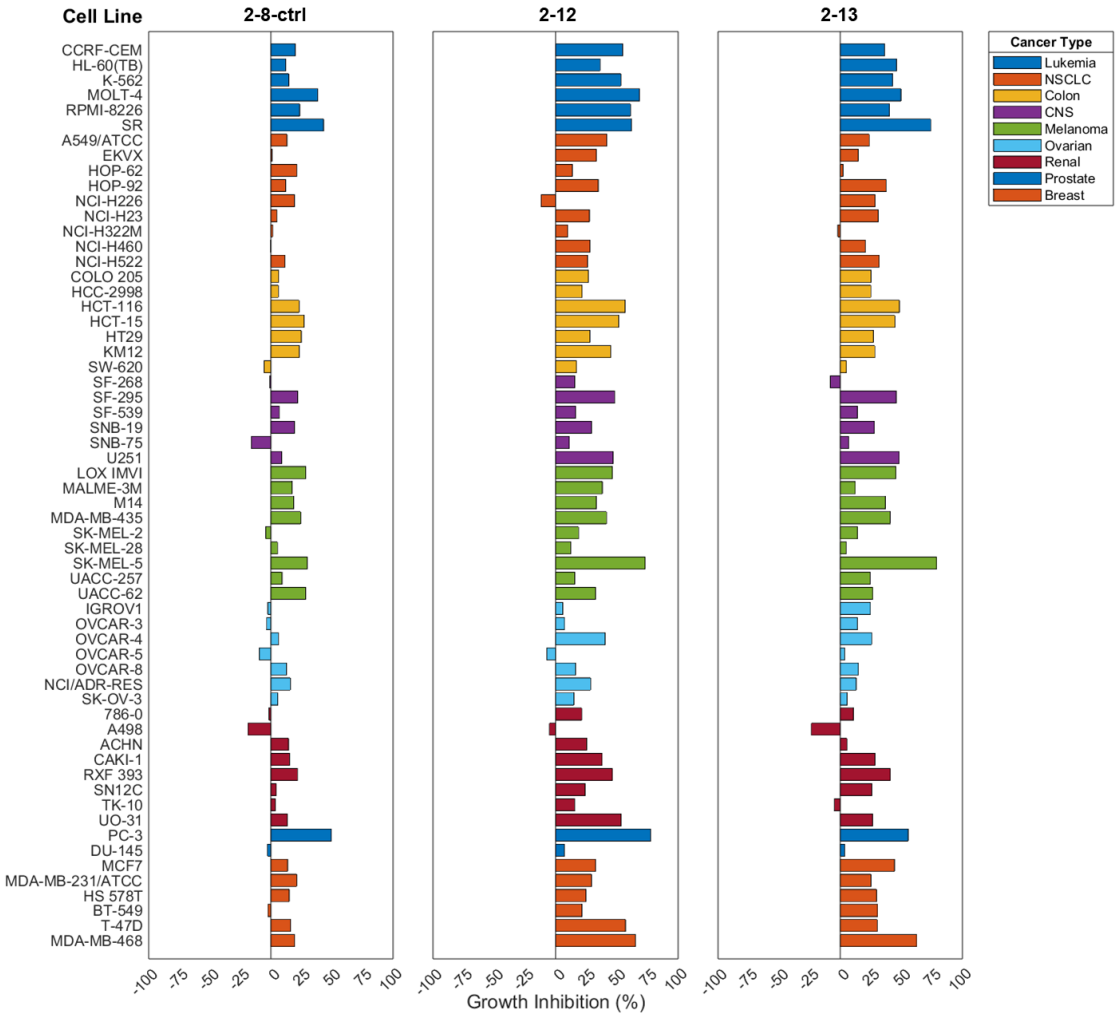

Figure 2.9 **Growth inhibition values for 10 μM treatments of 2-8-ctrl, 2-12 and 2-13 represented as a percent growth inhibition compared to untreated controls. A more positive value means a greater growth inhibition. Negative growth inhibition values suggest an increase in growth over the untreated control. The various colour groups represent different families of cancer (see legend).**

The similarity in inactivity of **2-12** and **2-13** is contradictory to the known activity of the two parent ruthenium complexes, **RAPTA-C** and **RAED-C**, with **RAPTA-C** displaying only antimetastatic activity and RAED-C being cytotoxic. These results suggest that the reported divergence between the activities of the two parent ruthenium complexes may

arise from differences in cellular uptake rather than the ancillary ligands leading to different mechanisms of action. Introduction of the hydrophobic SERM to the complexes may outweigh contributions to the overall lipophilicity of **2-12** and **2-13** by these ancillary ligands and their overall charges, leading to similar uptake and, therefore, GI profiles.

Surprisingly, all compounds, including **2-8-ctrl**, showed no similarity in anticancer activity to tamoxifen. Specifically considering the ER-bearing breast cancer cell lines, tamoxifen has been found to bind to the ER with the dimethylamine moiety buried in the binding pocket. This is unlikely to occur with **2-8-ctrl**, **2-12**, and **2-13** due to the bulkier phenyl group for **2-8-ctrl**, and ruthenium complex for **2-13** and **2-13**, replacing the dimethylamine group in tamoxifen. Docking studies with **2-8-ctrl** starting from the crystal structure of tamoxifen bound to the ER receptor were inconclusive and suggest that **2-8-ctrl,** and likely **2-13** and **2-13**, bind in a different conformation from tamoxifen. This may account for the lack of similarity between *in vitro* anticancer activity of tamoxifen and the molecules studied in this chapter. Again, at a dose of 10 μM, the complexes did not show a selectivity toward ER-positive cell lines, but rather showed good GI (relative to their parent ruthenium complexes) against all lines in the breast cancer family. This lack in selectivity may, again, be because the cells were treated at concentrations below the IC_{50} originally determined for the first generation Ru-SERM, **2-11**.

2.4. Conclusions

Three novel SERM-bearing ruthenium anticancer complexes of the RAPTA- and READ-scaffold were successfully synthesized and characterized. The aqueous solution studies suggest that following dissolution, the complexes undergo aqueous ligand exchange resulting in the loss of one of the chloride ligands. Initially, **2-11** was subjected to cytotoxicity assays against the ER-positive MCF7 and triple ER-negative MDA-MB-231 cell lines. The complex showed good activity of 46.9 and 72.0 μM against MCF7 and MDA-MB-231 cell lines, respectively. This was a 1.5-fold increase in activity toward the MCF7 cell line, suggesting the SERM was helping to selectively target the ER-positive breast cancer cells. This compound, as well as the structurally similar compounds **2-12** and **2-13** bearing the same SERM through a slightly modified linker, were then subject to the NCI-60 anticancer screen. One-dose experiments at 10 μM displayed mean GI of 17.9, 31.8, and 26.6 % for **2-11**, **2-12**, and **2-13**, respectively. This was a marked increase over the parent **RAPTA-C** and **RAED-C** parent ruthenium complexes which

displayed mean GI values of -0.04 and -1.93 %, respectively. These results validate the addition of a SERM via the arene-moiety of RAPTA- and RAED-type complexes to induce cytotoxicity, especially considering the non-cytotoxic **RAPTA-C**. Following COMPARE analyses between tamoxifen, the SERM-ligand **2-8-ctrl**, **2-12**, and **2-13** it could be concluded that the novel compounds function differently from tamoxifen but have strong similarities in activity to the SERM **2-8-ctrl**. The results suggest the ruthenium complex is acting to generally increase the cytotoxicity of the SERM, approximately 2-fold for both **2-12** and **2-13** over **2-8-ctrl**, rather than introducing distinct mechanisms of action from the parent RAPTA- and RAED-scaffolds.

3 ^{19}F Magnetic resonance imaging studies on redox and speciation processes of a Ru(III) anticancer complex*

3.1. Introduction

Ruthenium(III) anticancer complexes have become leading candidates in the search for non-platinum metal-based anticancer agents. These compounds, such as KP1019 (now BOLD-100), have shown promising anticancer activity with lower toxicity profiles than their platinum predecessors. Extensive efforts have gone into the understanding of their mechanisms of action and this has led to a thorough understanding of their interactions with a variety of biomolecules such as HSA and DNA. With that said, and even with BOLD-100 undergoing phase-II human clinical trials,[276] there still remain questions about their mode of anticancer activity.

Recently, ^{19}F MRI has been developed as a useful tool for studying inorganic anticancer complexes that contain paramagnetic metal centres. The paramagnetism of the metal modulates the relaxation rates of neighboring fluorine atoms, a unique consequence of the metal that can be exploited in various ways such as shortening overall data acquisition times. For example, ^{19}F MRI has been used to monitor the oxidation state of copper(II) complexes in oxygen deficient, or hypoxic, environments such as those encountered in tumours.[172,277–279] These low-oxygen environments are considered to be generally more reducing and the copper(II) (d^9, S = ½) is reduced to copper(I) (d^{10}, S = 0). As the Cu(I) is more labile and prefers different coordination geometries than Cu(II), the probe ligand is often released. The fluorine nuclei are, thus, no longer affected by the metal and changes in their resultant magnetic resonance properties can be used to differentiate signals from the in-tact complex. This permits for the direct sensing of hypoxia using ^{19}F MRI experiments tailored to differentiate the relaxation times. The fluorine atom itself presents as an attractive nucleus to observe in MRI for several reasons. It is an S = ½ nucleus with 100 percent isotopic abundance and is a relatively sensitive nucleus for NMR (83 % receptivity relative to ^{1}H).[280] Furthermore,

*This chapter is based on a published manuscript and is expanded upon with permission from the Royal Society of Chemistry: Spatial characterization of redox processes and speciation of Ru(III) anticancer complexes by ^{19}F magnetic resonance imaging. *Chem. Commun*, **2023**, 59, 623-626.

the amount of endogenous, mobile fluorine in the body is below the MRI detection limit so experiments are not hindered by background signals that are often an encumbrance in ^{1}H MRI experiments.[281]

In this chapter, a CF_3 modified BOLD-100-type complex was used as a model compound to develop ^{19}F MRI methods that spatially resolve uptake and speciation in tissue and in an MDA-MB-231 human breast cancer tumour. Several ^{1}H and ^{19}F MR experiments were optimized and used in tandem to determine the oxidation and aquation state of the complex in tissue models and in an excised tumour. A custom program was also written in MATLAB to process the images and determine the concentration of complex per voxel in the tumour. These methods lay the groundwork for using ^{19}F MRI to understand the mechanisms of action of fluorine modified Ru(III) anticancer agents and other ^{19}F-containing compounds in complex biological environments. With demonstrated anticancer activity, this work highlights how fluorinated ruthenium complexes of this type can also be used as hypoxia probes in a theranostic (therapeutic + diagnostic) approach.

3.2. Experimental

3.2.1. Synthesis

The materials 4-trifluromethyl-1*H*-imidazole (4-(CF_3)imidazole) and sodium tetraphenyl borate were purchased from Combi-Blocks and Alfa Inorganics and used without further purification. Hydrated ruthenium trichloride was purchased from Sigma Aldrich and purified by dissolving in concentrated hydrochloric acid and heating to dryness three times.

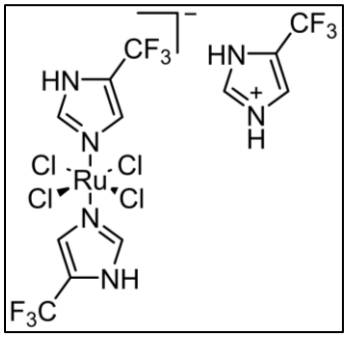

[*trans*-$RuCl_4$(4-(CF_3)imidazole][4-(CF_3)imidazoleH], **3-1**. **3-1** was synthesized following the method reported by Chang and coworkers with slight modification.[282] Hydrated ruthenium trichloride (208 mg, 1.0 mmol) was dissolved in hydrochloric acid (1M, 5 mL) and ethanol (5 mL). The solution was refluxed for 3 hours upon which the brown suspension turned clear red-orange. The solution was concentrated to half the original volume under vacuum then 4-(CF_3)imidazole (544 mg,

4.0 mmol) dissolved in hydrochloric acid (6M, 1 mL) was added at once. The solution was stirred at 60 °C for approximately 15 minutes or until a red-orange precipitate formed. The precipitate was collected by suction filtration, washed with hydrochloric acid (1M, 3x2 mL), cold ethanol (2 mL), and diethyl ether (3x2 mL) and dried under vacuum. Yield: 322 mg, 49 %. ^{1}H NMR (400 MHz, CD_3OD): δ -17.68, -16.29, 8.03, 8.66; ^{19}F NMR (376 MHz, CD_3OD): δ -68.4, -62.6.

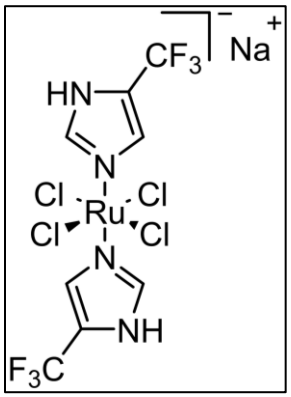

[*trans*-RuCl$_4$(4-(trifluoromethyl)imidazole][Na], **3-2**. **3-2** was synthesized following the method reported by Chang *et al*. with some modification.[282] **3-1** (100 mg, 0.15 mmol) was dissolved in acetone (10 mL) and sodium tetraphenyl borate (513 mg, 1.5 mmol) dissolved in acetone (5 mL) was added dropwise. The red-orange solution was stirred at room temperature overnight upon which the colour changed to dark brown. The solution was concentrated to a minimum volume under a stream of air and diethyl ether (15 mL) was added to induce a brown precipitate. The precipitate was collected by suction filtration, washed with cold acetone (3x2 mL), diethyl ether (3x2 mL), and dried under vacuum. Yield: 76 mg, 92 %; ^{1}H NMR (400 MHz, CD_3OD): δ -16.31, -17.66; ^{19}F NMR (376 MHz, CD_3OD): δ -68.3.

3.2.2. Tumour Growth and Excision*

Severely immunodeficient NRG mice were injected subcutaneously with 10^7 MDA-MB-231 human breast adenocarcinoma cells (American Type Culture Collection, ATCC, Manassas, Virginia, USA). Growth of the tumour was measured three times weekly with calipers and the tumour volume was calculated using the formula $volume = \frac{(length \times width^2)}{2}$. Once the tumour volume surpassed 800 mm^3, the animal was sacrificed, the tumour was excised, and subsequently stored on ice.

* Tumour preparation was performed by Devon Heroux under the supervision of Marcel Bally at the BC Cancer Agency, 686 West Broadway, Suite 500, Vancouver, BC, Canada, V5Z 1G1.

3.2.3. Sample Preparation

Buffered Solutions

For all liquid NMR samples, 4 mM solutions of **3-1** or **3-2** were prepared by in phosphate buffered saline (PBS) (NaCl (150 mM), KH_2PO_4 and K_2HPO_4 (10 mM), pH corrected to 7.4). For **3-2**, a 4 mM PBS solution of **3-1** was purged with N_2 and 1.5 equivalents of a reducing agent (sodium ascorbate, *L*-glutathione, or sodium dithionite (Sigma-Aldrich)) was added to reduce **3-1** to **3-2**.

Liquid Sample Preparation

For coaxial liquid solution MRI experiments, a 4 mM PBS solution of **3-1** was added to a 10 × 75 mm test tube. A 4 mM PBS solution of **3-2** was added to a 4 mm diameter NMR tube that was subsequently centred in the test tube containing the solution of **3-1**. The final heights of each solution were adjusted to 25 mm and the coaxial arrangement was centred in the 20 mm imaging coil using Styrofoam shims.

Liquid ^{19}F SNR Calibration Samples

Four PBS solutions of **3-1** at 1, 2.5, 5, and 10 mM were placed in individual 4 mm diameter NMR tubes and the volumes were topped up to be the same height (approximately 700 µL). These four NMR tubes were then placed into a 16 × 150 mm test tube which was subsequently filled with water to match the liquid height in the NMR tubes (35 mm). The test tube containing the NMR tubes was then placed inside the 20 mm imaging coil and aligned using Styrofoam shims.

Agar Sample Preparation

Agar (BioShop) was dissolved into boiling phosphate buffered saline (PBS) and stirred until completely dissolved resulting in a 1 % (w/v) solution. This solution was cooled to approximately 60 °C prior to adding **3-1** in order to minimize aqueous ligand exchange and ensure the agar did not solidify. The resulting concentration of the agar solution of **3-1** was 50 mM. The resulting brown solution was stirred briefly and quickly transferred to an NMR tube containing an inner coaxial tube and cooled to room temperature. A solution of **3-2** was prepared by stirring **3-1** with 1.5 equivalents of sodium ascorbate in PBS for 1 hour was prepared in advance prior to dissolving in a warmed agar solution. The resulting 50 mM agar solution of **3-2** was quickly transferred

into the coaxial tube and cooled to room temperature. The tube-in-tube NMR sample was then centered vertically in the 20 mm dual channel coil for the subsequent MR experiments.

Tissue Sample Preparation

Beef liver (Nesters Market, SFU) was cubed into approximately 1 cm^3 pieces which were subsequently suspended on glass beads inside a 10 × 75 mm test tube. A 4 mM PBS solution of either **3-1** or **3-2** was injected into the beef liver which then remained suspended in the same solution. The test tube was placed in the 20 mm imagine coil and centred using Styrofoam shims.

Tumour Sample Preparation

An approximately 0.7 mm diameter piece of the excised MDA-MB-231 tumour was placed in a 10 × 75 mm test tube and elevated on glass beads. A 4 mM PBS solution of either **3-1** or **3-2** was injected into the tumour which then remained suspended in the same solution. The test tube was placed into the 20 mm imaging coil and centred using Styrofoam shims.

3.2.4. Magnetic Resonance Parameters

Magnetic resonance imaging and spectroscopy was performed on a Bruker AVANCE III 400WB spectrometer. A Brucker MicWB40 probe with interchangeable RF coils was used and tuned for either ^{1}H (400 MHz) or ^{19}F (376 MHz). A water-cooled Bruker Micro2.5 MicWB40 gradient coil system was used and mounted inside the room temperature shim set. A 400 MHz, 20 mm dual channel $^{1}H/^{19}F$ birdcage coil was used for all measurements on this spectrometer.

T_1 Measurements

Typical parameters for ^{19}F T_1 measurements were as follows and were conducted without ^{1}H decoupling: sweep width, 60 ppm; transmitter offset, 1.50 ppm; pulse angle, 90°; pulse length 28.3 µs; acquisition time 0.33 s; recycle delay 0.50 s; number of dummy scans, 4; number of data points 32,768; number of scans, 4; pulse sequence, inversion recovery; relaxation delays, 0.1, 0.2, 0.3, 0.4, 0.5, 0.75, 1, 1.5, 2, and 4 seconds. The data was processed using TOPSPIN v2.1 with a 2 Hz exponential apodization and zero-filling to 32,768 prior to performing the Fourier transform. Values

for T_1 were obtained from the T_1 analysis routine in Topspin. Experiments were conducted both at ambient temperature and 37 °C using a Bruker BVT 3000 temperature control system that maintained a heated stream of air that was passed over the sample.

^{1}H CHESS Parameters

Typical parameters for a ^{1}H CHESS experiments involved collecting a sagittal image with a field of view (FOV) of 15 × 15 mm, slice thickness of 0.25 mm, and a voxel matrix size of 256 × 256. The RARE pulse sequence was used with a slice-selective 90° excitation pulse with: pulse length, 2.70 ms; bandwidth, 2000 Hz, attenuation, 20 dB, pulse shape, Bruker ParaVision5.1 – Hermite. A 180° refocusing pulse was used with: pulse length, 1.71 ms; bandwidth, 2000 Hz; attenuation, 10 dB; pulse shape, Bruker Paravision5.1 – Hermite. For these experiments, a repetition time (TR) of 500 ms and an echo time (TE) of 8.5 ms was used. A RARE factor of 4 (4 refocusing pulses) resulted in an acquisition time (TA) of 4 minutes for 10 averages.

^{19}F CHESS Parameters

Typical parameters for ^{19}F CHESS experiments involved collecting 20 mm thick axial slices with a FOV of 20 × 20 mm and a voxel matrix size of 64 × 64. A slice-selective 90° excitation pulse was used with: pulse length, 1.00 ms; bandwidth, 5400.0 Hz; attenuation, 16.5 dB; pulse shape, Bruker ParaVision5.1 – Hermite. A 180° refocusing pulse was used with: pulse length, 0.34 ms; bandwidth, 10058.8 Hz; attenuation, 0.5 dB; pulse shape, Bruker ParaVision5.1 – Hermite. For these experiments, a TR of 300 ms and an TE of 8.5 ms was used. A RARE factor of 4 resulted in an TA of 1 hour for 1000 averages.

^{19}F CSI Parameters

Typical parameters for ^{19}F CSI experiments involved an 8 × 8 voxel matrix over an axial slice with FOVs and slice thicknesses that varied depending on the sample. A basic pulse-acquire pulse sequence was used with a 90° excitation pulse: pulse length, 0.50 ms; bandwidth, 12420.0 Hz; attenuation, 10.1 dB; pulse shape, Bruker Paravision5.1 – sinc3. A TR of 300 ms and an TE of 6.5 ms was used which resulted in a TA of 6 minutes for 23 averages of 1024 scans. A Bruker Paravision5.1 weighted filter

was used in which more scans were collected for voxels toward the centre of the sample and the resulting 8 × 8 matrix was scaled to 16 × 16 with zero-filling.[283]

3.2.5. MRI Data Processing

^{19}F CHESS Data Processing

Raw data was imported from Bruker Paravision5.1 into MATLAB using MATLAB image processing toolbox. An open-source MRI MATLAB imaging processing toolbox by Starke and coworkers was used for processing noise.[284] ^{19}F CHESS images were loaded in MATLAB and the data were corrected for Rician noise bias corresponding to an RF coil with two receive elements using a lookup table included in the toolbox by Starke *et al.* The noise was then calculated as the standard deviation of the noise magnitude from square regions (10 × 10 voxels) in each of the four corners of the image that contained no signal. This noise was also corrected by a factor related to an RF coil with two receive elements. Next, the SNR for the whole image was calculated and voxels with an SNR < 2.74 was set to zero. Outliers were then removed by setting voxels to zero that lacked at least three signal containing neighbours (8 connected neighbours by edges and corners).

^{19}F CSI Data Processing

^{19}F CSI data were processed in MATLAB following their import using the MATLAB image processing toolbox. Each voxel was then normalized to the number of scans in each voxel, determined by the weighted filter set in Paravision5.1. The noise magnitude was calculated using a region in the spectra of each voxel containing no signal and averaged over all voxels. The SNR was then calculated in each voxel and this value was used to generate subsequent heat maps. Voxels with an SNR < 2.74 were set to zero and outliers were removed using the connected-neighbours method as for ^{19}F CHESS data processing.

Calculation of the Number of ^{19}F Atoms per Voxel

A custom program was written in MATLAB for the following data manipulation. Both anatomical ^{1}H CHESS and ^{19}F CSI data from the ^{19}F liquid calibration and tumour samples were imported into MATLAB using the image processing toolbox. The ^{1}H CHESS data was used to prompt the user to interactively select regions of interest (each

NMR tube) within the image. The program would then use these bounds to calculate the SNR within each tube from the complimentary ^{19}F CSI data. The program would then overlay a ^{19}F CSI SNR magnitude heatmap over the ^{1}H CHESS image. The SNR calculated in each tube-ROI was then used to generate a calibration curve of SNR versus concentration. Next, using the anatomical ^{1}H CHESS image of the MDA-MB-231 tumour sample, the program would prompt the user to select a ROI containing the tumour tissue. Using the selected bounds, the SNR from the ROI was calculated from the complementary ^{19}F CSI data. The concentration of the ROI was solved using the equation of the linear fit from the calibration curve and divided by the number of voxels within the ROI to give the concentration per voxel in the tumour tissue. The volume of each voxel was then used to calculated the number of ^{19}F atoms per voxel. The error in the resulting value was determined using the root mean square error (RMSE) and the standard deviation of the linear fit generated by the *polyfitn* function in MATLAB.

3.3. Results and Discussion

3.3.1. ^{19}F NMR Properties

The fluorine containing ligands of the complex studied in this chapter are a convenient way to study its redox and speciation processes in biologically relevant environments using ^{19}F MR techniques, such as NMR and MRI. The ligand has a sharp singlet at -61.9 ppm in MeOD in the ^{19}F NMR spectrum with a line width of 8.4 Hz. The resonance from the ligands coordinated to Ru(III) is observed as a slightly broader singlet in MeOD with a resonance shifted to -68.5 ppm with a linewidth of 12.9 Hz. This signal broadening arises from relaxation enhancement caused by the paramagnetic Ru(III) ion (d^5, S = ½). The broadening in the observed signal is due to a shortened T_2 relaxation time for the ^{19}F atoms versus the free ligand. By design, the ligand was chosen to locate the ^{19}F atom at an optimal distance from the ruthenium centre so that the T_2 relaxation time was not shortened excessively resulting in too much line broadening. The ruthenium centre also causes a shortening of T_1 relaxation times versus the free ligand. Both of these relaxation parameters are important considerations in both NMR and MRI. The T_1 value dictates the overall acquisition times as the repetition time (the time between excitation pulses) is typically set to 5 × T_1. The T_2 typically dictates the echo time, which is the time between the excitation pulse and signal observation.

Particularly with MRI, not only are both parameters important for the total time required for data acquisition but different tissues and compounds can be differentiated by weighting data collections for either parameter. Determining T_1 and T_2 relaxation values was an important initial consideration for subsequent MRI measurements of **3-2**. Temperature also has an affect on these relaxation parameters so experiments were conducted at room temperature and at biologically relevant 37 °C to ensure the values remained viable for NMR and MRI experiments. As one of the goals was to monitor the reduction of the ruthenium in tissue, the relaxation parameters of **3-2^{red}** were also measured in the same conditions. As the Ru(II) in **3-2^{red}** is diamagnetic (d^6, S = 0) it has no effect on the adjacent ^{19}F nuclei. The values for **3-2** and **3-2^{red}** are summarized in **Table 3.1** and were determined in a PBS solution at both 25 and 37 °C.

Table 3.1 **T_1 and T_2 (ms) relaxation values for 3-2 measured in PBS at 25 °C and 37 °C.**

	25 °C		37 °C	
	T1	T2	T1	T2
3-2	70.0	9.23	83.0	25.4
3-2red	250	207	210	135

As expected, the T_1 and T_2 values for **3-2** were found to be significantly shorter than the values for the reduced complex at both temperatures. Though T_2 for **3-2** was quite short at 9.23 ms, this was still long enough for measurement of NMR data. Presented in **Figure 3.1a** is an example of an inversion recovery experiment at 25 °C for **3-2** which was fit to an exponential (**Equation 1.11**) by the built-in algorithm in TopSpin2.1 in order to determine T_1. In **Figure 3.1b** is the Lorentzian-Gaussian peak-fit (MesReNova) used to determine the FWHH to find the T_2 values (**Equation 1.10**) for both **3-2** and **3-2^{red}** at 25 °C.

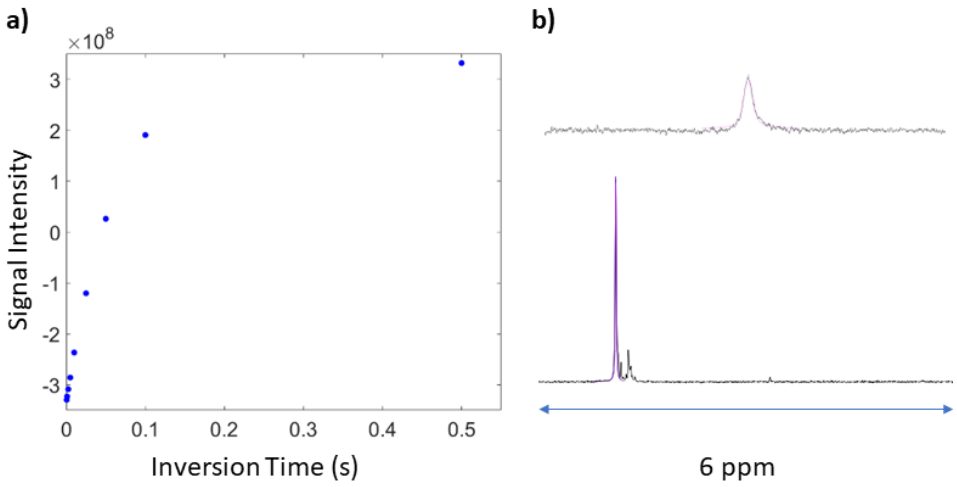

Figure 3.1 **a) Signal intensity versus inversion time for 3-2 PBS. b) Raw signals and their corresponding fits (navy) used for FWHH measurements for 3-2 and 3-2^{red}. In the spectrum for 3-2^{red} the second minor signal is attributed to aqueous ligand exchange of one of the chloro-ligands following reduction to the more labile Ru(II) complex.**

3.3.2. ^{19}F NMR Solution Studies

Ru(III) anticancer complexes such as BOLD-100 are considered to be 'prodrugs' and are known to exchange chloride ligands with water in aqueous media. Conveniently for **3-2**, these exchange events can be monitored by ^{19}F NMR as each species results in a unique resonance. To explore the behaviour of **3-2** in aqueous media, a 4 mM solution of **3-2** in PBS was incubated at 37 °C (154 mM NaCl) and ^{19}F spectra were collected at various timepoints over 18 hours. The parent complex presents a resonance at -64.6 ppm at 0 hours in PBS and remains as the predominant species after 6 hours. After 18 hours, minor singlets can be seen at -63.9, -61.9, and -61.8 ppm. The resonance at 61.9 ppm coincides well with the signal arising from free ligand in PBS (**Figure B.1**). The remaining signals can be attributed to the mono-aquo complexes in which either a chloro- or CF_3Im ligand is exchanged with water. The major species present after 18 hours is still the parent complex and the slow aquation agrees with previous reports for this complex.[282]

Another important consideration for Ru(III) anticancer complexes of this type is their ability to undergo reduction under biological conditions. This is especially pertinent since the target tumour environments for these complexes have regions of hypoxia considered to be generally more reducing than healthy tissues. Initially, studies in

nitrogen-purged PBS were conducted with several reducing agents to ensure the reduction of **3-2** could be resolved via ^{19}F NMR. Deoxygenated PBS was used to mimic the low-oxygen environments of tumours. It was found that the more biologically relevant reducing agents, such as sodium ascorbate (NaAsc) and glutathione (GSH), followed somewhat convoluted routes to generate **3-2^{red}**. As can be seen in **Figure 3.2a** and **b**, several resonances arise, especially with sodium ascorbate, over the first 30 minutes. Eventually, both reducing agents end up generating **3-2^{red}** after 1 hour. The SNR in the sodium ascorbate experiment is lower due to a precipitate forming over the course of the experiment. As this reducing agent is known to be a complex, 2-electron process, it is likely interacting with the ruthenium complex in a coordinate manner, generating insoluble products.[285] Finally, reduction with sodium dithionite (NaDT) was explored and this was found to give the most convenient route to **3-2^{red}** and was therefore used for all subsequent MRI experiments (**Figure 3.2c**). Throughout all the reduction experiments, a minor signal arose that is attributed to free $ImCF_3$ ligand (top spectrum in each **a**, **b**, and **c**). This free ligand arises following reduction to the Ru(II) which is more prone to ligand exchange.[282]

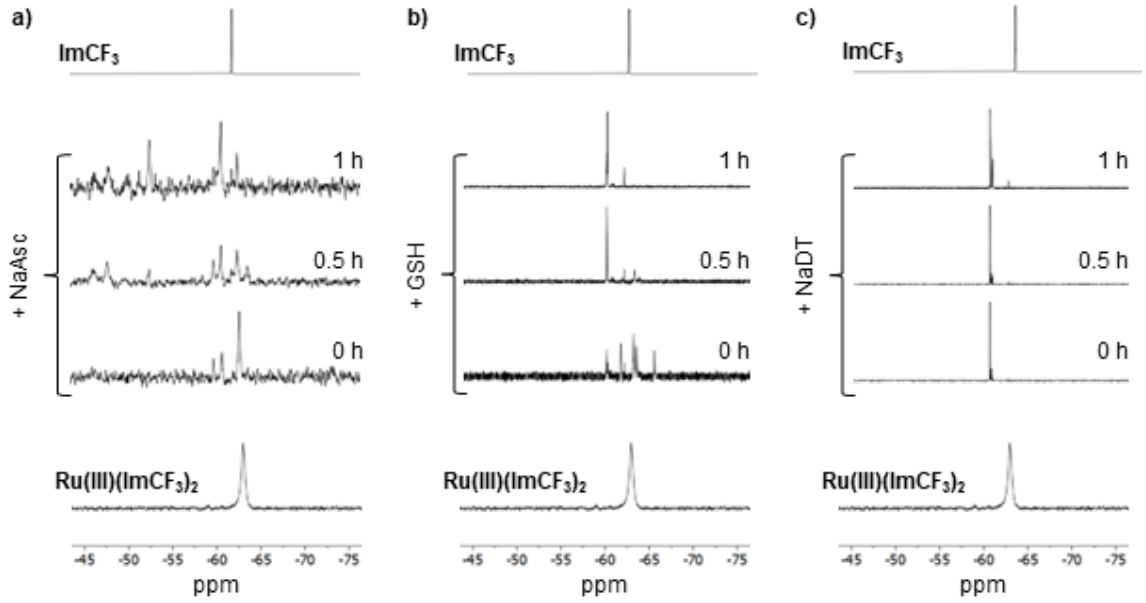

Figure 3.2 **Reduction of a 4 mM solution of 3-2 in nitrogen-purged PBS monitored by ^{19}F NMR over 1 hour by 1.5 equivalents a) sodium ascorbate, b) glutathione, and c) sodium dithionite. The top spectrum in each panel indicates the resonance from free $ImCF_3$ ligand in PBS.**

3.3.3. MRI Studies

With the NMR properties of **3-2** and **3-2^{red}** in hand, MRI studies could now be conducted in solution to optimize parameters for tissue experiments. As with the NMR studies, 4 mM solutions of **3-2** or **3-2^{red}** generated via addition of 1.5 equivalents of NaDT in PBS, were used for all subsequent MRI solution experiments. Firstly, the limit of detection of **3-2**, which is defined as SNR < 3 as the clinical standard for a true signal, for the MRI setup used was determined. This was found by generating a calibration curve using multiple concentrations of **3-2** in PBS and data from ^{1}H CHESS and ^{19}F CSI experiments and extrapolated to an SNR of 3 (**Figure B.2**). It was found that the resulting limit of detection was 430 μM. This was well below the clinical dose of a similar ruthenium anticancer complex, BOLD-100 (KP1019), so a concentration of 4 mM was used in subsequent experiments to give greater SNR in shorter acquisition times. Though a concentration of 4 mM seems high, especially for an anticancer compound, this would be the approximate dose a 75 kg human would receive in the phase-II clinical trials of the similar BOLD-100 anticancer agent being conducted by Bold Pharmaceuticals. They determined in the phase I trail that the complex has markedly low toxicity, allowing for a maximum tolerated dose of 625 mg/m^2.[286]

It was, next, pertinent to determine whether clinically relevant ^{19}F MRI experiments, such CHESS and CSI, could be used to differentiate between the resonances from **3-2** and **3-2^{red}** in a single experiment. This would show that the method could be used to follow possible reduction of the complex over time *in-vivo*. Thanks to the relatively short relaxation parameters for the complex a short TR of 300 ms and TE of 8.5 ms for CHESS and 6.5 ms for CSI experiments was used. This allowed for short acquisition times when compared to other ^{19}F MRI imaging agents, such as perfluorocarbons, that often display T_1 relaxation times on the order of seconds, requiring much longer TR for complete relaxation.[287] **Figure 3** shows the results of a coaxial tube experiment in which the inner and outer tubes contain a PBS solution of **3-2^{red}** and **3-2**, respectively. The ^{19}F CHESS experiment required 1 hour for ample signal to noise. This is displayed as a heatmap of SNR generated by a custom program written in MATLAB (see appendix **B**). This program removes Rician noise, sets voxels of SNR < 2.74 to zero, and removes outliers. This results in an image in which all voxels contain real signal arising from complexes. An example of how this improves image quality can be seen in **Figure B.3**. The two panels in **Figure 3.3b** show 64 × 64 voxel images

collected after different echo times following a single excitation pulse. The shorter relaxation times of the paramagnetic **3-2** allowed for its signal to be spatially resolved from the diamagnetic **3-2^{red}** in the same experiment. This demonstrates the advantages of paramagnetic relaxation enhancement (PRE), allowing for information from multiple oxidation states to be collected in a single experiment.

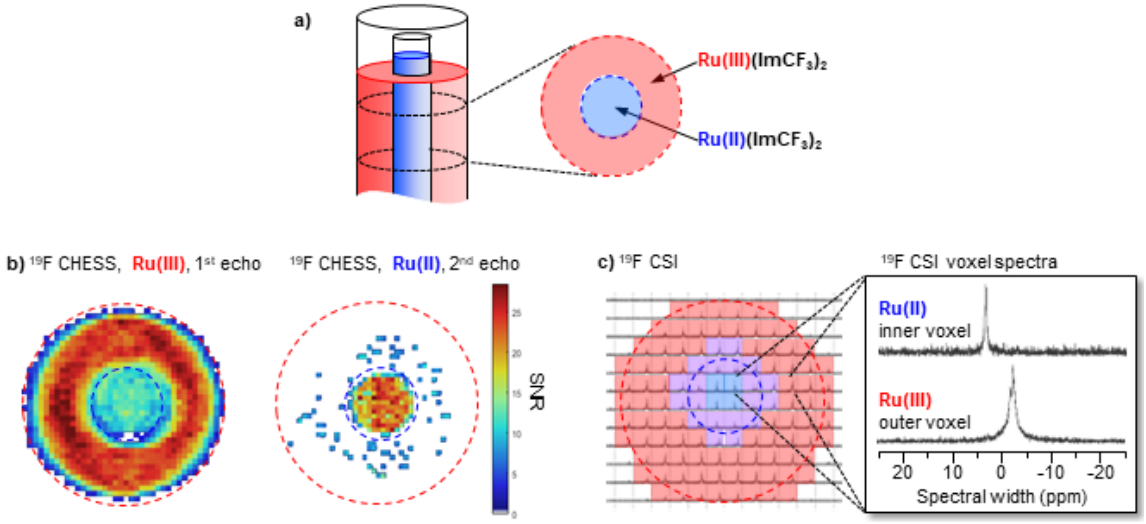

Figure 3.3 **a) Illustration of the coaxial tube setup containing 3-2 (outer) and 3-2red (inner) at 4 mM in PBS. b) 19F CHESS data collected over the coaxial tube setup presented as an SNR heatmap and highlighting the data collected following the initial echo (3-2, first panel), and subsequent 3 echoes (3-2red, second panel). c) 19F CSI matrix of the coaxial tube setup (first panel) and individual spectra from the outer tube and inner tubes highlighting the signals arising from 3-2 and 3-2red respectively.**

This ^{19}F CHESS image was used to align a complementary ^{19}F CSI experiment of the same sample. The resulting data is presented as a 16 × 16 matrix of individual ^{19}F spectra over the coaxial sample (**Figure 3.3c**). Though this is lower spatial resolution than the CHESS experiment, it presents much more information-rich voxels in which resonances from unique species can be resolved. This can be used to glean further information on what is occurring inside the samples, such as chemical changes, rather than just presenting as a map of signal magnitude as in CHESS experiment. Furthermore, since this experiment has lower spatial resolution, the total acquisition time was just 6 minutes. As can be seen in the panel highlighting spectra from the inner and outer tubes, this method was also able to resolve the resonances arising from **3-2^{red}** and

3-2 in a single experiment. The signal from **3-2^{red}** is not only narrower but is shifted downfield by approximately 7.5 ppm (3000 Hz).

After confirmation that it would be possible to resolve **3-2** and **3-2^{red}** in PBS solution it was important to validate these experiments using a tumour tissue model. For this, beef liver was used and was injected with 4 mM solutions of either **3-2** or **3-2^{red}** and placed in test tubes containing 4 mM of the same solution. For these experiments, instead of using ^{19}F CHESS, ^{1}H CHESS anatomical images were collected with a spatial resolution of 256 × 256 voxels. This allowed for more detailed images of the tissue and faster acquisition times, with data collections requiring only 4 minutes thanks to the large ^{1}H concentration. This detailed image was used to align subsequent ^{19}F CSI and the resulting 16 × 16 matrix required 6 minutes. These data are presented in **3.4** and showcase how the two experiments can complement each other in providing spatially resolved chemical information in tissue. A surprising result was the increased signal intensity observed in the ^{19}F CSI experiments for both **3-2** and **3-2^{red}** in the tissue versus the surrounding solution (**Figure 3.4a** and **b**, second panel). It was hypothesized that this signal enhancement could originate from two sources; 1) from T_1 relaxation enhancement caused by the solid tissue matrix, and 2) enhanced complex retention in the lipidic beef liver tissue.[288] Contribution to the increased signal intensity from a T_1 relaxation enhancement was found to be insignificant following experiments in which varying the TR from 100 – 1000 ms resulted in a negligible change in signal intensity. Therefore, it was concluded that the lipophilic complex[282] was being preferentially retained in the more lipidic (*vs.* the surrounding PBS solution) liver tissue. Promisingly, the ^{19}F CSI experiments were still able to spatially resolve the resonances arising from the complex in both oxidation states with the signal from **3-2^{red}** being downfield by approximately 4.5 ppm (1800 Hz) (**Figure 3.4a** and **b**, third panel). Another promising result was the resolution of a second minor signal from **3-2^{red}** within the tissue that is attributed to free $ImCF_3$ ligand. This suggested that not only could reduction processes be monitored but aqueous ligand exchange events could be spatially resolved in tissue.

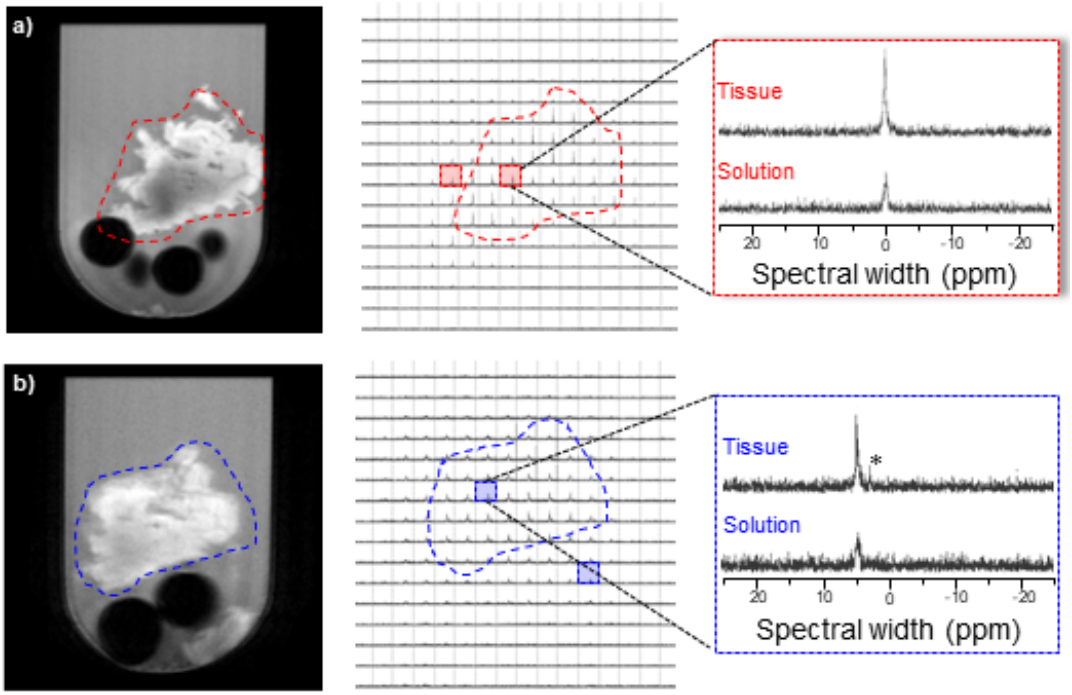

Figure 3.4 **Beef liver MRI experiments for a 4 mM PBS solution of a) 3-2 and b) 3-2^{red}. The first panel displays anatomical ^{1}H CHESS images of the beef liver elevated on glass beads in test tube. The second panel shows the corresponding ^{19}F CSI matrix and the third panel shows individual voxels from inside and outside the beef liver tissue. * Indicates signal arising from free ImCF$_3$ ligand.**

Next, using the optimized MRI parameters determined from the beef liver experiments, an excised MDA-MB-231 human breast adenocarcinoma tumour was subjected to the same set of complimentary ^{1}H CHESS and ^{19}F CSI experiments. Similarly, a 4 mM solution in PBS of either **3-2** or **3-2^{red}** was injected into the tumour which was placed into the same solution for imaging. Subcutaneous injection is commonplace for tumour treatment and presents as a viable method for the introduction of imaging agents *in-vivo*.[289–294] As with the beef liver, the combined acquisition time for both ^{1}H CHESS and ^{19}F CSI experiments was approximately 10 minutes. This acquisition time lies well within the range of clinical MRI procedures which typically take anywhere from 30 minutes to 2 hours.[295] The data collected from these experiments are presented in **Figure 3.5**.

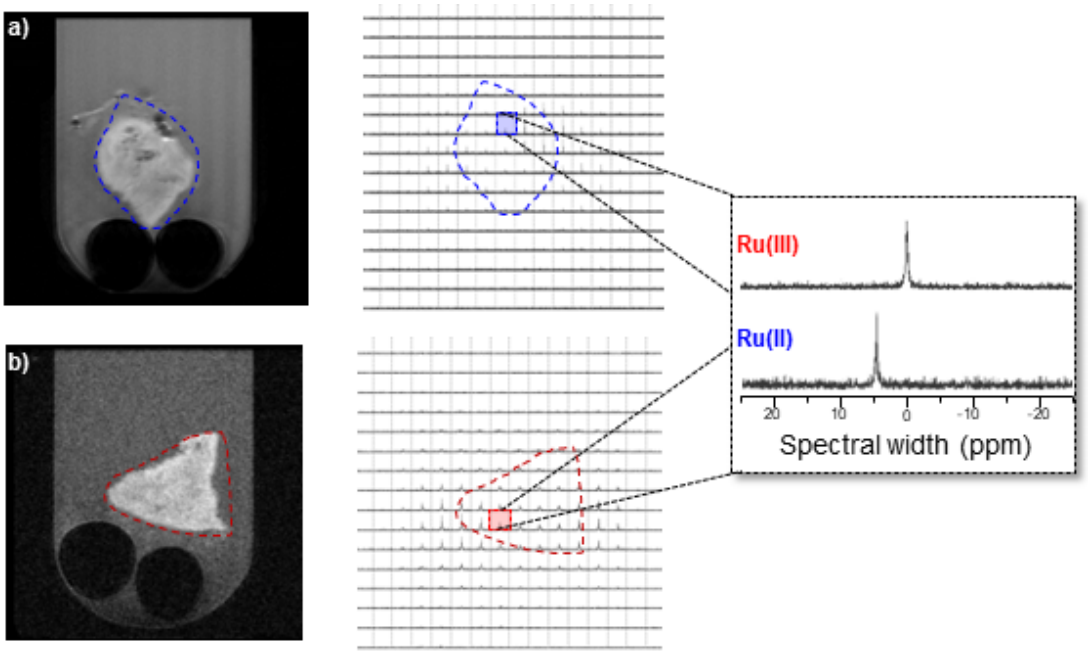

Figure 3.5 **MDA-MB-231 MRI experiments of a 4 mM PBS solution of a) 3-2 and b) 3-2^{red}. The first panel presents an anatomical ^{1}H CHESS of the tumour elevated on glass beads in a test tube. The second panel shows the corresponding ^{19}F CSI matrix and the third panel is an individual spectrum from within the tumour tissue from each experiment.**

Promisingly, the resonances from the reduced complex was distinguisable from the parent complex as it was shifted downfield by approximately 4.5 ppm (1800 Hz). Again, an increase in signal intensity was observed within the tumour tissue likely due to the more lipidic nature of the tumour as well as the tumour being encased in a basement membrane.[296] As with the beef liver experiments discussed above, varying the TR of ^{19}F CSI experiments from 100 – 1000 ms showed no significant change in signal intensity. This further supported retention of the complex in the tissue being the main cause of the observerd signal enhancement. To study whether ^{19}F CSI could be used to spatially resolve chemical changes to the complex over time, a tumour tissue sample was monitored over 12 hours following the injection of a 4 mM PBS solution of **3-2**. A new upfield resonance arose after 3 hours and became the dominant signal after 12 hours. Interestingly, this signal was not observed in the surrounding solution. It is possible that the more lipidic nature of the tumour tissue (*vs.* the surrounding buffer solution) helps to promote exchange to the neutral mono-aquo complex. Furthermore, this resonance was not attributed to the reduced complex, **3-2^{red}**, because of the upfield chemical shift (**Figure 3.6**). The line broadening and chemical shift of the new resonance matches well

with the chemical shift of previous reports of this and other mono-aquo Ru(III) anticancer complexes.[282]

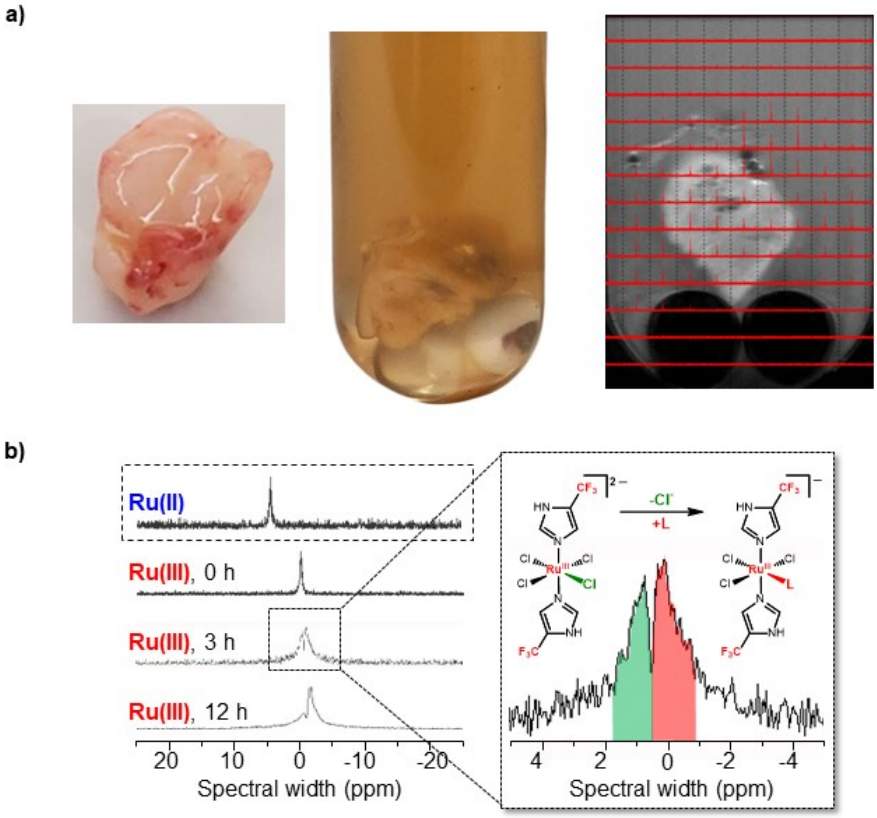

Figure 3.6 **a) Images of an excised MDA-MB-231 tumour (first panel), the tumour elevated on glass beads in a PBS solution of 4 mM of 3-2, following injection of the same solution (second panel), and an overlay of a ^{19}F CSI matrix on an anatomical ^{1}H CHESS image of the tumour in the test tube (third panel). b) Individual ^{19}F CSI spectra from within the tumour tissue of 3-2^{red} (top spectrum) and 3-2 over 12 hours (remaining 3 spectra). The second highlights the two species present after 3 hours and suggests the possible structure of the resulting species.**

Using the custom program written in MATLAB and the previously generated ^{19}F CSI SNR calibration curve, the number of ^{19}F atoms per voxel was calculated for the tumour sample. For this, a ROI over the tumour tissue was selected using the anatomical ^{1}H CHESS image. These bounds were then used to determine the SNR from the corresponding ^{19}F CSI matrix. The average SNR over the tumour tissue was found to be 18 for a 4 mM solution of **3-2**. This resulted in a voxel from within the tissue of 0.44 mm^3 containing 1.1 ± 0.4 × 10^{15} ^{19}F atoms. To put this in context, this SNR compares favourably against *in-vivo* MRI experiments with 5-fluorouracil which report a SNR of 22

using a larger voxel size of 800 mm^3 (one voxel covering a whole tumour within a mouse).[297] The SNR for **3-2** in tissue also compares well to metal-based complexes designed specifically for ^{19}F imaging that do not display intrinsic anticancer activity. For example, Srivastava and coworkers report a SNR of 10 from solution phantoms of 5 mM of a macrocyclic-Tm complex in rat blood with a voxel size of 2.5 mm^3.[298]

3.4. Conclusions

The work in this chapter demonstrates the versatility of ruthenium complexes as not only anticancer complexes but as imaging agents and hypoxia probes. The paramagnetic ruthenium centre allows for shorter acquisition times for both ^{19}F CHESS and ^{19}F CSI. Acceptable SNR and acquisition times for ^{1}H CHESS and complimentary ^{19}F CSI at clinically relevant concentrations show the potential for the fluorine-labeled Ru(III) complex used in this work to function as a theranostic. Furthermore, many ^{19}F metal-based hypoxia probes, such as Cu(II) complexes, shed their ligands following reduction and thus the metal species cannot be discerned via MRI. Thanks to the relative kinetic inertness of ruthenium compounds, such as the one studied in this chapter, they tend to hold onto their fluorinated ligand set following reduction to the more labile Ru(II) oxidation state. This allows for the investigation of chemical changes to the complex following reduction in hypoxic environments, providing a tool to shed light on the still-debated mechanism of action of Ru(III)-Keppler type anticancer complexes. In addition, as was presented in this chapter, the complex can also act as a hypoxia probe thanks to the different magnetic resonance properties of the reduced, diamagnetic Ru(II) complex.

4 Polymer nanoparticle encapsulation of fluorinated Ru(III) anticancer agents

4.1. Introduction

One of the limitations of ruthenium(III) anticancer complexes, like NAMI-A and BOLD-100, is their lack of stability in aqueous and biologically-relevant media. For example, it has even been suggested that complexes of this type shed their entire ligand set upon introduction into biological media such as human serum.[91] X-ray absorption near edge structure spectroscopic studies *in-vivo* have also pointed to a decomposition of the parent complexes following attack by sulfur- and amine/imine-, and carboxylate-containing protein residues.[299] A promising strategy to overcome this issue is to encapsulate the complexes in a particle that can protect them from ligand-exchange events with water and other nucleophilic biomolecules. Polymer nanoparticles (NPs) have begun to play a leading role in the encapsulation and delivery of many types of drugs. For example, poly(D,L-lactide-co-glycolide) (PLGA) nanoparticles have been used to encapsulate both platinum and Ru(III) anticancer agents and this strategy has led to increased aqueous stability and higher cytotoxicity than the free complexes.[227,229] PLGA is an attractive choice as it is already approved by the FDA for use in humans, it is relatively cheap, and contains ester bonds that can be readily degraded in-cell through hydrolysis following drug release. Diffusion often dominates drug release from PLGA NPs and lead to a sustained dose over longer periods compared to the administration of free drug. Their facile synthesis via nanoprecipitation provides relatively monodisperse NPs that fall within the ideal size range (100 – 300 nm) to take advantage of the enhanced permeability and retention effect (EPRe) in tumours, as discussed in section 1.4. Furthermore, acid terminated versions of PLGA also allow for the surface modification of the particles with targeting molecules, such as aptamers, which can increase selectivity towards target cancer cells.

In this chapter, fluorinated Ru(III) complexes of the KP1019-type were incapsulated in acid-terminated PLGA nanoparticles. A variety of loading conditions were explored to determine the optimal formulation for encapsulation of the ruthenium complexes. The complex with the highest encapsulation efficiency was selected for *in vitro* anticancer testing and compared to the reported activity of the free complex. The

fluorinated ligand set provided a spectroscopic handle for confirming encapsulation via ^{19}F NMR. The paramagnetic Ru(III) centre also allowed for encapsulation and release studies via EPR spectroscopy. ICP-MS methods were used to quantify the amount of drug encapsulated and released over time in PBS.

4.2. Experimental

4.2.1. Synthesis

The materials 5-trifluoromethyl-1*H*-indazole (5-(CF_3)indazole), 4-trifluromethyl-1*H*-imidazole (4-(CF_3)imidazole), Resomer® RG 502 (poly(D,L-lactide-*co*-glycolide; lactide:glycolide 50:50; acid terminated; MW 7000-17000) (PLGA), and Pluronic® F-127 (MW ~12600) were purchased from Sigma Aldrich and used without further purification. Hydrated ruthenium trichloride was purchased from Sigma Aldrich and purified by dissolving in concentrated hydrochloric acid and heating to dryness three times.

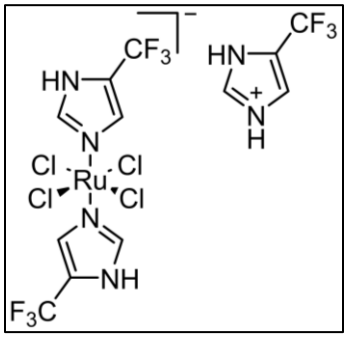

[*trans*-$RuCl_4$(4-(CF_3)imidazole][4-(CF_3)imidazoleH], 3-1. **3-1** was synthesized following the method reported by Chang and coworkers with slight modification.[282] Hydrated ruthenium trichloride (208 mg, 1.0 mmol) was dissolved in hydrochloric acid (1M, 5 mL) and ethanol (5 mL). The solution was then refluxed for 3 hours upon which the brown suspension turned clear red-orange. The solution was concentrated to half the volume under vacuum then 4-(CF_3)imidazole (544 mg, 4.0 mmol) dissolved in hydrochloric acid (6M, 1 mL) was added at once. The solution was stirred at 60 °C for approximately 15 minutes or until a red-orange precipitate formed. The precipitate was collected by suction filtration, washed with hydrochloric acid (1M, 3x2 mL), cold ethanol (2 mL), and diethyl ether (3x2 mL) and dried under vacuum. Yield: 322 mg, 49 %. ^1H NMR (400 MHz, CD_3OD): δ -17.68, -16.29, 8.03, 8.66; ^{19}F NMR (376 MHz, CD_3OD): δ -68.4, -62.6.

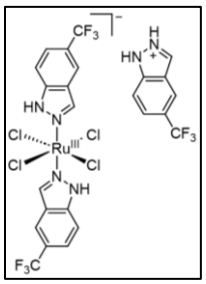

[*trans*-$RuCl_4$(5-(CF_3)indazole][5-(CF_3)indazoleH], 4-1. 4-1 was prepared following a procedure reported by Chang and coworkers with some modifications.[282] Hydrated ruthenium trichloride (208 mg, 1.0 mmol) was refluxed for three hours in hydrochloric acid (1M, 5 mL) and ethanol (5 mL). The solution was refluxed for 3 hours upon which the cloudy brown solution turned clear red. The solution was then concentrated to half the original volume under vacuum. 5-(CF_3)indazole (745 mg, 4.0 mmol) was dissolved in ethanol (2 mL) and added dropwise to the solution. The reaction was then heated to 60 °C for 15 minutes resulting in the formation of a bright red-orange precipitate. The precipitate was collected by suction filtration, washed with hydrochloric acid (1M, 3x2 mL), cold ethanol (2 mL), and diethyl ether (3x2 mL) and dried under vacuum. The filtrate was concentrated under vacuum to induce further precipitation, which was washed with hydrochloric acid (1M, 3x2 mL), cold ethanol (2 mL), and diethyl ether (3x2 mL). Yield: 546 mg, 68%; ^{1}H NMR (400 MHz, CD_3OD): δ 1.51, 2.77, 4.68, 7.60, 7.63, 7.72, 8.19, 8.25; ^{19}F NMR (376 MHz, CD_3OD): δ -65.3, -62.5.

4.2.2. Nanoparticle Formulations*

Nanoprecipitation method

The PLGA nanoparticles were prepared following the nanoprecipitation method[143] with slight modifications as reported by Keppler and coworkers.[229] An amount of **3a** or **4a** (1, 2.5, or 5 mg) and 20 mg of PLGA was dissolved in acetone (1.95 mL) and DCM (0.05 mL). The solution was stirred until both the polymer and complex were completely dissolved. The resulting solution was added dropwise to a 5 mL stirring solution of Pluronic F127 or TWEEN80 (0.1 %, w/v) in water. The resulting milky suspension was stirred for 30 minutes at room temperature, after which the organic solvents were removed under vacuum. The remaining solution was filtered through a 0.4 µm PTFE syringe filter to remove any polymer agglomerations. The nanoparticles were then washed with distilled water two times by size-exclusion centrifuge filtrations with a cutoff of 10 000 MW.

* ICP-AES and accompanying sample digestion was performed in the lab of Jurgen Gailer by Tristen Bridle at the University of Calgary, 2500 University Drive NW, Calgary, Alberta, Canada, T2N 1N4.

Determination of Ruthenium Encapsulation

To determine the amount of encapsulated ruthenium, samples were prepared as described above in triplicate at each initial compound loading (1, 2.5, or 5 mg). After the final wash, the nanoparticles were transferred to scintillation vials and lyophilized to dryness and the recovered mass was weighed. The resulting solid material was sent to Tristen Bridle at the University of Calgary for digestion and analysis via ICP-AES.

Nanoparticle Digestion

The solid nanoparticle material was quantitatively transferred to 35 mL digestion vessels using nitric acid (3 mL, 70 % w/w, PlasmaPure, for trace analysis, SCP Science). A stir bar and hydrogen peroxide (2.0 mL, ≥ 30 % w/w, for trace analysis, Sigma-Aldrich) was added to the vessel and the solution was stirred for 15 minutes at room temperature for pre-digestion. The digestion method “RTTBovineMuscle” was used to digest the material using the Discover SP-D 10/35 microwave digestion system (CEM Corporation) using the parameters outlined in **Table C.1**. Following digestion, the solution was quantitatively transferred to acid-washed 10 mL volumetric flasks and diluted to the mark with deionized water (18 MΩ·cm, Simplicity water purification system, Millipore).

Inductively Coupled Plasma – Atomic Emission Spectroscopy

Simultaneous multi-element specific detection of copper (324.754 nm), iron (259.940 nm), zinc (213.856 nm) and ruthenium (240.272 nm) of digested samples was performed on the Prodigy, high-dispersion, radial-view, ICP-AES (Teledyne Leeman Labs) with the following parameters: radio frequency power 1.3 kW, an argon gas coolant flow rate of 19 L/min, auxiliary flow rate of 0.5 L/min, and nebulizer gas pressure of 25 psi. Raw data was collected using the ICP-AES data acquisition and controller software and imported into Microsoft Excel for processing and comparison against a calibration curve created with a ruthenium standard (see **Appendix C**) (0-20 ppm Ru from a 1000 ppm ruthenium standard diluted in 10 mL volumetric flasks with nitric acid (3.0 mL) and deionized water).

Drug Release Studies

Leaching studies were performed following a modified procedure reported by Jusu and coworkers.[300] A leaching study at 37 °C over 72 hours was performed on **4-1**

encapsulated in PLGA NPs.. Triplicate 20 mg NP formulations of optimal 5 mg **4-1** initial loading were suspended in 20 mL of PBS at pH 7.4 with 0.2 % PF127 surfactant in 50 mL falcon tubes. These tubes were placed in a shaker at 37 °C rotating at 100 rpm. At approximately 2-hour intervals (except for overnight periods) the tubes were removed from the shaker and centrifuged at 4500 rpm for 10 minutes. Then, 1 mL aliquots of the supernatant were removed and 1 mL of fresh buffer was added back to the falcon tube. The nanoparticles were agitated to ensure complete resuspension following centrifugation and placed back into the incubator. 100 µL of the 1 mL aliquots was diluted with ultrapure nitric acid (2 %) to the 10 mL mark of volumetric flasks. The amount of ruthenium released was determined by ICP-MS and reported as the cumulative percentage of ruthenium released relative to the total amount encapsulated for these optimal formulations previously determined by ICP-AES.

Inductively Coupled Plasma – Mass Spectrometry

ICP-MS was performed on a Thermofisher iCAP Qc equipped with an aqueous liquid sample introduction autosampler. Argon flow was set to 0.3 mL/min. 102Ru was detected in KED mode with He used as the gas flowing into the collision cell. 1 mL injection volumes were used with simultaneous detection of In and Rh (Thermofisher) from a 10 ppb internal standard. Detected values of 102Ru were compared to a calibration curve determined from a ruthenium standard (Sigma-Aldrich) of 0.1, 1, 10, 100, and 500 ppb prepared in ultrapure nitric acid (2 %).

Dynamic Light Scattering and Zeta Potential

The size and surface charge of the PLGA NPs and **4-1** encapsulated PLGA NPs were measured via dynamic light scattering and zeta potential on a Malvern Zetasizer NS. All measurements were carried out at room temperature and formulations were diluted 10 × in water. Samples were placed in disposable DTS1070 folded capillary cells (Malvern Zetasizer Nano Series).

Encapsulation Calculations

The total recovered mass (RM) was calculated by dividing the total mass of formulation after lyophilization by the initial mass (a sum of the polymer and complex) used in each formulation. Encapsulation efficiency (EE) was calculated by dividing the number of moles of ruthenium used for each formulation by the number of moles of

ruthenium detected in each formulation by ICP-MS or ICP-AES. The mass of complex detected in each formulation was calculated using the moles of ruthenium detected in each sample by ICP-MS or ICP-AES. This mass was then used in determining the drug loading (DL) in each formulation by dividing the mass of complex detected by the recovered mass determined previously. These values were all multiplied by 100 percent and presented as a percentage.

4.2.3. EPR Studies

EPR experiments were performed at X-band (~9.4 GHz) on a Bruker EMXplus spectrometer with a Bruker PremiumX microwave bridge and high sensitivity resonator. Frozen solution spectra were collected at between 100 and 4 K. To maintain low temperature, a Bruker ER 4112HV temperature control system was used with a continuous flow cryostat that passed either nitrogen or helium cryogen gas over the sample. Samples of NP formulations were concentrated to 300 µL in PBS with 0.2 % PF127 surfactant or DMEM and were transferred to EPR tubes and immediately frozen in liquid nitrogen. The surfactant mitigated the need for a glassing agent such as glycerol. 'Denatured' NP formulations were first concentrated to dryness via centrifugation and dissolved in 300 µL of acetone, transferred to EPR tubes and immediately frozen in liquid nitrogen. Studies in DMEM involved suspending a 10 mg **4-1** PLGA NP formulation in 2 mL of DMEM followed by incubation at 37 °C over 72 h. Samples at various timepoints were transferred to EPR tubes and frozen immediately in liquid nitrogen. All simulations were conducted in MATLAB using the EasySpin program.[246]

4.2.4. Cytotoxicity Studies*

The A549 and SKOV3 cell lines were purchased from ATCC and maintained at 37 °C with 5 % CO_2 in DMEM (Gibco) and supplemented with 10 % FBS (Gibco) and 2 mM *L*-glutamine (Gibco). Cells were seeded at 2000 cells per well in quadruplicates in 384-well plates (Greiner Bio-One). Prior to treating the well, 20 mg preparations of PLGA NPs were passed through 0.8 µm sterile syringe filters. After 24 hours post seeding, the

* Cytotoxicity studies were performed by Devon Heroux under the supervision of Marcel Bally at the BC Cancer Agency, 686 West Broadway, Suite 500, Vancouver, BC, Canada, V5Z 1G1.

wells were treated with 0 to 10 μM (equivalent **4-1** concentration) of the NP formulation. After 72 h of incubation with the NP formulation, cells were treated with 4.8 μM of Hoescht33342 (Life Technologies) and 1 μM of ethidium homodimer I (Biotum) for 20 minutes to evaluate the total number of nuclei and dead cells. Plates were then imaged with an IN-Cell Analyzer 2500 (GE Healthcare) that uses an automated fluorescence microscope platform for high content screening. Cell counts were determined using the IN-Cell Developer Toolbox software. Cells were considered dead if > 30 % overlap of both stains was detected. Data were plotted using Prism 6.0 (GraphPad) and IC_{50} values were interpolated from the corresponding fitted dose-response curves. Statistical significance was calculated using one-way ANOVA with p-value < 0.05 considered to be significant.

4.3. Results and Discussion

4.3.1. Optimizing Nanoparticle Formulations

Many parameters need to be considered when generating polymer nanoparticles via the nanoprecipitation method, as employed in this chapter. Solvent ratios, surfactant percentage, initial drug to polymer ratio, drop rate, and stirring speed can all affect the size of the resulting particles. For the purposes of this study, robust techniques were employed, such as dropwise addition of the polymer-drug mixture to the aqueous media using a glass pipette and mechanical stirring using a stirring-hotplate and magnet, to ensure the techniques could be reproduced in any laboratory. This was important as expensive instruments, such as syringe pumps, or expensive facilities, such as clean rooms, for nanoparticle preparation can be prohibitive to the study of new formulations, at least at the academic level. Further expediting the efforts of this work was the initial study on the PLA polymer encapsulation of KP1019 by Keppler *et al*. that presented a good starting point for parameters that would have otherwise needed intensive study.[282] From this report, the optimal organic solvent mixture of 1.95 mL acetone and 0.05 mL dichloromethane was used in this work to dissolve the PLGA polymer and ruthenium complex prior to nanoprecipitation. The only major difference between the complexes used by Keppler *et al*. and in this chapter being the CF_3 groups. The surfactant, PF127, which is approved for clinical use, was used at 0.2 % (w/v) in 5 mL of water, also optimized by Keppler and coworkers. Other surfactants, such as TWEEN80, were

causing a relatively rapid colour change to green in formulations of **3-1**, indicating reduction of the ruthenium complex.

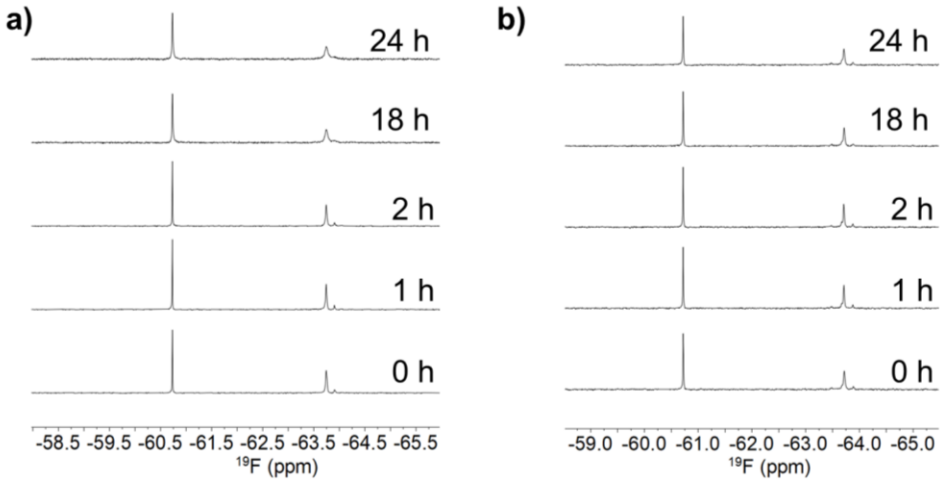

Figure 4.1 ^{19}F NMR of 4-1 in aqueous solution containing 0.2 % (w/v) a) PF127 and b) Tween80 surfactants over 24 hours.

This same surfactant driven reduction was also reported by Keppler for their PLA formulations.[282] Interestingly, reduction of **4-1** was not observed in either PF127 or TWEEN80 over the course of 24 hours (**Figure 4.1**). This is counterintuitive to their reported reduction potentials in PBS of -141 and +218 mV for **3-1** and **4-1**, respectively. This, therefore, may be due to the difference in ligand exchange rates of the two complexes and their resulting solubility in aqueous media. It has been reported that **4-1** and KP1019 quickly form monoaqua complexes in aqueous media that rapidly precipitate. In this case, there is no evidence of the formation of a monoaquo complex by ^{19}F NMR in the presence of surfactant. It is possible, then, that the surfactant may be forming micelles that stabilize the more lipophilic **4-1**, preventing ligand exchange and subsequent reduction. For **3-1**, the monoaquo complex is more soluble in water and once formed may allow for further chemical exchange with the TWEEN80 surfactant, followed by TWEEN80 mediated reduction. This is plausible as Keppler *et al* found the reduction of KP1019 by TWEEN80 involved the formation of a surfactant-complex coordinate interaction.[229] For these reasons, PF127 surfactant was used for the remaining experiments as no colour change or downfield signals in the ^{19}F NMR were observed for **4-1** over the course of 24 hours at room temperature.

Building on the reported optimized nanoprecipitation conditions by Keppler *et al* allowed for a focused study on how the initial amount of ruthenium complex affected

encapsulation efficiency, particle size, and surface charge. The formulations all used 20 mg of PLGA polymer. The results of these experiments are summarized in **Table 4.1**.

Table 4.1 Total recovered mass (RM), encapsulation efficiency (EE), and drug loading (DL) for PLGA NP formulations with 3-1 and 4-1 at varying initial loading amounts with respect to 20 mg of PLGA determined by ICP-AES.[a]

	4-1			3-1		
	1 mg	2 mg	5 mg	1 mg	2 mg	5 mg
RM (%)	90.3 ± 5	83.0 ± 4	75.5 ± 7	89.6 ± 10	90.4 ± 5	64.8 ± 8
EE (%)	20.2 ± 3	20.9 ± 4	14.0 ± 4	3.86 ± 2	2.51 ± 2	1.34 ± 0.9
DL (%)	1.11 ± 0.2	2.44 ± 0.4	3.64 ± 1	0.22 ± 0.1	0.25 ± 0.1	0.42 ± 0.3

[a] Errors are represented as ± the standard deviation of three separate formulations.

The total mass of recovered material for both preparations was similar for the 1, 2, and 5 mg initial drug loading, with slightly decreasing mass recovery as the drug loading increased. This was possibly due to an increased amount of charged complex affecting surface interactions between particles and increasing aggregates that were removed from the formulation via syringe filtration. The more lipophilic **4-1** resulted in significantly higher encapsulation efficiency, determined by comparing initial ruthenium loading versus ruthenium detected by ICP-AES. The drug loading, determined by comparing the mass of the complex detected by ICP-AES to the total mass of material recovered, for formulations with **4-1** was also higher than formulations with **3-1**. The difference in the encapsulation efficiency and drug loading between formulations with **4-1** and **3-1** can be attributed to their differences in reported lipophilicity, with **4-1** (log *D* = 1.4) being more hydrophobic than **3-1** (log *D* = -0.59).[282] The core of the PLGA nanoparticles, when prepared by nanoprecipitation in aqueous media, is comprised of lipophilic sections of the polymer with the more hydrophilic acid terminal groups facing outward. This promotes the encapsulations of lipophilic compounds such as **4-1**. Though the encapsulation efficiency for the 5 mg preparation of **4-1** was slightly lower than the 2 mg preparation, it resulted in the maximum drug loading. For this reason, the 5 mg loading, with 20 mg PLGA dissolved in 1.95 mL of acetone and 0.05 mL DCM and added dropwise to 5 mL of 0.2 % PF127 in water was chosen as the optimal formulation protocol for the remaining studies in this chapter.

Using the optimized **4-1** formulation, particle size distribution and surface charge data were collected via dynamic light scattering (DLS) and zeta-potential measurements. These data are presented in **Figure 4.2**.

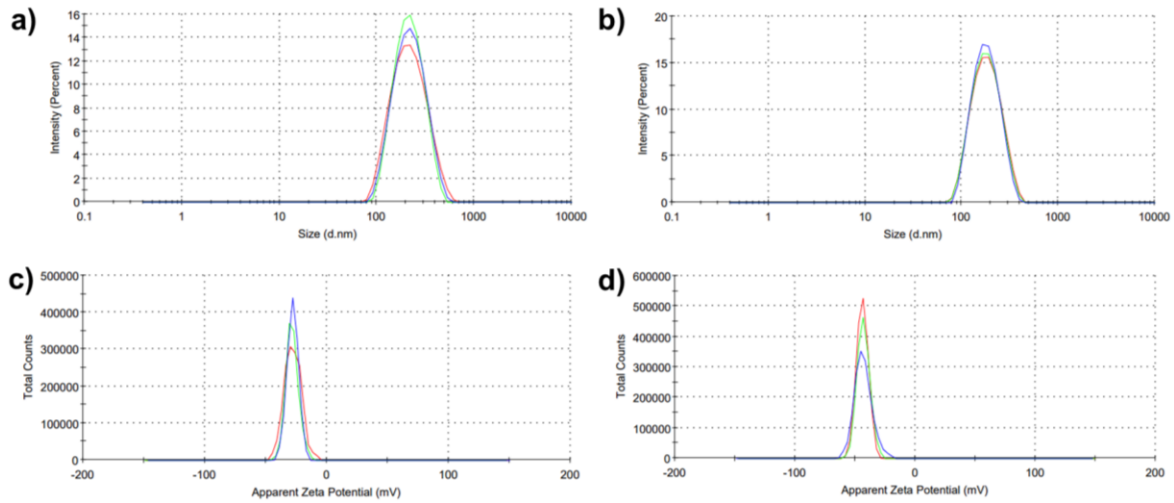

Figure 4.2 DLS and zeta potential measurements for the 4-1 NP formulation (a and c) and empty PLGA NPs (b and d).

As discussed above, particle size is important to take advantage of the EPRe with a diameter of 100 – 300 nm thought to be optimal. DLS measurements on triplicates of the **4-1** NP formulation resulted in an average particle diameter of 196.5 nm with a polydispersity index (PDI) of 0.139. The PDI estimates the distribution of size populations of a solution of particles and is calculated by:

$$PDI = \left(\frac{\sigma}{2a}\right)^2 \qquad \textbf{Equation 4.1}$$

where σ is the standard deviation of the particle diameter distribution and *a* is the mean particle diameter. A PDI value of 0 indicates a perfectly uniform size distribution where a value of 1 indicates a polydisperse sample. PDI values of 0.3 and below are considered to be acceptably homogeneous for polymer and lipid particles.[301] This suggests the particles fall nicely within the size range required to take advantage of the EPRe. Furthermore, the PDI of 0.139 suggests good monodispersity and that the formulation is easily reproducible under "normal" laboratory conditions. Interestingly, DLS measurements of empty PLGA NPs prepared under the same conditions displayed an average particle diameter of 169.4 nm with a PDI of 0.105. This shows that the particles

swell slightly upon encapsulation of **4-1** but remain within a good range of monodispersity.

It was next important to determine the surface charge of the particles to understand their colloidal stability. Generally, the more charged the surface of the particles, the greater repulsion between particles and, therefore, the less agglomeration in solution. Aggregation can lead to particle precipitation and an increase in their effective size, hindering accumulation via the EPRe and impacting cellular uptake. Aggregation can also make handling the particles difficult in situations, for example, when sterilization via syringe filtration is required. Zeta potential measurements of the NP formulation of **4-1** showed an average surface charge of -27.9 ± 7 mV. This falls within the surface charge range considered to be strongly anionic suggesting the NP formulation of **4-1** will have suitable particle-particle repulsion and colloidal stability.[302] The empty NP formulation displayed a surface charge of -43.9 ± 5 mV, demonstrating that the **4-1** NP formulations shows a significant decrease in surface charge. This is most likely due to the slightly acidic nature of **4-1**, especially considering the protonated $IndHCF_3^+$ counterion. This may cause an increase in pH of the aqueous surfactant solution during particle synthesis leading to more of the terminal COOH groups of the PLGA polymer to be protonated. However, this decrease in charged COO^- groups is not large enough to cause the particles to begin to aggregate, as confirmed by observations of solutions of the **4-1** NP formulation over several days at 4 °C which showed minimal particle settling. These data show how the choice of polymer terminal groups is important and how COOH terminated PLGA results in stable particle colloids in aqueous solutions.

4.3.2. Magnetic Resonance Spectroscopy

As described in chapter 3, the use CF_3-modified *N*-heterocyclic ligands in Ru(III) Keppler-type complexes provides a convenient ^{19}F spectroscopic handle for NMR and MRI experiments. The relaxation properties of the paramagnetic Ru(III) (d^5, S = ½) causes a broadening of the ^{19}F NMR signal attributed to the coordinated $ImCF_3$ ligands (-63.7 ppm, FWHH = 12.9 Hz). This also allows the narrower signal arising from the protonated ligand counterion (-60.7 ppm, FWHH = 3.7 Hz) to be readily differentiated in relevant solutions (**Figure 4.3a**). Following the encapsulation of **4-1** in the PLGA nanoparticles, both signals broaden significantly to a FWHH of 165 Hz and 227 Hz for

the counterion and coordinated ligands, respectively (**Figure 4.3b**). This is quite broad, especially for the diamagnetic counterion that is not typically affected by the paramagnetism of the Ru(III) centre when free in solution.

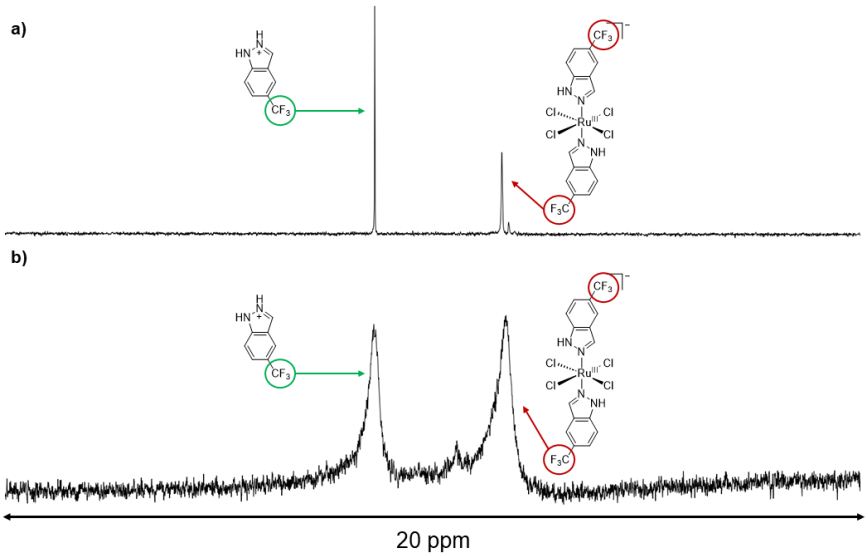

Figure 4.3 **^{19}F NMR in an aqueous 0.2 % PF127 solution of a) 4-1 free in solution and b) 4-1 encapsulated in PLGA NPs.**

These linewidth increases may be arising from anisotropic broadening if the complex is precipitating within the core of the particles and the signals become orientation dependant. Precipitation of drugs withing particles has been reported in similar in microparticles of PLGA in which encapsulated drugs were found to crystallize within the core of the particles.[300,303] However, it cannot be ruled out that the rotational correlation time (τ_c) of **4-1** is decreasing due to immobilization in the polymer matrix. Slower τ_c results in shorter T_2 relaxation times, also leading to broader NMR lines given by $FWHH = \frac{1}{\pi T_2^*}$. Using the results from the ICP-AES experiments, the effective ruthenium complex concentration (assuming no ligand exchange products) in an NMR sample volume of 650 µL was 1.35 mM. For example, solution samples of up to 25 mM have been collected for **3-1** and 5 mM for **4-1** and the resulting line widths are much narrower (see chapter 3 for spectra of **3-1**, and **Figure 4.3a** for a 5 mM solution of **4-1**). This was further explored using EPR spectroscopy by comparing frozen solution spectra of **4-1** to the **4-1** NP formulation and to the pure solid of **4-1**. These results are presented in **Figure 4.4**.

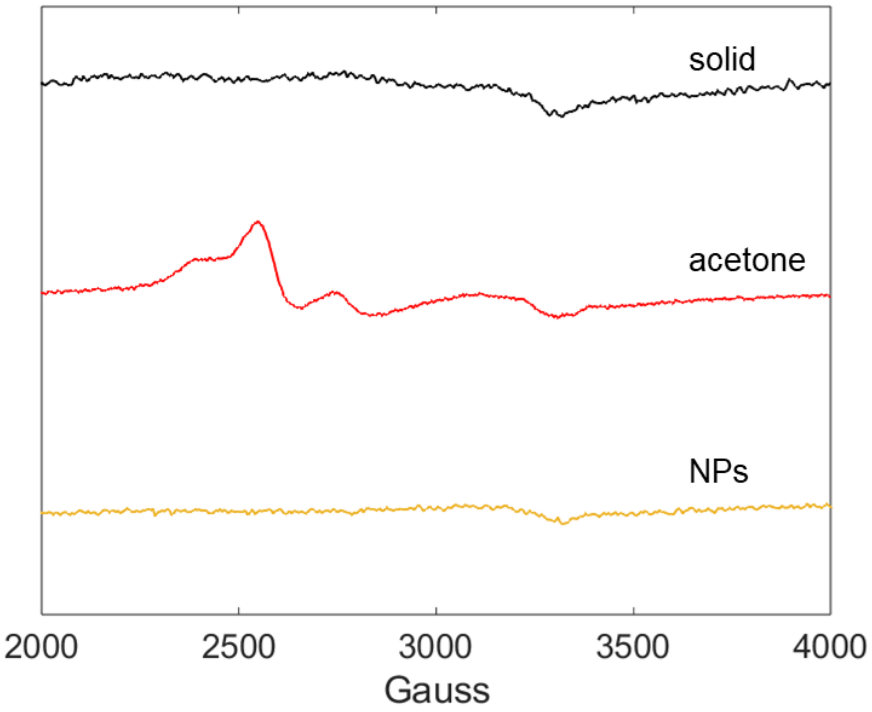

Figure 4.4 EPR spectra of collected at 100 K of solid 4-1 (black), 4-1 in DMSO (red), and 4-1 NP formulation in aqueous 0.2 % PF127 (yellow).

As can be seen in **Figure 4.4**, the uniaxial spectrum for **4-1** in acetone collected at 100 K is typical for octahedral Ru(III) complexes of this type.[73,92,282] The presence of a second species is possibly due to chloride exchange with water and is, again, typically observed for Ru(III) complexes of this type in water-miscible organic solvents such as acetone. Interestingly, practically no signal was observed for the **4-1** NP formulation. This was also observed for a spectrum collected on a pure solid sample of **4-1**. Interestingly, at 20 K a signal was detectable for the nanoparticle solution. At 4 K, the signal intensity increased significantly for the NP formulation, presenting a uniaxial spectrum resembling the free complex at 100 K in acetone (**Figure 4.5**).

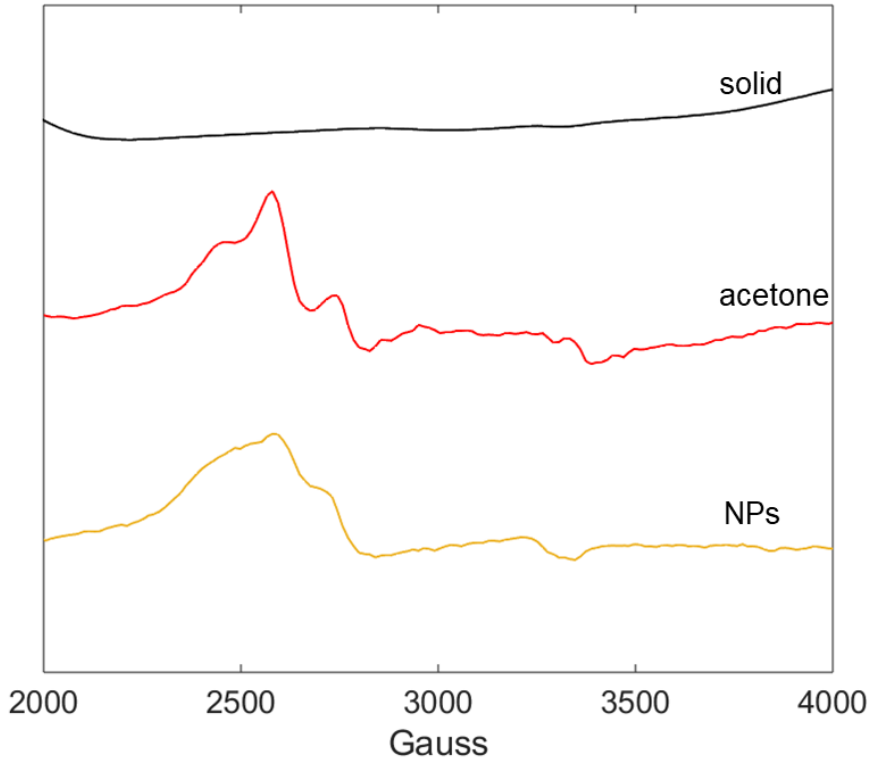

Figure 4.5 EPR spectra collected at 4 K of solid 4-1 (black), 4-1 in acetone (red), and the 4-1 NP formulation in 0.2 % aqueous PF127 (yellow).

These results confirm that the **4-1** is a highly concentrated solution within the particles rather than precipitating as a solid. Liquid helium temperatures were required to observe a signal because the electronic relaxation rates typically increase with concentration due to cross-relaxation between adjacent paramagnetic centres.[304,305] This high localized concentration within the particles would also explain the broadening observed in the ^{19}F NMR of the **4-1** NP formulation, although the shortening of the T_2 may, again, have two sources: 1) slower rotational correlation times due to interactions with the polymer matrix; and 2) cross relaxation from the paramagnetic ruthenium centres. Unfortunately, the short T_2 relaxation time hindered further exploration of the formulation via magnetic resonance methods. For example, ^{19}F DOSY was used to show that the complexes diffusion rate decreased from water to the more viscous 0.2 % aqueous PF127 solution, but the signals from within the **4-1** NP formulation were undetectable even when a weak field gradient was applied because the signals completely relaxed following the shortest possible diffusion time (**Figure C.2**).

Although the high concentration of Ru(III) complexes within the particles was deleterious toward magnetic resonance studies, it proved favourable for the sustained

release of the complex from the NPs. This was evaluated using EPR spectra of frozen solutions collected at two separate timepoints during incubation of the **4-1** formulation in cell growth media (DMEM) at 37 °C. These measurements showed a new signal following 72 h of incubation (**Figure 4.6**). This signal did not resemble the spectrum observed for **4-1** free in acetone, even following denaturing of the particles with excess acetone, and was likely a species formed through coordinate interactions with the polymer. This signal is similar to reports of Ru(III) complexes interacting with cell membranes reported by Walsby and Webb,[244] and agrees with the suggestion of Keppler and coworkers of KP1019 adducts with components of their NP formulation.[229] Promisingly, these results show that **4-1** is able to slowly diffuse into aqueous media and remains as Ru(III) even in media containing chemical reducing agents such as cystine.[306] These results highlight the utility of polymer nanoparticles to 'protect' metal complexes susceptible to redox and ligand exchange reactions in biological media. Furthermore, the minimal signal intensity after 72 h of incubation in DMEM indicates a slow diffusion of **4-1** from the particles which is advantages for delivering a sustained dose.

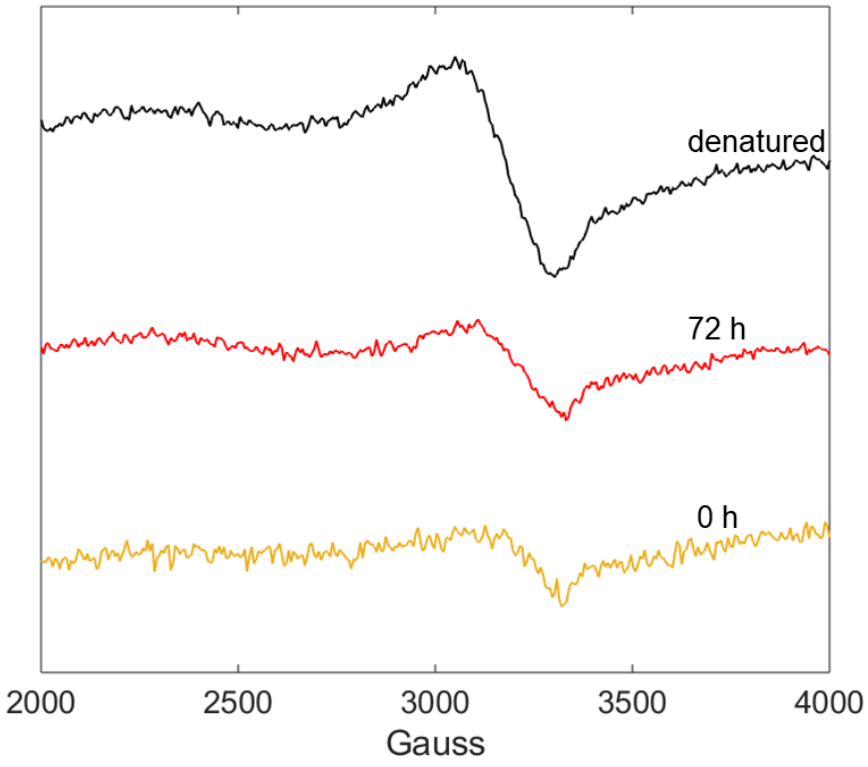

Figure 4.6 **EPR spectra collected at 100 K of the 4-1 NP formulation in DMEM at 0 h (yellow), 72 h (red), and after addition of 30 % acetone to the 72 h DMEM solution to 'denature' the NPs (black).**

4.3.3. Drug Release Studies by ICP-MS

While the encapsulation efficiency of a nanoparticle-drug formulation is important, the rate of the release of the drug is equally as pertinent. Ideally, the drug is released over a duration longer than the free drug would be from a cell or excreted from the body. To study the release of **4-1** from the PLGA NPs, the drug loaded particles were suspended in PBS for a final concentration of 1 mg of particles per mL. At various timepoints the solution was subject to centrifugation and the supernatant was analyzed for ruthenium content via ICP-MS. **Figure 4.7** summarizes the resulting release of **4-1** over the course of 72 h.

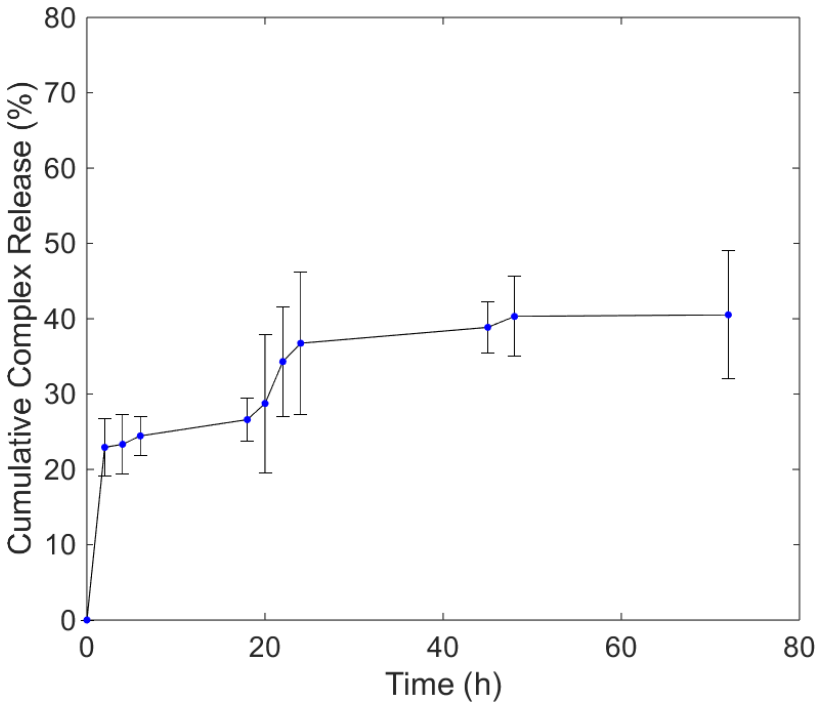

Figure 4.7 **Release of 4-1 from PLGA NPs in PBS measured by ICP-MS over 72 h. The amount released is presented as a cumulative percentage with respect to the total drug loading. Error bars are calculated from the standard deviation from three replicates.**

During the first 2 hours, approximately 25 % of **4-1** is released from the particles. This initial burst is consistent with similar NP formulations of anticancer drugs such as cisplatin.[227] It has been suggested that this initial burst is due to encapsulated drug nearer to the surface of the particles that quickly swell with water. The drug near the surface is then able to rapidly diffuse, while the remaining drug diffuses more slowly as more solvent diffuses into the core of the particles. By 72 hours, approximately 42 % of

4-1 is released. This relatively slow release suggests the target tissue would receive a sustained dose on a time scale on the order of cell division. This is certainly promising for *in vitro* cytotoxicity studies as typically cells are incubated with a drug for 72 hours. This presents a more realistic-to-*in-vivo* dose regime than a high dose of a complex dealt all at once, as is typical with free-drug cytotoxicity assays.

4.3.4. Cytotoxicity Studies

The impact of NP encapsulation on the activity of 4-1 was evaluated using *in vitro* assays. In this study, AS549 and SW480 cells were subject to incubation with varying concentrations of a 10 mg preparation of the optimal **4-1** PLGA NP formulation. These results are presented in **Figure 4.8** and are compared to the anticancer activity previously reported for KP1019 and its fluorinated derivative, free **4-1**. The concentrations used to calculate the IC_{50} values for the **4-1** formulations were obtained using ICP-AES data collected on samples that had undergone a sterilization-by-filtration which resulted in a loss of recovered material.

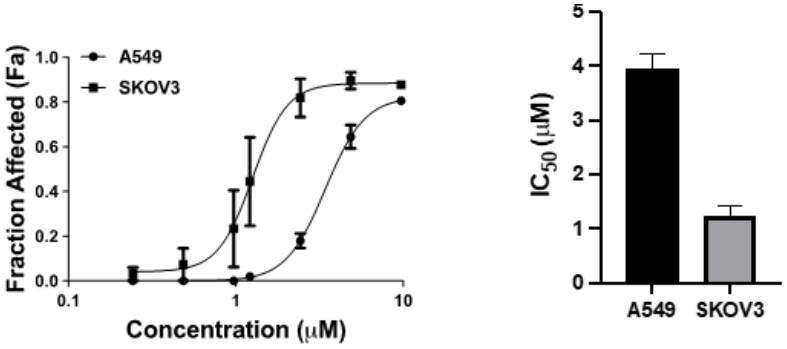

Compound	IC_{50} (μM)	
	A549	SKOV3
KP1019	24.3 ± 10[307]	84.7[a,308]
4-1	N/A	21.0 ± 4[282]
4-1 NP formulation	3.97 ± 0.3	1.25 ± 0.2

Figure 4.8 ***In vitro*** **anticancer activity of the optimal 4-1 NP formulation represented as a) the fraction of cells affected versus concentration and b) corresponding concentrations in μM at 50 % fraction affected determined from the sigmoidal fit of the fraction affected versus concentration. c) Reported IC_{50} values against A549 and SKOV3 cell lines for KP1019, free 4-1, and the 4-1 NP formulation. [a] This value is reported as the 50 % growth inhibition concentration.**

Promisingly, the **4-1** PLGA NP formulations displayed an increase in activity over both KP1019 and **4-1** alone against the ovarian cancer SKOV3 cell line, with a 67.7- and 16.8-fold increase in activity, respectively. The **4-1** NP formulation also showed a 6.1-fold increase in anticancer activity versus KP1019 against the A549 non-small cell lung carcinoma cell line. The increase in activity of the **4-1** NP formulation over the free **4-1** is most likely arising from several important advantages the NP carriers are providing. Firstly, as the complexes are slowly released from the particles, they are unlikely to undergo aqueous ligand exchange resulting in insoluble products prior to cell uptake. Cell uptake may also be increased as the internalisation mechanism is likely now dominated by endocytosis of the larger particles.[309,310] Furthermore, the sustained dose of Ru(III) species delivered by the NP formulation, over the entire period of incubation, allows for a longer period of activity rather than a burst of activity that would be encountered when cells are treated with free **4-1**. Essentially this means for the same dose of **4-1**, the NP formulations allows for more of the dose to be effective over the same duration.

4.4. Conclusions

The work presented in this chapter highlights the utility of exploring different delivery methods for well established, metal-based anticancer complexes. As the encapsulation in the clinically approved PLGA NPs is robust, this presented a method to greatly increase the anticancer activity of metal compounds without adding serious synthetic complexity or cost. Furthermore, since many metal complexes suffer from the paradox of ligand exchange – one of their main mechanisms of action but also one of the main routes to inactivation or off target activity – PLGA NP encapsulation provides a convenient route to mitigate chemical reactions prior to drug release. The size of the NPs also allows for tumour targeting through the EPRe. As one of the challenges to the clinical development of KP1019 was solubility and aqueous stability,[100] the work here presents as another route, rather than chemical modification of the complex, to improve the pharmacological properties of Ru(III) drug candidates.

5 Magnetic resonance studies of the solution behaviour of the copper anticancer complex Cas III-ia

5.1. Introduction

As discussed in section 1.3, copper complexes have been widely explored for their anticancer activity. Cu(II)(bpy) systems, in particular, have had their properties extensively studied not just for biological activity but also in the solid state[311–314] and in solution.[315–319] It is clear that for Cu(II)(bpy) systems in aqueous solutions, the ligand set and structure upon dissolution is dependent on the conditions of the media, such as pH, or the presence of nucleophiles. These complexes typically undergo hydrolysis to form $[Cu(bipy)(OH)(H_2O)]^+$ and $[Cu(bipy)(OH)_2]$ quite rapidly, followed by the formation of hydroxyl bridged dimers which typically precipitate. As described in the introduction to this thesis, casiopeinas-type Cu(II) complexes have been extensively studied for their anticancer activity. A wide variety of derivatives with phenanthroline and bipyridine ligands have been reported and *in vitro* studies have shown promising activity against a range of cancer cell lines.[204,207,209] These studies, led by Ruiz-Azura and co workers, have even seen the variant CasIII-ia enter Phase-I clinical trials in Mexico. CasIII-ia, in which the bpy ligand is 4,4'-dimylethyl-2,2'-dipyridyl (dmbpy), experiences a similar fate to other Cu(bipy) complexes upon dissolution into biologically relevant media. The structure of CasIII-ia has been well studied in the solid state[320] but information on its solution behaviour is surprisingly sparse given its clinical advancement. Some solution studies on CasIII-type complexes by EPR, ENDOR, and UV-Vis in co-solvents, such as 1:1 ethanol-DMF[321] or pure methanol,[320] have been reported but it is still important to study these systems in a solvent system that is biologically relevant. Since CasIII-ia is currently in clinical trials,[322] it is pertinent to understand the species generated following dissolution in biologically relevant media. An array of derivatives of CasIII-ia have been patented, in which the dmbpy backbone remains and the ancillary ligand set is anything from diacetylacetone to amino acids, but literature evidence suggests that the ancillary ligands have little influence on biological activity.[323]

The work in this chapter looks to fill the gap in the literature on the biologically relevant solution behaviour of CasIII-ia. EPR, NMR, and UV-Vis, are used to

characterize the species that arise following dissolution. Furthermore, interactions with important biomolecules and macromolecules, such as histidine and HSA, are explored using the same techniques. Finally, room temperature in-cell EPR was conducted to explore the behaviour of CasIII-ia *in vitro*. This work will shine light on how complexes of this type behave in biologically relevant media and whether the ancillary ligand set remains coordinated upon aqueous dissolution, informing on the next generation of Cas-type copper complexes.

5.2. Experimental

5.2.1. Synthesis

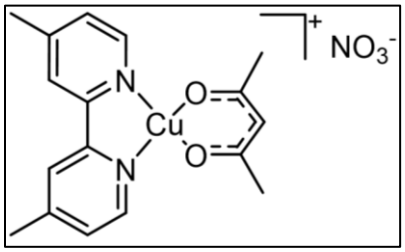

[(4,4'- dimethyl -2,2'- dipyridine) Cu (diacetyl acetonate)] [NO_3], CasIII-ia. **CasIII-ia** was synthesized as previously reported with some modifications.[324] Hydrated copper nitrate (242 mg, 1.0 mmol) was dissolved in methanol (25 mL). Then, acetylacetone (113 µL, 1.1 mmol) and 4,4'-dimethyl-2,2-dipyridine (184 mg, 1.0 mmol) was added to the blue solution. Then the pH was adjusted to approximately 6 using a concentrated methanolic solution of NaOH (6 M). The solution was stirred at room temperature and after 1 hour a blue precipitate formed. The precipitate was collected via suction filtration and the remaining solution was left to evaporate at room temperature. This yielded further blue precipitate which was also collected by suction filtration. The blue solid was recrystallized from hot ethanol yielding blue crystals. Yield: 148 mg, 36 %; MS (ESI^+): *m/z* 346.07 $[M]^+$ calc'd, 346.07 $[M]^+$ (found); Elemental analysis %: calc'd ($C_{17}H_{20}CuN_3O_5 \bullet H_2O$): C 48.72, H 5.18, N 9.82; found: C 48.92, H 5.08, N 9.23.

5.2.2. UV-Vis Spectroscopy

UV-Vis spectroscopy was performed at room temperature on a Cary 1E spectrophotometer. Samples were placed in a quartz cuvette with a volume of 1.0 mL and path length of 1.0 cm. Spectra were collected at a scan rate of 2 nm/s. Solutions of CasIII-ia were prepared in methanol, water, water:glycerol 70:30, or buffer (acetate (pH 5.0), MES (pH 6.5), or PBS (pH 7.4)) at a concentration of 50 µM.

5.2.3. EPR Studies

EPR experiments were performed at X-band (~9.4 GHz) on a Bruker EMXplus spectrometer with a Bruker PremiumX microwave bridge and high sensitivity resonator. Frozen solution spectra were collected at 100 K. To maintain low temperature, a Bruker ER 4112HV temperature control system was used with a continuous flow cryostat that passed nitrogen cryogen gas over the sample. CassIII-ia solution were prepared at 1 mM in MeOH, water, buffer (acetate, MES, or PBS), or media and 50 or 150 µL aliquots were transferred to a capillary tube or EPR tube for room temperature and frozen solution experiments, respectively. For titration experiments, stock solutions of CasIII-ia in buffer were prepared at 1 mM and then varying equivalents of histidine or HSA were added. Samples were then transferred to capillaries or EPR tubes for room temperature and frozen solution experiments, respectively. For whole-cell EPR measurement, LNCaP cells were incubated with 1 mM CasIII-ia for 4 h followed by the addition of trypsin. Fresh, sterile PBS was added and the cells were gently removed from the flask and placed in Falcon tubes and pelletized via centrifugation. The cells were then resuspended in 100 µL of sterile PBS and placed in a modified flat-cell EPR tube. LNCaP cells were also immediately tripysinized and concentrated as above followed by the addition of CasIII-ia from a 50 mM DMSO stock to a final concentration of 500 µM and sample volume of 100 µL. This suspension was then transferred to the modified flat-cell EPR tube for immediate data collection.

5.2.4. Cell Culture*

LNCaP cells were grown in RPMI 1640 cell growth media (Corning cellgro) supplemented with L-glutamine, 10 % FBS (Gibco), 100 mg/mL penicillin (BioWhittaker), 100 mg/mL streptomycin (Lonza). Incubation was carried out at 37 °C, 20 % O_2, and 5 % CO_2. Cells were then lysed using trypsin and transferred to fresh PBS and dosed with 0.5 – 1 mM CasIII-ia from a 20 mM DMSO stock or dosed with CasIII-ia prior to lysing. Cells were concentrated via centrifugation, resuspended in fresh PBS and transferred to the modified EPR flat cell.

* LNCaP cells were cultured by Raymond Lo under the supervision of Tim Beischlag at Simon Fraser University, 8888 University Drive, Burnaby, BC, Canada, V5A1S6

5.3. Results and Discussion

5.3.1. UV-Vis Solution Studies

Prior to exploring the behaviour of CasIII-ia via magnetic resonance methods, it was first important to understand its behaviour in buffered solutions at various pH values. It has been shown that similar copper complexes with N,N-bidentate ligands can begin to form copper-aqua and copper-hydroxide complexes rapidly in the pH range of 6.0 and above. Solutions of CasIII-ia were prepared in acetate (pH 5.0), MES (pH 6.5), and PBS (pH 7.4) to a final concentration of 100 µM. These solutions were incubated at room temperature over 24 hours and UV-Vis spectra were collected at various timepoints (**Figure 5.1**).

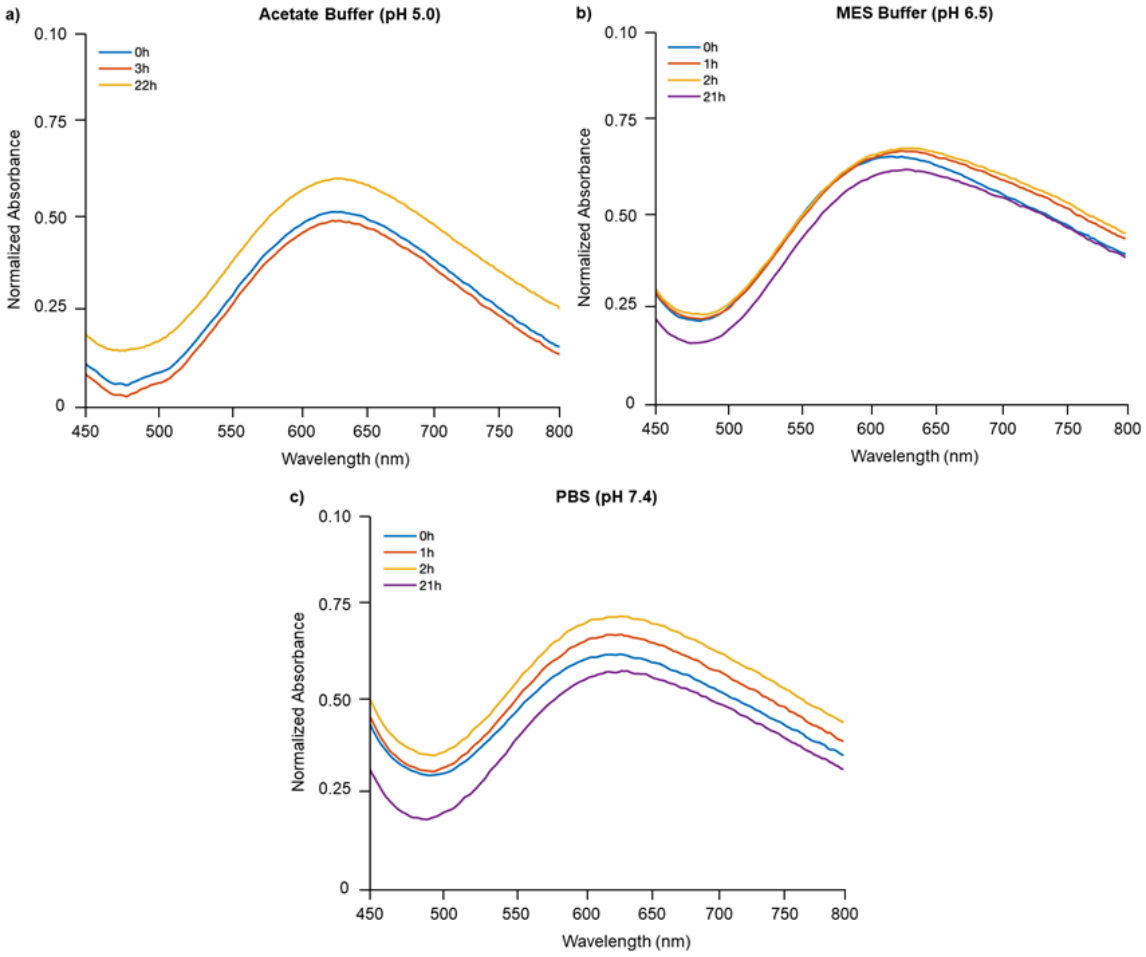

Figure 5.1 **UV-Vis spectra of CasIII-ia at 100 µM over 24 hours in a) acetate buffer at pH 5.0, b) MES buffer at pH 6.5, and c) PBS at pH 7.4.**

The λ_{max} for the d-d transitions of the complex in acetate, MES, and PBS buffers was 638, 633, and 631 nm, respectively. This corresponds to a typical d-d transition for CasIII-ia.[325,326] Interestingly, even at the higher pH of 7.4 in PBS, the UV-vis spectra change did not change significantly over 24 hours. These data indicate that no major hydrolysis occurs or that, if there is a hydrolysis event, it is instantaneous upon dissolution. Given the aqueous exchange rate for Cu(II) ions in water (~ 10^9 s^{-1}),[327] it is likely the that the latter is occurring with a rapid loss of the acac ligand. These experiments also suggest that the buffers were not forming coordinate interactions with the CasIII-ia. The change in absorbance magnitude over the 24 hours is likely due to the minor formation of copper-hydroxide insoluble following acac exchange with water.

5.3.2. NMR Solution Studies

Although Cu(II) is paramagnetic, useful information can still be obtained about the behaviour of CasIII-ia in solution via ^{1}H NMR. Upon dissolution into D_2O, CasIII-ia presents two broad signals at 1.68 and -4.89 ppm (**Figure D.1**). These signals have been attributed to the dimethyl and 3,5- and 3',5'-protons of the 4,4'-dimethylbipyridine (dmbpy) ligand coordinated to the paramagnetic Cu(II). The FWHH values of 344 and 842 Hz for these resonances suggest a significant T_2 relaxation enhancement brought on by the paramagnetic Cu(II). This relaxation enhancement results in the remaining protons of the dmbpy ligand that are closer to the copper centre being unobservable by NMR due to extensive line broadening. Interestingly, a third peak at 2.28 ppm with a FWHH of only 13 Hz was also observed. This signal matches well to the dimethyl resonance of diacetlyacetone (acac) in D_2O and the chemical shift and narrower line width suggest that the coordinated acac is at least partially hydrolysed upon dissolution in D_2O (**Figure 5.2**). As the signal intensity did not change over 3 hours, it is likely that this hydrolysis reaches equilibrium instantaneously following dissolution.

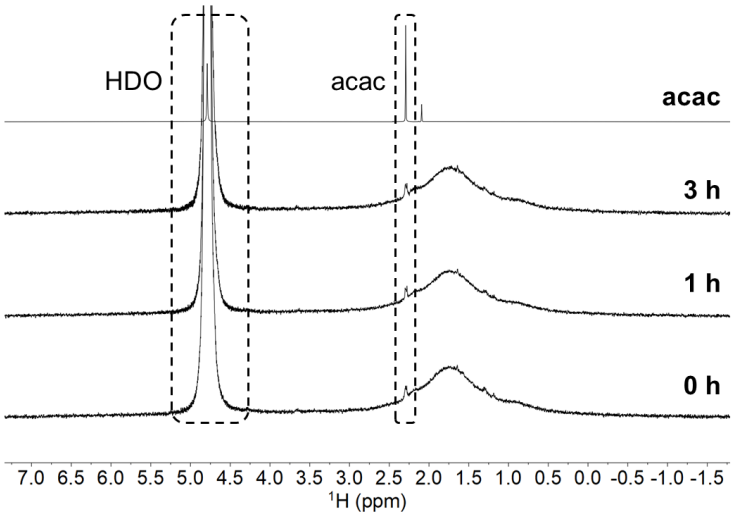

Figure 5.2 **^{1}H NMR in of diacetylacetone (top) in D_2O and CasIII-ia in D_2O over 3 hours (bottom 3 spectra) highlighting the free acac signal in the CasIII-ia spectra.**

Next, studies were performed in acetate (pH 5.0), MES (pH 6.5), and PBS (pH 7.4) buffers over 24 hours and no major changes were observed, as with the UV-Vis studies. Similarly to the experiments performed in D_2O, a signal at 2.29 ppm for all buffers was observed. This was attributed to free acac and was confirmed by the addition of acac to the solutions after the 24-hour spectra were collected (**Figure 5.3**). This is further evidence that the ancillary acac ligand is hydrolysed immediately upon dissolution in aqueous media and occurs even in more acidic conditions such as the pH 5.0 acetate buffered solution. The lack of a signal corresponding to the methyl protons of acac coordinated to Cu(II) is unlikely to be due to paramagnet relaxation enhancement as they are 4 bonds away from the copper centre. This is the same number of bonds away from the Cu(II) as the 3,5- and 3',5'-protons of the dmbpy. Since both the UV-Vis and NMR data suggested that there were no major differences in the behaviours of CasIII-ia in the three different buffers, PBS was used in all remaining buffered solution studies due to its physiological relevance.

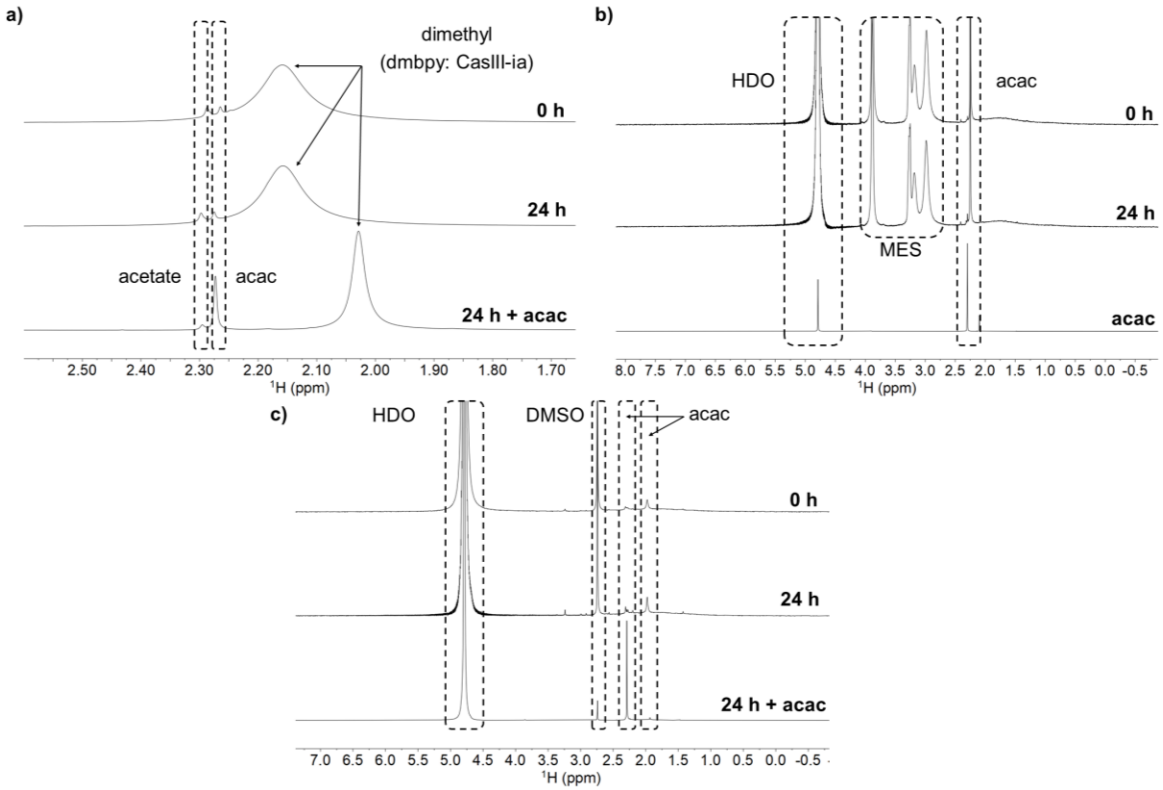

Figure 5.3 **^{1}H NMR spectra of CasIII-ia at 0 and 24 h after dissolution in a) acetate buffer (pH 5.0) with the bottom spectrum showing the 24 h solution with the addition of diacetylacetone. The shift in the dimethyl resonance from the dmbpy ligand is attributed to a change in ionic strength of the solution following dissolution of addition acac. b) MES buffer (pH 6.5) with the bottom spectrum showing diacetylacetone in MES buffer, and c) PBS (pH (7.4) with the bottom spectrum showing the 24 h solution with the addition of diacetylacetone. An additional resonance is attributed to deprotonated acac as the pH of the PBS approaches its pKa (pKa = 8.9).**

As CasIII-ia has been shown to bind with HSA[323] it was important to, first, understand the behaviour of the amino acid residue of HSA that would be most likely to form coordinate interactions with the copper. HSA has several Cu(II) binding sites, such as the N-terminal site (NTS) and the metal binding site A, that contain histidine residues capable of forming coordinate interactions, typically through the N7 imine and C2 amine nitrogen of histidine.[328] **Figure 5.4** shows the ^{1}H NMR spectra resulting from addition of one equivalent of histidine to a PBS solution of CasIII-ia over 24 h. Interestingly, no histidine signals were observed likely due to paramagnetic relaxation enhancement resulting from a coordinate interaction with the copper. The signal corresponding to free

acac is observable throughout and does not change in intensity suggesting the acac is immediately displaced by histidine upon dissolution.

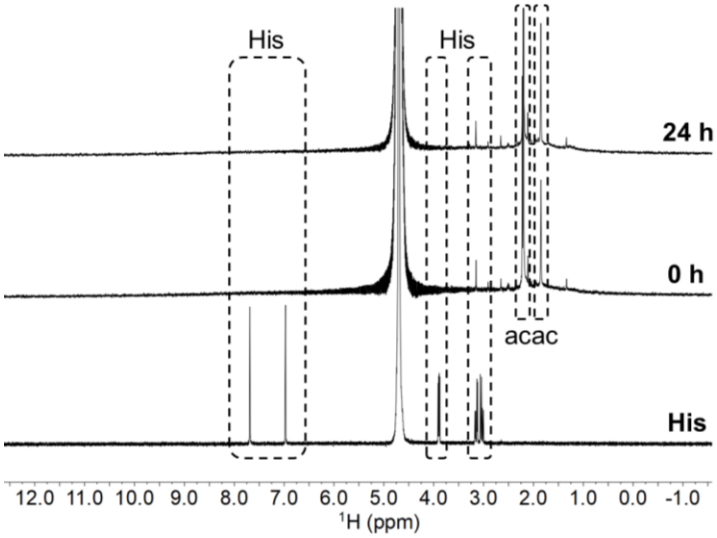

Figure 5.4 **^{1}H NMR 0 h (top) and 24 h (middle) after the addition of one equivalent of histidine to a PBS solution of CasIII-ia. These spectra are compared to a ^{1}H NMR spectrum of a PBS solution of histidine (bottom).**

5.3.3. EPR Solution Studies

EPR is a powerful tool to understand the resulting coordination environment of Cu(II) complexes, like CasIII-ia, in aqueous media and more complex mixtures. Cu(II) complexes have been well studied in aqueous media and the breadth of EPR data on compounds similar to CasIII-ia provides a good foundation for data interpretation.[173,190,329,330] Some investigations have been conducted on CasIII-ia in non-aqueous solvents, and in more complex aqueous mixtures such as buffered HSA solutions and shed some light on its behaviour and coordination environment.[321,331] The work in this section looks to expand on this literature and provide a better understanding of the behaviour of CasIII-ia in relevant aqueous mixtures ranging from buffer to whole-cells. To first gain a clear picture the spectroscopic properties of the species present following synthesis, CasIII-ia was dissolved in methanol and frozen solution EPR experiments were conducted (**Figure 5.5**).

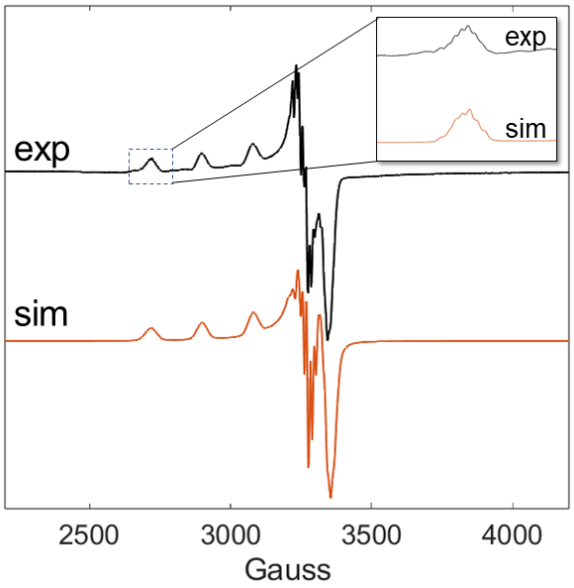

Figure 5.5 **Frozen solution (100 K) EPR spectrum of CasIII-ia at 1 mM in MeOH (exp) and the corresponding simulation (sim). Inset depicting the nitrogen hyperfine observed and simulated in the $g_{\parallel}$ region.**

As methanol is less nucleophilic than water, the resulting Cu complex in a methanolic solution should contain the original ligand set. The simulation is best fit with a single copper species with $g_{\parallel}$ = 2.245 and $g_{\perp}$ = 2.057. The $A_{\parallel}^{Cu}$ of 558 MHz is typical for square planar Cu(II) species and similar to those values reported for CasIII-ia in other non-aqueous solutions.[321] Further hyperfine can be seen in the $g_{\parallel}$ region and is best simulated with two equivalent nitrogen atoms with $A_{\parallel}^{N}$ = 35 MHz and can be attributed to the symmetric dmbpy ligand. This is displayed in the inset of **Figure 5.5** and matches reported nitrogen hyperfine values for CasIII-ia and similar Cu(II) complexes bearing symmetric N,N-donor ligands. The $g_{\perp}$ region presents a complex pattern of hyperfine coupling that was best fit with one Cu and two equivalent N atoms with $A_{\perp}^{Cu}$ = 45 MHz and $A_{\perp}^{N}$ = 38 MHz.

Table 5.1 Selected EPR parameters from frozen solution simulation of CasIII-ia in various aqueous mixtures. Hyperfine contribution from N-atoms was simulated with 2-symmetric N-donors for each unique ligand (i.e. N1 is the hyperfine contribution from the 2N atoms of dmbpy).

Species	$g_{\parallel}$	$g_{\perp}$	$A_{\parallel}^{Cu}$	$A_{\perp}^{Cu}$	$A_{\parallel}^{N1}$	$A_{\perp}^{N1}$	$A_{\parallel}^{H}/A_{\parallel}^{N2}$	$A_{\perp}^{H}/A_{\perp}^{N2}$
Cas-PBS1	2.243	2.057	560	46	40	33	10/-	3/-
Cas-PBS2	2.293	2.058	530	46	30	33	10/-	3/-
Cu-aq	2.27	2.031	130	60	-	-	-	-
Cas-His1	2.236	2.058	560	46	40	33	-/36	-/30
Cas-HSA1	2.256	2.06	505	38	40	36	-/38	-/32
Cas-HSA2	2.186	2.045	565	40	36	38	-/38*	-/32*

* Cas-HSA2 was simulated with hyperfine contribution from 2N atoms ($A_{\parallel}^{N1}$) from the dmbpy ligand and only 1 additional N atom ($A_{\parallel}^{N2}$) from HSA.

Examination of the frozen solution spectrum of CasIII-ia in PBS showed evidence of a complex mixture of species, likely due to a combination of the above aquo- and hydroxyl-species (**Figure 5.6**). As can be seen in the $g_{\parallel}$ region, multiple species containing large $A_{\parallel}^{Cu}$ typical of square planar Cu(II) complexes are visible. The $g_{\perp}$ region is also quite complex, also consistent with multiple species in solution. This mixture of species was best simulated with two different Cu(II) species containing contribution from a dmbpy ligand and one additional rhombic Cu(II) species with no contribution from N-atoms to the hyperfine system. The g-and A-values for these species are summarized in **Table 5.1**.

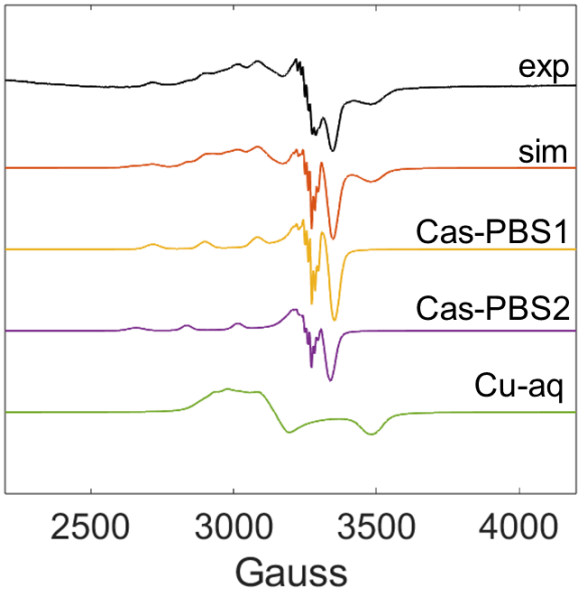

Figure 5.6 **Frozen solution EPR spectrum (exp) and simulation (sim) of a PBS solution of CasIII-ia (1 mM). The simulation is displayed as the sum of the species Cas-PBS1, CasPBS2, and Cu-aq.**

The two species containing the dmbpy ligands both have $A_{\parallel}^{Cu}$ values of 560 MHz and matches well with reported values for similar Cu(II) complexes in aqueous media. These complexes, $[(dmbpy)Cu(H_2O)_2]^{2+}$ and $[(dmbpy)Cu(H_2O)(OH)]^{+}$, have been labeled as Cu-PBS1 and CuPBS2, respectively. The NMR experiments in PBS discussed above suggest there is unlikely to be a $[(dmbpy)Cu(acac)]^{+}$ species present. The $g_{\perp}$ region for these species is complex and was best simulated with one $A_{\perp}^{Cu}$ value of 46 MHz and two equivalent $A_{\perp}^{N}$ values of 33 MHz with slightly different g-values of 2.0573 and 2.0575. Further broadening by including two $A_{\perp}^{H}$ values of 3 MHz, as suggested by Folli and coworkers,[321] arising from the dmbpy protons nearest the Cu(II) centre resulted in the best fit. A broad signal at g = 1.926 suggested a third copper species was present in solution. A broadened feature with $A_{\parallel}^{Cu}$ of 130 MHz corresponding to this was added to the sum of the Cu-PBS1 and Cu-PBS2 simulations and gave the best fit to the experimental region. This species was labeled as a Cu-aq and likely corresponds to a solvated $Cu(II)\bullet(H_2O)_x$ ion and g- and A-values match well to other similar Cu systems in aqueous media.[332] This species is thought to arise from complete hydrolysis of the original ligand set and results in a minor contribution of free copper to the solution. It should be noted that frozen solution EPR spectra of CasIII-ia incubated at room temperature over 24 hours resulted in no major change in the relative distribution of the

simulated species and matches well with the UV-Vis and NMR experiments in buffer (**Figure D.2 and D.3**). These data again suggest that the acac ligand is immediately hydrolysed upon dissolution in PBS while the dmbpy ligand remains coordinated over 24 hours.

With an understanding of the coordination environment of CasIII-ia in PBS, more complex aqueous solutions were investigated. Initial experiments involved the titration of histidine into PBS solution of CasIII-ia. The frozen solution spectra of the resulting titrations are presented in **Figure 5.7**.

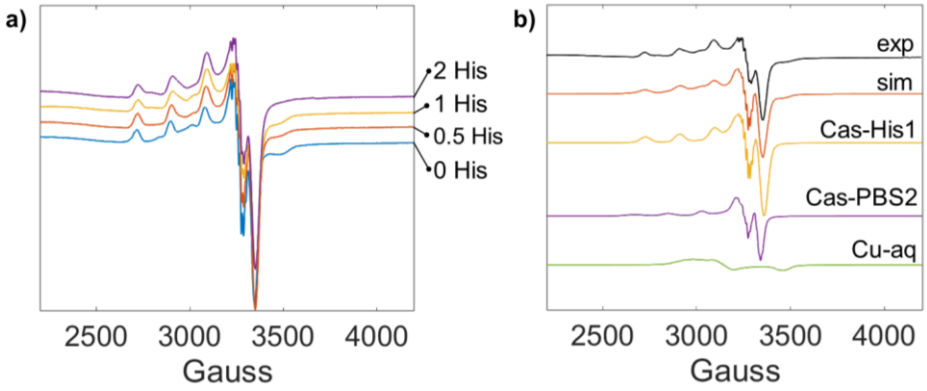

Figure 5.7 **a) Frozen solution (100 K) EPR spectra of the titration of histidine into a 1 mM PBS solution of CasIII-ia. b) Frozen solution EPR spectrum of a 1 mM PBS solution of CasIII-ia with 1 equivalent of histidine (exp), the corresponding simulation (sim), and the species summed to form the simulation (Cas-His1, Cas-PBS2, Cu-aq).**

In the frozen solution spectrum, a feature in the $g_{\perp}$ region decreases as the amount of histidine is increase from 0 to 2 equivalents. This is due to the sequestration of the Cu-aq species as more coordinating histidine is added to the solution. In the $g_{\parallel}$ region, a small shift of the g value occurs between 0 and 0.5 equivalents of histidine. This is attributed to the Cas-PBS1 species being coordinated by the histidine which replaces the aqua-ligands. There is a second species evident in the $g_{\parallel}$ region throughout the titration that has been attributed to a small contribution from Cas-PBS2 as the simulated parameters best match that species from the PBS experiments. This species is likely more favourable than Cas-PBS1 in the presence of a coordinating molecule like histidine as the OH^- ligand results in a neutral complex. Upon addition of 1 equivalent of histidine, a second minor species is indicated by changes in the $g_{\parallel}$ region and is likely a minor contribution from a bis-histidine Cu species in which a minor amount of the dmbpy

ligand is out-competed under these conditions. These results match well with other similar Cu(II) complexes in aqueous mixtures of histidine and shed light on the manner in which histidine containing proteins, such as HSA, interact with CasIII-ia. Simulation of the frozen solution spectrum resulting from the addition of 1 equivalent of HSA is presented in **Figure 5.7b**. This was best fit with a new CasIII-ia-histidine species, labelled Cas-His1 ([(dmbpy)(histidine)Cu]$^{2+}$), Cas-PBS2, and contribution from Cu-aq. The complex hyperfine in the $g_{\perp}$ region was best fit with the Cas-His1 species having contribution from 4N atoms with hyperfine values of $A_{\parallel}^{N}$ of 40 MHz and $A_{\perp}^{N}$ of 33 MHz for 2N from the dmbpy ligand and $A_{\parallel}^{N}$ of 36 MHz and $A_{\perp}^{N}$ of 30 MHz from 2N contribution from histidine.

In room-temperature titrations, a general broadening in the EPR spectrum is observed increasing from 0 to 10 equivalents of histidine (**Figure 5.8a**). The room-temperature simulation of the solution containing CasIII-ia and two equivalents of histidine is best fit with a single Cas species with hyperfine contributions from two N-atoms from the dmby ligand and two nitrogen atoms from the histidine. This, again, suggests that acac has been replaced by a histidine following hydrolysis of the acac. The room temperature species Cas-His(1+2) is likely an average of Cas-His1 and Cas-PBS2 observed in frozen solution experiments (see above). A Cu-aq species provides additional broadening resulting in the best fit and matches well with the frozen solution simulation. The parameters for each species are summarized in **Table 5.1**.

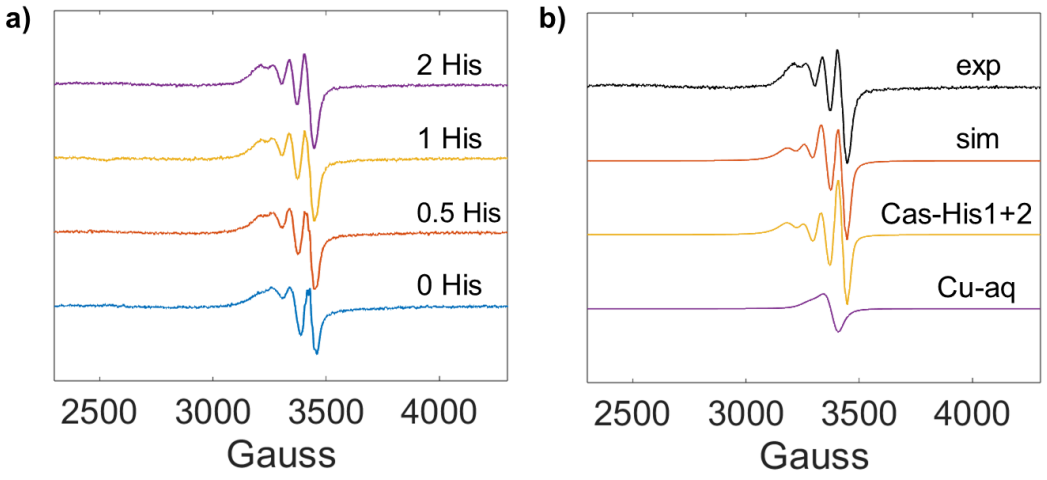

Figure 5.8 **a) Room temperature EPR spectra from the titration of 0 – 2 equivalents of histidine into a 1 mM solution of CasIII-ia in PBS. b) Simulation of the room temperature EPR spectrum of CasIII-ia in PBS following the addition of 2 equivalents of histidine.**

With an understanding of how histidine interacts with CasIII-ia, similar EPR titration experiments with HSA were conducted at room temperature and 100 K. For the frozen solution experiment, 1 equivalent of HSA was added to a PBS solution of CasIII-ia. This was allowed to stir for 30 minutes at room temperature and was then subjected to centrifuge filtration to ensure the only remaining copper species were HSA bound. These results and the corresponding simulations are presented in **Figure 5.9**.

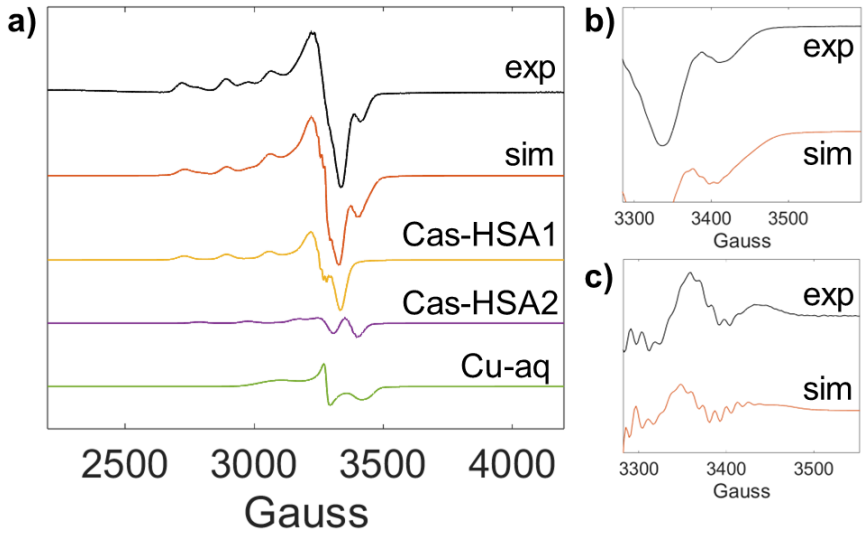

Figure 5.9 **a) Frozen solution EPR spectrum of CasIII-ia in buffer with 1 equivalent of HSA (exp), the corresponding simulation (sim), and the species that are summed to comprise the simulation (Cas-HSA1, Cas-HSA2, Cu-aq). b) Expansion of the g_3 region and c) second derivative of the same region highlighting the nitrogen hyperfine.**

Examining the $g_{\parallel}$ region reveals the presence of at least two species. The first species is labeled as Cas-HSA1 and was best simulated with contribution from only 3 nitrogen atoms. This suggests contribution from the dmbpy ligand and coordination from another nitrogen-containing amino acid residue from HSA, such as histidine, with water occupying the other coordination site. This does not rule out another possible binding mode (3N,O) in which the dmbpy-Cu complex is coordinated by an N,O-containing residue such as glycine or lysine. The simulation parameters are consistent with those observed for similar copper complexes and copper 3N,O interactions formed with the tripeptide glycyl-L-histidyl-L-lysine.[333] Another copper species, labeled Cas-HSA2, was best simulated with $g_{\parallel}$ = 2.186 and $g_{\perp}$ = 2.045 and with $A_{\parallel}^{Cu}$ = 565 MHz and $A_{\perp}^{Cu}$ = 38 MHz. The g-values for this species were different from any of the species simulated in

the previous experiments. A species of this type has been reported for similar copper complexes in solution with HSA and has been assigned to a copper ion bound to the N-terminus site with none of the parent ligands remaining coordinated.[201,331] Though this is possibly the coordination mode that produces this second Cu(II) species, additional hyperfine was observed in the $g_{\perp}$ region that was not reported for other similar copper complexes (**Figure 5.9b,c**). This suggests that instead of the N-terminus site out-competing the dmbpy ligand, it remains coordinated to the copper, with a residue from the N-terminus site replacing the acac ligand and distorting the geometry about the copper from square planar such that the g-values, particularly $g_{\parallel}$, are shifted. Consistent with the above EPR experiments, a third species labeled Cu-aq provided additional broadening to the simulation that gave the best fit and can be attributed to a contribution from a free aqueous copper ion. These experiments are mostly consistent with previous studies of copper complexes, including Cas-type compounds, interacting with HSA. Interestingly, these data again highlight the stability of the dmbpy-copper coordination as the ligand appears to be competing with the high-copper-affinity (k_D = 1 pM) HSA N-terminus metal binding site.[328]

Further investigations into the interactions of HSA with CasIII-ia were performed by titrating HSA into a PBS solution of CasIII-ia and recording the EPR spectra at room temperature. When paramagnetic metal complexes are free to rotate in solution, their resulting EPR spectra typically average to be isotropic. When these complexes are bound to a large macromolecule, such as HSA, their spectra can begin to resemble frozen solution spectra as the rotational correlation time becomes long enough on the EPR timescale. This provides further evidence for the coordinate interactions of copper complexes with HSA. The resulting data for the room temperature titration of HSA into a 1 mM solution of CasIII-ia in PBS are presented in **Figure 5.10**.

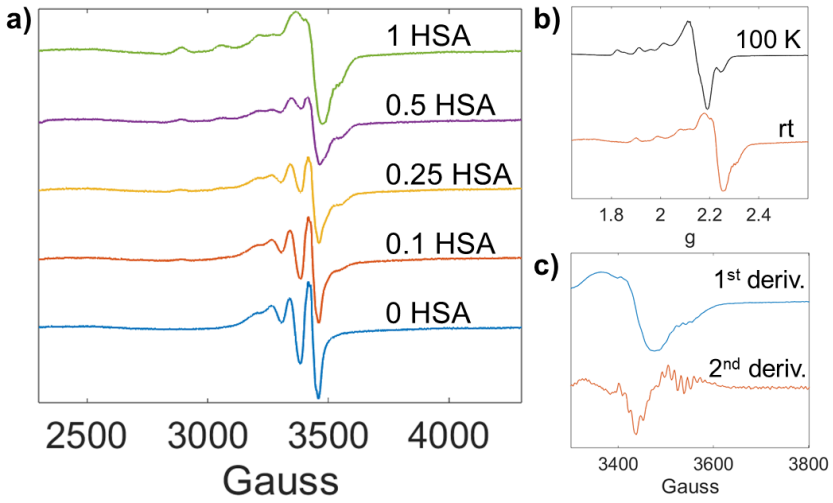

Figure 5.10 **a) Room-temperature EPR spectra of the titration of 0 – 2 equivalents of HAS into a 1 mM PBS solution of CasIII-ia. b) Comparison of the frozen solution (top) and room temperature (bottom) spectra following the addition of 1 equivalent of HSA to a 1 mM PBS solution of CasIII-ia. c) 1st (top) and 2nd (bottom) derivative of the room temperature EPR spectrum of following the addition of 1 equivalent of HSA to a 1 mM PBS solution of CasIII-ia highlighting the hyperfine in the $g_{\perp}$ region.**

Unlike the room-temperature histidine titration experiments, upon the addition of 0.5 equivalents of HSA, the spectrum begins to resemble the frozen solution CasIII-ia spectra discussed above. Upon the addition of 1 equivalent of HSA, a $g_{\parallel}$ region with features clearly resembling that of a Cu(II) frozen solution spectra is present (**Figure 5.10b**). Interestingly, additional hyperfine structure is observed in the $g_{\perp}$ region not observed in a previous EPR study of CasIII-ia and HSA (**Figure 5.10c**).[331] This suggests that the dmbpy ligand remains coordinated in the Cas-HSA species, with the hyperfine arising from the strong N-donors. When simulating the spectra from 0 to 1 equivalent of HSA, the Cas-PBS species decreases in intensity while a species labeled Cas-HAS(1+2) increases in intensity. When normalized, this intensity increases in a linear relation to the equivalents of HSA added (**Figure 5.11**). The correlation time for Cas-PBS and Cas-HAS(1+2) were determined from spectral simulations to be $10^{-10.2}$ and $10^{-7.5}$ s, respectively, and show how the CasIII-ia complex interacting with HSA results in a several order of magnitude decrease in rotational correlation time versus the unbound species. For this room-temperature system, it was not necessary to add a separate Cas-HSA (i.e. Cas-HSA2) for the simulation as the single species labeled Cas-HSA(1+2) provided an adequate fit and is likely an average of the Cas-HSA1 and Cas-HSA2

species simulated in the frozen solution experiments. Again, a third species labeled Cu-aq provides a broadening to the overall simulation giving the best fit. The relative spectral intensities of the different species were determined from the simulation and plotted versus the log of the concentration of HSA added. This shows a correlation between the increase in concentration of the Cas-HSA(1+2) species as the Cas-PBS species decreases. Contribution from the free copper (Cu-aq) species, interestingly, remains at about 20 percent throughout the titration (**Figure 5.11b**).

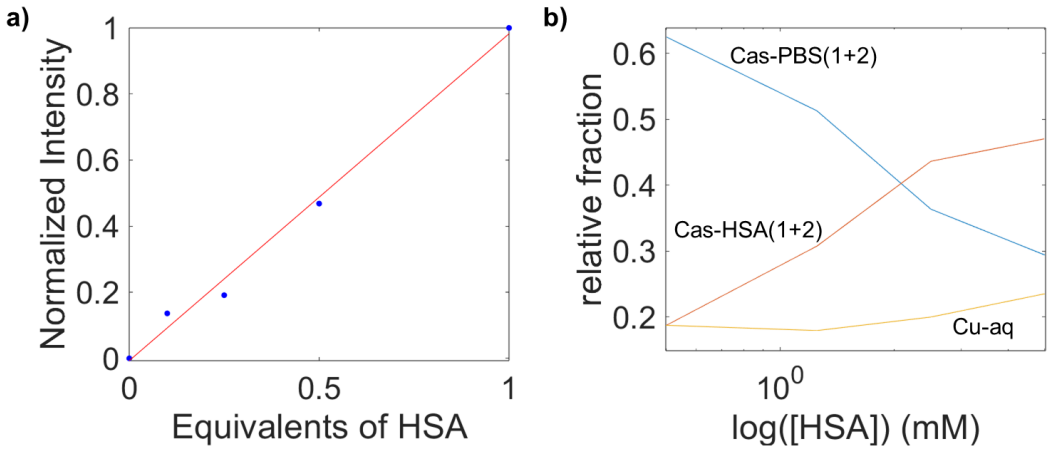

Figure 5.11 **a) Normalized intensity from the g_{II} region of the room temperature EPR spectra attributed to the formation of a CasIII-ia-HSA species versus equivalents of HSA added to a 1 mM PBS solution of CasIII-ia. b) Relative contribution of each simulated species from the room temperature simulations of the titration of HSA into a 1 mM PBS solution of CasIII-ia.**

Lastly, interactions of CasIII-ia with LnCaP cells were explored via room-temperature EPR. The first experiment involved the incubation of CasIII-ia (500 μM) and LnCaP cells for 4 hours at 37 °C. The cells were then lysed, concentrated in sterile PBS, and transferred to a modified flat-cell EPR tube. No signal was observed for this sample, which suggested either lack of uptake into the cells as the extracellular CasIII-ia would have been washed away or that the copper complex was being reduced following incubation. The reported $E_{1/2}$ value of -338 ± 4 and subsequent reduction experiments with glutathione suggest CasIII-ia will eventually be reduced once within a cell.[210] CasIII-ia was also incubated with cell media (DMEM) to ensure the media was not participating in any copper reduction or coordinate interactions and the spectra resembled that of CasIII-ia in PBS (**Figure D.4**).

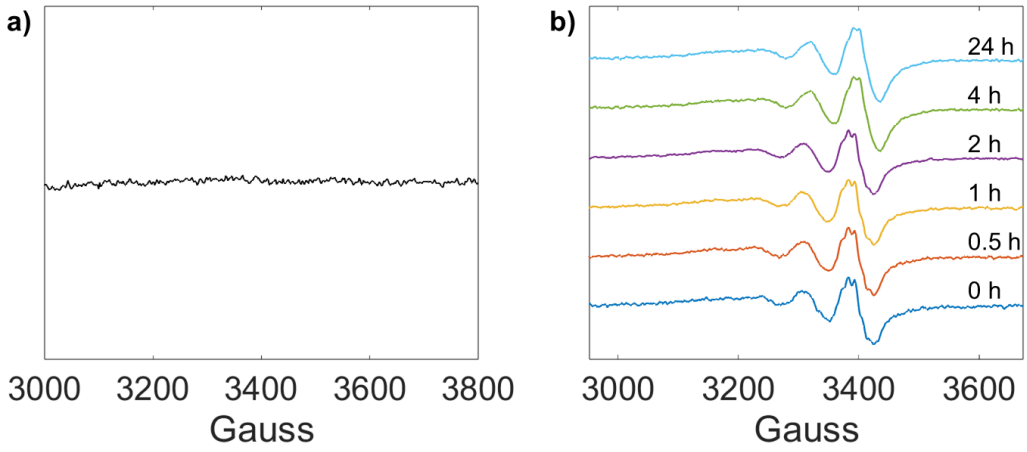

Figure 5.12 **a) Room temperature EPR spectrum of LnCaP cells following incubation with 500 μM of CasIII-ia for 4 hours. b) Room temperature EPR spectra of LnCaP cells over 24 hours immediately following the addition of 500 μM of CasIII-ia.**

To observe the behaviour of CasIII-ia in the presence of LnCaP cell over time, cells were lysed prior to the addition of 500 μM of CasIII-ia (**Figure 5.12b**). Again, the solution was transferred to the modified flat-cell EPR tube and spectra were collected over 24 h. Surprisingly, virtually no change in the signal and signal intensity was observed over the course of the experiment. No species arose which indicated coordinate interactions with larger macromolecules, such as proteins or cell membranes. Interestingly, there was only a minor change in signal intensity over the duration of the data collection. One of the mechanisms of action proposed for CasIII-ia involves the initial in-cell reduction of the Cu(II) to Cu(I) prior to ROS generation via Fenton-like chemistry. These experiments suggest reduction of the copper is not occurring in the presence of tripsinized LnCaP cells over the course of 24 hours. Though the cells were unlikely to be proliferating in the EPR flat cell, intracellular reducing agents, such as glutathione or ascorbate, would still be present and capable of reducing the CasIII-ia complex if it was entering the cell via passive diffusion. This suggests the lack of signal observed from the previous experiment is likely due to lack of CasIII-ia uptake rather than in-cell reduction.

5.4. Conclusions

The aqueous solution behaviour, as well as protein and cell interactions, of the anticancer complex CasIII-ia have been further elucidated, building on the literature of

similar Cu(II) complexes. The work herein clarifies the resulting species in biologically-relevant solutions that had, thus far, remained mostly speculation. The combination of UV-Vis, NMR, and EPR has allowed for the determination of the species present in buffer and suggests that the acac ligand is immediately hydrolysed upon dissolution. This is an important realization as of upwards of 15 derivatives of CasIII-ia have been patented in which the acac is replaced with a variety of bidentate systems, such as amino acids. The results herein suggest that the ancillary ligand may only aid in initial solubility and is unlikely to be pertinent to the overall anticancer activity, corroborating previous SAR studies on the suite of CasIII-ia derivatives. Following extensive simulations, the parent species present in biologically relevant buffers has been assigned to $[(dmbpy)Cu(H_2O)_2]^{2+}$ and $[(dmbpy)Cu(H_2O)(OH)]^{+}$ with some contribution of an aquated free Cu(II) species. Interestingly, even in the presence of strongly coordinating ligands, such as histidine and HSA, the NMR and EPR results suggest that the dmbpy ligand remains coordinated. This is contrary to other systems, many containing tridentate N-donor ligands, which have been reported to eventually lose this backbone N-donor under nucleophilic conditions. The Cas-HSA species determined by EPR simulations suggests coordinate interactions with the protein. This highlights the need for hydrolysis of the ancillary ligand to enable binding to HSA, which is particularly important since the protein is one of the main transport vehicles for Cas-type complexes to cells.[328,331]

6 Synthesis, characterization, and biological activity of a dinuclear Ru(II)-Ru(III) anticancer complex

6.1. Introduction

Both Ru(II) and Ru(III) have been of great interest in the development of novel metal-based anticancer complexes. An impressive amount of work has gone into understanding their mechanisms of action and into their derivatization.[63,100,334,335] Ru(III)-type anticancer complexes, such as KP1339, are currently being explored for the treatment of cancer in human clinical trials. KP1339, now marketed as BOLD-100 by Bold Pharmaceuticals, is even being investigated for the treatment of Covid-19, further demonstrating the utility of this scaffold for biological activity.[336] Ru(II)-arene type anticancer complexes have also been widely studied both for their promising cytotoxicity but also in the prevention of secondary tumour formation.[265,337] These complexes, such as RAPTA-C and RAED-C, though structurally similar, show how minor alterations to their ligand set can lead to different biological activities, as discussed in section 1.2.2. More recently, complexes have been developed that combine two biologically-active metal centres to give novel drug candidates with unique chemical properties and mechanisms of action.[338] For example, our group developed a suite of ruthenium(II)-arene complexes coupled to Fc that showed synergistic cytotoxicity over the individual complexes.[339]

In this chapter, NAMI-A type ruthenium(III) complexes were linked to a ruthenium(II)-arene complex by aromatic N,N-donor ligands with varied chain lengths. The combination of these two different medicinally-relevant Ru centres has the potential to provide multiple mechanisms of action which may lead to increased cytotoxicity over the mononuclear complexes and mitigate acquired resistance pathways. Conveniently, the Ru(III) centre is paramagnetic and allows for the study of the structure and solution behaviour of the dinuclear complexes by EPR spectroscopy. EPR and cyclic voltammetry (CV) were also used to investigate if the metal centres were in partial oxidation states from electronic communication across the conjugated bridging ligand.

6.2. Experimental

6.2.1. Synthesis

The materials hydrated ruthenium trichloride, dimethyl sulfoxide (DMSO), tetraphenylphosphonium chloride, pyrazine, pyrimidine, 4,4'-bipyridine, 1,3-di(pyridine-4-yl)propane, and α-phellandrene were purchased from Sigma Aldrich and used without further purification.

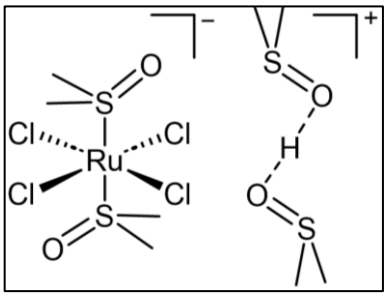

[*trans*-((DMSO-S)$_2$RuCl$_4$][((CH$_3$)$_2$SO-S)$_2$H], 6-1. 6-1 was synthesized following the procedure reported by Alessio *et al*.[340] Hydrated ruthenium trichloride (150 mg, 0.72 mmol) was dissolved in dimethyl sulfoxide (0.7 mL) and concentrated HCl (1 mL). The solution was then refluxed for 30 minutes upon which its colour changed from deep red to orange. The solution was cooled to room temperature and diethyl ether was added to induce precipitation of orange crystals. The crystals were collected by vacuum filtration and washed with diethyl ether (3x1 mL) and used without further purification. Yield: 304 mg, 76 %.

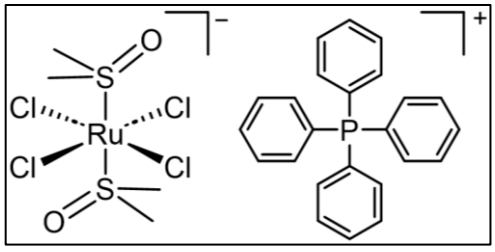

[*trans*-((DMSO-S)$_2$RuCl$_4$][(PPh$_4$)], 6-2. To an aqueous solution (6 mL) of **6-1** (300 mg, 0.61 mmol) was added tetraphenylphosphonium chloride (340 mg, 0.92 mmol) in water (3 mL). A yellow solid formed immediately upon addition of the tetraphenylphosphonium chloride and the suspension was allowed to stir for an additional 30 minutes to ensure complete counterion exchange. The precipitate was collected by suction filtration and washed with diethyl ether (3x2 mL) and used without further purification. Yield: 364 mg, 81 %.

The tetraphenylphosphonium compensated ruthenium complexes containing monodentate pyridyl-type ligands [(DMSO-S)(L)RuCl$_4$][PPh$_4$] (where L is a monodentate nitrogen donor) were synthesized according to the reported synthesis of NAMI-A with slight modifications.[340] The general procedure for **6-3** – **6-6** is as follows: **6-2** (100 mg, 0.13 mmol) was dissolved in acetone (5 mL) when L (4 equivalents) dissolved in acetone

(5 mL) was added dropwise. The solution was stirred at room temperature for 6 hours upon which diethyl ether was added until a precipitate formed. The precipitate was collected by suction filtration and washed with diethyl ether (3x2 mL) and dried under vacuum.

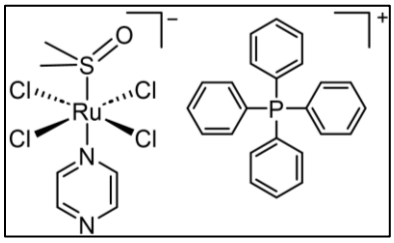

[(DMSO-S)(pyrazine)RuCl$_4$][PPh$_4$], 6-3. Where L was pyrazine. A yellow powder was collected. Yield: 69.3 mg, 72 %; ^{1}H NMR (400 MHz, DMSO-d$_6$): δ -12.49, -1.26, 2.08, 7.71-7.96.

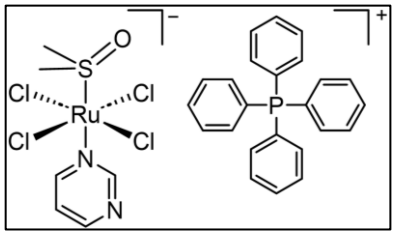

[(DMSO-S)(pyrimidine)RuCl$_4$][PPh$_4$], 6-4. Where L was pyrimidine. A yellow powder was collected. Yield: 74.1 mg, 77 %; ^{1}H NMR (500 MHz, acetone-d$_6$): δ -12.09, -5.47, -0.23, 6.79, 7.91-8.04.

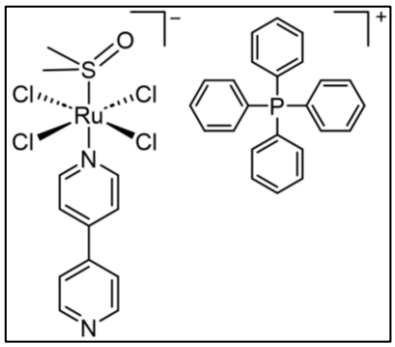

[(DMSO-S)(4,4'-dipyridyl)RuCl$_4$][PPh$_4$], 6-5: Where L was 4,4'-bipyridine. A yellow-brown powder was collected. Yield: 88.1 mg, 83 %; ^{1}H NMR (500 MHz, CDCl$_3$): δ -12.76, -3.77, 1.25, 7.26-7.93.

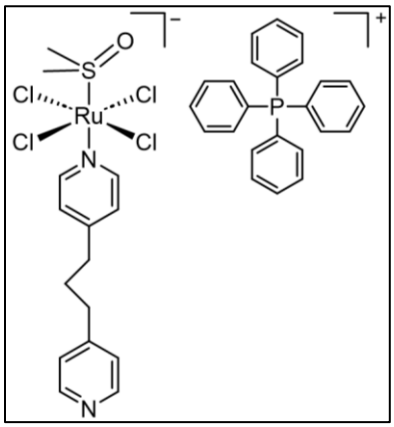

[(DMSO-S) (1,3-di(pyridine-4-yl)propane) RuCl$_4$] [PPh$_4$], 6-6: A brown powder was collected. Yield: 70.0 mg, 66 %; ^{1}H NMR (500 MHz, acetone-d$_6$): δ -12.22, -5.03, -0.03, 1.18, 2.05, 2.75, 6.35, 7.22, 7.90-8.04.

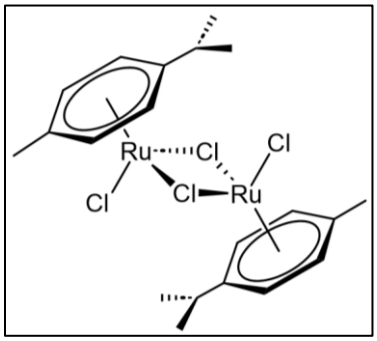

[(*p*-cyemene)RuCl$_2$]$_2$. **[(*p*-cyemene)RuCl$_2$]$_2$** was synthesized as reported by Bennett and coworkers.[264] Ruthenium trichloride (200 mg, 0.77 mmol) was dissolved in ethanol (10 mL) and α-phellandrene (1 mL, 7.7 mmol) was added at once. The solution was refluxed overnight then cooled to room temperature upon which deep red crystals began to precipitate. The reaction was placed in the freezer to allow for further precipitation. The crystals were then collected by suction filtration and washed with diethyl ether (3 x 5 mL) and dried under vacuum. The filtrate was concentrated under vacuum and placed in the freezer to induce further precipitation. Yield: 132 mg, 66 %; ^{1}H NMR (400 MHz, $CDCl_3$): δ 1.26 (d, J = 6.93 Hz, 6H), 2.14 (s, 3H), 2.91 (sept, J = 6.95 Hz, 1H), 5.33 (d, J = 5.82 Hz, 2H), 5.46 (d, J = 6.07 Hz, 2H).

The general procedure for the synthesis of the dinuclear Ru(II)-Ru(III) complexes **6-7** – **6-10** was as follows: [(*p*-cyemene)RuCl$_2$]$_2$ (50 mg, 0.08 mmol) was dissolved in DCM (10 mL). **6-3** – **6-6** (0.16 mmol) was dissolved in DCM (10 mL) and added dropwise to the stirred solution. The mixture was allowed to stir overnight at room temperature upon which the colour generally changed from red to light brown. Diethyl ether (40 mL) was then added to induce a yellow to yellow-brown precipitate that was collected by suction filtration and washed with diethyl ether (3x5 mL).

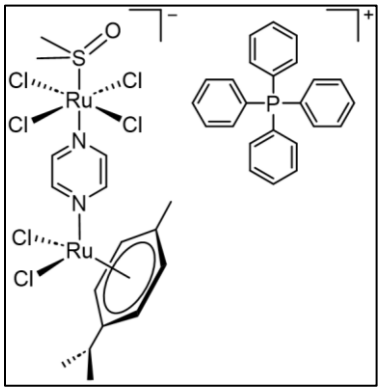

[(*p*-cyemene)Cl$_2$Ru(μ-pyrazine)RuCl$_4$(DMSO-S)] [PPh$_4$], **6-7**. A yellow-brown powder was collected. Single yellow crystals suitable for x-ray crystallography were grown via slow evaporation in DCM:Et$_2$O (1:1) over 1 week. Yield: 126 mg, 75 %; ^{1}H NMR (500 MHz, $CDCl_3$): δ -13.04, -4.61, -3.69, 1.28 (d, J = 6.94 Hz, 6H), 2.16 (s, 3H), 2.93 (sept, J = 7.07 Hz, 1H), 5.34 (d, J = 5.85 Hz, 2H), 5.48 (d, J = 5.97 Hz, 2H), 7.73-8.07 (m, 16H), 8.50-8.66 (m, 4H).

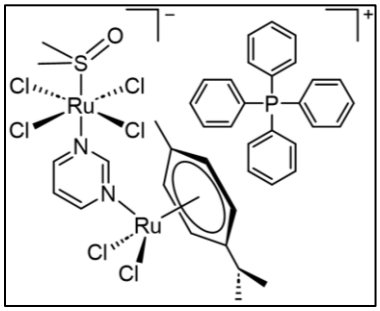

[(*p*-cyemene) Cl_2Ru (μ-pyrimidine) $RuCl_4$ (DMSO-S)] [PPh_4], **6-8**. A tan powder was collected. Yield: 105 mg, 63 %; ^{1}H NMR (500 MHz, $CDCl_3$): δ -12.43, -8.82, -5.49, -1.08, 1.29 (d, J = 7.06 Hz, 6H), 1.49, 2.17 (s, 3H), 2.93 (sept, J = 6.97 Hz, 1H), 5.34 (d, J = 5.08 Hz, 2H), 5.48 (d, J = 5.06 Hz, 2H), 7.81-8.09 (m, 16H), 8.13-8.35 (m, 4H).

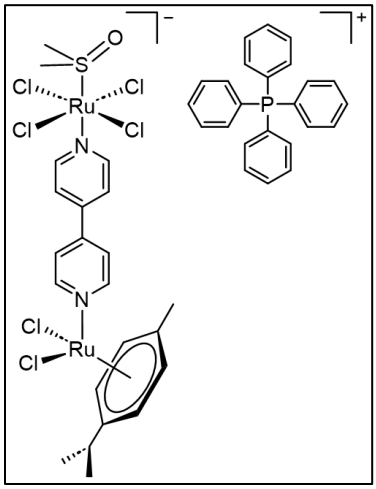

[(*p*-cyemene) Cl_2Ru (μ-4,4'-dipyridyl) $RuCl_4$ (DMSO- S)] [PPh_4], 6-9. A red-brown powder was collected. Yield: 158 mg, 88 %; ^{1}H NMR (500 MHz, $CDCl_3$): δ -12.51, -3.71, -1.51, 1.41, 1.82, 2.30, 2.69, 3.12, 5.48, 5.64, 7.73-8.17.

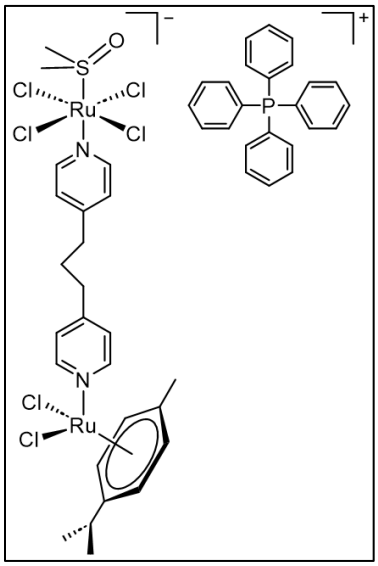

[(*p*- cyemene) Cl_2Ru (μ-1,3-di (pyridine -4- yl) propane) $RuCl_4$ (DMSO-S)] [PPh_4], **6-10**. A yellow power was collected. Yield: 98.6 mg, 53 %; ^{1}H NMR (500 MHz, $CDCl_3$): δ -12.69, -4.95, -0.39, 1.21, 1.29, 1.38, 1.91, 2.16, 2.93, 3.48, 5.31, 5.34, 5.48, 8.15-8.27, 8.38-8.56.

6.2.2. X-ray Crystallography

Single crystal X-ray diffraction was conducted on a Bruker SMART diffractometer equipped with an APEX II CCD area detector. A Cu Kα fine focus sealed tube (λ =

1.54178 nm) and a Mo Kα fine focus sealed tube (λ = 0.71073 nm) with an operating power of 1.5 kW (50 kV, 30 mA) was used and filtered with a graphite monochromator. The temperature was regulated at 150 K using an Oxford Cryosystems Cryostream. Structures were solved using SHELXL and further refinement was performed on SHELXL and OLEX 2.0. Ball-and-stick diagrams of **6-7** were generated in OLEX 2.0. Crystal data, data collection parameters, and structural details are available in CIF files attached as supporting information.

6.2.3. Cyclic Voltammetry

For cyclic voltammetry, 10 mM stock solutions of **6-7** were prepared in DMSO to increase aqueous solubility. Corresponding cyclic voltammograms were collected on a CH Instruments 660 potentiostat using a Ag/AgCl (1 M KCl) reference electrode, a platinum wire counter electrode, and a basal plane graphite working electrode. Experiments were conducted in aqueous in 10 mM PBS buffer (pH 7.4, 150 mM NaCl). Potassium ferricyanide was used as a calibration standard. Th final concentration of **6-7** was 150 μM with a final volume of 3 mL resulting in 1.5 % DMSO. Scans were conducted at a rate of 25 mV/s.

6.2.4. UV-Vis Aqueous Stability Studies

UV-Vis data was collected on a Cary 100 Bio UV-Vis spectrophotometer with a temperature controlled sample holding block kept at 37 °C using a heated water circulator. Stock solutions of **6-7** were prepared in DMSO and diluted in PBS (pH 7.4, 0, 75, or 150 mM NaCl) and 1.5, 25, 50 % DMSO at a final sample volume of 1 mL. Scans were collected every 5 minutes over the course of an hour at a scan rate of 4 nm/s.

6.2.5. EPR Spectroscopy

EPR spectra were collected at X-band (~ 9.4 GHz) on a Bruker EMXplus spectrometer equipped with a PremiumX microwave bridge, HS resonator, and Bruker ESR900 cryostat. Samples were cooled to 100 K using a Bruker ER 4112HV helium temperature control system that passed nitrogen cryogen gas through the continuous flow cryostat and over the sample tube. Samples were prepared by dissolving **6-7** in 300

μL of acetone to a final concentration of 1 mM, transferred to an EPR tube and immediately frozen in liquid nitrogen prior to data collection.

6.2.6. Cytotoxicity Studies*

The A549 and SKOV3 cell lines were purchased from ATCC and maintained at 37 °C with 5 % CO_2 in DMEM (Gibco) and supplemented with 10 % FBS (Gibco) and 2 mM *L*-glutamine (Gibco). Cells were seeded at 2000 cells per well in quadruplicates in 384-well plates (Greiner Bio-One). Prior to treating the well, 20 mg preparations of PLGA NPs were passed through 0.8 μm sterile syringe filters. After 24 hours post seeding, the wells were treated with 0 to 10 μM (equivalent **4-1** concentration) of the NP formulation. After 72 h of incubation with the NP formulation, cells were treated with 4.8 μM of Hoescht33342 (Life Technologies) and 1 μM of ethidium homodimer I (Biotum) for 20 minutes in order to evaluate the total number of nuclei and dead cells. Plates were then imaged with an IN-Cell Analyzer 2500 (GE Healthcare) that uses an automated fluorescence microscope platform for high content screening. Cell counts were determined using the IN-Cell Developer Toolbox software. Cells were considered dead if > 30 % overlap of both stains was detected. Data were plotted using Prism 6.0 (GraphPad) and IC_{50} values were interpolated from the corresponding fitted dose-response curves. Statistical significance was calculated using one-way ANOVA with p-value < 0.05 considered to be significant.

6.3. Results and Discussion

6.3.1. Synthesis and Characterization

Syntheses of the parent ruthenium compounds was relatively straightforward. This involved following the well-documented syntheses of [*trans*-((DMSO-S)$_2$RuCl$_4$][((CH$_3$)$_2$SO-S)$_2$H] (**6-1**) and the Ru-dimer [(*p*-cyemene)RuCl$_2$]$_2$. To synthesize the dinuclear complexes, the desired bridging N,N-ligand was stirred at room temperature with **6-1** followed by the addition of the Ru-dimer each at 1 equivalent to give the resulting dinuclear complex (**Scheme 6.1**). Though these syntheses were straightforward on paper, the resulting characterization presented some difficulty. Simple

* Cytotoxicity studies were performed by Devon Heroux under the supervision of Marcel Bally at the BC Cancer Agency, 686 West Broadway, Suite 500, Vancouver, BC, Canada, V5Z 1G1.

^{1}H NMR experiments proved convoluted due to the paramagnetism of the Ru(III) centre. This resulted in a significant broadening in the resonances from protons on the bridging ligands while the chemical shift of the cymene protons from the dimer remained virtually unchanged (see appendix E). ESI-MS was also attempted in both positive and negative mode, but the instability of the complexes under ESI conditions caused the complexes to break into their parent species, if they were detected at all. X-ray crystallography was then attempted to confirm the formation of the dinuclear complexes. Fortunately, suitable crystals for x-ray diffraction were grown for **6-7** and the structure was elucidated in the solid state (**Figure 6.1a**). Unfortunately, attempts to grow crystals for the other dinuclear complexes resulted in homo-dimers of the Ru(III) complexes bridged by the N,N-donor ligands (**Figure 6.1b**). Therefore, because of lack of evidence of the synthesis of the remaining suite of dinuclear complexes, **6-7** was selected as a model complex for further study in this chapter.

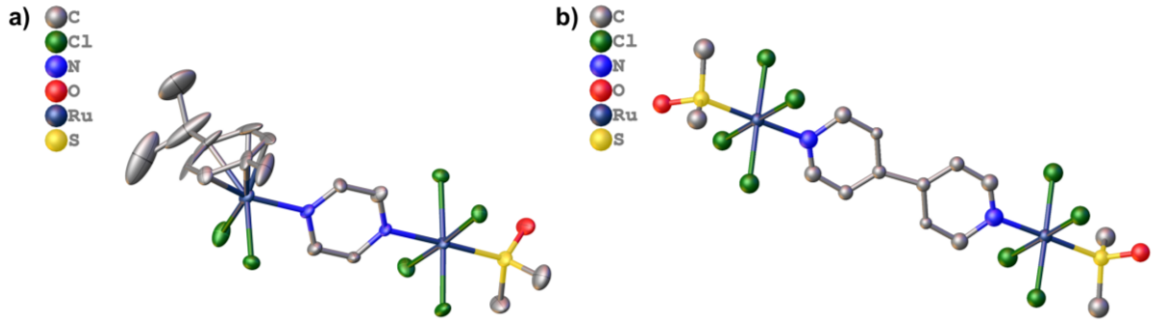

Figure 6.1 **Molecular structures determined by x-ray crystallography for a) 6-7 with ellipsoids drawn at the 50 % probability level and b) the Ru(III) homodimer resulting from the attempted synthesis of 6-9. For the homodimer, low data quality during x-ray diffraction, with an I/σ value of 0.9, did not allow for a complete anisotropic solution of the solid state structure and, therefore, the isotropic solution is depicted above.**

6.3.2. Characterisation by EPR

EPR is a powerful tool to determine the coordination environment about a paramagnetic metal centre. This is particularly useful in situations when typical methods of characterisation such as NMR and MS become difficul due to the chemical properties of the complex. For **6-7**, EPR was used to confirm the presence of the Ru(III) atom and the nature of its ligand environment.

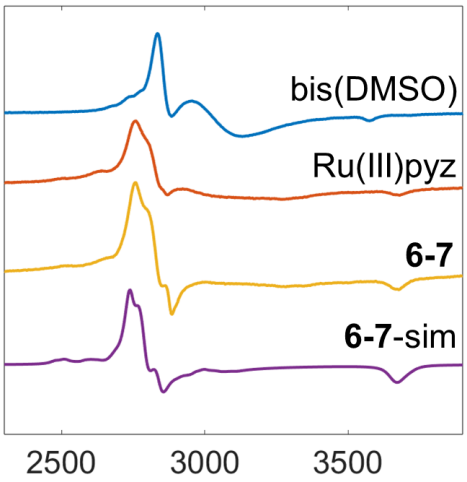

Figure 6.2 **Frozen solution spectra of 1 mM acetone solution of [bis(DMSO-s)$RuCl_4$][Na] (bis(DMSO), blue line), [(pyrazine)(DMSO-S)$RuCl_4$][Na] (Ru(III)pyz, red line), 6-7 (yellow line), and the simulation of 6-7 (6-7-sim, purple line).**

The frozen solution spectra of **6-7**, its parent complex [(pyrazine)(DMSO-S)$RuCl_4$][Na], and the starting material [bis(DMSO-s)$RuCl_4$][Na] (bis-DMSO) in acetone are presented in (**Figure 6.2**). The EPR of each species varies slightly from the previous with subsequent synthetic steps. Particularly important in the confirmation of the synthesis of **6-7** is the differences in the EPR spectra of [(pyrazine)(DMSO-S)Ru(III)Cl_4]$^-$ (Ru(III)pyz) and **6-7**. Ru(III)pyz presents a typical uniaxial spectrum with some broadening due to nitrogen hyperfine from the pyrazine ligand. The spectrum for **6-7** has more well defined hyperfine features than that of Ru(III)pyz. Upon simulation, this is best fit with three g-values of g_1 = 2.425, g_2 = 2.405, and g_3 = 1.829. This slight deviation from a uniaxial geometry likely reflects the steric bulk of the Ru(II)pyz ligand whereas with Ru(III)pyz the pyrazine ligand does not incur enough steric bulk to provide the same distortions. Interestingly, a large A^{N}_{g2} value of 170 MHz provided the best fit of the hyperfine features in this region. It possible this large coupling arises from an induction effect cause by Ru(II) coordination to the pyrazine which strengthens its σ-donation to the Ru(III) centre versus pyrazine alone. Ruthenium hyperfine values (S = 5/2 for ^{99}Ru and ^{101}Ru with natural abundances of 12.7 and 17.1 %, respectively) in the g_1 and g_2 regions of 350 MHz provided additional broadening and fit well the satellite features observed in this area.

6.3.3. Aqueous Stability Studies

NAMI-type complexes are known to undergo ligand exchange in aqueous media. This is suggested to be one of the mechanisms of activation prior to interactions with biomolecules such as DNA. Typically, complexes of this type first lose their DMSO ligand to hydrolysis followed by loss of one or more chloride ligands. To study the behaviour of **6-7** in buffer, UV-Vis experiments were conducted under a variety of buffered conditions (**Figure 6.3**). Initially, studies were performed on 200 μM phosphate buffer solutions of **6-7** while the concentration of Cl^- was varied in each experiment. At all Cl^- concentrations, only one isosbestic point was observed suggesting a single ligand exchange event over the course of the experiments. Furthermore, the rate at which the new λ_{max} arose did not change at different Cl^- concentrations suggesting the event was not the hydrolysis of one of the chloride ligands.

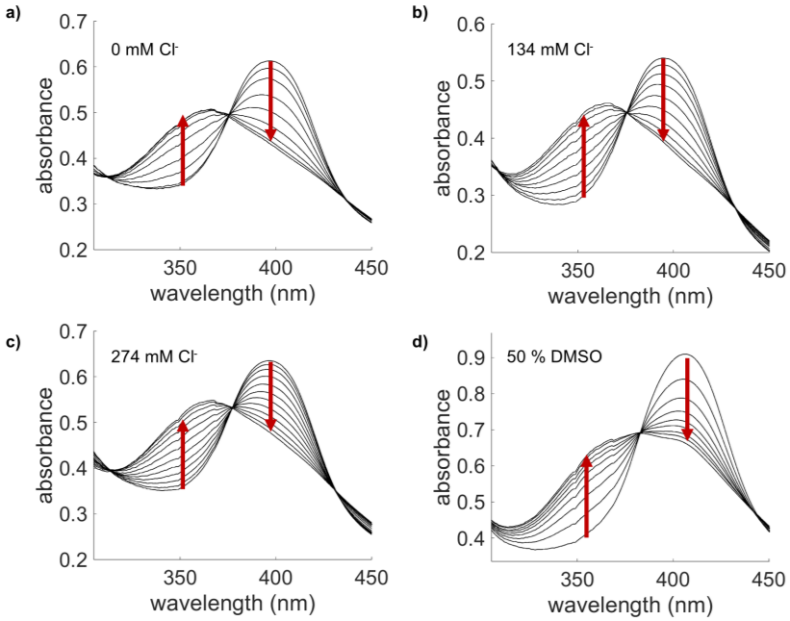

Figure 6.3 **UV-Vis absorbance spectra of a 200 μM solution of 6-7 in phosphate buffer with a) 0 mM Cl^-, b) 134 mM Cl^-, c) 274 mM Cl^-, and d) 134 mM Cl^- with 50 % DMSO.**

Next, the UV-Vis experiment was repeated with 50 % DMSO solution with 154 mM Cl^- (phosphate buffered saline, PBS). A single isosbestic point was observed again, suggesting a single ligand exchange event. In this case, the rate of increase of the new signal was slowed by the excess DMSO present in the solution. This allowed for the first

ligand exchange event upon dissolution in PBS to be characterised as the hydrolysis of the DMSO ligand and matches well with previous reports of similar mononuclear Ru(III) anticancer complexes. It should be noted that chloride hydrolysis may be occurring at the same time and does not result in an observable change to the UV-vis spectrum. A diaqua complex in which one of the chlorides and the DMSO is exchanged has been reported to be the major species present ca. 15 minutes following dissolution of NAMI-A in aqueous media.[341,342]

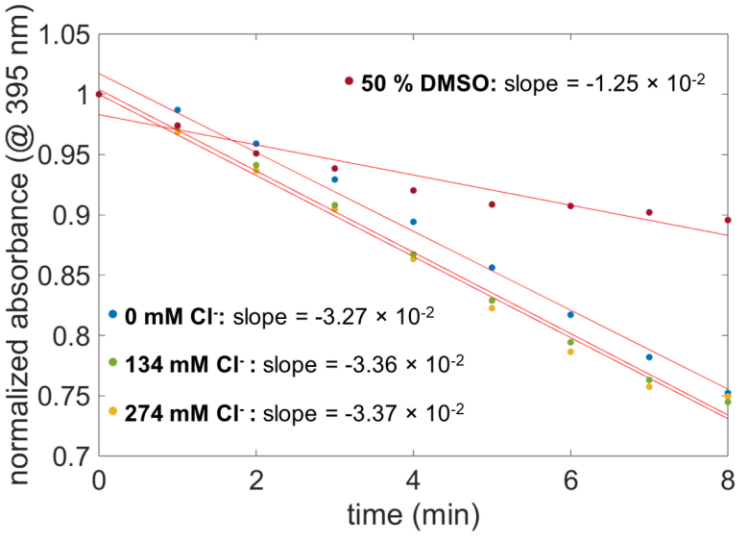

Figure 6.4 **Normalized absorbance at 395 nm versus time from the UV-Vis absorption spectra of a 200 µM solution of 6-7 in PB with 50 % DMSO with 134 mM Cl^-, and 0, 134, and 274 mM Cl^-. The corresponding linear fits for each experiment were determined using the polyfit function in MATLAB and are displayed as a red line.**

Plotting the maximum absorbance at 395 nm versus time allows for an understanding of the DMSO exchange rate and how the different PBS additives effect this rate (**Figure 6.4**). The slope for the absorbance versus time when varying just Cl^- concentrations remains virtually the same at approximately -3.3×10^{-2}. When 50 % DMSO is added to the buffer, the magnitude of the slope is approximately halved to -1.25×10^{-2} over the first 10 minutes of the experiment.

6.3.4. Electrochemistry

An often-postulated mechanism of action for Ru(III) anticancer complexes is based on the 'activation-by-reduction' hypothesis. This suggests that Ru(III) complexes

are prodrugs that exhibit their anticancer activity following in-cell reduction. Once reduced, the complexes can then begin cytotoxic ROS production via redox cycling in fenton-type chemistry. The Ru(II) is also more labile and can exchange chloro- and other ligands more readily, eventually leading to coordinate biomolecule interactions. Therefore, it is important to understand the reduction potential of novel Ru(III) complexes to establish if they will be reduced in biological environments.

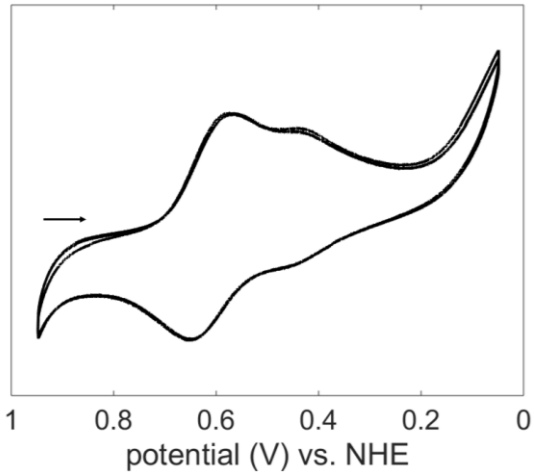

Figure 6.5 Cyclic voltammogram of a 1 mM PBS solution of 6-7 prepared from a 20 mM DMSO stock solution for 5 % DMSO in the final dilution. Three consecutive scans are plotted using a scan rate of 20 mV/s. Scan direction is indicated by the black arrow.

To explore the reduction potential of **6-7**, cyclic voltammetry was performed in degassed PBS (pH 7.4) (**Figure 6.5**). A reversible redox couple with an $E^{\circ\prime}$ value of 615 mV was observed and is assigned to the $Ru^{III/II}$ couple of the Ru(III) moiety of the complex. This is higher than the reported value of 235 mV for NAMI-A and the increase may be attributed to strong π-backbonding into the Ru(II)pyz system.[343,344] A second, broader couple is present with an $E^{\circ\prime}$ of 442 mV. This couple is likely arising from multiple species forming following ligand exchange in the aqueous buffer. Since hydrolysis is likely occurring following the reduction of the parent complex these new species may be overlapping in the resulting CV and causing the observed broadening. A redox couple for the Ru(II) species was not observed as it would likely occur at a potential outside the working range of the aqueous PBS buffer.[339] Somewhat surprisingly, the $Ru^{III/II}$ couple is strongly shifted from similar mononuclear Ru(III) complexes. Though the EPR suggests no electronic 'communication' across the pyrazine bridge, in that there is not a ruthenium in a partial oxidation state, the Ru(III) in

this system is relatively electron deficient. With that said, these results still suggest that the reduction potential for **6-7** falls within a biologically relevant range. For example, biological reducing agents such as GSH and ascorbate have a reduction potential of -240[345] and -66 mV (at pH 7.0),[346] respectively. Furthermore, the peak-to-peak separation for the $Ru^{II/III}$ couple of 63 mV suggests reversibility[347] and that the complex could participate in the catalytic generation of ROS, leading to cytotoxicity.

6.3.5. Cytotoxicity Studies

The *in vitro* anticancer activity of **6-7** was assessed against the ovarian cancer cell line SKOV3 and non-small cell lung cancer A549 cell line. Cells were treated with the sodium compensated form of the dinuclear complex for 72 h with concentrations ranging from 0 to 200 μM with 1 % DMSO. The sodium compensated form provided increased aqueous solubility mitigating the formation of precipitates. IC_{50} values were determined by fitting a sigmoidal curve to the dose-response data using a four-parameter logistic model. This data is presented in **Figure 6.6**. Cells were also dosed with a vehicle (DMSO) and hydrated ruthenium trichloride controls which showed no affect on cell growth.

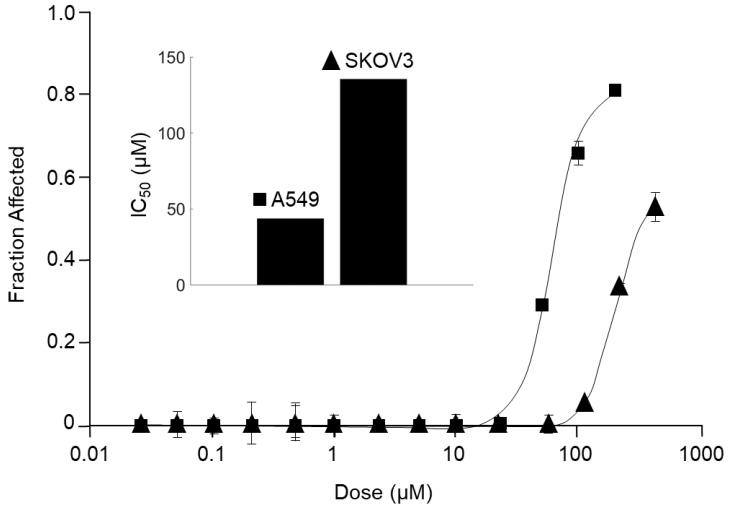

Figure 6.6 Dose-response curves for 6-7 following incubation at varying concentrations with A549 (squares) and SKOV3 (triangles) cancer cell lines. The inset shows the IC_{50} values against each cell line determined from the sigmoidal curve fit to the dose-response data.

The dinuclear complex **6-7** displayed moderate to good cytotoxicity with IC_{50} values of 43.73 and 133.5 μM against A549 and SKOV3, respectively. In previous

works, it was found that the parent Ru complexes bearing a pyridine ligand were essentially inactive against HT29 (Ru(II)-pyr) and SW480 (Ru(III)-pyr) cell lines.[339,348–350] The results for **6-7** compared to the general inactivity of the parent Ru complexes suggests a synergism giving rise to new biological activity. It is possible that bridging the two complexes provides favourable lipophilicity leading to greater cellular uptake than the individual compounds. A trend of increasing lipophilicity leading to greater *in vitro* anticancer activity has been noted for similar mononuclear ruthenium complexes.[282,350]

6.4. Conclusions

The synthesis of several dinuclear Ru(II)-Ru(III) complexes was attempted, with the successful characterization of the pyrazine bridged compound. The aqueous solution behaviour was characterized for this complex, showing loss of DMSO for water within the first 10 minutes following dissolution. EPR studies showed a single Ru(III) species present in solution with an axial geometry typica for Ru(III) anticancer complexes of this type. CV experiments showed that the Ru(III) moiety will likely be reduced under biological conditions with an $E^{\circ\prime}$ of 442 mV. These data also suggested there was no electronic communication across the bridging pyrazine ligand. *In vitro* anticancer testing of this complex showed good activity against A549 non-small cell lung cancer cells with an IC_{50} of 43.73 μM. This was greater than the general biological activity of the parent Ru(II) and Ru(III) complexes alone. The work herein demonstrates the utility of combining ruthenium anticancer complexes known to be relatively inactive to induce new biological activity.

7 Conclusions and future work

7.1. Expanding on Ru(II)-arene chemistry

Much of the work in this thesis explored new applications for families of ruthenium anticancer complexes considered to be well studied and the development of magnetic resonance methods to study their mechanisms. Chapter 2 involved development of Ru(II)-arene anticancer complexes by modifying their structure through the arene moiety with a selective estrogen receptor modulator. In general, this resulted in increased anticancer activity over both the RAPTA-C and RAED-C parent scaffolds. This showed the benefits of designing new molecules off the backbone of well-studied complexes. Chapter 3 explored the use of CF_3-modified Ru(III) Keppler-type complexes for ^{19}F magnetic resonance imaging. These complexes, which had already shown good anticancer activity, proved to also function as useful imaging probes that could shine light on the elusive mechanisms of action of this family of anticancer compounds. A central concept of these two chapters is the development of novel ruthenium compounds with theranostic (diagnostic + therapeutic) potential. Further developments in this area could involve novel arene ligands, accessed via the chemistry developed in Chapter 2, with ^{19}F imaging tags (**Figure 7.1**).

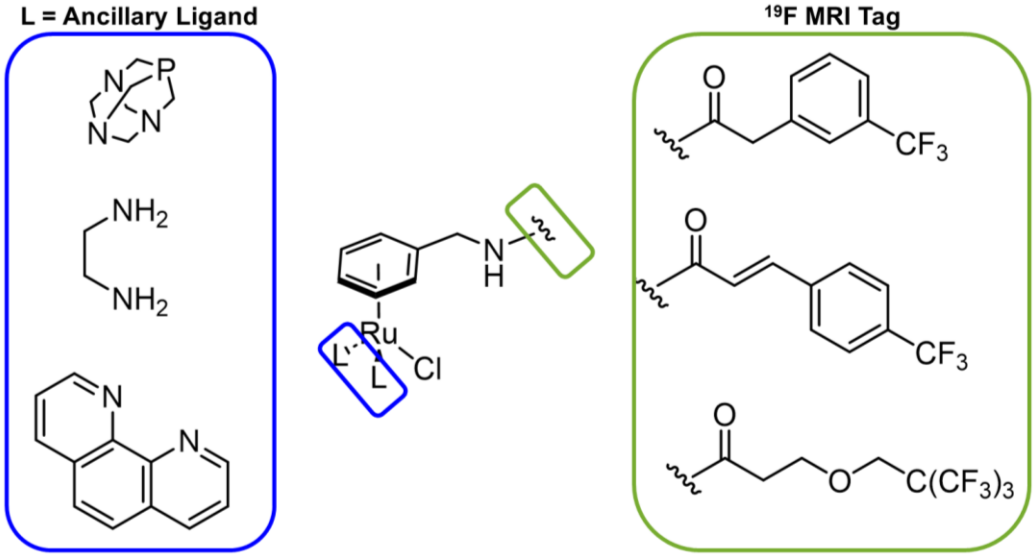

Figure 7.1 Ru(II)-arene ^{19}F MRI agents with potential anticancer activity.

It can be seen how this modular approach would allow access to a library of complexes. Each ^{19}F MRI tag could be appended to the reduced benzylamine through HATU coupling chemistry and coordinated to the ruthenium in refluxing ethanol as discussed in Chapter 2. Finally, an ancillary ligand could be chosen to help optimize parameters such as lipophilicity and ligand exchange kinetics. The chemistries chosen here are robust and one could imagine expanding a library of complexes like these using high throughput technologies – for both synthesis and cytotoxicity assays. Using the ^{19}F MRI and data processing techniques developed in Chapter 3, these complexes could quickly be screen for their use as ^{19}F imaging agents, allowing for their fate in biologically relevant tissues to be resolved spatially.

The original design of the Ru(II)-arene-SERM complexes was to create RAPTA- and RAED-type compounds with targeted activity toward ER+ cancer cells. Interestingly, the SERM complexes showed only a slight increase in activity toward ER+ MCF-7 cells versus triple negative MDA-MB-231 cells, with the NCI-60 results pointing toward a general rather than targeted increase in activity over RAPTA-C and RAED-C. This same approach, similar to the design of ferrocifen, could be used to created Ru(II)-arene complexes that target specific organelles, such as mitochondria. This approach has proven effective with interest in mitochondrial targeting agents employing positively charged phosphonium. Again, using the Birch reduction chemistry developed in Chapter 2, one could imagine the development of a library of mitochondrial-targeting Ru(II)-arene complexes modified through the arene (**Figure 7.2a**).

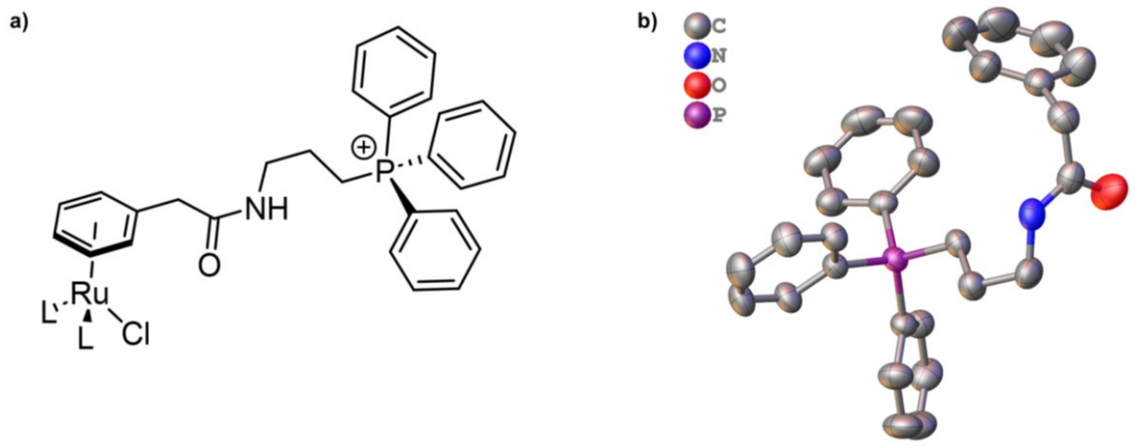

Figure 7.2 **a) The proposed structure for a Ru(II) anticancer complex with a triphenylphosphonium mitochondria-targeting moiety coupled through the arene ligand. L could be any number of ancillary ligands with examples depicted in Figure 7.1. b) The crystal structure of a triphenylphosphonium ligand with ellipsoids drawn at the 50 % probability level. Hydrogen atoms are omitted for clarity.**

The ancillary ligands could be chosen to provide optimal solubility, cell uptake, and aqueous stability. The coupling of a triphenyl phosphonium to a reduced phenylacetic acid using HATU chemistry has already proven viable, with the crystal structure of the ligand depicted in **Figure 7.2b**.

7.2. Nanoparticle Decoration

The promising results of encapsulating a CF_3-modified Ru(III) Keppler-type complex in polymer nanoparticles presented in Chapter 4 just scrapes the surface of the possibilities nanoparticles bring to the table for metal complexes in medicine. Many groups have reported taking the PLGA polymer formulation a step further by appending PEG groups to improve nanoparticle stability and bioavailability. It has been shown that PEGylated PLGA nanoparticles circulate in the blood stream longer than PLGA nanoparticles. Furthermore, carboxylic acid terminated PEG can be employed that allows further decoration of the nanoparticles with anything from macromolecules, such as aptamers, to small molecules, such as biotin.[351] The work in Chapter 4 provides a foundation for further studies in which, for examples, the nanoparticles are designed to specifically target cancer cells. This approach has been explored for the encapsulation of non-metal and metal containing drugs in nanoparticles decorated with aptamers and antibodies.[214,227,351]

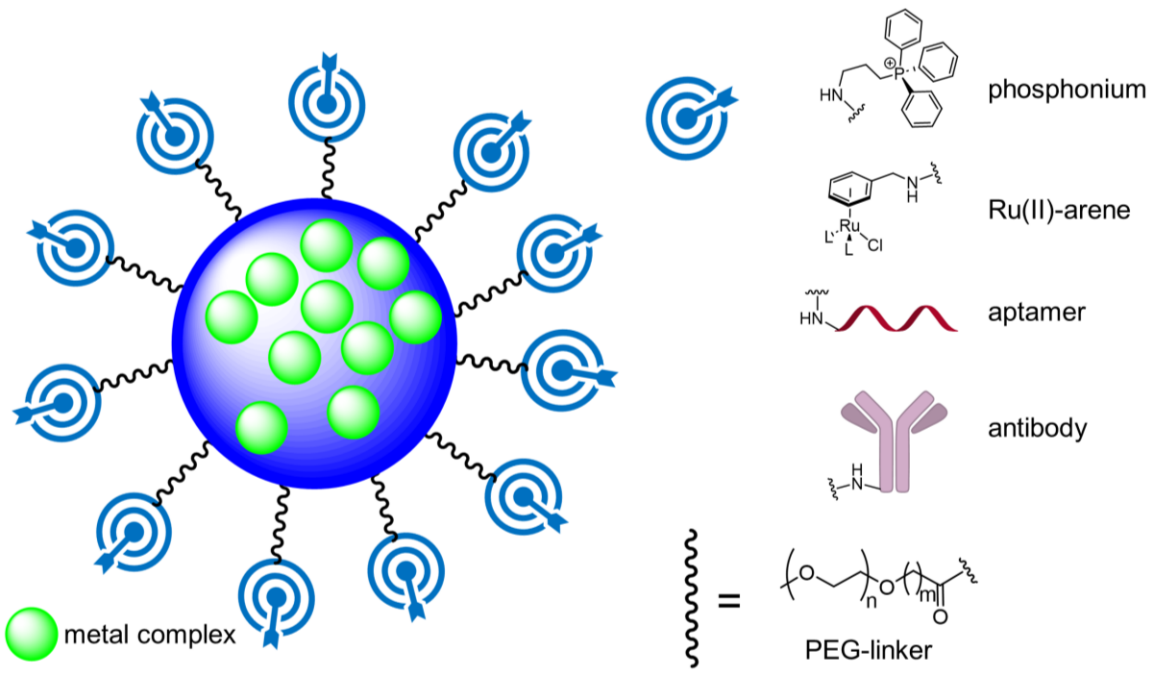

Figure 7.3 Potential modes of decoration for PLGA nanoparticles for the encapsulation of metal complexes.

Conveniently, since the polymers used in NP formulation are carboxylic acid terminated, a range of decoration possibilities using the chemistries explored in Chapter 2 could be used. Through HATU coupling chemistry, the nanoparticles can be decorated with anything from mitochondria-targeting phosphonium groups to ^{19}F MRI tags or even with Ru(II)-arene complexes to increase anticancer activity. Encapsulating metal-anticancer complexes in nanoparticles is in its infancy compared to non-metal drugs and presents as an exciting route to breathing new life into well studied complexes. Furthermore, the COVID-19 pandemic has led to a massive scale-up of lipid nanoparticle development which could be applied to metal-based anticancer complex formulations like the ones presented in Chapter 4.

7.3. Concluding Remarks

The work summarized in this thesis involved the exploration and development of metal-based anticancer complexes. Chapter 2 describes the coupling of a SERM to the RAPTA- and RAED-family of Ru(II)-arene complexes that induced novel biological activity. Chapter 3 presented CF_3-modified Keppler-type Ru(III) complexes and developed techniques for them to be used as ^{19}F MRI imaging agents. Chapter 4 looked

at the encapsulation of those same Ru(III) complexes in PLGA nanoparticles that proved to increase their cytotoxicity over 10-fold of that of the free complexes. Chapter 5 presented data to fill the gap in the general understanding of the behaviour of the Cu(II) anticancer complex CasIII-ia in aqueous media, in the presence of biologically relevant molecules such as HSA, and in cells. Finally, Chapter 6 presented a complex combining the efforts in Chapters 2 and 3 in the development of a novel dinuclear Ru(II)-Ru(III) complex that displayed increased activity of its parent components.

A major theme throughout this thesis involved the use of magnetic resonance spectroscopy. Whether it be NMR, MRI, or EPR, this thesis shows that approaching the field of metal-based therapeutics through the spectroscopist's lens can breath new life into compounds considered to be fully explored. Another major theme in this thesis was the use of robust chemistries to tackle common pitfalls of metal-based anticancer complexes. By presenting ways to increase activity of metal compounds through techniques, such as HATU coupling or polymer nanoparticle encapsulation, that can be used in any lab, the work herein presents accessible methods to introduce novel activities to well-studied metal complexes.

References

(1) Rosenberg, B.; Van Camp, L.; Krigas, T. Inhibition of Cell Division in Escherichia Coli by Electrolysis Products from a Platinum Electrode. *Nature* **1965**, *205* (4972), 698–699.

(2) Dasari, S.; Tchounwou, P. B. Cisplatin in Cancer Therapy: Molecular Mechanisms of Action. *Eur. J. Pharmacol.* **2014**, *740*, 364–378.

(3) Harder, H. C.; Rosenberg, B. Inhibitory Effects of Anti-Tumor Platinum Compounds on DNA, RNA and Protein Syntheses in Mammalian Cells *in vitro*. *Int. J. Cancer* **1970**, *6* (2), 207–216.

(4) Jamieson, E. R.; Lippard, S. J. Structure, Recognition, and Processing of Cisplatin−DNA Adducts. *Chem. Rev.* **1999**, *99* (9), 2467–2498.

(5) Wheate, N. J.; Walker, S.; Craig, G. E.; Oun, R. The Status of Platinum Anticancer Drugs in the Clinic and in Clinical Trials. *Dalt. Trans.* **2010**, *39* (35), 8113–8127.

(6) Oun, R.; Moussa, Y. E.; Wheate, N. J. The Side Effects of Platinum-Based Chemotherapy Drugs: A Review for Chemists. *Dalt. Trans.* **2018**, *47* (19), 6645–6653.

(7) Shen, D. W.; Pouliot, L. M.; Hall, M. D.; Gottesman, M. M. Cisplatin Resistance: A Cellular Self-Defense Mechanism Resulting from Multiple Epigenetic and Genetic Changes. *Pharmacol. Rev.* **2012**, *64* (3), 706–721.

(8) Galluzzi, L.; Senovilla, L.; Vitale, I.; Michels, J.; Martins, I.; Kepp, O.; Castedo, M.; Kroemer, G. Molecular Mechanisms of Cisplatin Resistance. *Oncogene* **2012**, *31* (15), 1869–1883.

(9) Chen, S. H.; Chang, J. Y. New Insights into Mechanisms of Cisplatin Resistance: From Tumor Cell to Microenvironment. *Int. J. Mol. Sci.* **2019**, *20* (17).

(10) Xiao, Y.; Lin, F. T.; Lin, W. C. ACTL6A Promotes Repair of Cisplatin-Induced DNA Damage, a New Mechanism of Platinum Resistance in Cancer. *Proc. Natl. Acad. Sci. U. S. A.* **2021**, *118* (3).

(11) Stordal, B.; Davey, M. Understanding Cisplatin Resistance Using Cellular Models. *IUBMB Life* **2007**, *59* (11), 696–699.

(12) Choi, C. H.; Cha, Y. J.; An, C. S.; Kim, K. J.; Kim, K. C.; Moon, S. P.; Lee, Z. H.; Min, Y. D. Molecular Mechanisms of Heptaplatin Effective against Cisplatin-Resistant Cancer Cell Lines: Less Involvement of Metallothfionein. *Cancer Cell Int.* **2004**, *4*, 1–12.

(13) Alberto, M. E.; Lucas, M. F. A.; Pavelka, M.; Russo, N. The Second-Generation Anticancer Drug Nedaplatin: A Theoretical Investigation on the Hydrolysis Mechanism. *J. Phys. Chem. B* **2009**, *113* (43), 14473–14479.

(14) Downing, K.; Jensen, B. P.; Grant, S.; Strother, M.; George, P. Quantification and Clinical Application of Carboplatin in Plasma Ultrafiltrate. *J. Pharm. Biomed. Anal.* **2017**, *138*, 373–377.

(15) Obreshkova, D.; Ivanova, S.; Yordanova-Laleva, P. Influence of Chemical Structure and Mechanism of Hydrolysis on Pharmacological Activity and Toxicological Profile of Approved Platinum Drugs. *Pharmacia* **2022**, *69* (3), 645–653.

(16) Graham, M. A.; Lockwood, G. F.; Greenslade, D.; Brienza, S.; Bayssas, M.; Gamelin, E. Clinical Pharmacokinetics of Oxaliplatin: A Critical Review. *Clin. Cancer Res.* **2000**, *6* (4), 1205–1218.

(17) McKeage, M. J. Lobaplatin: A New Antitumour Platinum Drug. *Expert Opin. Investig. Drugs* **2001**, *10* (1), 119–128.

(18) Shimada, M.; Itamochi, H.; Kigawa, J. Nedaplatin: A Cisplatin Derivative in Cancer Chemotherapy. *Cancer Manag. Res.* **2013**, *5* (1), 67–76.

(19) Cheung, Y. W.; Cradock, J. C.; Rao Vishnuvajjala, B.; Flora, K. P. Stability of Cisplatin, Iproplatin, Carboplatin, and Tetraplatin in Commonly Used Intravenous Solutions. *Am. J. Hosp. Pharm.* **1987**, *44* (1), 124–130.

(20) Johnstone, T. C.; Suntharalingam, K.; Lippard, S. J. The Next Generation of Platinum Drugs: Targeted Pt(II) Agents, Nanoparticle Delivery, and Pt(IV) Prodrugs. *Chem. Rev.* **2016**, *116* (5), 3436–3486.

(21) Pötsch, I.; Baier, D.; Keppler, B. K.; Berger, W. CHAPTER 12 Challenges and Chances in the Preclinical to Clinical Translation of Anticancer Metallodrugs. In *Metal-based Anticancer Agents*; The Royal Society of Chemistry, 2019; pp 308–347.

(22) Moreno-Alcántar, G.; Picchetti, P.; Casini, A. Gold Complexes in Anticancer Therapy: From New Design Principles to Particle-Based Delivery Systems. *Angew. Chemie - Int. Ed.* **2023**, *202218000*.

(23) Yeo, C. I.; Ooi, K. K.; Tiekink, E. R. T. Gold-Based Medicine: A Paradigm Shift in Anti-Cancer Therapy? *Molecules* **2018**, *23* (6), 14–23.

(24) Chitambar, C. R. Gallium-Containing Anticancer Compounds. *Future Med. Chem.* **2012**, *4* (10), 1257–1272.

(25) Santini, C.; Pellei, M.; Gandin, V.; Porchia, M.; Tisato, F.; Marzano, C. Advances in Copper Complexes as Anticancer Agents. *Chem. Rev.* **2014**, *114* (1), 815–862.

(26) Hussain, A.; AlAjmi, M. F.; Rehman, M. T.; Amir, S.; Husain, F. M.; Alsalme, A.; Siddiqui, M. A.; AlKhedhairy, A. A.; Khan, R. A. Copper(II) Complexes as Potential Anticancer and Nonsteroidal Anti-Inflammatory Agents: *In vitro* and in Vivo Studies. *Sci. Rep.* **2019**, *9* (1), 1–17.

(27) Marzano, C.; Pellei, M.; Tisato, F.; Santini, C. Copper Complexes as Anticancer Agents. *Anticancer. Agents Med. Chem.* **2009**, *9* (2), 185–211.

(28) Wang, Z. Y. Arsenic Compounds as Anticancer Agents. *Cancer Chemother. Pharmacol.* **2001**, *48* (SUPPL. 1), 72–76.

(29) Khairul, I.; Wang, Q. Q.; Jiang, Y. H.; Wang, C.; Naranmandura, H. Metabolism, Toxicity and Anticancer Activities of Arsenic Compounds. *Oncotarget* **2017**, *8* (14), 23905–23926.

(30) Swindell, E. P.; Hankins, P. L.; Chen, H.; Miodragović, C. D. S. U.; O'Halloran, T. V. Anticancer Activity of Small-Molecule and Nanoparticulate Arsenic(III) Complexes. *Inorg. Chem.* **2013**, *52* (21), 12292–12304.

(31) Hoonjan, M.; Jadhav, V.; Bhatt, P. Arsenic Trioxide: Insights into Its Evolution to an Anticancer Agent. *J. Biol. Inorg. Chem.* **2018**, *23* (3), 313–329.

(32) Ellahioui, Y.; Prashar, S.; Gómez-Ruiz, S. Anticancer Applications and Recent Investigations of Metallodrugs Based on Gallium, Tin and Titanium. *Inorganics* **2017**, *5* (1).

(33) Cini, M.; Bradshaw, T. D.; Woodward, S. Using Titanium Complexes to Defeat Cancer: The View from the Shoulders of Titans. *Chem. Soc. Rev.* **2017**, *46* (4), 1040–1051.

(34) Tshuva, E. Y.; Miller, M. Metallo-Drugs: Development and Action of Anticancer Agents; Sigel, A., Sigel, H., Freisinger, E., Sigel, R. K. O., Eds.; De Gruyter; pp 219–250.

(35) Konkankit, C. C.; Marker, S. C.; Knopf, K. M.; Wilson, J. J. Anticancer Activity of Complexes of the Third Row Transition Metals, Rhenium, Osmium, and Iridium. *Dalt. Trans.* **2018**, *47* (30).

(36) Knopf, K. M.; Murphy, B. L.; Macmillan, S. N.; Baskin, J. M.; Barr, M. P.; Boros, E.; Wilson, J. J. *In vitro* Anticancer Activity and in Vivo Biodistribution of Rhenium(I) Tricarbonyl Aqua Complexes. *J. Am. Chem. Soc.* **2017**, *139* (40), 14302–14314.

(37) Collery, P.; Desmaele, D.; Vijaykumar, V. Design of Rhenium Compounds in Targeted Anticancer Therapeutics. *Current Pharmaceutical Design*. 2019, pp 3306–3322.

(38) Marker, S. C.; King, A. P.; Granja, S.; Vaughn, B.; Woods, J. J.; Boros, E.; Wilson, J. J. Exploring the in Vivo and *in vitro* Anticancer Activity of Rhenium Isonitrile Complexes. *Inorg. Chem.* **2020**, *59* (14), 10285–10303.

(39) Leonidova, A.; Gasser, G. Underestimated Potential of Organometallic Rhenium Complexes as Anticancer Agents. *ACS Chem. Biol.* **2014**, *9* (10), 2180–2193.

(40) Meier-Menches, S. M.; Gerner, C.; Berger, W.; Hartinger, C. G.; Keppler, B. K. Structure-Activity Relationships for Ruthenium and Osmium Anticancer Agents-towards Clinical Development. *Chem. Soc. Rev.* **2018**, *47* (3), 909–928.

(41) Bruijnincx, P. C. A.; Sadler, P. J. Controlling Platinum, Ruthenium, and Osmium Reactivity for Anticancer Drug Design. *Adv. Inorg. Chem.* **2009**, *61* (09), 1–62.

(42) Hanif, M.; Babak, M. V.; Hartinger, C. G. Development of Anticancer Agents: Wizardry with Osmium. *Drug Discov. Today* **2014**, *19* (10), 1640–1648.

(43) Zhang, P.; Huang, H. Future Potential of Osmium Complexes as Anticancer Drug Candidates, Photosensitizers and Organelle-Targeted Probes. *Dalt. Trans.* **2018**, *47* (42), 14841–14854.

(44) Cao, J. J.; Zheng, Y.; Wu, X. W.; Tan, C. P.; Chen, M. H.; Wu, N.; Ji, L. N.; Mao, Z. W. Anticancer Cyclometalated Iridium(III) Complexes with Planar Ligands: Mitochondrial DNA Damage and Metabolism Disturbance. *J. Med. Chem.* **2019**, *62* (7), 3311–3322.

(45) Ma, D.; Wu, C.; Wu, K.; Leung, C. Iridium (III) Complexes Targeting Apoptotic Cell. *Molecules* **2019**, *24* (Iii), 2739.

(46) Sharma S, A.; P, S.; Roy, N.; Paira, P. Advances in Novel Iridium (III) Based Complexes for Anticancer Applications: A Review. *Inorganica Chim. Acta* **2020**, *513* (June), 119925.

(47) Liu, Z.; Habtemariam, A.; Pizarro, A. M.; Fletcher, S. A.; Kisova, A.; Vrana, O.; Salassa, L.; Bruijnincx, P. C. A.; Clarkson, G. J.; Brabec, V.; Sadler, P. J. Organometallic Half-Sandwich Iridium Anticancer Complexes. *J. Med. Chem.* **2011**, *54* (8), 3011–3026.

(48) Hearn, J. M.; Hughes, G. M.; Romero-Canelón, I.; Munro, A. F.; Rubio-Ruiz, B.; Liu, Z.; Carragher, N. O.; Sadler, P. J. Pharmaco-Genomic Investigations of Organo-Iridium Anticancer Complexes Reveal Novel Mechanism of Action. *Metallomics* **2018**, *10* (1), 93–107.

(49) Trondl, R.; Heffeter, P.; Kowol, C. R.; Jakupec, M. A.; Berger, W.; Keppler, B. K. NKP-1339, the First Ruthenium-Based Anticancer Drug on the Edge to Clinical Application. *Chem. Sci.* **2014**, *5* (8), 2925–2932.

(50) Bergamo, A.; Sava, G. Ruthenium Anticancer Compounds: Myths and Realities of the Emerging Metal-Based Drugs. *Dalt. Trans.* **2011**, *40* (31), 7817–7823.

(51) Lin, K.; Zhao, Z. Z.; Bo, H. Ben; Hao, X. J.; Wang, J. Q. Applications of Ruthenium Complex in Tumor Diagnosis and Therapy. *Front. Pharmacol.* **2018**, *9* (NOV), 1–10.

(52) Lee, S. Y.; Kim, C. Y.; Nam, T. G. Ruthenium Complexes as Anticancer Agents: A Brief History and Perspectives. *Drug Des. Devel. Ther.* **2020**, *14*, 5375–5392.

(53) Reedijk, B. J. Metal-Ligand Exchange Kinetics in Platinum and Ruthenium Complexes. *Platin. Met. Rev.* **2008**, *52* (1), 2–11.

(54) Taube, H. Rates and Mechanisms of Substitution in Inorganic Complexes in Solution. *Chem. Rev.* **1952**, *50* (1), 69–126.

(55) Helm, L.; Merbach, A. E. Water Exchange on Metal Ions: Experiments and Simulations. *Coord. Chem. Rev.* **1999**, *187* (Copyright (C) 2017 American Chemical Society (ACS). All Rights Reserved.), 151–181.

(56) Jones, M. R.; Duncan, D.; Storr, T. Introduction to Ligand Design in Medicinal Inorganic Chemistry. *Ligand Des. Med. Inorg. Chem.* **2014**, *9781118488*, 1–8.

(57) Mu, C.; Walsby, C. J. Ruthenium Anticancer Compounds with Biologically-Derived Ligands. In *Ligand Design in Medicinal Inorganic Chemistry*; Storr, T., Ed.; John Wiley & Sons, Ltd., 2014; pp 405–437.

(58) Dabrowiak, J. C. Responsive Metal Complexes. *Met. Med.* **2017**, 217–244.

(59) Boros, E.; Dyson, P. J.; Gasser, G. Classification of Metal-Based Drugs According to Their Mechanisms of Action. *Chem* **2020**, *6* (1), 41–60.

(60) Dwyer, F. P.; Gyarfas, E. C.; Rogers, W. P.; Koch, J. H. Biological Activity of Complex Ions. *Nature* **1952**, *170* (4318), 190–191.

(61) Tsuruo, T.; Iida, H.; Tsukagoshi, S.; Sakurai, Y. Growth Inhibition of Lewis Lung Carcinoma by an Inorganic Dye, Ruthenium Red. **1980**, *71* (1), 151–154.

(62) Anghileri, L. J. The in Vivo Inhibition of Tumor Growth by Ruthenium Red: Its Relationship with the Metabolism of Calcium in the Tumor. *Zeitschrift f*[illegible]*r Krebsforsch. und Klin. Onkol.* **1975**, *83* (3), 213–217.

(63) Clarke, M. J. Ruthenium Metallopharmaceuticals. *Coord. Chem. Rev.* **2002**, *232* (1–2), 69–93.

(64) Clarke, M. J. The Potential of Ruthenium in Anticancer Pharmaceuticals. In *Inorganic Chemistry in Biology and Medicine*; ACS Symposium Series; AMERICAN CHEMICAL SOCIETY, 1980; Vol. 140, pp 157–180.

(65) Mestroni, G.; Alessio, E.; Sava, G.; Pacor, S.; Coluccia, M.; Boccarelli, A. Water-Soluble Ruthenium(III)-Dimethyl Sulfoxide Complexes: Chemical Behaviour and Pharmaceutical Properties. *Met. Based. Drugs* **1994**, *1* (1), 41–63.

(66) Alessio, E.; Mestroni, G.; Nardin, G.; Attia, W. M.; Calligaris, M.; Sava, G.; Zorzet, S. Cis- and Trans-Dihalotetrakis(Dimethyl Sulfoxide)Ruthenium(II) Complexes (RuX2(DMSO)4; X = Cl, Br): Synthesis, Structure, and Antitumor Activity. *Inorg. Chem.* **1988**, *27* (23), 4099–4106.

(67) Keppler, B. K.; Rupp, W. Antitumor Activity of Imidazolium-Bisimidazole-Tetrachlororuthenate (III). *J. Cancer Res. Clin. Oncol.* **1986**, *111* (2), 166–168.

(68) Keppler, B. K.; Rupp, W.; Juhl, U. M.; Endres, H.; Niebl, R.; Balzer, W. Synthesis, Molecular Structure, and Tumor-Inhibiting Properties of Imidazolium Trans-Bis(Imidazole)Tetrachlororuthenate(III) and Its Methyl-Substituted Derivatives. *Inorg. Chem.* **1987**, *26* (26), 4366–4370.

(69) Keppler, B. K.; Henn, M.; Juhl, U. M.; Berger, M. R.; Niebl, R.; Wagner, F. E. New Ruthenium Complexes for the Treatment of Cancer BT - Ruthenium and Other Non-Platinum Metal Complexes in Cancer Chemotherapy; Baulieu, E., Forman, D. T., Ingelman-Sundberg, M., Jaenicke, L., Kellen, J. A., Nagai, Y., Springer, G. F., Träger, L., Will-Shahab, L., Wittliff, J. L., Eds.; Springer Berlin Heidelberg: Berlin, Heidelberg, 1989; pp 41–69.

(70) Seelig, M. H.; Berger, M. R.; Keppler, B. K. *Antineoplastic Activity of Three Ruthenium Derivatives against Chemically Induced Colorectal Carcinoma in Rats*; 1992; Vol. 118.

(71) Kapitza, S.; Pongratz, M.; Jakupec, M. A.; Heffeter, P.; Berger, W.; Lackinger, L.; Keppler, B. K.; Marian, B. Heterocyclic Complexes of Ruthenium(III) Induce Apoptosis in Colorectal Carcinoma Cells. *J. Cancer Res. Clin. Oncol.* **2005**, *131* (2), 101–110.

(72) Kersten, L.; Bräunlich, H.; Keppler, B. K.; Gliesing, C.; Wendelin, M.; Westphal, J. Comparative Nephrotoxicity of Some Antitumour-Active Platinum and Ruthenium Complexes in Rats. *J. Appl. Toxicol.* **1998**, *18* (2), 93–101.

(73) Cetinbas, N.; Webb, M. I.; Dubland, J. A.; Walsby, C. J. Serum-Protein Interactions with Anticancer Ru(III) Complexes KP1019 and KP418 Characterized by EPR. *JBIC J. Biol. Inorg. Chem.* **2010**, *15* (2), 131–145.

(74) Henke, M. M.; Richly, H.; Drescher, A.; Grubert, M.; Alex, D.; Thyssen, D.; Jaehde, U.; Scheulen, M. E.; Hilger, R. A. Pharmacokinetic Study of Sodium Trans[Tetrachlorobis(1H-Indazole)-Ruthenate (III)]/-Indazole Hydrochloride (1:1.1) (FFC14A) in Patients with Solid Tumors. *Int. J. Clin. Pharmacol. Ther.* **2009**, *47* (01), 58–60.

(75) Trondl, R.; Heffeter, P.; Kowol, C. R.; Jakupec, M. A.; Berger, W.; Keppler, B. K. NKP-1339, the First Ruthenium-Based Anticancer Drug on the Edge to Clinical Application. *Chem. Sci.* **2014**, *5* (8), 2925–2932.

(76) Burris, H. A.; Bakewell, S.; Bendell, J. C.; Infante, J.; Jones, S. F.; Spigel, D. R.; Weiss, G. J.; Ramanathan, R. K.; Ogden, A.; Von Hoff, D. Safety and Activity of IT-139, a Ruthenium-Based Compound, in Patients with Advanced Solid Tumours: A First-in-Human, Open-Label, Dose-Escalation Phase I Study with Expansion Cohort. *ESMO Open* **2016**, *1* (6).

(77) Fuereder, T.; Berger, W. Metal Drugs Become Targeted. *ESMO Open* **2017**, *2* (3).

(78) Bold Therapeutics - Technology https://www.bold-therapeutics.com/technology (accessed 2023 -04 -10).

(79) Sava, G.; Pacor, S.; Mestroni, G.; Alessio, E. Na[Trans-RuCl4(DMSO)Im], a Metal Complex of Ruthenium with Antimetastatic Properties. *Clin. Exp. Metastasis* **1992**, *10* (4), 273–280.

(80) Leijen, S.; Burgers, S. A.; Baas, P.; Pluim, D.; Tibben, M.; van Werkhoven, E.; Alessio, E.; Sava, G.; Beijnen, J. H.; Schellens, J. H. M. Phase I/II Study with Ruthenium Compound NAMI-A and Gemcitabine in Patients with Non-Small Cell Lung Cancer after First Line Therapy. *Invest. New Drugs* **2015**, *33* (1), 201–214.

(81) Bakewell, S.; Conde, I.; Fallah, Y.; McCoy, M.; Jin, L.; Shajahan-Haq, A. N. Inhibition of DNA Repair Pathways and Induction of ROS Are Potential Mechanisms of Action of the Small Molecule Inhibitor Bold-100 in Breast Cancer. *Cancers (Basel).* **2020**, *12* (9), 1–19.

(82) Küng, A.; Pieper, T.; Wissiack, R.; Rosenberg, E.; Keppler, B. K. Hydrolysis of the Tumor-Inhibiting Ruthenium(III) Complexes HIm Trans-[RuCl4(Im)2] and HInd Trans-[RuCl4(Ind)2] Investigated by Means of HPCE and HPLC-MS. *JBIC J. Biol. Inorg. Chem.* **2001**, *6* (3), 292–299.

(83) Kratz, F.; Hartmann, M.; Keppler, B.; Messori, L. The Binding Properties of Two Antitumor Ruthenium(III) Complexes to Apotransferrin. *J. Biol. Chem.* **1994**, *269* (4), 2581–2588.

(84) Bouma, M.; Nuijen, B.; Jansen, M. T.; Sava, G.; Flaibani, A.; Bult, A.; Beijnen, J. H. A Kinetic Study of the Chemical Stability of the Antimetastatic Ruthenium Complex NAMI-A. *Int. J. Pharm.* **2002**, *248* (1), 239–246.

(85) Bacac, M.; Hotze, A. C. G.; Schilden, K. van der; Haasnoot, J. G.; Pacor, S.; Alessio, E.; Sava, G.; Reedijk, J. The Hydrolysis of the Anti-Cancer Ruthenium Complex NAMI-A Affects Its DNA Binding and Antimetastatic Activity: An NMR Evaluation. *J. Inorg. Biochem.* **2004**, *98* (2), 402–412.

(86) Küng, A.; Pieper, T.; Wissiack, R.; Rosenberg, E.; Keppler, B. K. Hydrolysis of the Tumor-Inhibiting Ruthenium(III) Complexes HIm Trans-[RuCl4(Im)2] and HInd Trans-[RuCl4(Ind)2] Investigated by Means of HPCE and HPLC-MS. *JBIC J. Biol. Inorg. Chem.* **2001**, *6* (3), 292–299.

(87) Malina, J.; Novakova, O.; Keppler, B. K.; Alessio, E.; Brabec, V. Biophysical Analysis of Natural, Double-Helical DNA Modified by Anticancer Heterocyclic Complexes of Ruthenium(III) in Cell-Free Media. *JBIC J. Biol. Inorg. Chem.* **2001**, *6* (4), 435–445.

(88) Groessl, M.; Tsybin, Y. O.; Hartinger, C. G.; Keppler, B. K.; Dyson, P. J. Ruthenium versus Platinum: Interactions of Anticancer Metallodrugs with Duplex Oligonucleotides Characterised by Electrospray Ionisation Mass Spectrometry. *JBIC J. Biol. Inorg. Chem.* **2010**, *15* (5), 677–688.

(89) Webb, M. I.; Walsby, C. J. Control of Ligand-Exchange Processes and the Oxidation State of the Antimetastatic Ru(Iii) Complex NAMI-A by Interactions with Human Serum Albumin. *Dalt. Trans.* **2011**, *40* (6), 1322–1331.

(90) Cetinbas, N.; Webb, M. I.; Dubland, J. A.; Walsby, C. J. Serum-Protein Interactions with Anticancer Ru(III) Complexes KP1019 and KP418 Characterized by EPR. *JBIC J. Biol. Inorg. Chem.* **2010**, *15* (2), 131–145.

(91) Levina, A.; Aitken, J. B.; Gwee, Y. Y.; Lim, Z. J.; Liu, M.; Singharay, A. M.; Wong, P. F.; Lay, P. A. Biotransformations of Anticancer Ruthenium(III) Complexes: An X-Ray Absorption Spectroscopic Study. *Chem. – A Eur. J.* **2013**, *19* (11), 3609–3619.

(92) Webb, M. I.; Walsby, C. J. Albumin Binding and Ligand-Exchange Processes of the Ru(Iii) Anticancer Agent NAMI-A and Its Bis-DMSO Analogue Determined by ENDOR Spectroscopy. *Dalt. Trans.* **2015**, *44* (40), 17482–17493.

(93) Gransbury, G. K.; Kappen, P.; Glover, C. J.; Hughes, J. N.; Levina, A.; Lay, P. A.; Musgrave, I. F.; Harris, H. H. Comparison of KP1019 and NAMI-A in Tumour-Mimetic Environments†. *Metallomics* **2016**, *8* (8), 762–773.

(94) Bijelic, A.; Theiner, S.; Keppler, B. K.; Rompel, A. X-Ray Structure Analysis of Indazolium Trans-[Tetrachlorobis(1H-Indazole)Ruthenate(III)] (KP1019) Bound to Human Serum Albumin Reveals Two Ruthenium Binding Sites and Provides Insights into the Drug Binding Mechanism. *J. Med. Chem.* **2016**, *59* (12), 5894–5903.

(95) Messori, L.; Merlino, A. Ruthenium Metalation of Proteins: The X-Ray Structure of the Complex Formed between NAMI-A and Hen Egg White Lysozyme. *Dalt. Trans.* **2014**, *43* (16), 6128–6131.

(96) Chiniadis, L.; Giastas, P.; Bratsos, I.; Papakyriakou, A. Insights into the Protein Ruthenation Mechanism by Antimetastatic Metallodrugs: High-Resolution X-Ray Structures of the Adduct Formed between Hen Egg-White Lysozyme and NAMI-A at Various Time Points. *Inorg. Chem.* **2021**.

(97) Casini, A.; Temperini, C.; Gabbiani, C.; Supuran, C. T.; Messori, L. The X-Ray Structure of the Adduct between NAMI-A and Carbonic Anhydrase Provides Insights into the Reactivity of This Metallodrug with Proteins. *ChemMedChem* **2010**, *5* (12), 1989–1994.

(98) Liu, M.; Lim, Z. J.; Gwee, Y. Y.; Levina, A.; Lay, P. A. Characterization of a Ruthenium(III)/NAMI-A Adduct with Bovine Serum Albumin That Exhibits a High Anti-Metastatic Activity. *Angew. Chemie Int. Ed.* **2010**, *49* (9), 1661–1664.

(99) Novohradský, V.; Bergamo, A.; Cocchietto, M.; Zajac, J.; Brabec, V.; Mestroni, G.; Sava, G. Influence of the Binding of Reduced NAMI-A to Human Serum Albumin on the Pharmacokinetics and Biological Activity. *Dalt. Trans.* **2015**, *44* (4), 1905–1913.

(100) Alessio, E.; Messori, L. NAMI-A and KP1019/1339, Two Iconic Ruthenium Anticancer Drug Candidates Face-to-Face: A Case Story in Medicinal Inorganic Chemistry. *Molecules* **2019**, *24* (10), 1995.

(101) Schluga, P.; Hartinger, C. G.; Egger, A.; Reisner, E.; Galanski, M.; Jakupec, M. A.; Keppler, B. K. Redox Behavior of Tumor-Inhibiting Ruthenium(Iii) Complexes and Effects of Physiological Reductants on Their Binding to GMP. *Dalt. Trans.* **2006**, No. 14, 1796–1802.

(102) Bergamo, A.; Masi, A.; Peacock, A. F. A.; Habtemariam, A.; Sadler, P. J.; Sava, G. In Vivo Tumour and Metastasis Reduction and *in vitro* Effects on Invasion Assays of the Ruthenium RM175 and Osmium AFAP51 Organometallics in the Mammary Cancer Model. *J. Inorg. Biochem.* **2010**, *104* (1), 79–86.

(103) Wang, F.; Habtemariam, A.; van der Geer, E. P. L.; Fernández, R.; Melchart, M.; Deeth, R. J.; Aird, R.; Guichard, S.; Fabbiani, F. P. A.; Lozano-Casal, P.; Oswald, I. D. H.; Jodrell, D. I.; Parsons, S.; Sadler, P. J. Controlling Ligand Substitution Reactions of Organometallic Complexes: Tuning Cancer Cell Cytotoxicity. *Proc. Natl. Acad. Sci. U. S. A.* **2005**, *102* (51), 18269 LP – 18274.

(104) Zeng, L.; Gupta, P.; Chen, Y.; Wang, E.; Ji, L.; Chao, H.; Chen, Z. S. The Development of Anticancer Ruthenium(II) Complexes: From Single Molecule Compounds to Nanomaterials. *Chemical Society Reviews*. 2017, pp 5771–5804.

(105) Allardyce, C. S.; Dyson, P. J.; Ellis, D. J.; Heath, S. L. [Ru(H6-p-Cymene)Cl2(Pta)] (Pta = 1,3,5-Triaza-7-Phosphatricyclo-[3.3.1.1]Decane): A Water Soluble Compound That Exhibits PH Dependent DNA Binding Providing Selectivity for Diseased Cells. *Chem. Commun.* **2001**, No. 15, 1396–1397.

(106) Allardyce, C. S.; Dyson, P. J.; Ellis, D. J.; Salter, P. A.; Scopelliti, R. Synthesis and Characterisation of Some Water Soluble Ruthenium(II)-Arene Complexes and an Investigation of Their Antibiotic and Antiviral Properties. *J. Organomet. Chem.* **2003**, *668* (Copyright (C) 2015 American Chemical Society (ACS). All Rights Reserved.), 35–42.

(107) Allardyce, C. S.; Dyson, P. J. Metal-Based Drugs That Break the Rules. *Dalt. Trans.* **2016**, *45* (8), 3201–3209.

(108) Bergamo, A.; Masi, A.; Dyson, P. J.; Sava, G. Modulation of the Metastatic Progression of Breast Cancer with an Organometallic Ruthenium Compound. *Int. J. Oncol.* **2008**, *33* (6), 1281–1289.

(109) Scolaro, C.; Bergamo, A.; Brescacin, L.; Delfino, R.; Cocchietto, M.; bor Laurenczy, G.; Geldbach, T. J.; Sava, G.; Dyson, P. J. *In vitro* and in Vivo Evaluation of Ruthenium(II)-Arene PTA Complexes. **2005**.

(110) Renfrew, A. K.; Phillips, A. D.; Egger, A. E.; Hartinger, C. G.; Bosquain, S. S.; Nazarov, A. A.; Keppler, B. K.; Gonsalvi, L.; Peruzzini, M.; Dyson, P. J. Influence of Structural Variation on the Anticancer Activity of RAPTA-Type Complexes: Ptn versus Pta. *Organometallics* **2009**, *28* (4), 1165–1172.

(111) Ang, W. H.; Daldini, E.; Scolaro, C.; Scopelliti, R.; Juillerat-Jeannerat, L.; Dyson, P. J. Development of Organometallic Ruthenium-Arene Anticancer Drugs That Resist Hydrolysis. *Inorg. Chem.* **2006**, *45* (22), 9006–9013.

(112) Scolaro, C.; Chaplin, A. B.; Hartinger, C. G.; Bergamo, A.; Cocchietto, M.; Keppler, B. K.; Sava, G.; Dyson, P. J. Tuning the Hydrophobicity of Ruthenium(Ii)–Arene (RAPTA) Drugs to Modify Uptake, Biomolecular Interactions and Efficacy. *Dalt. Trans.* **2007**, No. 43, 5065–5072.

(113) Scolaro, C.; Geldbach, T. J.; Rochat, S.; Dorcier, A.; Gossens, C.; Bergamo, A.; Cocchietto, M.; Tavernelli, I.; Sava, G.; Rothlisberger, U.; Dyson, P. J. Influence of Hydrogen-Bonding Substituents on the Cytotoxicity of RAPTA Compounds. *Organometallics* **2006**, *25* (3), 756–765.

(114) Mu, C.; Walsby, C. J. Ruthenium Anticancer Compounds with Biologically-Derived Ligands. *Ligand Design in Medicinal Inorganic Chemistry*. May 23, 2014, pp 405–437.

(115) Wolters, D. A.; Stefanopoulou, M.; Dyson, P. J.; Groessl, M. Combination of Metallomics and Proteomics to Study the Effects of the Metallodrug RAPTA-T on Human Cancer Cells. *Metallomics* **2012**, *4* (11), 1185–1196.

(116) Casini, A.; Gabbiani, C.; Sorrentino, F.; Rigobello, M. P.; Bindoli, A.; Geldbach, T. J.; Marrone, A.; Re, N.; Hartinger, C. G.; Dyson, P. J.; Messori, L. Emerging Protein Targets for Anticancer Metallodrugs: Inhibition of Thioredoxin Reductase and Cathepsin B by Antitumor Ruthenium(II)−Arene Compounds. *J. Med. Chem.* **2008**, *51* (21), 6773–6781.

(117) Meggers, E.; Atilla-Gokcumen, G. E.; Bregman, H.; Maksimoska, J.; Mulcahy, S. P.; Pagano, N.; Williams, D. S. Exploring Chemical Space with Organometallics: Ruthenium Complexes as Protein Kinase Inhibitors. *Synlett* **2007**, *2007* (08), 1177–1189.

(118) Zhang, L.; Carroll, P.; Meggers, E. Ruthenium Complexes as Protein Kinase Inhibitors. *Org. Lett.* **2004**, *6* (4), 521–523.

(119) Meggers, E. Exploring Biologically Relevant Chemical Space with Metal Complexes. *Current Opinion in Chemical Biology*. Elsevier Current Trends June 1, 2007, pp 287–292.

(120) Morris, R. E.; Aird, R. E.; Murdoch, P. del S.; Chen, H.; Cummings, J.; Hughes, N. D.; Parsons, S.; Parkin, A.; Boyd, G.; Jodrell, D. I.; Sadler, P. J. Inhibition of Cancer Cell Growth by Ruthenium(II) Arene Complexes. *J. Med. Chem.* **2001**, *44* (22), 3616–3621.

(121) Chen, H.; Parkinson, J. A.; Parsons, S.; Coxall, R. A.; Gould, R. O.; Sadler, P. J. Organometallic Ruthenium(II) Diamine Anticancer Complexes: Arene-Nucleobase Stacking and Stereospecific Hydrogen-Bonding in Guanine Adducts. *J. Am. Chem. Soc.* **2002**, *124* (Copyright (C) 2015 American Chemical Society (ACS). All Rights Reserved.), 3064–3082.

(122) Adhireksan, Z.; Davey, G. E.; Campomanes, P.; Groessl, M.; Clavel, C. M.; Yu, H.; Nazarov, A. A.; Yeo, C. H. F.; Ang, W. H.; Dröge, P.; Rothlisberger, U.; Dyson, P. J.; Davey, C. A. Ligand Substitutions between Ruthenium–Cymene Compounds Can Control Protein versus DNA Targeting and Anticancer Activity. *Nat. Commun.* **2014**, *5* (1), 3462.

(123) Smith, G. S.; Therrien, B. Targeted and Multifunctional Arene Ruthenium Chemotherapeutics. *Dalt. Trans.* **2011**, *40* (41), 10793–10800.

(124) Pettinari, R.; Marchetti, F.; Condello, F.; Pettinari, C.; Lupidi, G.; Scopelliti, R.; Mukhopadhyay, S.; Riedel, T.; Dyson, P. J. Ruthenium(II)–Arene RAPTA Type Complexes Containing Curcumin and Bisdemethoxycurcumin Display Potent and Selective Anticancer Activity. *Organometallics* **2014**, *33* (14), 3709–3715.

(125) Bar-Sela, G.; Schaffer, R. E. and M. Curcumin as an Anti-Cancer Agent: Review of the Gap Between Basic and Clinical Applications. *Current Medicinal Chemistry*. 2010, pp 190–197.

(126) Biersack, B.; Zoldakova, M.; Effenberger, K.; Schobert, R. (Arene)Ru(II) Complexes of Epidermal Growth Factor Receptor Inhibiting Tyrphostins with Enhanced Selectivity and Cytotoxicity in Cancer Cells. *Eur. J. Med. Chem.* **2010**, *45* (5), 1972–1975.

(127) Ang, W. H.; Parker, L. J.; De Luca, A.; Juillerat-Jeanneret, L.; Morton, C. J.; Lo Bello, M.; Parker, M. W.; Dyson, P. J. Rational Design of an Organometallic Glutathione Transferase Inhibitor. *Angew. Chemie Int. Ed.* **2009**, *48* (21), 3854–3857.

(128) Miyanishi, K.; Takayama, T.; Ohi, M.; Hayashi, T.; Nobuoka, A.; Nakajima, T.; Takimoto, R.; Kogawa, K.; Kato, J.; Sakamaki, S.; Niitsu, Y. Glutathione S-Transferase-π Overexpression Is Closely Associated with K-Ras Mutation during Human Colon Carcinogenesis. *Gastroenterology* **2001**, *121* (4), 865–874.

(129) Păunescu, E.; Soudani, M.; Martin, P.; Scopelliti, R.; Lo Bello, M.; Dyson, P. J. Organometallic Glutathione S-Transferase Inhibitors. *Organometallics* **2017**, *36* (17), 3312–3321.

(130) Sau, A.; Pellizzari Tregno, F.; Valentino, F.; Federici, G.; Caccuri, A. M. Glutathione Transferases and Development of New Principles to Overcome Drug Resistance. *Arch. Biochem. Biophys.* **2010**, *500* (2), 116–122.

(131) Perez, R. P.; Hamilton, T. C.; Ozols, R. F.; Young, R. C. Mechanisms and Modulation of Resistance to Chemotherapy in Ovarian Cancer. *Cancer* **1993**, *71* (4 S), 1571–1580.

(132) Townsend, D. M.; Tew, K. D. The Role of Glutathione-S-Transferase in Anti-Cancer Drug Resistance. *Oncogene* **2003**, *22* (47), 7369–7375.

(133) Wee, H. A.; Khalaila, I.; Allardyce, C. S.; Juillerat-Jeanneret, L.; Dyson, P. J. Rational Design of Platinum(IV) Compounds to Overcome Glutathione-S-Transferase Mediated Drug Resistance. *J. Am. Chem. Soc.* **2005**, *127* (5), 1382–1383.

(134) Parker, L. J.; Dyson, P. J.; Bello, M. Lo; Parker, M. W. Platinum- and Ruthenium-Based Anticancer Compounds, Inhibition of Glutathione Transferase P1-1 BT - Encyclopedia of Metalloproteins; Kretsinger, R. H., Uversky, V. N., Permyakov, E. A., Eds.; Springer New York: New York, NY, 2013; pp 1704–1710.

(135) Peklak-Scott, C.; Smitherman, P. K.; Townsend, A. J.; Morrow, C. S. Role of Glutathione S -Transferase P1-1 in the Cellular Detoxification of Cisplatin. *Mol. Cancer Ther.* **2008**, *7* (10), 3247–3255.

(136) Wee, H. A.; Daldini, E.; Juillerat-Jeanneret, L.; Dyson, P. J. Strategy to Tether Organometallic Ruthenium-Arene Anticancer Compounds to Recombinant Human Serum Albumin. *Inorg. Chem.* **2007**, *46* (22), 9048–9050.

(137) Nazarov, A. A.; Meier, S. M.; Zava, O.; Nosova, Y. N.; Milaeva, E. R.; Hartinger, C. G.; Dyson, P. J. Protein Ruthenation and DNA Alkylation: Chlorambucil-Functionalized RAPTA Complexes and Their Anticancer Activity. *Dalt. Trans.* **2015**, *44* (Copyright (C) 2017 American Chemical Society (ACS). All Rights Reserved.), 3614–3623.

(138) Shi, S.; Zhao, J.; Geng, X.; Yao, T.; Huang, H.; Liu, T.; Zheng, L.; Li, Z.; Yang, D.; Ji, L. Molecular “Light Switch” for G-Quadruplexes and i-Motif of Human Telomeric DNA: [Ru(Phen)2(Dppz)]2+. *Dalt. Trans.* **2010**, *39* (10), 2490–2493.

(139) Shi, S.; Geng, X.; Zhao, J.; Yao, T.; Wang, C.; Yang, D.; Zheng, L.; Ji, L. Interaction of [Ru(Bpy)2(Dppz)]2+ with Human Telomeric DNA: Preferential Binding to G-Quadruplexes over i-Motif. *Biochimie* **2010**, *92* (4), 370–377.

(140) Tan, C.; Wu, S.; Lai, S.; Wang, M.; Chen, Y.; Zhou, L.; Zhu, Y.; Lian, W.; Peng, W.; Ji, L.; Xu, A. Synthesis, Structures, Cellular Uptake and Apoptosis-Inducing Properties of Highly Cytotoxic Ruthenium-Norharman Complexes. *Dalt. Trans.* **2011**, *40* (34), 8611–8621.

(141) Song, H.; Kaiser, J. T.; Barton, J. K. Crystal Structure of Δ-[Ru(Bpy)2dppz]2+ Bound to Mismatched DNA Reveals Side-by-Side Metalloinsertion and Intercalation. *Nat. Chem.* **2012**, *4* (8), 615–620.

(142) Zhao, F.; Wang, W.; Wu, W. A Novel Ruthenium Polypyridyl Complex for the Selective Imaging and Photodynamic Targeting of the Golgi Apparatus. *Dalt. Trans.* **2021**, *50* (10), 3536–3541.

(143) Griffith, C.; Dayoub, A. S.; Jaranatne, T.; Alatrash, N.; Mohamedi, A.; Abayan, K.; Breitbach, Z. S.; Armstrong, D. W.; Macdonnell, F. M. Cellular and Cell-Free Studies of Catalytic DNA Cleavage by Ruthenium Polypyridyl Complexes Containing Redox-Active Intercalating Ligands. *Chem. Sci.* **2017**, *8* (5), 3726–3740.

(144) Puckett, C. A.; Barton, J. K. Mechanism of Cellular Uptake of a Ruthenium Polypyridyl Complex. *Biochemistry* **2008**, *47* (45), 11711–11716.

(145) Komor, A. C.; Barton, J. K. The Path for Metal Complexes to a DNA Target. *Chem. Commun.* **2013**, *49* (35), 3617–3630.

(146) Gill, M. R.; Cecchin, D.; Walker, M. G.; Mulla, R. S.; Battaglia, G.; Smythe, C.; Thomas, J. A. Targeting the Endoplasmic Reticulum with a Membrane-Interactive Luminescent Ruthenium(Ii) Polypyridyl Complex. *Chem. Sci.* **2013**, *4* (12), 4512–4519.

(147) Deng, Z.; Gao, P.; Yu, L.; Ma, B.; You, Y.; Chan, L.; Mei, C.; Chen, T. Ruthenium Complexes with Phenylterpyridine Derivatives Target Cell Membrane and Trigger Death Receptors-Mediated Apoptosis in Cancer Cells. *Biomaterials* **2017**, *129*, 111–126.

(148) Monro, S.; Colón, K. L.; Yin, H.; Roque, J.; Konda, P.; Gujar, S.; Thummel, R. P.; Lilge, L.; Cameron, C. G.; McFarland, S. A. Transition Metal Complexes and Photodynamic Therapy from a Tumor-Centered Approach: Challenges, Opportunities, and Highlights from the Development of TLD1433. *Chem. Rev.* **2019**, *119* (2), 797–828.

(149) Djukic, J.-P.; Sortais, J.-B.; Barloy, L.; Pfeffer, M. Cycloruthenated Compounds – Synthesis and Applications. *Eur. J. Inorg. Chem.* **2009**, *2009* (7), 817–853.

(150) Gaiddon, C.; Jeannequin, P.; Bischoff, P.; Pfeffer, M.; Sirlin, C.; Loeffler, J. P. Ruthenium (II)-Derived Organometallic Compounds Induce Cytostatic and Cytotoxic Effects on Mammalian Cancer Cell Lines through P53-Dependent and P53-Independent Mechanisms. *J. Pharmacol. Exp. Ther.* **2005**, *315* (3), 1403 LP – 1411.

(151) Leyva, L.; Sirlin, C.; Rubio, L.; Franco, C.; Le Lagadec, R.; Spencer, J.; Bischoff, P.; Gaiddon, C.; Loeffler, J.-P.; Pfeffer, M. Synthesis of Cycloruthenated Compounds as Potential Anticancer Agents. *Eur. J. Inorg. Chem.* **2007**, *2007* (19), 3055–3066.

(152) Fetzer, L.; Boff, B.; Ali, M.; Xiangjun, M.; Collin, J.-P.; Sirlin, C.; Gaiddon, C.; Pfeffer, M. Library of Second-Generation Cycloruthenated Compounds and Evaluation of Their Biological Properties as Potential Anticancer Drugs: Passing the Nanomolar Barrier. *Dalt. Trans.* **2011**, *40* (35), 8869–8878.

(153) Iengo, E.; Mestroni, G.; Geremia, S.; Calligaris, M.; Alessio, E. Novel Ruthenium(III) Dimers Na2[{trans-RuCl4(Me2SO-S)}2(μ-L)] and [{mer,Cis-RuCl3(Me2SO-S)(Me2SO-O)}2(μ-L)] (L = Bridging Heterocyclic N-Donor Ligand) Closely Related to the Antimetastatic Complex Na[Trans-RuCl4(Me2SO-S)(Him)]†. *J. Chem. Soc. Dalt. Trans.* **1999**, No. 19, 3361–3371.

(154) Bergamo, A.; Stocco, G.; Gava, B.; Cocchietto, M.; Alessio, E.; Serli, B.; Iengo, E.; Sava, G. Distinct Effects of Dinuclear Ruthenium(III) Complexes on Cell Proliferation and on Cell Cycle Regulation in Human and Murine Tumor Cell Lines. *J. Pharmacol. Exp. Ther.* **2003**, *305* (2), 725 LP – 732.

(155) Bratsos, I.; Jedner, S.; Gianferrara, T.; Alessio, E. Ruthenium Anticancer Compounds: Challenges and Expectations. *CHIMIA International Journal for Chemistry*. pp 692–697.

(156) Chen, H.; Parkinson, J. A.; Nováková, O.; Bella, J.; Wang, F.; Dawson, A.; Gould, R.; Parsons, S.; Brabec, V.; Sadler, P. J. Induced-Fit Recognition of DNA by Organometallic Complexes with Dynamic Stereogenic Centers. *Proc. Natl. Acad. Sci.* **2003**, *100* (25), 14623 LP – 14628.

(157) Mendoza-Ferri, M.-G.; Hartinger, C. G.; Eichinger, R. E.; Stolyarova, N.; Severin, K.; Jakupec, M. A.; Nazarov, A. A.; Keppler, B. K. Influence of the Spacer Length on the *in vitro* Anticancer Activity of Dinuclear Ruthenium−Arene Compounds. *Organometallics* **2008**, *27* (11), 2405–2407.

(158) Kim, B.-E.; Nevitt, T.; Thiele, D. J. Mechanisms for Copper Acquisition, Distribution and Regulation. *Nat. Chem. Biol.* **2008**, *4* (3), 176–185.

(159) Linder, M. C. *Biochemistry of Copper*; Springer US: Boston, MA, 1991.

(160) Liu, N.; Lo, L. S.; Askary, S. H.; Jones, L.; Kidane, T. Z.; Trang, T.; Nguyen, M.; Goforth, J.; Chu, Y.-H.; Vivas, E.; Tsai, M.; Westbrook, T.; Linder, M. C. Transcuprein Is a Macroglobulin Regulated by Copper and Iron Availability. *J. Nutr. Biochem.* **2007**, *18* (9), 597–608.

(161) Zhou, B.; Gitschier, J. HCTR1: A Human Gene for Copper Uptake Identified by Complementation in Yeast. *Proc. Natl. Acad. Sci. U. S. A.* **1997**, *94* (14), 7481–7486.

(162) Mondola, P.; Damiano, S.; Sasso, A.; Santillo, M. The Cu, Zn Superoxide Dismutase: Not Only a Dismutase Enzyme. *Front. Physiol.* **2016**, *7*.

(163) Blanco, A.; Blanco, G. Amino Acid Metabolism. In *Medical Biochemistry*; Elsevier, 2017; pp 367–399.

(164) Xie, H.; Kang, Y. Role of Copper in Angiogenesis and Its Medicinal Implications. *Curr. Med. Chem.* **2009**, *16* (10), 1304–1314.

(165) Azmanova, M.; Pitto-Barry, A. Oxidative Stress in Cancer Therapy: Friend or Enemy? *ChemBioChem* **2022**, *23* (10).

(166) Gaetke, L. M.; Chow, C. K. Copper Toxicity, Oxidative Stress, and Antioxidant Nutrients. *Toxicology* **2003**, *189* (1–2), 147–163.

(167) Gaur, K.; Vázquez-Salgado, A.; Duran-Camacho, G.; Dominguez-Martinez, I.; Benjamín-Rivera, J.; Fernández-Vega, L.; Carmona Sarabia, L.; Cruz García, A.; Pérez-Deliz, F.; Méndez Román, J.; Vega-Cartagena, M.; Loza-Rosas, S.; Rodriguez Acevedo, X.; Tinoco, A. Iron and Copper Intracellular Chelation as an Anticancer Drug Strategy. *Inorganics* **2018**, *6* (4), 126.

(168) Ji, P.; Wang, P.; Chen, H.; Xu, Y.; Ge, J.; Tian, Z.; Yan, Z. Potential of Copper and Copper Compounds for Anticancer Applications. *Pharmaceuticals* **2023**, *16* (2).

(169) Conry, R. R. Copper: Inorganic & Coordination ChemistryBased in Part on the Article Copper: Inorganic & Coordination Chemistry by Rebecca R. Conry & Kenneth D. Karlin Which Appeared in the Encyclopedia of Inorganic Chemistry, First Edition . . *Encycl. Inorg. Chem.* **2006**.

(170) Kitajima, N.; Moro-oka, Y. Copper-Dioxygen Complexes. Inorganic and Bioinorganic Perspectives. *Chem. Rev.* **1994**, *94* (3), 737–757.

(171) Hosseinzadeh, P.; Marshall, N. M.; Chacón, K. N.; Yu, Y.; Nilges, M. J.; New, S. Y.; Tashkov, S. A.; Blackburn, N. J.; Lu, Y. Design of a Single Protein That Spans the Entire 2-V Range of Physiological Redox Potentials. *Proc. Natl. Acad. Sci. U. S. A.* **2016**, *113* (2), 262–267.

(172) Prosser, K. E.; Xie, D.; Chu, A.; MacNeil, G. A.; Varju, B. R.; Kadakia, R. T.; Que, E. L.; Walsby, C. J. Copper(II) Pyridyl Aminophenolates: Hypoxia-Selective, Nucleus-Targeting Cytotoxins, and Magnetic Resonance Probes. *Chem. – A Eur. J.* **2021**, *27* (38), 9839–9849.

(173) Prosser, K. E.; Walsby, C. J. Electron Paramagnetic Resonance as a Tool for Studying the Mechanisms of Paramagnetic Anticancer Metallodrugs. *Eur. J. Inorg. Chem.* **2017**, *2017* (12), 1573–1585.

(174) Denoyer, D.; Clatworthy, S. A. S.; Cater, M. A. 16. COPPER COMPLEXES IN CANCER THERAPY. In *Metallo-Drugs: Development and Action of Anticancer Agents*; Sigel, A., Sigel, H., Freisinger, E., Sigel, R. K. O., Eds.; De Gruyter, 2018; pp 469–506.

(175) Wang, T.; Guo, Z. Copper in Medicine: Homeostasis, Chelation Therapy and Antitumor Drug Design. *Curr. Med. Chem.* **2006**, *13* (5), 525–537.

(176) Saryan, L. A.; Ankel, E.; Krishnamurti, C.; Petering, D. H.; Elford, H. Comparative Cytotoxic and Biochemical Effects of Ligands and Metal Complexes Of.α.-N-Heterocyclic Carboxaldehyde Thiosemicarbazones. *J. Med. Chem.* **1979**, *22* (10), 1218–1221.

(177) Antholine, W. E.; Knight, J. M.; Petering, D. H. Inhibition of Tumor Cell Transplantability by Iron and Copper Complexes of 5-Substituted 2-Formylpyridine Thiosemicarbazones. *J. Med. Chem.* **1976**, *19* (2), 339–341.

(178) Scovill, J. P.; Klayman, D. L.; Franchino, C. F. 2-Acetylpyridine Thiosemicarbazones. 4. Complexes with Transition Metals as Antimalarial and Antileukemic Agents. *J. Med. Chem.* **1982**, *25* (10), 1261–1264.

(179) Easmon, J.; Pürstinger, G.; Heinisch, G.; Roth, T.; Fiebig, H. H.; Holzer, W.; Jäger, W.; Jenny, M.; Hofmann, J. Synthesis, Cytotoxicity, and Antitumor Activity of Copper(II) and Iron(II) Complexes of 4N-Azabicyclo[3.2.2]Nonane Thiosemicarbazones Derived from Acyl Diazines. *J. Med. Chem.* **2001**, *44* (13), 2164–2171.

(180) Milunović, M. N. M.; Palamarciuc, O.; Sirbu, A.; Shova, S.; Dumitrescu, D.; Dvoranová, D.; Rapta, P.; Petrasheuskaya, T. V.; Enyedy, E. A.; Spengler, G.; Ilic, M.; Sitte, H. H.; Lubec, G.; Arion, V. B. Insight into the Anticancer Activity of Copper(Ii) 5-Methylenetrimethylammonium-Thiosemicarbazonates and Their Interaction with Organic Cation Transporters. *Biomolecules* **2020**, *10* (9), 1–30.

(181) Sîrbu, A.; Palamarciuc, O.; Babak, M. V.; Lim, J. M.; Ohui, K.; Enyedy, E. A.; Shova, S.; Darvasiová, D.; Rapta, P.; Ang, W. H.; Arion, V. B. Copper(Ii) Thiosemicarbazone Complexes Induce Marked ROS Accumulation and Promote Nrf2-Mediated Antioxidant Response in Highly Resistant Breast Cancer Cells. *Dalt. Trans.* **2017**, *46* (12), 3833–3847.

(182) Ruiz, R.; García, B.; Garcia-Tojal, J.; Busto, N.; Ibeas, S.; Leal, J. M.; Martins, C.; Gaspar, J.; Borrás, J.; Gil-García, R.; González-Álvarez, M. Biological Assays and Noncovalent Interactions of Pyridine-2-Carbaldehyde Thiosemicarbazonecopper(II) Drugs with [Poly(DA-DT)] 2 , [Poly(DG-DC)] 2 , and Calf Thymus DNA. *J. Biol. Inorg. Chem.* **2010**, *15* (4), 515–532.

(183) Paterson, B. M.; Donnelly, P. S. Copper Complexes of Bis(Thiosemicarbazones): From Chemotherapeutics to Diagnostic and Therapeutic Radiopharmaceuticals. *Chem. Soc. Rev.* **2011**, *40* (5), 3005–3018.

(184) Xie, F.; Wei, W. [64Cu]Cu-ATSM: An Emerging Theranostic Agent for Cancer and Neuroinflammation. *Eur. J. Nucl. Med. Mol. Imaging* **2022**, *49* (12), 3964–3972.

(185) Starosta, R.; Stokowa, K.; Florek, M.; Król, J.; Chwiłkowska, A.; Kulbacka, J.; Saczko, J.; Skała, J.; Jezowska-Bojczuk, M. Biological Activity and Structure Dependent Properties of Cuprous Iodide Complexes with Phenanthrolines and Water Soluble Tris (Aminomethyl) Phosphanes. *J. Inorg. Biochem.* **2011**, *105* (8), 1102–1108.

(186) Teyssot, M. L.; Jarrousse, A. S.; Chevry, A.; De Haze, A.; Beaudoin, C.; Manin, M.; Nolanilvia, S. P.; Díez-González; Morel, L.; Gautier, A. Toxicity of Copper(I)-NHC Complexes against Human Tumor Cells: Induction of Cell Cycle Arrest, Apoptosis, and DNA Cleavage. *Chem. - A Eur. J.* **2009**, *15* (2), 314–318.

(187) Ramakrishnan, S.; Rajendiran, V.; Palaniandavar, M.; Periasamy, V. S.; Srinag, B. S.; Krishnamurthy, H.; Akbarsha, M. A. Induction of Cell Death by Ternary Copper(II) Complexes of l-Tyrosine and Diimines: Role of Coligands on DNA Binding and Cleavage and Anticancer Activity. *Inorg. Chem.* **2009**, *48* (4), 1309–1322.

(188) Xing, T.-T.; Zhan, S.-H.; Li, Y.-T.; Wu, Z.-Y.; Yan, C.-W. Synthesis and Structure of a New Tetracopper(II) Complex WithN-Benzoate-N′-[2-(2-Hydroxyethylamino)Ethyl]Oxamide as Bridging Ligand:*In vitro*anticancer Activities and DNA- and BSA-Binding Studies. *J. Coord. Chem.* **2013**, *66* (18), 3149–3169.

(189) Serment-Guerrero, J.; Cano-Sanchez, P.; Reyes-Perez, E.; Velazquez-Garcia, F.; Bravo-Gomez, M. E.; Ruiz-Azuara, L. Genotoxicity of the Copper Antineoplastic Coordination Complexes Casiopeinas®. *Toxicol. Vitr.* **2011**, *25* (7), 1376–1384.

(190) Prosser, K. E.; Chang, S. W.; Saraci, F.; Le, P. H.; Walsby, C. J. Anticancer Copper Pyridine Benzimidazole Complexes: ROS Generation, Biomolecule Interactions, and Cytotoxicity. *J. Inorg. Biochem.* **2017**, *167*, 89–99.

(191) Campbell, N. H.; Karim, N. H. A.; Parkinson, G. N.; Gunaratnam, M.; Petrucci, V.; Todd, A. K.; Vilar, R.; Neidle, S. Molecular Basis of Structure-Activity Relationships between Salphen Metal Complexes and Human Telomeric DNA Quadruplexes. *J. Med. Chem.* **2012**, *55* (1), 209–222.

(192) Mohan, N.; Vidhya, C. V.; Suni, V.; Mohamed Ameer, J.; Kasoju, N.; Mohanan, P. V.; Sreejith, S. S.; Prathapachandra Kurup, M. R. Copper(Ii) Salen-Based Complexes as Potential Anticancer Agents. *New J. Chem.* **2022**, *46* (26), 12540–12550.

(193) Ghosh, K.; Kumar, P.; Mohan, V.; Singh, U. P.; Kasiri, S.; Mandal, S. S. Nuclease Activity via Self-Activation and Anticancer Activity of a Mononuclear Copper(II) Complex: Novel Role of the Tertiary Butyl Group in the Ligand Frame. *Inorg. Chem.* **2012**, *51* (6), 3343–3345.

(194) Aliaga-Alcalde, N.; Marqués-Gallego, P.; Kraaijkamp, M.; Herranz-Lancho, C.; Den Dulk, H.; Görner, H.; Roubeau, O.; Teat, S. J.; Weyhermüller, T.; Reedijk, J. Copper Curcuminoids Containing Anthracene Groups: Fluorescent Molecules with Cytotoxic Activity. *Inorg. Chem.* **2010**, *49* (20), 9655–9663.

(195) Tan, J.; Wang, B.; Zhu, L. DNA Binding and Oxidative DNA Damage Induced by a Quercetin Copper(II) Complex: Potential Mechanism of Its Antitumor Properties. *J. Biol. Inorg. Chem.* **2009**, *14* (5), 727–739.

(196) Gracia-Mora, I.; Ruiz-Ramírez, L.; Gómez-Ruiz, C.; Tinoco-Méndez, M.; Márquez-Quiñones, A.; Lira, L. R. De; Marín-Hernández, Á.; Macías-Rosales, L.; Bravo-Gómez, M. E. Knigth's Move in the Periodic Table, from Copper to Platinum, Novel Antitumor Mixed Chelate Copper Compounds, Casiopeinas, Evaluated by an *in vitro* Human and Murine Cancer Cell Line Panel. *Met. Based. Drugs* **2001**, *8* (1), 19–28.

(197) Carvallo-Chaigneau, F.; Trejo-Solís, C.; Gómez-Ruiz, C.; Rodríguez-Aguilera, E.; MacÍas-Rosales, L.; Cortés-Barberena, E.; Cedillo-Peláez, C.; Gracia-Mora, I.; Ruiz-Azuara, L.; Madrid-Marina, V.; Constantino-Casas, F. Casiopeina III-Ia Induces Apoptosis in HCT-15 Cells *in vitro* through Caspase-Dependent Mechanisms and Has Antitumor Effect in Vivo. *BioMetals* **2008**, *21* (1), 17–28.

(198) Miranda-Calderón, J. E.; Macías-Rosales, L.; Gracia-Mora, I.; Ruiz-Azuara, L.; Faustino-Vega, A.; Gracia-Mora, J.; Bernad-Bernad, M. J. Effect of Casiopein III-Ia Loaded into Chitosan Nanoparticles on Tumor Growth Inhibition. *J. Drug Deliv. Sci. Technol.* **2018**, *48* (June), 1–8.

(199) Bravo-Gómez, M. E.; Campero-Peredo, C.; García-Conde, D.; Mosqueira-Santillán, M. J.; Serment-Guerrero, J.; Ruiz-Azuara, L. DNA-Binding Mode of Antitumoral Copper Compounds (Casiopeinas®) and Analysis of Its Biological Meaning. *Polyhedron* **2015**, *102*, 530–538.

(200) Chikira, M.; Tomizawa, Y.; Fukita, D.; Sugizaki, T.; Sugawara, N.; Yamazaki, T.; Sasano, A.; Shindo, H.; Palaniandavar, M.; Antholine, W. E. DNA-Fiber EPR Study of the Orientation of Cu(II) Complexes of 1,10-Phenanthroline and Its Derivatives Bound to DNA: Mono(Phenanthroline)-Copper(II) and Its Ternary Complexes with Amino Acids. *J. Inorg. Biochem.* **2002**, *89* (3–4), 163–173.

(201) Rivero-Müller, A.; De Vizcaya-Ruiz, A.; Plant, N.; Ruiz, L.; Dobrota, M. Mixed Chelate Copper Complex, Casiopeina IIgly®, Binds and Degrades Nucleic Acids: A Mechanism of Cytotoxicity. *Chem. Biol. Interact.* **2007**, *165* (3), 189–199.

(202) Alemón-Medina, R.; Breña-Valle, M.; Muñoz-Sánchez, J. L.; Gracia-Mora, M. I.; Ruiz-Azuara, L. Induction of Oxidative Damage by Copper-Based Antineoplastic Drugs (Casiopeínas®). *Cancer Chemother. Pharmacol.* **2007**, *60* (2), 219–228.

(203) Alemón-Medina, R.; Muñoz-Sánchez, J. L.; Ruiz-Azuara, L.; Gracia-Mora, I. Casiopeína IIgly Induced Cytotoxicity to HeLa Cells Depletes the Levels of Reduced Glutathione and Is Prevented by Dimethyl Sulfoxide. *Toxicol. Vitr.* **2008**, *22* (3), 710–715.

(204) Alemón-Medina, R.; Bravo-Gómez, M. E.; Gracia-Mora, M. I.; Ruiz-Azuara, L. Comparison between the Antiproliferative Effect and Intracellular Glutathione Depletion Induced by Casiopeína IIgly and Cisplatin in Murine Melanoma B16 Cells. *Toxicol. Vitr.* **2011**, *25* (4), 868–873.

(205) Kachadourian, R.; Brechbuhl, H. M.; Ruiz-Azuara, L.; Gracia-Mora, I.; Day, B. J. Casiopeína IIgly-Induced Oxidative Stress and Mitochondrial Dysfunction in Human Lung Cancer A549 and H157 Cells. *Toxicology* **2010**, *268* (3), 176–183.

(206) Marín-Hernández, A.; Gracia-Mora, I.; Ruiz-Ramírez, L.; Moreno-Sánchez, R. Toxic Effects of Copper-Based Antineoplastic Drugs (Casiopeinas®) on Mitochondrial Functions. *Biochem. Pharmacol.* **2003**, *65* (12), 1979–1989.

(207) Hernández-Esquivel, L.; Marín-Hernández, A.; Pavón, N.; Carvajal, K.; Moreno-Sánchez, R. Cardiotoxicity of Copper-Based Antineoplastic Drugs Casiopeinas Is Related to Inhibition of Energy Metabolism. *Toxicol. Appl. Pharmacol.* **2006**, *212* (1), 79–88.

(208) López-Rodríguez, A.; Cárabez-Trejo, A.; Rosas-Sánchez, F.; Mejía, C.; Ruiz-Azuara, L.; Miledi, R.; Martínez-Torres, A. The Metal-Coordinated Casiopeína IIIEa Induces the Petite-like Phenotype in Saccharomyces Cerevisiae. *BioMetals* **2011**, *24* (6), 1189–1196.

(209) De Vizcaya-Ruiz, A.; Rivero-Muller, A.; Ruiz-Ramirez, L.; Kass, G. E. N.; Kelland, L. R.; Orr, R. M.; Dobrota, M. Induction of Apoptosis by a Novel Copper-Based Anticancer Compound, Casiopeina II, in L1210 Murine Leukaemia and CH1 Human Ovarian Carcinoma Cells. *Toxicol. Vitr.* **2000**, *14* (1), 1–5.

(210) Bravo-Gómez, M. E.; García-Ramos, J. C.; Gracia-Mora, I.; Ruiz-Azuara, L. Antiproliferative Activity and QSAR Study of Copper(II) Mixed Chelate [Cu(N-N)(Acetylacetonato)]NO3 and [Cu(N-N)(Glycinato)]NO3 Complexes, (Casiopeínas®). *J. Inorg. Biochem.* **2009**, *103* (2), 299–309.

(211) Patel, M. N.; Joshi, H. N.; Patel, C. R. Copper(II) Complexes with Norfloxacin and Neutral Terpyridines: Cytotoxic, Antibacterial, Superoxide Dismutase and DNA-Interaction Approach. *Polyhedron* **2012**, *40* (1), 159–167.

(212) Barve, A.; Kumbhar, A.; Bhat, M.; Joshi, B.; Butcher, R.; Sonawane, U.; Joshi, R. Mixed-Ligand Copper(II) Maltolate Complexes: Synthesis, Characterization, DNA Binding and Cleavage, and Cytotoxicity. *Inorg. Chem.* **2009**, *48* (19), 9120–9132.

(213) Li, X.; Li, Y. T.; Wu, Z. Y.; Zheng, Y. J.; Yan, C. W. Synthesis, Structure, DNA-Binding Properties and Cytotoxic Activities of a New One-Dimensional Polymeric Copper(II) Complex with N-Benzoate-N′-[3-(2- Hydroxyl-Ethylammino)Propyl]Oxamide as Ligand. *Inorganica Chim. Acta* **2012**, *385*, 150–157.

(214) Avramović, N.; Mandić, B.; Savić-Radojević, A.; Simić, T. Polymeric Nanocarriers of Drug Delivery Systems in Cancer Therapy. *Pharmaceutics* **2020**, *12* (4), 1–17.

(215) Masood, F. Polymeric Nanoparticles for Targeted Drug Delivery System for Cancer Therapy. *Mater. Sci. Eng. C* **2016**, *60*, 569–578.

(216) Danquah, M. K.; Zhang, X. A.; Mahato, R. I. Extravasation of Polymeric Nanomedicines across Tumor Vasculature. *Adv. Drug Deliv. Rev.* **2011**, *63* (8), 623–639.

(217) McDonald, D. M.; Thurston, G.; Baluk, P. Endothelial Gaps as Sites for Plasma Leakage in Inflammation. *Microcirculation* **1999**, *6* (1), 7–22.

(218) Shen, Z.; Nieh, M. P.; Li, Y. Decorating Nanoparticle Surface for Targeted Drug Delivery: Opportunities and Challenges. *Polymers (Basel).* **2016**, *8* (3), 1–18.

(219) Odeh, F.; Nsairat, H.; Alshaer, W.; Ismail, M. A.; Esawi, E.; Qaqish, B.; Bawab, A. A.; Ismail, S. I. Aptamers Chemistry: Chemical Modifications and Conjugation Strategies. *Molecules* . 2020.

(220) Aravind, A.; Varghese, S. H.; Veeranarayanan, S.; Mathew, A.; Nagaoka, Y.; Iwai, S.; Fukuda, T.; Hasumura, T.; Yoshida, Y.; Maekawa, T.; Kumar, D. S. Aptamer-Labeled PLGA Nanoparticles for Targeting Cancer Cells. *Cancer Nanotechnol.* **2012**, *3* (1), 1–12.

(221) Saunders, R. A.; Helveston, E. M. Coated Vicryl (Polyglactin 910) Suture in Extraocular Muscle Surgery. *Ophthalmic Surg.* **1979**, *10* (7), 13–18.

(222) Farokhzad, O. C.; Cheng, J.; Teply, B. A.; Sherifi, I.; Jon, S.; Kantoff, P. W.; Richie, J. P.; Langer, R. Targeted Nanoparticle-Aptamer Bioconjugates for Cancer Chemotherapy <Em>in Vivo</Em> *Proc. Natl. Acad. Sci.* **2006**, *103* (16), 6315 LP – 6320.

(223) Langer, R. S.; Peppas, N. A. Present and Future Applications of Biomaterials in Controlled Drug Delivery Systems. *Biomaterials* **1981**, *2* (4), 201–214.

(224) Kamaly, N.; Yameen, B.; Wu, J.; Farokhzad, O. C. Degradable Controlled-Release Polymers and Polymeric Nanoparticles: Mechanisms of Controlling Drug Release. *Chem. Rev.* **2016**, *116* (4), 2602–2663.

(225) Ulery, B. D.; Nair, L. S.; Laurencin, C. T. Biomedical Applications of Biodegradable Polymers. *J. Polym. Sci. Part B Polym. Phys.* **2011**, *49* (12), 832–864.

(226) Makadia, H. K.; Siegel, S. J. Poly Lactic-Co-Glycolic Acid (PLGA) as Biodegradable Controlled Drug Delivery Carrier. *Polymers* . 2011.

(227) Dhar, S.; Gu, F. X.; Langer, R.; Farokhzad, O. C.; Lippard, S. J. Targeted Delivery of Cisplatin to Prostate Cancer Cells by Aptamer Functionalized Pt(IV) Prodrug-PLGA–PEG Nanoparticles. *Proc. Natl. Acad. Sci.* **2008**, *105* (45), 17356 LP – 17361.

(228) Runge, R.; Naumann, A.; Miederer, M.; Kotzerke, J.; Brogsitter, C. Up-Regulation of PSMA Expression *In vitro* as Potential Application in Prostate Cancer Therapy. *Pharmaceuticals* **2023**, *16* (4), 538.

(229) Fischer, B.; Heffeter, P.; Kryeziu, K.; Gille, L.; Meier, S. M.; Berger, W.; Kowol, C. R.; Keppler, B. K. Poly(Lactic Acid) Nanoparticles of the Lead Anticancer Ruthenium Compound KP1019 and Its Surfactant-Mediated Activation. *Dalt. Trans.* **2014**, *43* (3), 1096–1104.

(230) Claridge, T. D. W. Introduction. In *High-Resolution NMR Techniques in Organic Chemistry*; Claridge, T. D. W. B. T.-H.-R. N. M. R. T. in O. C. (Third E., Ed.; Elsevier: Boston, 2016; pp 1–10.

(231) Ernst, R. R.; Anderson, W. A. Application of Fourier Transform Spectroscopy to Magnetic Resonance. *Rev. Sci. Instrum.* **1966**, *37* (1), 93–102.

(232) Garroway, A. N.; Grannell, P. K.; Mansfield, P. Image Formation in NMR by a Selective Irradiative Process. *J. Phys. C Solid State Phys.* **1974**, *7* (24), L457–L462.

(233) Blamire, A. M. The Technology of MRI — the next 10 Years? *Br. J. Radiol.* **2008**, *81* (968), 601–617.

(234) Elmaoğlu, M.; Çelik, A. Fundamentals of Magnetic Resonance Imaging BT - MRI Handbook: MR Physics, Patient Positioning, and Protocols; Elmaoğlu, M., Çelik, A., Eds.; Springer US: Boston, MA, 2012; pp 7–23.

(235) Elmaoğlu, M.; Çelik, A. The Relaxation Concept in MRI BT - MRI Handbook: MR Physics, Patient Positioning, and Protocols; Elmaoğlu, M., Çelik, A., Eds.; Springer US: Boston, MA, 2012; pp 25–46.

(236) Hennig, J.; Nauerth, A.; Friedburg, H. RARE Imaging: A Fast Imaging Method for Clinical MR. *Magn. Reson. Med.* **1986**, *3* (6), 823–833.

(237) Kiefer, B. Turbo Spin-Echo Imaging BT - Echo-Planar Imaging: Theory, Technique and Application; Schmitt, F., Stehling, M. K., Turner, R., Eds.; Springer Berlin Heidelberg: Berlin, Heidelberg, 1998; pp 583–604.

(238) Ridgway, J. P. Cardiovascular Magnetic Resonance Physics for Clinicians: Part I. *J. Cardiovasc. Magn. Reson.* **2010**, *12* (1), 71.

(239) Elmaoğlu, M.; Çelik, A. MRI Pulse Sequences BT - MRI Handbook: MR Physics, Patient Positioning, and Protocols; Elmaoğlu, M., Çelik, A., Eds.; Springer US: Boston, MA, 2012; pp 47–68.

(240) Morris, K. F.; Johnson, C. S. Diffusion-Ordered Two-Dimensional Nuclear Magnetic Resonance Spectroscopy. *J. Am. Chem. Soc.* **1992**, *114* (8), 3139–3141.

(241) Morris, G. A. Diffusion-Ordered Spectroscopy. *eMagRes*. December 15, 2009.

(242) Abragam, A.; Bleaney, B. *Electron Paramagnetic Resonance of Transition Ions*; Oxford University Press, 2012.

(243) Telser, J. A Perspective on Applications of Ligand-Field Analysis: Inspiration from Electron Paramagnetic Resonance Spectroscopy of Coordination Complexes of Transition Metal Ions. *J. Braz. Chem. Soc.* **2006**, *17* (8), 1501–1515.

(244) Webb, M. I.; Walsby, C. J. EPR as a Probe of the Intracellular Speciation of Ruthenium(Iii) Anticancer Compounds. *Metallomics* **2013**, *5* (12), 1624–1633.

(245) Prosser, K. E.; Walsby, C. J. Electron Paramagnetic Resonance as a Tool for Studying the Mechanisms of Paramagnetic Anticancer Metallodrugs. *Eur. J. Inorg. Chem.* **2017**, *2017* (12), 1573–1585.

(246) Stoll, S.; Schweiger, A. EasySpin, a Comprehensive Software Package for Spectral Simulation and Analysis in EPR. *J. Magn. Reson.* **2006**, *178* (1), 42–55.

(247) An, K.-C. Selective Estrogen Receptor Modulators. *Asian Spine J* **2016**, *10* (4), 787–791.

(248) García-Becerra, R.; Santos, N.; Díaz, L.; Camacho, J. Mechanisms of Resistance to Endocrine Therapy in Breast Cancer: Focus on Signaling Pathways, MiRNAs and Genetically Based Resistance. *Int. J. Mol. Sci.* **2013**, *14* (1), 108–145.

(249) Top, S.; Tang, J.; Vessieres, A.; Carrez, D.; Provot, C.; Jaouen, G. Ferrocenyl Hydroxytamoxifen: A Prototype for a New Range of Estradiol Receptor Site-Directed Cytotoxics. *Chem. Commun.* **1996**, No. Copyright (C) 2014 American Chemical Society (ACS). All Rights Reserved., 955–956.

(250) Jaouen, G.; Vessières, A.; Top, S. Ferrocifen Type Anti Cancer Drugs. *Chemical Society Reviews*. 2015, pp 8802–8817.

(251) Pigeon, P.; Top, S.; Vessières, A.; Huché Michel; Hillard, E. A.; Salomon, E.; Jaouen, G. Selective Estrogen Receptor Modulators in the Ruthenocene Series. Synthesis and Biological Behavior. *J. Med. Chem.* **2005**, *48* (8), 2814–2821.

(252) Top, S.; Vessières, A.; Pigeon, P.; Rager, M.-N.; Huché, M.; Salomon, E.; Cabestaing, C.; Vaissermann, J.; Jaouen, G. Selective Estrogen-Receptor Modulators (SERMs) in the Cyclopentadienylrhenium Tricarbonyl Series: Synthesis and Biological Behaviour. *ChemBioChem* **2004**, *5* (8), 1104–1113.

(253) Top, S.; Kaloun, E. B.; Vessières, A.; Laïos, I.; Leclercq, G.; Jaouen, G. The First Titanocenyl Dichloride Moiety Vectorised by a Selective Estrogen Receptor Modulator (SERM). Synthesis and Preliminary Biochemical Behaviour. *J. Organomet. Chem.* **2002**, *643–644*, 350–356.

(254) He, Y.; Groleau, S.; -Gaudreault, R.; Caron, M.; Thérien, H.-M.; Bérubé, G. Synthesis and *in vitro* Biological Evaluation of New Triphenylethylene Platinum (II) Complexes. *Bioorg. Med. Chem. Lett.* **1995**, *5* (19), 2217–2222.

(255) Bérubé, G.; He, Y.; Groleau, S.; Séné, A.; Thérien, H.-M.; Caron, M. The Synthesis and Characterization of New Triphenylethylene Platinum(II) Complexes. *Inorganica Chim. Acta* **1997**, *262* (2), 139–145.

(256) Top, S.; Kaloun, E. B.; Vessières, A.; Leclercq, G.; Laïos, I.; Ourevitch, M.; Deuschel, C.; McGlinchey, M. J.; Jaouen, G. Tamoxifen Derivatives for Delivery of the Antitumoral (DACH)Pt Group: Selective Synthesis by McMurry Coupling, and Biochemical Behaviour. *ChemBioChem* **2003**, *4* (8), 754–761.

(257) Ding, S.; Qiao, X.; Kucera, G. L.; Bierbach, U. Design of a Platinum–Acridine–Endoxifen Conjugate Targeted at Hormone-Dependent Breast Cancer. *Chem. Commun.* **2013**, *49* (24), 2415–2417.

(258) Yu, D. D.; Huss, J. M.; Li, H.; Forman, B. M. Identification of Novel Inverse Agonists of Estrogen-Related Receptors ERRγ and ERRβ. *Bioorganic Med. Chem.* **2017**, *25* (5), 1585–1599.

(259) Daigle, D. J.; Decuir, T. J.; Robertson, J. B.; Darensbourg, D. J. 1,3,5-Triaz-7-Phosphatricyclo[3.3.1.13,7]Decane and Derivatives. *Inorganic Syntheses*. January 1, 1998, pp 40–45.

(260) Vichai, V.; Kirtikara, K. Sulforhodamine B Colorimetric Assay for Cytotoxicity Screening. *Nat. Protoc.* **2006**, *1* (3), 1112–1116.

(261) Birch, A. J. Reduction by Dissolving Metals. Part I. *J. Chem. Soc.* **1944**, No. 0, 430–436.

(262) Kaur, G.; Mahajan, M. P.; Pandey, M. K.; Singh, P.; Ramisetti, S. R.; Sharma, A. K. Design, Synthesis, and Anti-Breast Cancer Evaluation of New Triarylethylene Analogs Bearing Short Alkyl- and Polar Amino-/Amido-Ethyl Chains. *Bioorg. Med. Chem. Lett.* **2016**, *26* (8), 1963–1969.

(263) An, K.-C. Selective Estrogen Receptor Modulators. *Asian Spine J.* **2016**, *10* (4), 787.

(264) Bennett, M. A.; Huang, T.-N.; Matheson, T. W.; Smith, A. K.; Ittel, S.; Nickerson, W. 16. (H6-Hexamethylbenzene)Ruthenium Complexes. *Inorganic Syntheses*. January 1, 1982, pp 74–78.

(265) Scolaro, C.; Bergamo, A.; Brescacin, L.; Delfino, R.; Cocchietto, M.; Laurenczy, G.; Geldbach, T. J.; Sava, G.; Dyson, P. J. *In vitro* and in Vivo Evaluation of Ruthenium(II)-Arene PTA Complexes. *J. Med. Chem.* **2005**, *48* (12), 4161–4171.

(266) Murray, B. S.; Babak, M. V; Hartinger, C. G.; Dyson, P. J. The Development of RAPTA Compounds for the Treatment of Tumors. *Coord. Chem. Rev.* **2016**, *306* (Copyright (C) 2017 American Chemical Society (ACS). All Rights Reserved.), 86–114.

(267) Rausch, M.; Dyson, P. J.; Nowak-Sliwinska, P. Recent Considerations in the Application of RAPTA-C for Cancer Treatment and Perspectives for Its Combination with Immunotherapies. *Advanced Therapeutics*. Wiley September 28, 2019, p 1900042.

(268) Scolaro, C.; Hartinger, C. G.; Allardyce, C. S.; Keppler, B. K.; Dyson, P. J. Hydrolysis Study of the Bifunctional Antitumour Compound RAPTA-C, [Ru(Eta6-p-Cymene)Cl2(Pta)]. *J Inorg Biochem* **2008**, *102* (Copyright (C) 2017 U.S. National Library of Medicine.), 1743–1748.

(269) Dorcier, A.; Ang, W. H.; Bolano, S.; Gonsalvi, L.; Juillerat-Jeannerat, L.; Laurenczy, G.; Peruzzini, M.; Phillips, A. D.; Zanobini, F.; Dyson, P. J. *In vitro* Evaluation of Rhodium and Osmium RAPTA Analogues: The Case for Organometallic Anticancer Drugs Not Based on Ruthenium. *Organometallics* **2006**, *25* (Copyright (C) 2017 American Chemical Society (ACS). All Rights Reserved.), 4090–4096.

(270) Kilpin, K. J.; Cammack, S. M.; Clavel, C. M.; Dyson, P. J. Ruthenium(Ii) Arene PTA (RAPTA) Complexes: Impact of Enantiomerically Pure Chiral Ligands. *J. Chem. Soc. Dalt. Trans.* **2013**, *42* (2), 2008–2014.

(271) Zaki, M.; Hairat, S.; Aazam, E. S. *Scope of Organometallic Compounds Based on Transition Metal-Arene Systems as Anticancer Agents: Starting from the Classical Paradigm to Targeting Multiple Strategies*; Royal Society of Chemistry, 2019; Vol. 9.

(272) Horwitz, K. B.; Costlow, M. E.; McGuire, W. L. MCF-7: A Human Breast Cancer Cell Line with Estrogen, Androgen, Progesterone, and Glucocorticoid Receptors. *Steroids* **1975**, *26* (6), 785–795.

(273) Frasor, J.; Stossi, F.; Danes, J. M.; Komm, B.; Lyttle, C. R.; Katzenellenbogen, B. S. Selective Estrogen Receptor Modulators: Discrimination of Agonistic versus Antagonistic Activities by Gene Expression Profiling in Breast Cancer Cells. *Cancer Res.* **2004**, *64* (4), 1522–1533.

(274) Triple-negative Breast Cancer https://www.cancer.org/cancer/breast-cancer/about/types-of-breast-cancer/triple-negative.html (accessed 2023 -04 -11).

(275) Paull, K. D.; Shoemaker, R. H.; Hodes, L.; Monks, A.; Scudiero, D. A.; Rubinstein, L.; Plowman, J.; Boyd, M. R. Display and Analysis of Patterns of Differential Activity of Drugs against Human Tumor Cell Lines: Development of Mean Graph and COMPARE Algorithm. *J. Natl. Cancer Inst.* **1989**, *81* (14), 1088–1092.

(276) Bold Therapeutics https://www.bold-therapeutics.com/technology.

(277) Xie, D.; Yu, M.; Kadakia, R. T.; Que, E. L. F Magnetic Resonance Activity-Based Sensing Using Paramagnetic Metals. **2019**.

(278) Xie, D.; King, T. L.; Banerjee, A.; Kohli, V.; Que, E. L. Exploiting Copper Redox for 19F Magnetic Resonance-Based Detection of Cellular Hypoxia. *J. Am. Chem. Soc.* **2016**, *138* (9), 2937–2940.

(279) Xie, D.; Kim, S.; Kohli, V.; Banerjee, A.; Yu, M.; Enriquez, J. S.; Luci, J. J.; Que, E. L. Hypoxia-Responsive 19 F MRI Probes with Improved Redox Properties and Biocompatibility. *Inorg. Chem.* **2017**, *56* (11), 6429–6437.

(280) Harris, R. K. N.M.R. and the Periodic Table. In *Chemical Society Reviews*; 1976; Vol. 5, pp 1–22.

(281) Ruiz-Cabello, J.; Barnett, B. P.; Bottomley, P. A.; Bulte, J. W. M. Fluorine (19F) MRS and MRI in Biomedicine. *NMR Biomed.* **2011**, *24* (2), 114–129.

(282) Chang, S. W.; Lewis, A. R.; Prosser, K. E.; Thompson, J. R.; Gladkikh, M.; Bally, M. B.; Warren, J. J.; Walsby, C. J. CF3 Derivatives of the Anticancer Ru(III) Complexes KP1019, NKP-1339, and Their Imidazole and Pyridine Analogues Show Enhanced Lipophilicity, Albumin Interactions, and Cytotoxicity. *Inorg. Chem.* **2016**, *55* (10), 4850–4863.

(283) Schär, M.; Strasser, B.; Dydak, U. CSI and SENSE CSI. *eMagRes*. June 2016, pp 1291–1306.

(284) Starke, L.; Niendorf, T.; Waiczies, S. Data Preparation Protocol for Low Signal-to-Noise Ratio Fluorine-19 MRI; Pohlmann, A., Niendorf, T., Eds.; Springer US: New York, NY, 2021; pp 711–722.

(285) Khan, M. M. T.; Shukla, R. S. Kinetic and Spectroscopic Study of the Formation of an Intermediate Ruthenium(III) Ascorbate Complex in the Oxidation of L-Ascorbic Acid. *Polyhedron* **1991**, *10* (23–24), 2711–2715.

(286) Bold Therapeutics https://www.bold-therapeutics.com/technology (accessed 2021 -07 -25).

(287) Wu, T.; Li, A.; Chen, K.; Peng, X.; Zhang, J.; Jiang, M.; Chen, S.; Zheng, X.; Zhou, X.; Jiang, Z.-X. Perfluoro-Tert-Butanol: A Cornerstone for High Performance Fluorine-19 Magnetic Resonance Imaging. *Chem. Commun.* **2021**, *57* (63), 7743–7757.

(288) Enser, M.; Hallett, K. G.; Hewett, B.; Fursey, G. A. J.; Wood, J. D.; Harrington, G. The Polyunsaturated Fatty Acid Composition of Beef and Lamb Liver. *Meat Sci.* **1998**, *49* (3), 321–327.

(289) Srinivas, M.; Morel, P. A.; Ernst, L. A.; Laidlaw, D. H.; Ahrens, E. T. Fluorine-19 MRI for Visualization and Quantification of Cell Migration in a Diabetes Model. *Magn. Reson. Med.* **2007**, *58* (4), 725–734.

(290) Chapelin, F.; Capitini, C. M.; Ahrens, E. T. Fluorine-19 MRI for Detection and Quantification of Immune Cell Therapy for Cancer. *J. Immunother. Cancer* **2018**, *6* (1), 105.

(291) Bouchlaka, M. N.; Ludwig, K. D.; Gordon, J. W.; Kutz, M. P.; Bednarz, B. P.; Fain, S. B.; Capitini, C. M. 19F-MRI for Monitoring Human NK Cells in Vivo. *Oncoimmunology* **2016**, *5* (5), e1143996–e1143996.

(292) Li, Q.; Feng, Z.; Song, H.; Zhang, J.; Dong, A.; Kong, D.; Wang, W.; Huang, P. 19F Magnetic Resonance Imaging Enabled Real-Time, Non-Invasive and Precise Localization and Quantification of the Degradation Rate of Hydrogel Scaffolds in Vivo. *Biomater. Sci.* **2020**, *8* (12), 3301–3309.

(293) Yu, J.-X.; Kodibagkar, V. D.; Hallac, R. R.; Liu, L.; Mason, R. P. Dual 19F/1H MR Gene Reporter Molecules for in Vivo Detection of β-Galactosidase. *Bioconjug. Chem.* **2012**, *23* (3), 596–603.

(294) Jordan, B. F.; Cron, G. O.; Gallez, B. Rapid Monitoring of Oxygenation by 19F Magnetic Resonance Imaging: Simultaneous Comparison with Fluorescence Quenching. *Magn. Reson. Med.* **2009**, *61* (3), 634–638.

(295) MRI for Cancer https://www.radiologyinfo.org/en/info/bodymr.

(296) Bosnian, F. T.; Havenith, M.; Cleutjens, J. P. M. Basement Membranes in Cancer. *Ultrastruct. Pathol.* **1985**, *8* (4), 291–304.

(297) Shepelytskyi, Y.; Fox, M. S.; Davenport, K.; Li, T.; Albert, M. S.; Davenport, E. In-Vivo Retention of 5-Fluorouracil Using 19F Magnetic Resonance Chemical Shift Imaging in Colorectal Cancer in a Murine Model. *Sci. Rep.* **2019**, *9* (1), 13244.

(298) Srivastava, K.; Weitz, E. A.; Peterson, K. L.; Marjańska, M.; Pierre, V. C. Fe- and Ln-DOTAm-F12 Are Effective Paramagnetic Fluorine Contrast Agents for MRI in Water and Blood. *Inorg. Chem.* **2017**, *56* (3), 1546–1557.

(299) Blazevic, A.; Hummer, A. A.; Heffeter, P.; Berger, W.; Filipits, M.; Cibin, G.; Keppler, B. K.; Rompel, A. Electronic State of Sodium Trans-[Tetrachloridobis(1H-Indazole)Ruthenate(III)] (NKP-1339) in Tumor, Liver and Kidney Tissue of a SW480-Bearing Mouse. *Sci. Rep.* **2017**, *7* (1), 1–8.

(300) Jusu, S. M.; Obayemi, J. D.; Salifu, A. A.; Nwazojie, C. C.; Uzonwanne, V.; Odusanya, O. S.; Soboyejo, W. O. Drug-Encapsulated Blend of PLGA-PEG Microspheres: *In vitro* and in Vivo Study of the Effects of Localized/Targeted Drug Delivery on the Treatment of Triple-Negative Breast Cancer. *Sci. Rep.* **2020**, *10* (1), 1–23.

(301) Danaei, M.; Dehghankhold, M.; Ataei, S.; Hasanzadeh Davarani, F.; Javanmard, R.; Dokhani, A.; Khorasani, S.; Mozafari, M. R. Impact of Particle Size and Polydispersity Index on the Clinical Applications of Lipidic Nanocarrier Systems. *Pharmaceutics* **2018**, *10* (2), 1–17.

(302) Clogston, J. D.; Patri, A. K. Zeta Potential Measurement. In *Methods in Molecular Biology*; 2011; Vol. 697, pp 63–70.

(303) Tamani, F.; Hamoudi, M. C.; Danede, F.; Willart, J. F.; Siepmann, F.; Siepmann, J. Towards a Better Understanding of the Release Mechanisms of Caffeine from PLGA Microparticles. *J. Appl. Polym. Sci.* **2020**, *137* (25), 1–12.

(304) Sung-wook Hong; Yongmin Chang; Moon-jung Hwang; Il-su Rhee; Duk-Sik Kang. Determination of Electron Spin Relaxation Time of Gadolinium-Chealted MRI Contrast Agents by Using an X-Band EPR Technique. *Investigative Magnetic Resonance Imaging*. 2000, pp 27–33.

(305) Electron Paramagnetic Resonance and Relaxation. In *The Physics of Polarized Targets*; Niinikoski, T. O., Ed.; Cambridge University Press: Cambridge, 2020; pp 98–154.

(306) Harrison, D. C.; Quastel, J. H. The Reduction Potential of Cysteine. *Biochem. J.* **1928**, *22* (3), 683–688.

(307) Kuhn, P. S.; Büchel, G. E.; Jovanović, K. K.; Filipović, L.; Radulović, S.; Rapta, P.; Arion, V. B. Osmium(III) Analogues of KP1019: Electrochemical and Chemical Synthesis, Spectroscopic Characterization, x-Ray Crystallography, Hydrolytic Stability, and Antiproliferative Activity. *Inorg. Chem.* **2014**, *53* (20), 11130–11139.

(308) Bytzek, A. K.; Koellensperger, G.; Keppler, B. K.; Hartinger, C. G. Biodistribution of the Novel Anticancer Drug Sodium Trans-[Tetrachloridobis(1H-Indazole)Ruthenate(III)] KP-1339/IT139 in Nude BALB/c Mice and Implications on Its Mode of Action. *J. Inorg. Biochem.* **2016**, *160*, 250–255.

(309) He, C.; Hu, Y.; Yin, L.; Tang, C.; Yin, C. Effects of Particle Size and Surface Charge on Cellular Uptake and Biodistribution of Polymeric Nanoparticles. *Biomaterials* **2010**, *31* (13), 3657–3666.

(310) Behzadi, S.; Serpooshan, V.; Tao, W.; Hamaly, M. A.; Alkawareek, M. Y.; Dreaden, E. C.; Brown, D.; Alkilany, A. M.; Farokhzad, O. C.; Mahmoudi, M. Cellular Uptake of Nanoparticles: Journey inside the Cell. *Chem. Soc. Rev.* **2017**, *46* (14), 4218–4244.

(311) McWhinnie, W. R. Infra-Red Spectra of Some Sulphato (and Perchlorato) Complexes of Copper(II)—II. *J. Inorg. Nucl. Chem.* **1964**, *26* (1), 21–24.

(312) Crutchley, R. J.; Hynes, R.; Gabe, E. J. Five- and Four-Coordinate Copper(II) Complexes of 2,2'-Bipyridine and Phenylcyanamide Anion Ligands: Crystal Structures, Cyclic Voltammetry, and Electronic Absorption Spectroscopy. *Inorg. Chem.* **1990**, *29* (24), 4921–4928.

(313) Reger, D. L.; Huff, M. F.; Lebioda, L. Structure of (2,2'-Bipyridine)Bis(Difluorophosphinato)Copper(II), (Bpy)Cu(PF2O2)2. *Acta Crystallogr. Sect. C Cryst. Struct. Commun.* **1991**, *47* (6), 1167–1169.

(314) Gavioli, G. B.; Borsari, M.; Menabue, L.; Saladini, M.; Sola, M.; Battaglia, L. Pietro; Corradi, A. B.; Pelosi, G. Ternary Copper(II) Complexes with 2,2′-Bipyridine and N-Tosyl-Substituted Amino Acids. Part 2. Crystal and Molecular Structure of Aqua(2,2′-Bipyridine)Bis(N-Tosyl-DL-Asparaginato-O)Copper(II) Dihydrate and (2,2′-Bipyridine)(N-Tosyl-DL-Asparaginato-NO)Copp. *J. Chem. Soc., Dalt. Trans.* **1990**, No. 1, 97–100.

(315) Martell, A. E.; Chaberek, S.; Courtney, R. C.; Westerback, S.; Hyytiainen, H. Hydrolytic Tendencies of Metal Chelate Compounds. I. Cu(II) Chelates. *J. Am. Chem. Soc.* **1957**, *79* (12), 3036–3041.

(316) Ryl, L. B.; Ronay, G. S.; Fowkes, F. M. Equilibria in Aqueous Solutions of Copper(II) Chelates with α A′-Dipyridyl, o-Phenanthroline and Ethylenediamine. *J. Phys. Chem.* **1958**, *62* (7), 798–801.

(317) Gustafson, R. L.; Martell, A. E. Hydrolytic Tendencies of Metal Chelate Compounds. V. Hydrolysis and Dimerization of Copper(II) Chelates of 1,2-Diamines 1. *J. Am. Chem. Soc.* **1959**, *81* (3), 525–529.

(318) Noack, M.; Gordon, G. Oxygen-17 NMR and Copper EPR Linewidths in Aqueous Solutions of Copper(II) Ion and 2,2′-Dipyridine. *J. Chem. Phys.* **1968**, *48* (6), 2689–2699.

(319) Marov, I. N.; Belyaeva, V. K.; Smirnova, E. B.; Dolmanova, I. F. Electron Spin Resonance Spectra of Copper(II) Bipyridyl Complexes. *Inorg. Chem.* **1978**, *17* (6), 1667–1669.

(320) García-Ramos, J. C.; Gutiérrez, A. G.; Vázquez-Aguirre, A.; Toledano-Magaña, Y.; Alonso-Sáenz, A. L.; Gómez-Vidales, V.; Flores-Alamo, M.; Mejía, C.; Ruiz-Azuara, L. The Mitochondrial Apoptotic Pathway Is Induced by Cu(II) Antineoplastic Compounds (Casiopeínas®) in SK-N-SH Neuroblastoma Cells after Short Exposure Times. *BioMetals* **2017**, *30* (1), 43–58.

(321) Folli, A.; Ritterskamp, N.; Richards, E.; Platts, J. A.; Murphy, D. M. Probing the Structure of Copper(II)-Casiopeina Type Coordination Complexes [Cu(O-O)(N-N)]+ by EPR and ENDOR Spectroscopy. *J. Catal.* **2021**, *394*, 220–227.

(322) Aguilar-Jiménez, Z.; González-Ballesteros, M.; Dávila-Manzanilla, S. G.; Espinoza-Guillén, A.; Ruiz-Azuara, L. Development and *In vitro* and In Vivo Evaluation of an Antineoplastic Copper(II) Compound (Casiopeina III-Ia) Loaded in Nonionic Vesicles Using Quality by Design. *Int. J. Mol. Sci.* **2022**, *23* (21).

(323) Elena Bravo-Gómez, M.; Dávila-Manzanilla, S.; Flood-Garibay, J.; Ángel Muciño-Hernández, M.; Mendoza, Á.; Carlos García-Ramos, J.; Moreno-Esparza, R.; Ruiz-Azuara, L. Secondary Ligand Effects on the Cytotoxicity of Several Casiopeína's Group II Compounds Secondary Ligand Effects on the Cytotoxicity of Several Casiopeína's Group II Compounds Article. *Chem. Soc* **2012**, *2012* (1), 85–92.

(324) Ramírez-Palma, L. G.; Espinoza-Guillén, A.; Nieto-Camacho, F.; López-Guerra, A. E.; Gómez-Vidales, V.; Cortés-Guzmán, F.; Ruiz-Azuara, L. Intermediate Detection in the Casiopeina–Cysteine Interaction Ending in the Disulfide Bond Formation and Copper Reduction. *Molecules* **2021**, *26* (19).

(325) Miranda-Calderón, J. E.; Medina-Torres, L.; Tinoco-Mendez, M.; Moreno-Esparza, R.; Ruiz-Ramirez, L.; Gracia-Mora, J.; Gracia-Mora, I.; Bernad-Bernad, M. J. Characterization of Physical Interaction between Casiopeina III-Ia and Chitosan. Toward a Cas III-Ia Drug Delivery System. *Carbohydr. Res.* **2011**, *346* (1), 121–126.

(326) Tovar-Tovar, A.; Ruiz-Ramírez, L.; Campero, A.; Romerosa, A.; Moreno-Esparza, R.; Rosales-Hoz, M. J. Structural and Reactivity Studies on 4,4′-Dimethyl-2,2′- Bipyridine Acetylacetonate Copper(II) Nitrate (CASIOPEINA III-Ia®) with Methionine, by UV-Visible and EPR Techniques. *J. Inorg. Biochem.* **2004**, *98* (6), 1045–1053.

(327) Helm, L.; Merbach, A. E. Water Exchange on Metal Ions: Experiments and Simulations. *Coord. Chem. Rev.* **1999**, *187*, 151–181.

(328) Bal, W.; Sokołowska, M.; Kurowska, E.; Faller, P. Binding of Transition Metal Ions to Albumin: Sites, Affinities and Rates. *Biochim. Biophys. Acta - Gen. Subj.* **2013**, *1830* (12), 5444–5455.

(329) Prosser, K. E.; Xie, D.; Chu, A.; MacNeil, G. A.; Varju, B. R.; Kadakia, R. T.; Que, E. L.; Walsby, C. J. Copper(II) Pyridyl Aminophenolates: Hypoxia-Selective, Nucleus-Targeting Cytotoxins, and Magnetic Resonance Probes. *Chem. – A Eur. J.* **2021**, *27* (38), 9839–9849.

(330) Bennett, B.; Kowalski, J. M. *EPR Methods for Biological Cu(II): L-Band CW and NARS Dedication. This Chapter Is Dedicated to Graeme R. Hanson, a Valued Friend and Colleague, Who Passed Away on February 24th, 2015.*, 1st ed.; Elsevier Inc., 2015; Vol. 563.

(331) Correia, I.; Borovic, S.; Cavaco, I.; Matos, C. P.; Roy, S.; Santos, H. M.; Fernandes, L.; Capelo, J. L.; Ruiz-Azuara, L.; Pessoa, J. C. Evaluation of the Binding of Four Anti-Tumor Casiopeínas® to Human Serum Albumin. *J. Inorg. Biochem.* **2017**, *175* (April), 284–297.

(332) Prosser, K. E. Spectroscopy and Mechanisms of Redox-Active Copper-Based Anticancer Complexes, Simon Fraser University, 2019.

(333) Lau, S. J.; Sarkar, B. The Interaction of Copper(II) and Glycyl-L-Histidyl-L-Lysine, a Growth-Modulating Tripeptide from Plasma. *Biochem. J.* **1981**, *199* (3), 649–656.

(334) Melchart, M.; Sadler, P. J. Ruthenium Arene Anticancer Complexes; Wiley-VCH Verlag GmbH & Co. KGaA, 2006; pp 39–64.

(335) Yan, Y. K.; Melchart, M.; Habtemariam, A.; Sadler, P. J. Organometallic Chemistry, Biology and Medicine: Ruthenium Arene Anticancer Complexes. **2005**.

(336) Munteanu, A.-C.; Uivarosi, V. Ruthenium Complexes in the Fight against Pathogenic Microorganisms. An Extensive Review. *Pharmaceutics* . 2021.

(337) Nowak-Sliwinska, P.; van Beijnum, J. R.; Casini, A.; Nazarov, A. A.; Wagnieres, G.; van den Bergh, H.; Dyson, P. J.; Griffioen, A. W. Organometallic Ruthenium(II) Arene Compounds with Antiangiogenic Activity. *J. Med. Chem.* **2011**, *54* (Copyright (C) 2014 American Chemical Society (ACS). All Rights Reserved.), 3895–3902.

(338) Giorgi, E.; Binacchi, F.; Marotta, C.; Cirri, D.; Gabbiani, C.; Pratesi, A. Highlights of New Strategies to Increase the Efficacy of Transition Metal Complexes for Cancer Treatments. *Molecules* **2023**, *28* (1).

(339) Mu, C.; Prosser, K. E.; Harrypersad, S.; Macneil, G. A.; Panchmatia, R.; Thompson, J. R.; Sinha, S.; Warren, J. J.; Walsby, C. J. Activation by Oxidation: Ferrocene-Functionalized Ru(II)-Arene Complexes with Anticancer, Antibacterial, and Antioxidant Properties. *Inorg. Chem.* **2018**, *57* (24), 15247–15261.

(340) Alessio, E.; Balducci, G.; Calligaris, M.; Costa, G.; Attia, W. M.; Mestroni, G. Synthesis, Molecular Structure, and Chemical Behavior of Hydrogen Trans-Bis(Dimethyl Sulfoxide)Tetrachlororuthenate(III) and Mer-Trichlorotris(Dimethyl Sulfoxide)Ruthenium(III): The First Fully Characterized Chloride-Dimethyl Sulfoxide-Ruthenium(III) Comp. *Inorg. Chem.* **1991**, *30* (4), 609–618.

(341) Vargiu, A. V.; Robertazzi, A.; Magistrato, A.; Ruggerone, P.; Carloni, P. The Hydrolysis Mechanism of the Anticancer Ruthenium Drugs NAMI-A and ICR Investigated by DFT-PCM Calculations. *J. Phys. Chem. B* **2008**, *112* (14), 4401–4409.

(342) Bacac, M.; Hotze, A. C. G.; Schilden, K. van der; Haasnoot, J. G.; Pacor, S.; Alessio, E.; Sava, G.; Reedijk, J. The Hydrolysis of the Anti-Cancer Ruthenium Complex NAMI-A Affects Its DNA Binding and Antimetastatic Activity: An NMR Evaluation. *J. Inorg. Biochem.* **2004**, *98* (2), 402–412.

(343) Sava, G.; Bergamo, A.; Zorzet, S.; Gava, B.; Casarsa, C.; Cocchietto, M.; Furlani, A.; Scarcia, V.; Serli, B.; Iengo, E.; Alessio, E.; Mestroni, G. Influence of Chemical Stability on the Activity of the Antimetastasis Ruthenium Compound NAMI-A. *Eur. J. Cancer* **2002**, *38* (3), 427–435.

(344) Reisner, E.; Arion, V. B.; Guedes Da Silva, M. F. C.; Lichtenecker, R.; Eichinger, A.; Keppler, B. K.; Kukushkin, V. Y.; Pombeiro, A. J. L. Tuning of Redox Potentials for the Design of Ruthenium Anticancer Drugs - An Electrochemical Study of [Trans-RuCl4L(DMSO)]- and [Trans-RuCl4L2]- Complexes, Where L = Imidazole, 1,2,4-Triazole, Indazole. *Inorg. Chem.* **2004**, *43* (22), 7083–7093.

(345) Khazim, K.; Giustarini, D.; Rossi, R.; Verkaik, D.; Cornell, J. E.; Cunningham, S. E. D.; Mohammad, M.; Trochta, K.; Lorenzo, C.; Folli, F.; Bansal, S.; Fanti, P. Glutathione Redox Potential Is Low and Glutathionylated and Cysteinylated Hemoglobin Levels Are Elevated in Maintenance Hemodialysis Patients. *Transl. Res.* **2013**, *162* (1), 16–25.

(346) Borsook, H.; Keighley, G. Oxidation-Reduction Potential of Ascorbic Acid (Vitamin C). *Proc. Natl. Acad. Sci.* **1933**, *19* (9), 875–878.

(347) Elgrishi, N.; Rountree, K. J.; McCarthy, B. D.; Rountree, E. S.; Eisenhart, T. T.; Dempsey, J. L. A Practical Beginner's Guide to Cyclic Voltammetry. *J. Chem. Educ.* **2017**, acs.jchemed.7b00361.

(348) Mu, C.; Chang, S. W.; Prosser, K. E.; Leung, A. W. Y.; Santacruz, S.; Jang, T.; Thompson, J. R.; Yapp, D. T. T.; Warren, J. J.; Bally, M. B.; Beischlag, T. V; Walsby, C. J. Induction of Cytotoxicity in Pyridine Analogues of the Anti-Metastatic Ru(III) Complex NAMI-A by Ferrocene Functionalization. *Inorg. Chem.* **2016**, *55* (Copyright (C) 2016 American Chemical Society (ACS). All Rights Reserved.), 177–190.

(349) Mu, C. Mechanisms of New Ru-Ferrocene and Binuclear Ru Metallochemotherapeutics and the Ru Metastasis Inhibitor NAMI-A By, Simon Fraser University, 2016.

(350) Sava, G.; Pacor, S.; Bergamo, A.; Cocchietto, M.; Mestroni, G.; Alessio, E. Effects of Ruthenium Complexes on Experimental Tumors: Irrelevance of Cytotoxicity for Metastasis Inhibition. *Chem. Biol. Interact.* **1995**, *95* (1–2), 109–126.

(351) Juan, A.; Cimas, F. J.; Bravo, I.; Pandiella, A.; Ocaña, A.; Alonso-Moreno, C. An Overview of Antibody Conjugated Polymeric Nanoparticles for Breast Cancer Therapy. *Pharmaceutics* **2020**, *12* (9), 1–20.

Appendix A.

Supplementary Information for Chapter 2

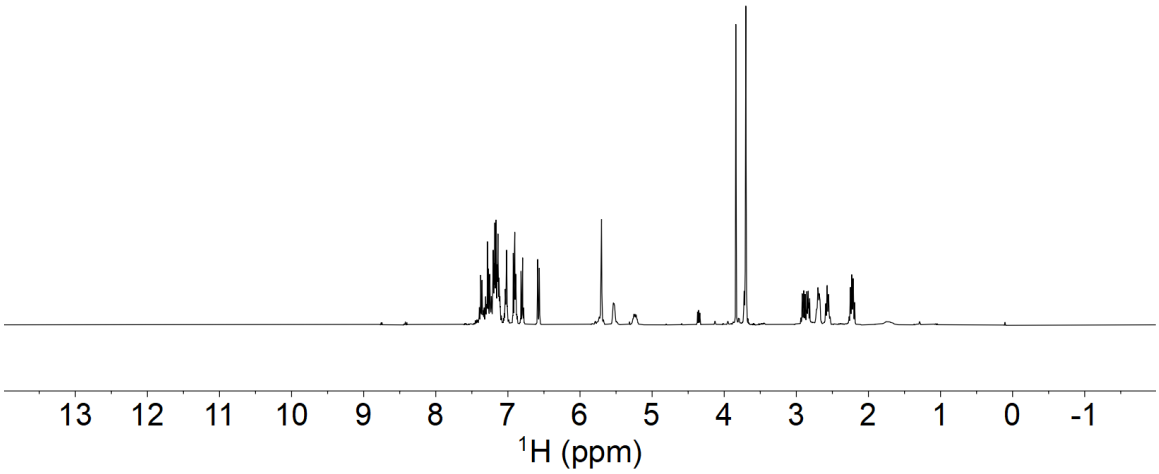

Figure A.1 **^{1}H NMR of 2-8 in $CDCl_3$**

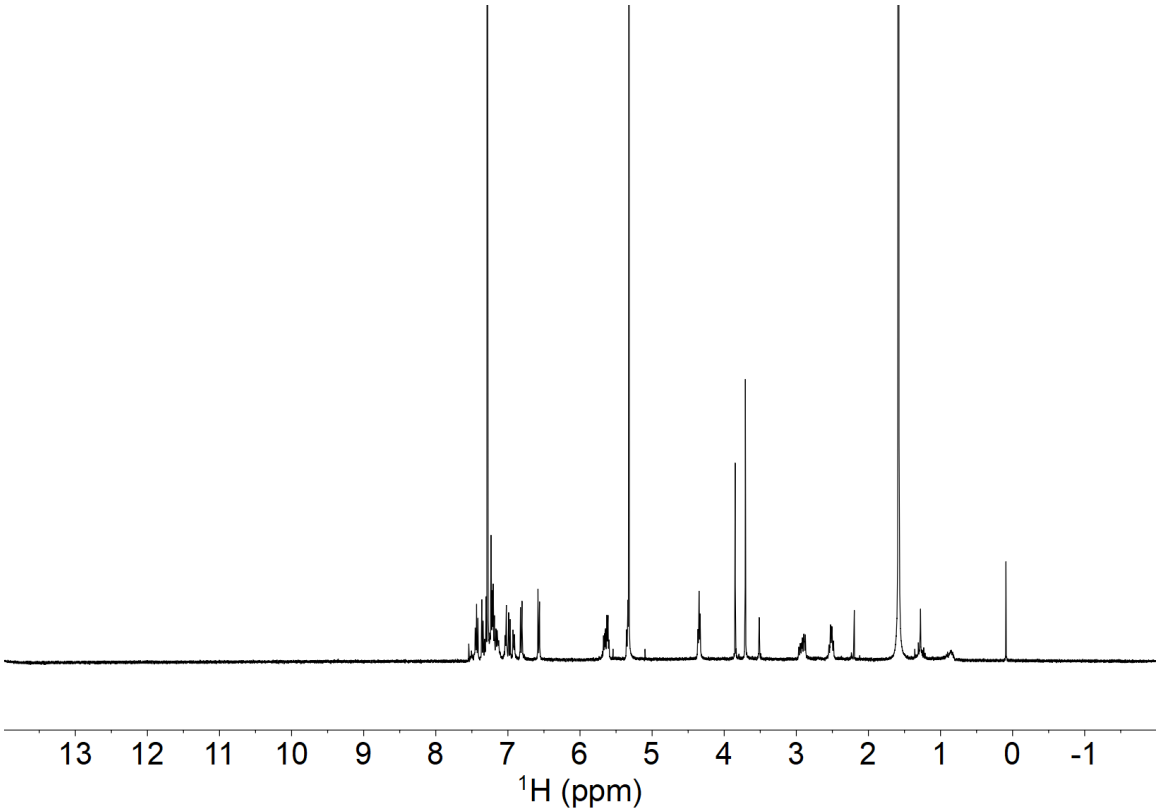

Figure A.2 ^{1}H NMR of 2-1 in $CDCl_3$.

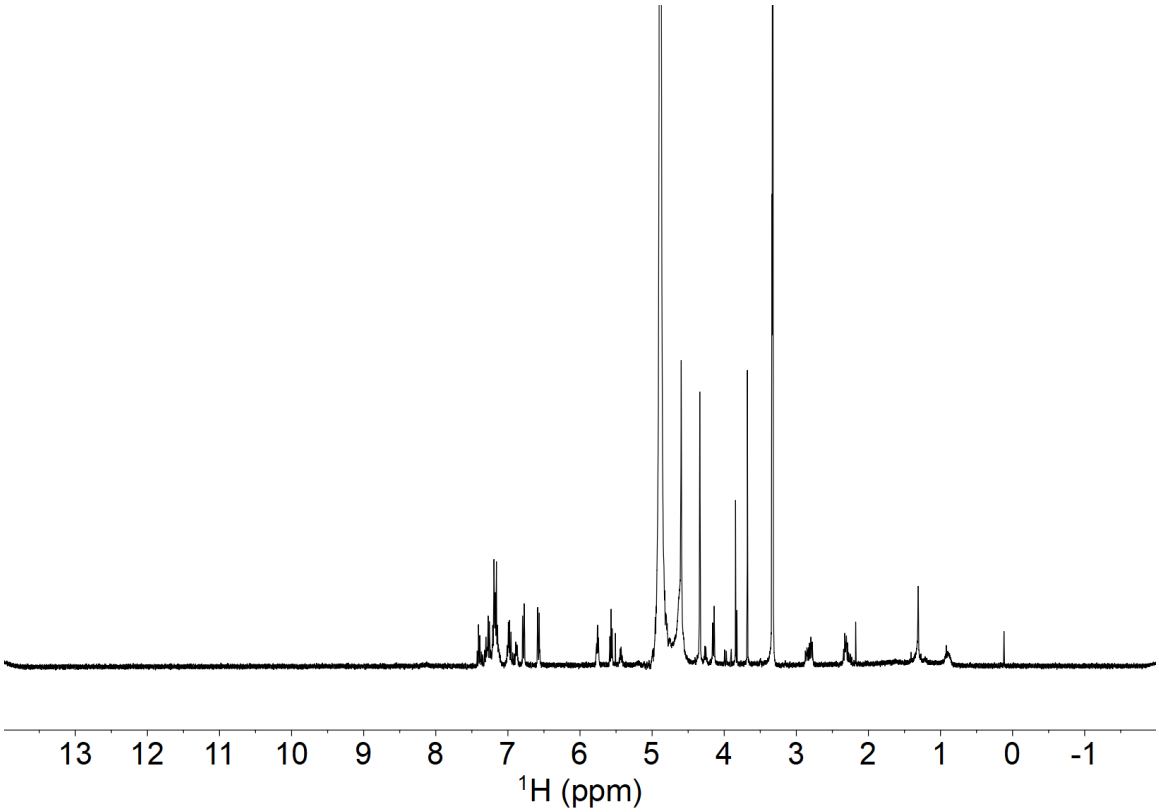

Figure A.3 ^{1}H NMR of 2-12 in MeOD.

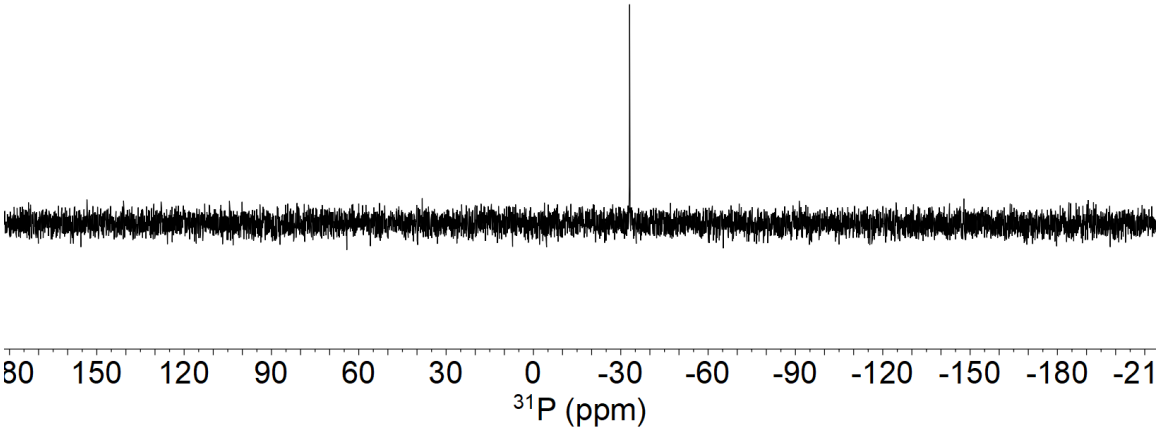

Figure A.4 ^{31}P NMR of 2-12 in MeOD.

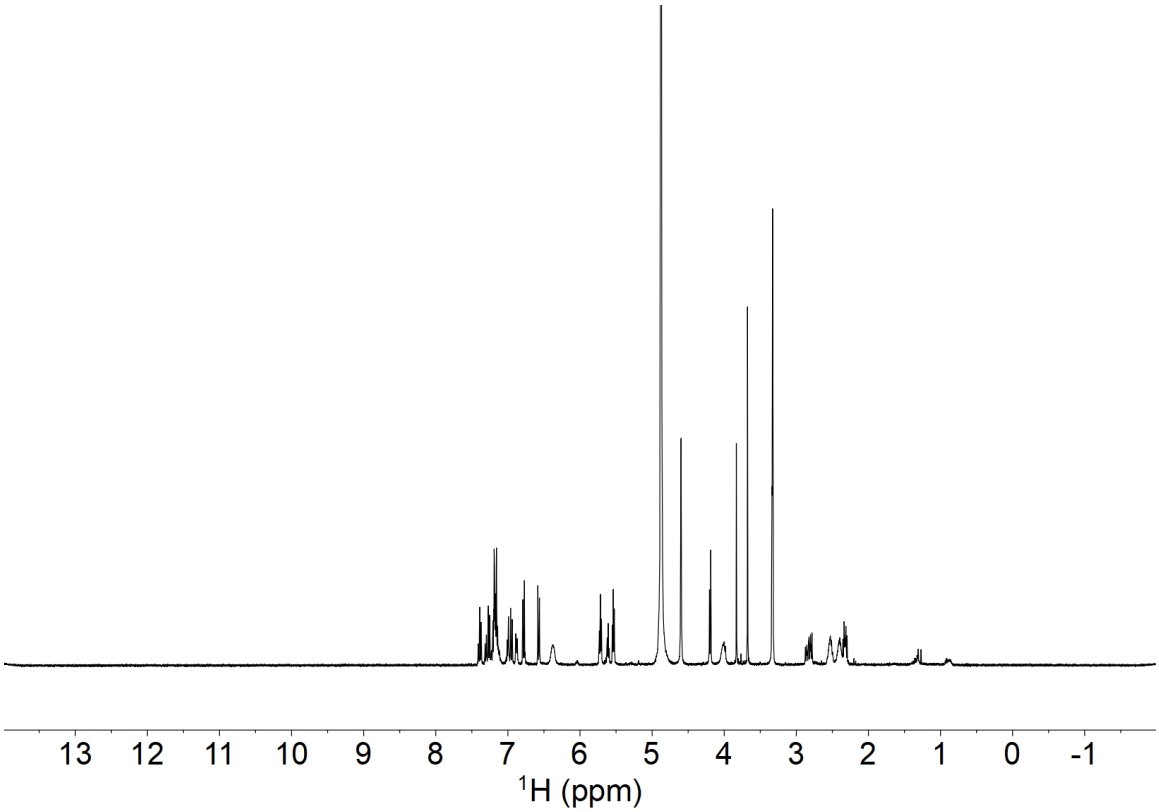

Figure A.5 ^{1}H NMR of 2-13 in MeOD.

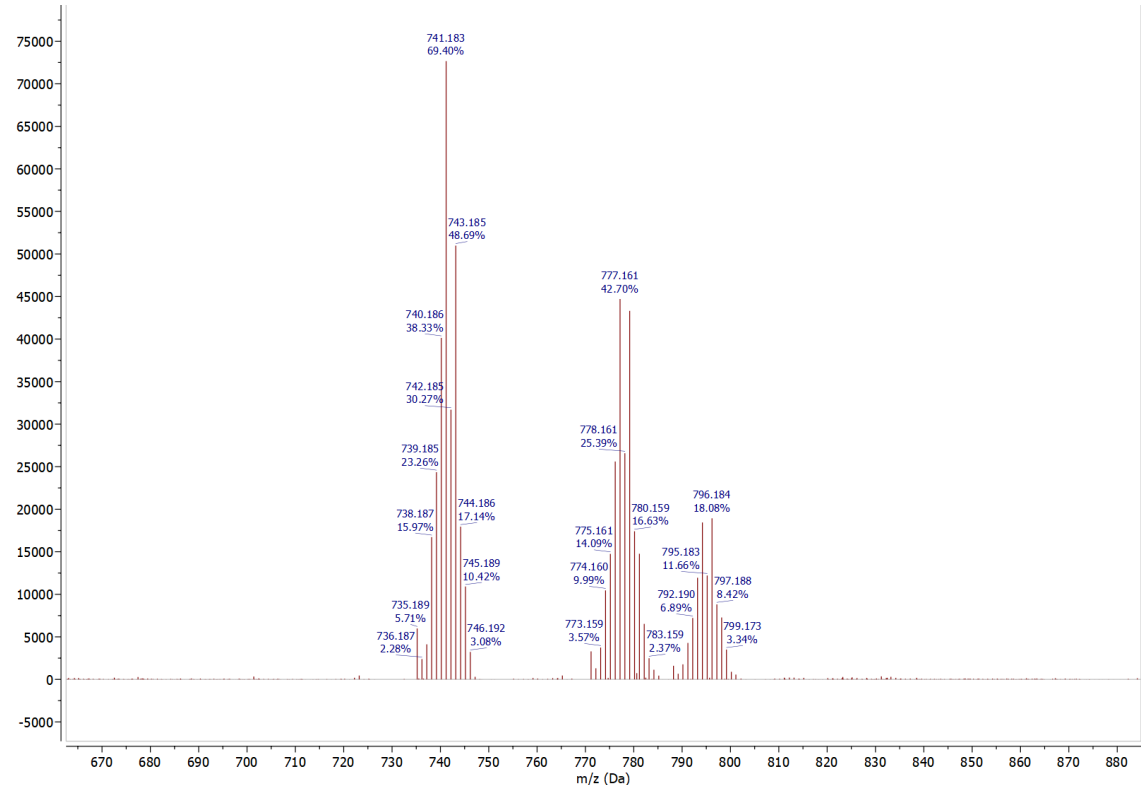

Figure A.6 ESI-MS of 2-12 (ESI$^+$) *m/z*: 776.70 $[M]^+$ (calc'd), 741.18 $[M\text{-}Cl]^+$ (found), 777.16 $[M+H]^+$ (found), 796.18 $[M+NH_4]^+$ (found).

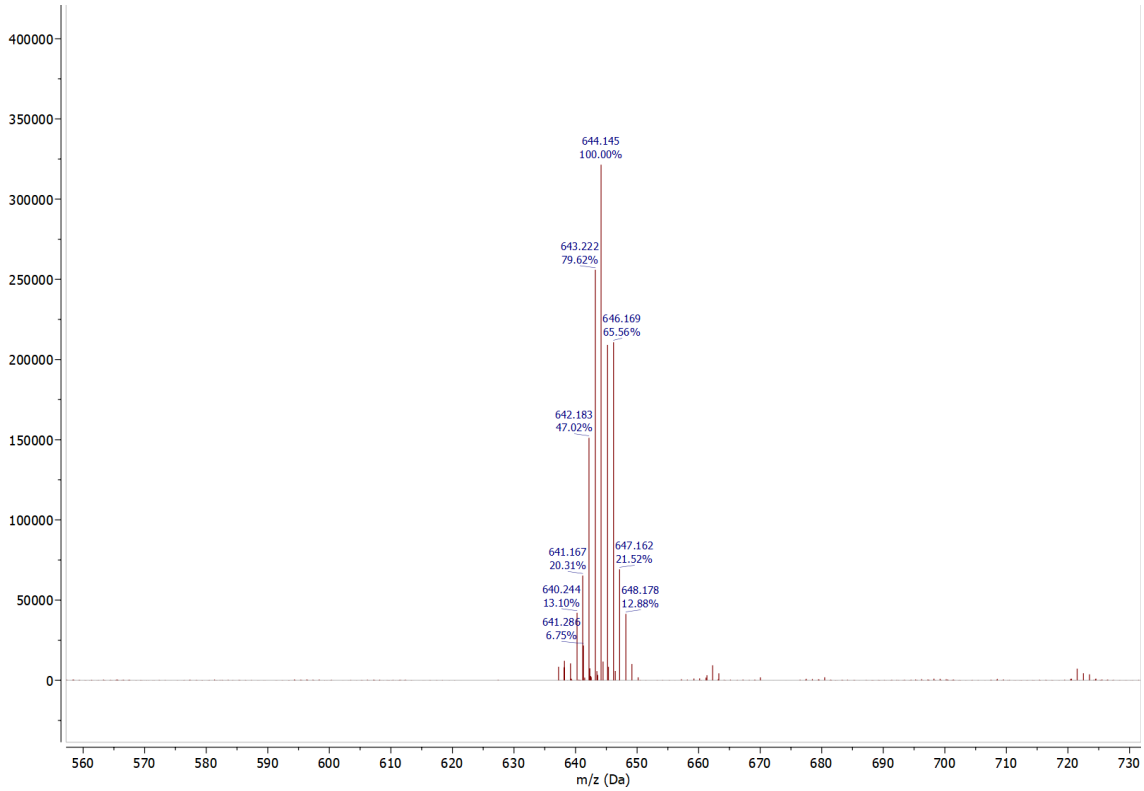

Figure A.7 ESI-MS of 2-13 (ESI$^+$) *m/z*: 644.16 [M$^+$] (calc'd), 644.15 [M$^+$] (found).

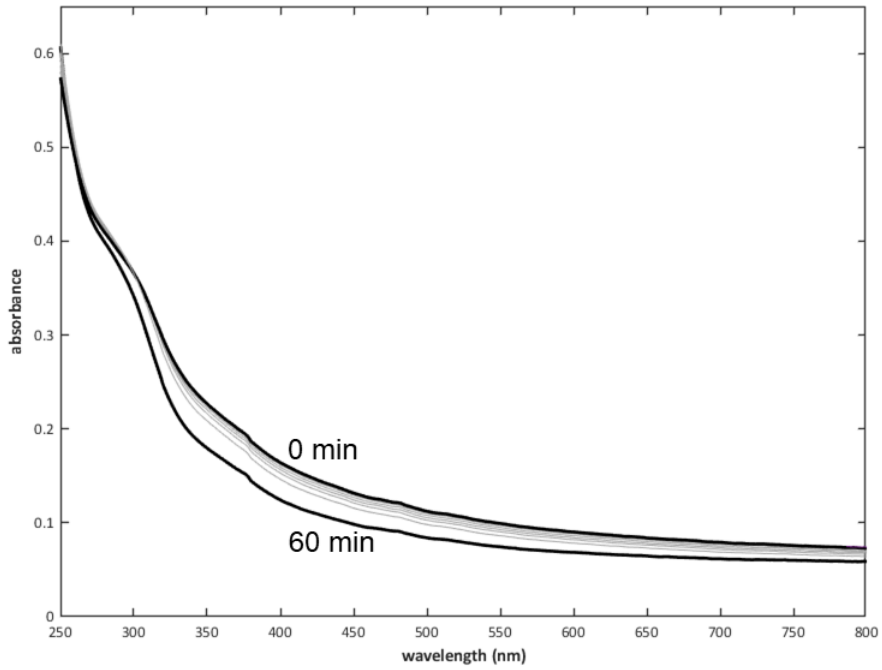

Figure A.8 UV-Vis of a 200 µM solution of 2-11 in MES (174 mM NaCl) buffer with 1 % DMSO take at 2-minute intervals of 1 h at 25 °C.

Table A.1 NCI-60 growth percent data for RAPTA-C

Cell Line	Growth %	Cell Line	Growth %
CCRF-CEM	99.37753	M14	103.1775
HL-60(TB)	94.21694	MDA-MB-435	100.6158
K-562	103.6246	SK-MEL-2	112.2188
MOLT-4	105.2486	SK-MEL-28	103.3034
RPMI-8226	99.71236	SK-MEL-5	103.5372
SR	103.2158	UACC-257	105.2111
A549/ATCC	99.85004	UACC-62	91.72961
EKVX	92.60963	IGROV1	93.90961
HOP-62	110.9211	OVCAR-3	107.0991
HOP-92	97.41675	OVCAR-4	100.6749
NCI-H226	98.29499	OVCAR-5	102.3827
NCI-H322M	91.79908	OVCAR-8	101.2602
NCI-H460	102.6827	NCI/ADR-RES	104.5392
NCI-H522	97.89661	SK-OV-3	106.1113
COLO 205	110.4879	786-0	95.9542
HCC-2998	108.0614	A498	104.8399
HCT-116	112.5473	ACHN	99.03637
HCT-15	96.51938	CAKI-1	92.29827
HT29	107.6529	RXF 393	115.4616
KM12	103.1478	SN12C	92.52356
SW-620	100.9112	TK-10	100.2068
SF-268	102.6525	UO-31	91.29799
SF-295	103.7979	PC-3	92.06134
SF-539	99.97848	DU-145	107.9908
SNB-19	98.05172	MCF7	97.49849
SNB-75	93.10061	MDA-MB-231/ATCC	94.34051
U251	105.4391	HS 578T	105.4706
LOX IMVI	10.5591	BT-549	122.7921
MALME-3M	97.13483	T-47D	106.3011

Table A.2 NCI-60 growth percent data for RAED-C

Cell Line	Growth %	Cell Line	Growth %
CCRF-CEM	96.97402	M14	97.95417
HL-60(TB)	106.3519	MDA-MB-435	117.3797
K-562	102.5375	SK-MEL-2	105.567
MOLT-4	96.2446	SK-MEL-28	109.6969
RPMI-8226	102.7508	SK-MEL-5	84.01701
SR	105.797	UACC-257	94.24042

A549/ATCC	94.35083	UACC-62	93.59341
EKVX	88.12917	IGROV1	112.4906
HOP-62	101.2321	OVCAR-3	117.612
HOP-92	90.9713	OVCAR-4	103.8928
NCI-H226	100.1811	OVCAR-5	106.5526
NCI-H23	102.7066	OVCAR-8	101.3904
NCI-H322M	106.6053	NCI/ADR-RES	102.5993
NCI-H460	129.7829	SK-OV-3	97.63181
NCI-H522	92.4755	786-0	94.17974
COLO 205	117.9825	A498	94.96873
HCC-2998	102.8052	ACHN	110.7426
HCT-116	103.1825	CAKI-1	93.31125
HCT-15	103.8747	RXF 393	106.8724
HT29	101.9853	SN12C	99.31207
KM12	109.0838	TK-10	94.45847
SW-620	117.6317	UO-31	96.16993
SF-268	107.1848	PC-3	100.3677
SF-295	88.7578	DU-145	114.7475
SF-539	104.6174	MCF7	91.65062
SNB-19	98.24533	MDA-MB-231/ATCC	102.3125
SNB-75	86.82521	HS 578T	95.11296
U251	95.87251	BT-549	100.9156
LOX IMVI	102.5364	T-47D	101.0277
MALME-3M	100.3306	MDA-MB-468	117.079

Table A.3 NCI-60 growth percent data for 2-8-ctrl.

Cell Line	Growth %	Cell Line	Growth %
CCRF-CEM	80.08967	M14	81.38701
HL-60(TB)	87.77778	MDA-MB-435	75.64847
K-562	85.30199	SK-MEL-2	104.186
MOLT-4	61.53906	SK-MEL-28	94.70148
RPMI-8226	76.4608	SK-MEL-5	70.29076
SR	56.88229	UACC-257	90.88475
A549/ATCC	86.90524	UACC-62	71.60783
EKVX	99.03791	IGROV1	102.5894
HOP-62	78.98337	OVCAR-3	103.3395
HOP-92	87.88786	OVCAR-4	94.01373
NCI-H226	80.7429	OVCAR-5	109.526
NCI-H23	95.33668	OVCAR-8	87.20577
NCI-H322M	98.63423	NCI/ADR-RES	84.08201

NCI-H460	100.4909	SK-OV-3	94.31959
NCI-H522	88.65572	786-0	101.6181
COLO 205	93.57932	A498	118.8105
HCC-2998	93.95503	ACHN	85.59697
HCT-116	76.88738	CAKI-1	84.72954
HCT-15	72.8041	RXF 393	78.36951
HT29	75.15594	SN12C	95.55759
KM12	76.82209	TK-10	96.26977
SW-620	105.4769	UO-31	86.51414
SF-268	100.8542	PC-3	50.45013
SF-295	78.07075	DU-145	102.7077
SF-539	93.31195	MCF7	86.28173
SNB-19	80.69733	MDA-MB-231/ATCC	78.91035
SNB-75	115.9139	HS 578T	84.97567
U251	91.21044	BT-549	102.5674
LOX IMVI	71.47109	T-47D	83.89252
MALME-3M	82.68546	MDA-MB-468	80.52109

Table A.4 NCI-60 growth percent data for 2-11.

Cell Line	Growth %	Cell Line	Growth %
CCRF-CEM	67.17969	MDA-MB-435	64.77303
HL-60(TB)	66.85271	SK-MEL-2	97.50755
K-562	51.64845	SK-MEL-28	96.83083
MOLT-4	62.19572	SK-MEL-5	57.8364
RPMI-8226	64.65131	UACC-257	101.0219
SR	73.81824	UACC-62	57.16341
A549/ATCC	80.17399	IGROV1	88.38908
EKVX	75.48736	OVCAR-3	75.22275
HOP-62	102.0096	OVCAR-4	64.77878
HOP-92	75.88859	OVCAR-5	108.2028
NCI-H226	75.71758	OVCAR-8	91.74563
NCI-H322M	83.68665	NCI/ADR-RES	81.87156
NCI-H460	87.62971	SK-OV-3	131.7468
NCI-H522	85.00758	786-0	94.56412
COLO 205	103.7883	A498	92.82081
HCC-2998	94.4573	ACHN	65.79005
HCT-116	78.58492	CAKI-1	56.19209
HCT-15	66.0575	RXF 393	99.83317
HT29	81.28194	SN12C	77.29562
KM12	72.90117	TK-10	120.0032

SW-620	90.07411	UO-31	78.189
SF-268	95.5888	PC-3	68.82809
SF-295	70.69965	DU-145	97.5909
SF-539	94.50652	MCF7	74.69832
SNB-19	87.15623	MDA-MB-231/ATCC	66.4335
SNB-75	86.68801	HS 578T	93.85314
U251	80.42969	BT-549	106.708
LOX IMVI	68.45231	T-47D	63.26835
MALME-3M	88.63636	MDA-MB-468	66.73982
M14	89.199		

Table A.5 NCI-60 growth percent data for 2-12.

Cell Line	Growth %	Cell Line	Growth %
CCRF-CEM	45.20275	M14	66.77203
HL-60(TB)	63.77484	MDA-MB-435	58.57324
K-562	46.80355	SK-MEL-2	81.35105
MOLT-4	31.48807	SK-MEL-28	87.70969
RPMI-8226	38.99338	SK-MEL-5	26.89403
SR	38.25283	UACC-257	84.34325
A549/ATCC	58.15198	UACC-62	67.36343
EKVX	66.63545	IGROV1	94.07687
HOP-62	86.37241	OVCAR-3	92.58561
HOP-92	65.16836	OVCAR-4	59.56133
NCI-H226	111.8951	OVCAR-5	107.0515
NCI-H23	72.31483	OVCAR-8	83.64378
NCI-H322M	89.99897	NCI/ADR-RES	71.52571
NCI-H460	71.84324	SK-OV-3	85.05449
NCI-H522	73.92199	786-0	78.75193
COLO 205	73.1841	A498	104.9649
HCC-2998	78.31731	ACHN	74.6474
HCT-116	43.25672	CAKI-1	61.9449
HCT-15	48.5912	RXF 393	53.56602
HT29	71.9953	SN12C	75.88205
KM12	55.16704	TK-10	84.5608
SW-620	82.84913	UO-31	46.44274
SF-268	84.37074	PC-3	22.60716
SF-295	51.98768	DU-145	92.97258
SF-539	83.5911	MCF7	67.33223
SNB-19	70.76356	MDA-MB-231/ATCC	70.73573

SNB-75	88.68784	HS 578T	75.16163
U251	53.11935	BT-549	78.48299
LOX IMVI	53.62488	T-47D	42.96681
MALME-3M	61.87368	MDA-MB-468	34.99468

Table A.6 NCI-60 growth percent data for 2-13.

Cell Line	Growth %	Cell Line	Growth %
CCRF-CEM	63.82058	M14	63.01402
HL-60(TB)	53.96292	MDA-MB-435	59.12778
K-562	57.10645	SK-MEL-2	85.78441
MOLT-4	50.28518	SK-MEL-28	95.30104
RPMI-8226	59.61186	SK-MEL-5	21.05891
SR	26.08929	UACC-257	75.57229
A549/ATCC	76.3923	UACC-62	73.29809
EKVX	85.22968	IGROV1	75.20551
HOP-62	97.77822	OVCAR-3	86.0537
HOP-92	62.58652	OVCAR-4	74.4208
NCI-H226	71.44306	OVCAR-5	96.52991
NCI-H23	68.92115	OVCAR-8	85.05308
NCI-H322M	101.9847	NCI/ADR-RES	86.95063
NCI-H460	79.59184	SK-OV-3	94.4271
NCI-H522	68.1077	786-0	89.19335
COLO 205	74.76314	A498	123.5844
HCC-2998	75.09186	ACHN	94.66164
HCT-116	51.63013	CAKI-1	71.54398
HCT-15	55.38614	RXF 393	58.9457
HT29	72.85073	SN12C	74.22859
KM12	71.818	TK-10	104.6645
SW-620	94.86275	UO-31	73.53316
SF-268	108.1505	PC-3	44.41854
SF-295	54.23086	DU-145	96.56122
SF-539	86.0093	MCF7	55.58938
SNB-19	72.00812	MDA-MB-231/ATCC	74.90477
SNB-75	93.21803	HS 578T	70.30935
U251	51.76763	BT-549	69.32681
LOX IMVI	54.41691	T-47D	69.82412
MALME-3M	87.64731	MDA-MB-468	37.30592

Appendix B.

Supplementary Information for Chapter 3

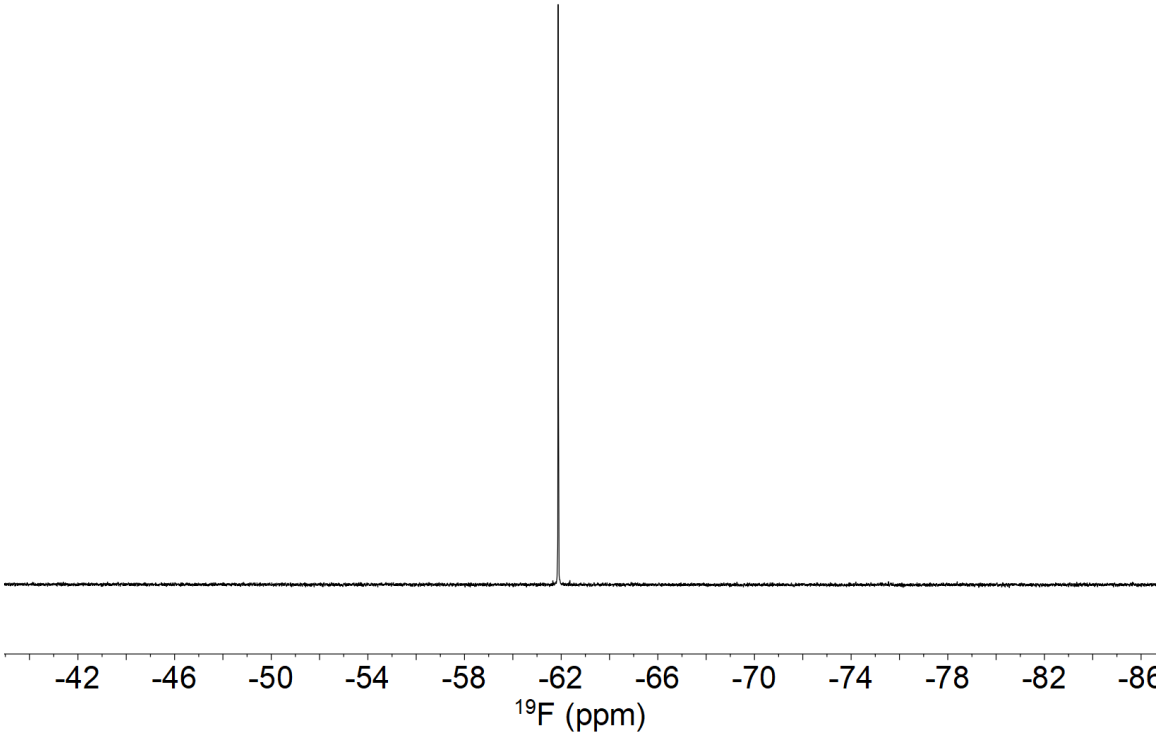

Figure B.1 ^{19}F NMR of 4-(trifluoromethyl)imidazole in PBS.

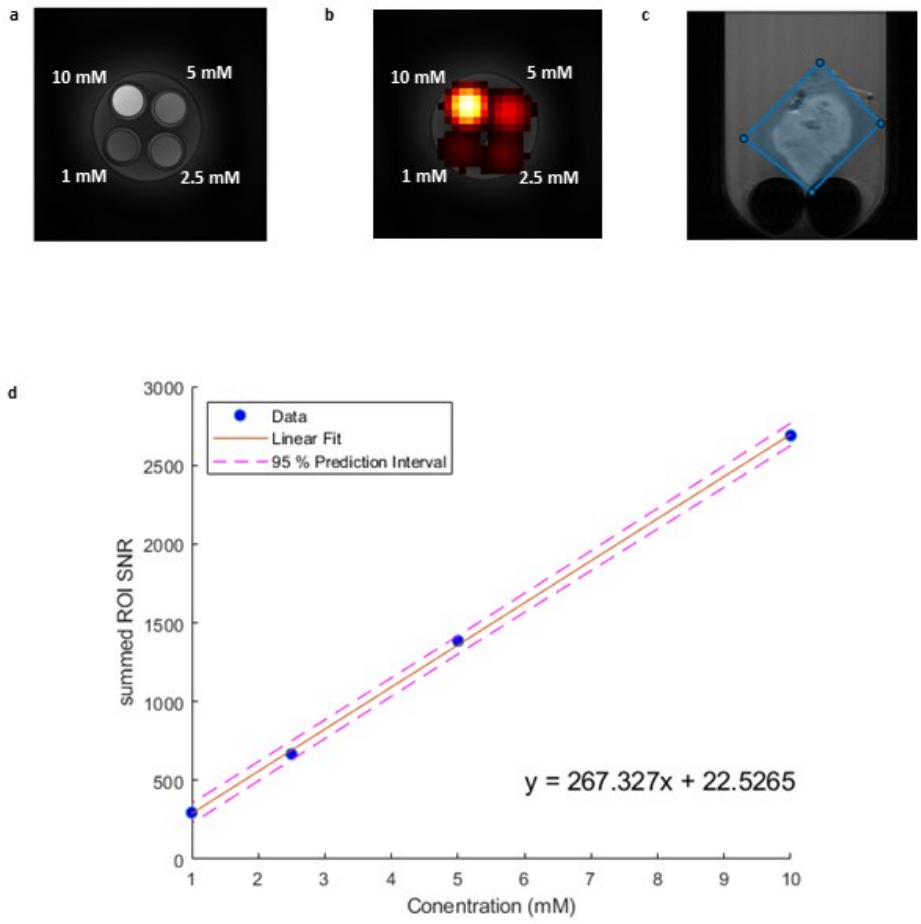

Figure B.2 **a) ^{1}H CHESS image of NMR tubes of varied concentration of 3-1 in PBS nested in a test tube filled with PBS. b) ^{19}F CSI SNR magnitude overlay. c) Tumour ROI. d) Calibration curve of SNR vs concentration generated from the data in a) and b).**

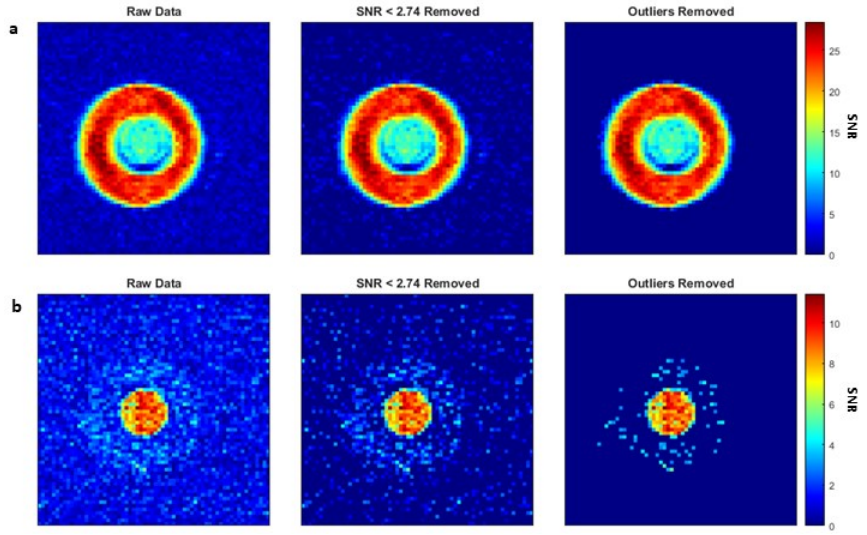

Figure B.3 **Heat maps displaying each step of noise reduction processing of ^{19}F CHESS images highlighting the a) Ru(III) signal and b) Ru(II) signal of 3-1 in a coaxial tube arrangement.**

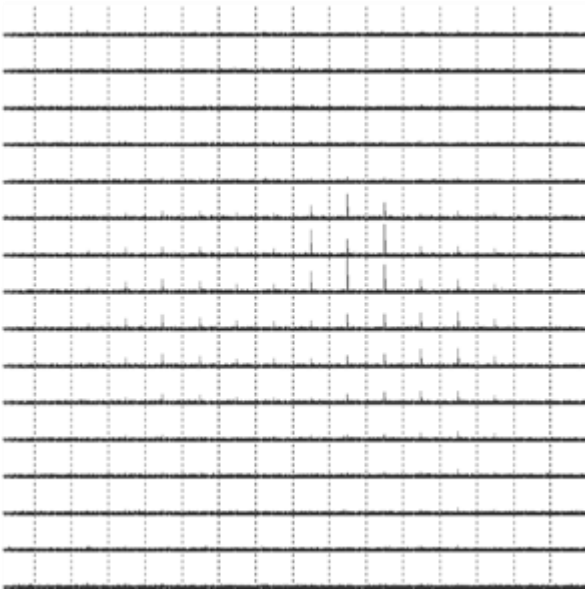

Figure B.4 **^{19}F CSI matrix of a piece of beef liver following injection of a 4 mM PBS solution of Ru(III)(ImCF$_3$)$_2$ with a TR of 100 ms.**

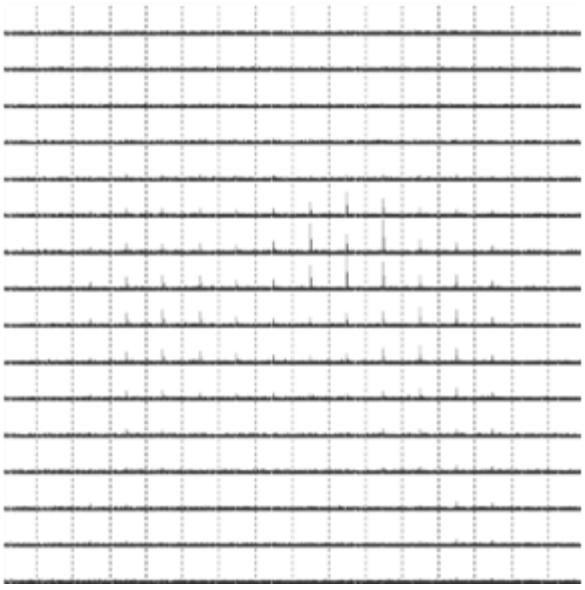

Figure B.5 **^{19}F CSI matrix of a piece of beef liver following injection of a 4 mM PBS solution of Ru(III)(ImCF$_3$)$_2$ with a TR of 300 ms.**

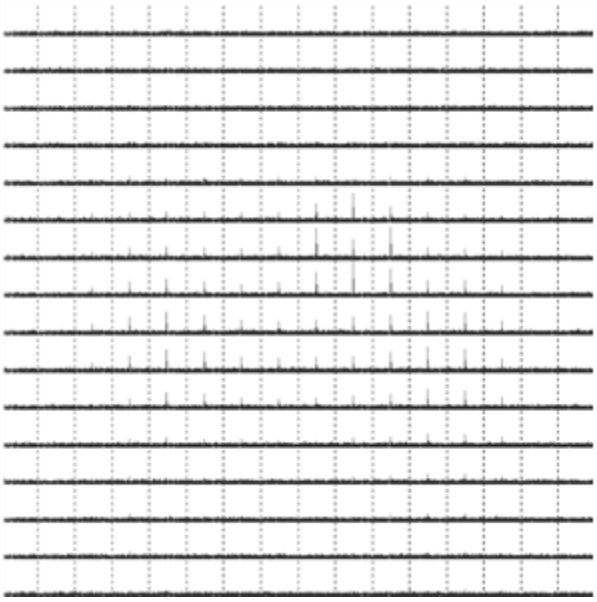

Figure B.6 **^{19}F CSI matrix of a piece of beef liver following injection of a 4 mM PBS solution of Ru(III)(ImCF$_3$)$_2$ with a TR of 1000 ms.**

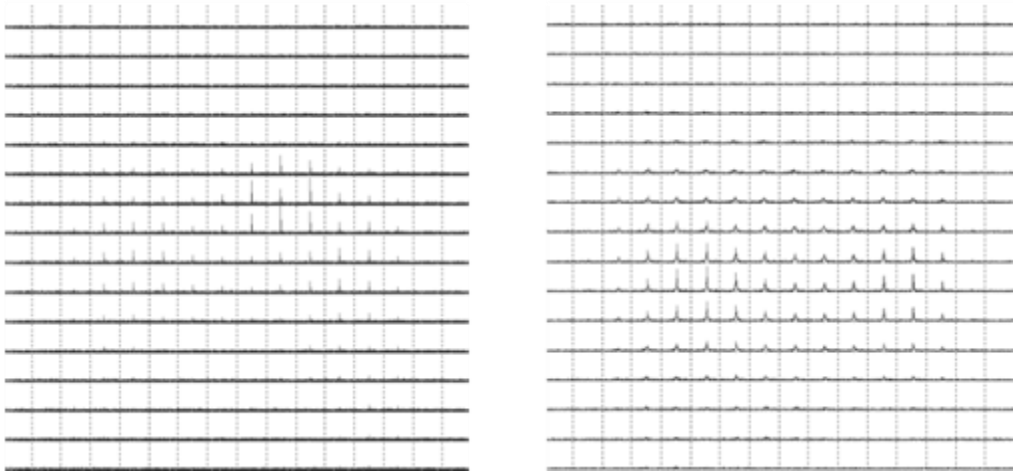

Figure B.7 **^{19}F CSI matrix of an MBA-MB-231 human breast adenocarcinoma tumour following an injection of a 4 mM PBS solution of a) Ru(III)(ImCF$_3$)$_2$ and b) Ru(II)(ImCF$_3$)$_2$. Following the injection, the tumour was placed in a test tube containing the same solution for imaging.**

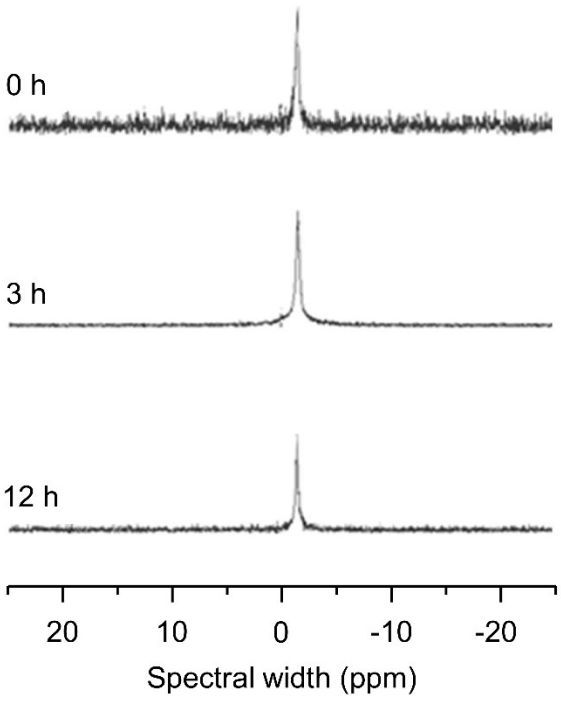

Figure B.8 **Individual ^{19}F CSI spectra from surrounding solution of MBA-MB-231 human breast adenocarcinoma tumour tissue at 0, 3, and 12 h following injection of a 4 mM solution of Ru(III)(ImCF$_3$)$_2$.**

Appendix C.

Supplementary Information for Chapter 4

Table C.1 PLGA NP microwave digestion parameters.

Stage		Temperature	Ramp time (min)	Hold time (min)	Pressure (psi)	Power (watts)	Stirring
1		200	3:00	4:00	300	300	Medium
	Temperature profile: “ramp to temp”						

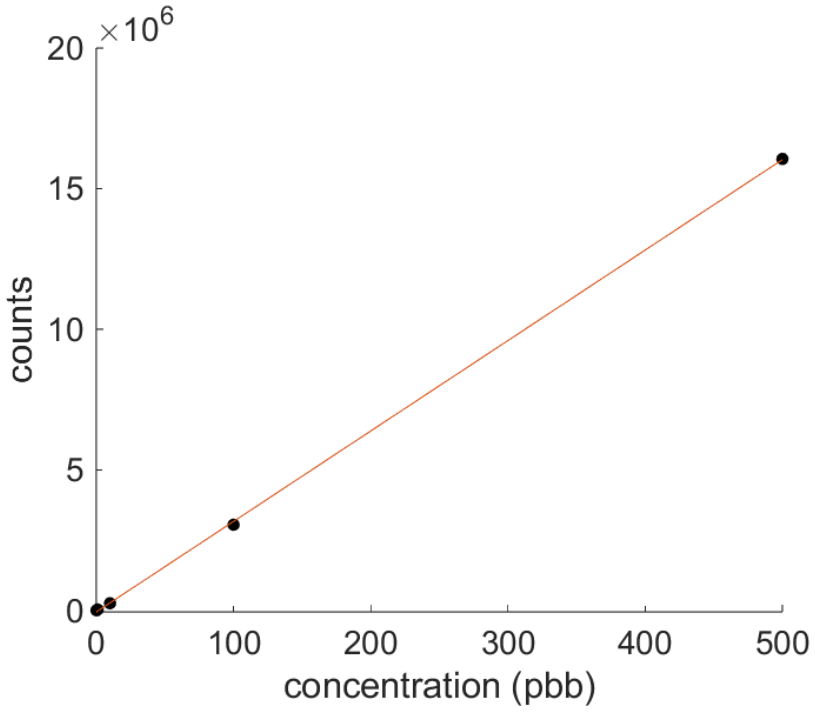

Figure C.1 ICP-MS calibration curve generated from ruthenium standard solutions.

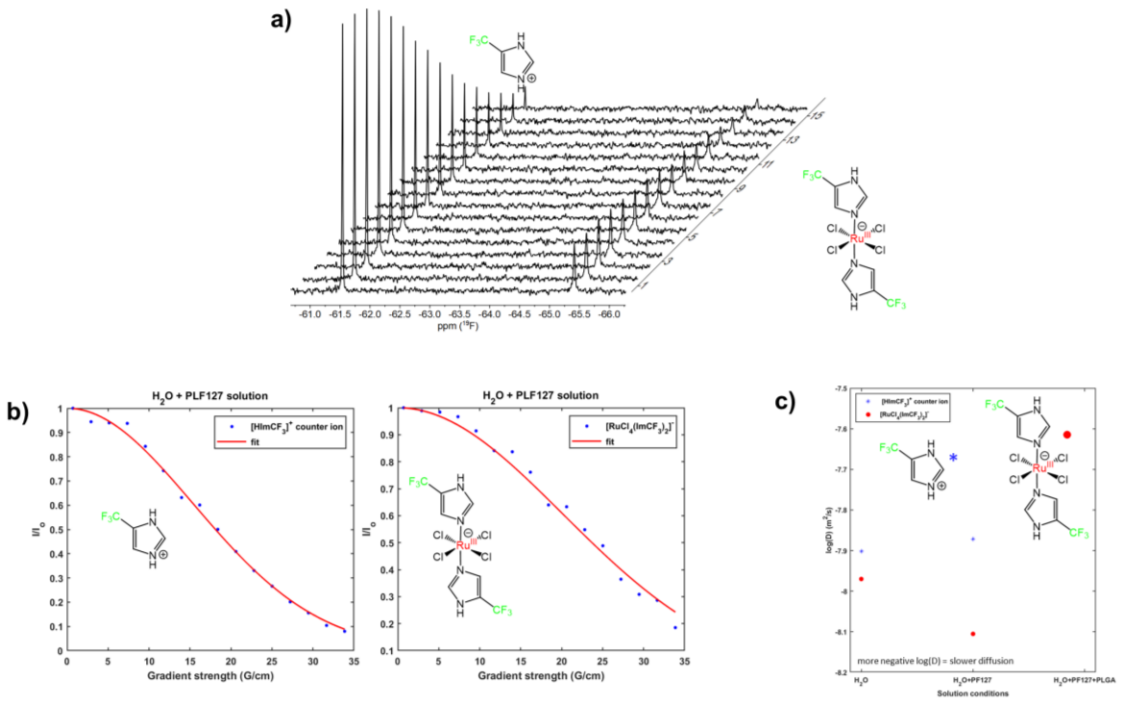

Figure C.2 **a) Examples of a series of ^{19}F DOSY experiments for 3-1 in an aqueous PF127 solution. b) A gaussian git to the decay of the intensities from a). c) Diffusion constants in water and aqueous PF127. Experiments of the NP formulation were not possible due to paramagnetic relaxation enhancement.**

Appendix D.

Supplementary Information for Chapter 5

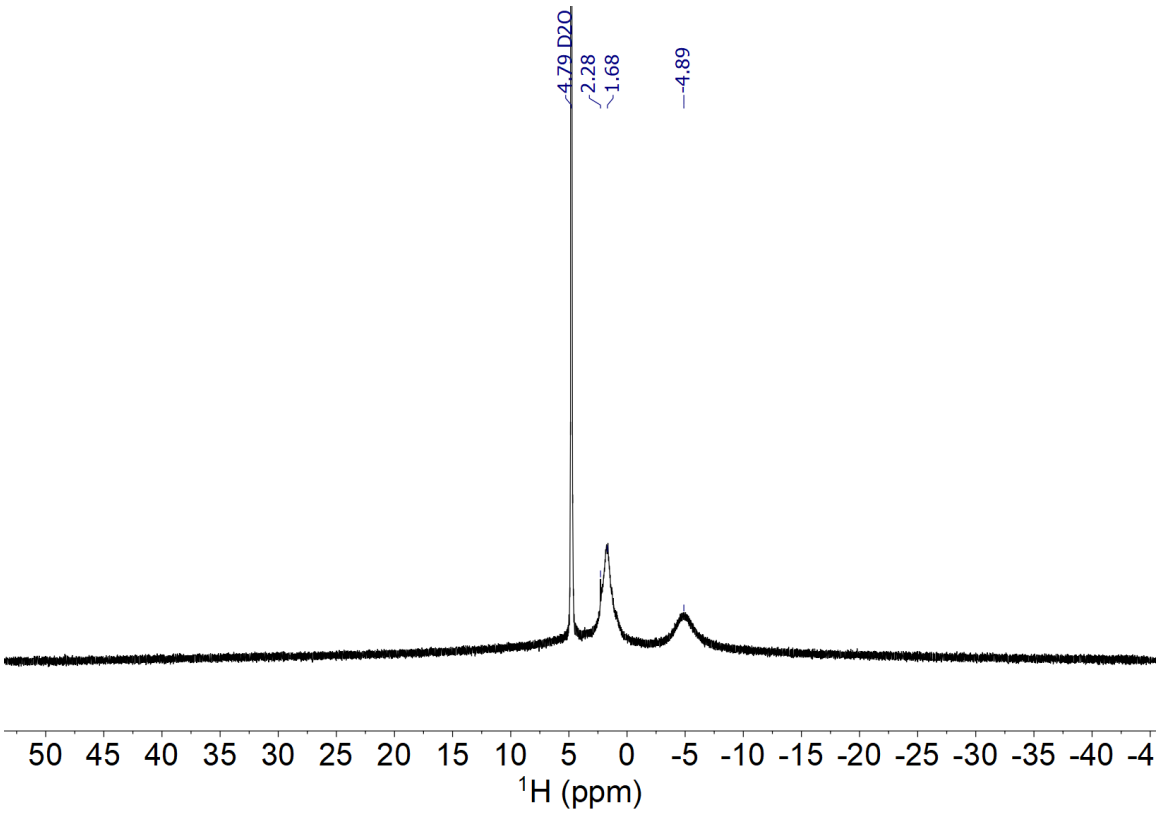

Figure D.1 ^{1}H NMR of CasIII-ia in D_2O.

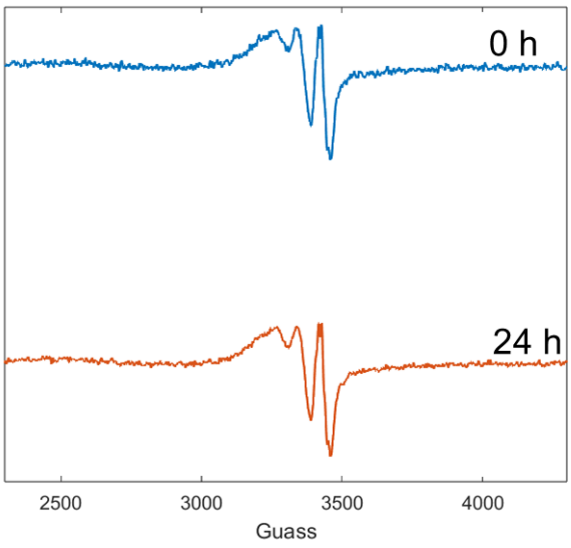

Figure D.2 **Room temperature EPR spectra of CasIII-ia in PBS 0 and 24 hours after dissolution.**

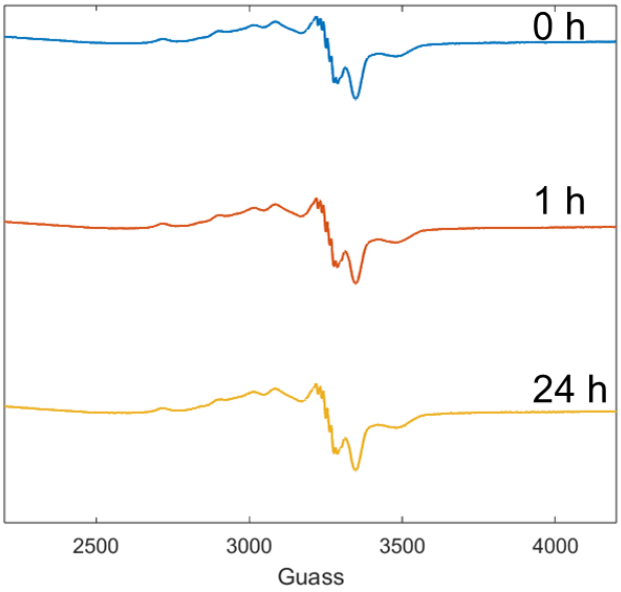

Figure D.3 **Frozen solution EPR spectra of CasIII-ia in PBS 0, 1, and 24 hours after dissolution.**

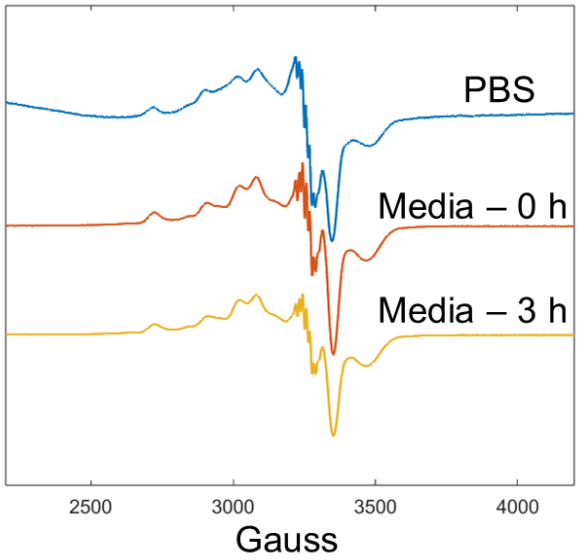

Figure D.4 **Frozen solution EPR spectra of CasIII-ia in cell culture media (DMEM) at 0 and 3 hours following dissolution and in PBS for comparison.**